

# **Relevance of *in vitro* metabolism models for PET radiotracer development**

Inaugural-Dissertation

zur

Erlangung des Doktorgrades

der Mathematisch-Naturwissenschaftlichen Fakultät

der Universität zu Köln

vorgelegt von

Daniela Schneider

aus Aalen

Druckerei der Forschungszentrum Jülich GmbH, Jülich

2017

Berichterstatter:

Prof. Dr. J. Ermert

Prof. Dr. U. Baumann

Tag der letzten mündlichen Prüfung:

05.07.2017

Diese Arbeit wurde im Zeitraum von Februar 2014 bis April 2017 am Institut für Neurowissenschaften und Medizin (Teilinstitute INM-2 und INM-5) des Forschungszentrums Jülich unter Anleitung von Herrn Prof. Dr. J. Ermert angefertigt.



## Abstract

The application of positron emission tomography (PET) as a tool for molecular imaging of the brain is limited by the availability of suitable radiotracers. In radiotracer development, success or failure of a novel compound is determined by numerous physicochemical and pharmacological factors of which metabolism represents a particularly important one. Hence, an initial assessment of the metabolic properties of a candidate radiotracer at an early stage of the development process prior to expensive and time-consuming animal studies is desirable. Various *in vitro* metabolism models are available for the evaluation of candidate drugs in the pharmaceutical sector, however, since drug and tracer applications differ fundamentally (especially with regard to the amount of administered substance) the question rises whether these models are also capable of providing relevant and valid data for the evaluation of radiotracers. In the present work, this question was examined using three xanthine-derived adenosine A<sub>1</sub> receptor (A<sub>1</sub>AR) ligands, 8-cyclopentyl-3-(3-fluoropropyl)-1-propylxanthine (CPFPX), 8-cyclobutyl-3-(3-fluoropropyl)-1-propylxanthine (CBX) and 3-(3-fluoropropyl)-8-(1-methylcyclobutyl)-1-propylxanthine (MCBX) as model compounds. Radioligands for imaging adenosine receptors *in vivo* are of particular interest for biomedical research since this receptor system has been associated with numerous physiological functions (e.g. regulation of sleep) and pathophysiological conditions (e.g. Alzheimer's and Parkinson's disease). *In vivo* metabolic stability and metabolite patterns of the three A<sub>1</sub>AR ligands were investigated in the rat model and compared to *in vitro* data generated in rat liver microsomes. Prior to the characterisation of the microsomal metabolism of the test compounds, the influence of incubation conditions on the *in vitro* test results was assessed and the microsomal assay was optimised in order to provide physiologically relevant data. Metabolic activity in liver microsomes was strongly influenced by the pH value of the buffer medium and the type and concentration of the organic solvent used to solubilise the test compounds. Variations of incubation matrix composition resulted in variations of individual substrate depletion values of up to 500%, whereas substrate depletion ratios proved to be highly constant. *In vitro* microsomal half-lives ( $t_{1/2}$ ) of the compounds were determined and expressed as ratios for the purpose of later *in vitro-in vivo* comparison. The  $t_{1/2}$  ratios ( $\pm$  SE) of CBX:CPFPX, MCBX:CPFPX and CBX:MCBX were  $3.1 \pm 0.11$ ,  $1.4 \pm 0.029$  and  $2.2 \pm 0.033$ . *In vivo* metabolic stability of the <sup>18</sup>F-labelled compounds were assessed in anaesthetised rats via blood analysis. Plasma clearance (CL) values were calculated and expressed as inversed ratios to facilitate direct comparison with *in vitro*  $t_{1/2}$  ratios. The inversed CL ratios ( $\pm$  SE) of [<sup>18</sup>F]CBX:[<sup>18</sup>F]CPFPX, [<sup>18</sup>F]MCBX:[<sup>18</sup>F]CPFPX and [<sup>18</sup>F]CBX:[<sup>18</sup>F]MCBX were  $2.6 \pm 0.12$ ,  $0.82 \pm 0.019$  and  $3.1 \pm 0.15$ . *In vitro*  $t_{1/2}$  ratios deviated between 19 and 71% from inverse CL ratios. These deviations can be considered small in view of the reduced complexity of the microsomal model and the multitude of physiological parameters affecting *in vivo* pharmacokinetics of a substance. Visual comparison of metabolite profiles generated *in vitro* and *in vivo* revealed a high degree of similarity. In conclusion, both quantitative and qualitative aspects of radiotracer metabolism could be reasonably well predicted by microsomal data. This result encourages the implementation of *in vitro* metabolism studies as an integral part of PET radiotracer development.



## Kurzzusammenfassung

Der Einsatz der Positronenemissionstomographie (PET) für die molekulare Bildgebung des Gehirns wird durch die Verfügbarkeit geeigneter Radiotracer limitiert. Bei der Entwicklung von Radiotracern entscheiden zahlreiche physikochemische und physiologische Faktoren über Erfolg oder Misserfolg einer neuen Verbindung, allen voran der Metabolismus der Substanz im Körper. Deshalb ist eine erste Beurteilung der metabolischen Eigenschaften des potentiellen Radiotracers in einer frühen Entwicklungsphase noch vor Durchführung teurer und aufwendiger Tierstudien wünschenswert. Der Pharmabranche stehen zahlreiche *in vitro*-Modelle zur Vorhersage des Metabolismus von Medikamentenkandidaten zur Verfügung, allerdings stellt sich die Frage, ob diese Modelle auch im Hinblick auf die Evaluierung von Radiotracern valide Daten liefern können, da sich Medikamente und Radiotracer in ihrer Anwendung fundamental unterscheiden (besonders hinsichtlich der verabreichten Substanzmengen). In der vorliegenden Arbeit wurde diese Fragestellung am Beispiel dreier xanthinbasierter Adenosin A<sub>1</sub> Rezeptorliganden (A<sub>1</sub>AR-Liganden), 8-Cyclopentyl-3-(3-fluorpropyl)-1-propylxanthin (CPFPX), 8-Cyclobutyl-3-(3-fluorpropyl)-1-propylxanthin (CBX) und 3-(3-Fluorpropyl)-8-(1-methylcyclobutyl)-1-propylxanthin (MCBX) untersucht. Radioliganden für die *in vivo*-Bildgebung von Adenosinrezeptoren sind von besonderem Interesse für die biomedizinische Forschung, da dieses Rezeptorsystem mit zahlreichen physiologischen Funktionen (z.B. der Schlafregulation) aber auch mit pathologischen Zuständen (z.B. der Alzheimer- und Parkinson-Krankheit) in Zusammenhang gebracht wird. Die metabolische Stabilität der drei A<sub>1</sub>AR-Liganden und ihre Metabolitenprofile wurden *in vivo* in der Ratte untersucht und mit *in vitro*-Daten verglichen, die mittels Rattenlebermikrosomen gewonnen wurden. Vor der eigentlichen Charakterisierung des mikrosomalen Metabolismus der Testsubstanzen wurde der Einfluss der Inkubationsbedingungen auf die Resultate der *in vitro*-Tests untersucht und das Mikrosomen-Assay im Hinblick auf die Generierung physiologisch relevanter Daten optimiert. Die metabolische Aktivität der Lebermikrosomen wurde stark vom pH-Wert des Puffers und der Art und Konzentration des zur Auflösung der Testsubstanzen verwendeten Lösungsmittels beeinflusst. Änderungen in der Zusammensetzung der Inkubationsmatrix führten zu einer Veränderung der individuellen Abbauraten der Verbindungen um bis zu 500%, während die Zahlenverhältnisse der Abbauraten zueinander sehr konstant blieben. Die mikrosomalen *in vitro*-Halbwertszeiten ( $t_{1/2}$ ) der Verbindungen wurden bestimmt und zum Zwecke des *in vitro-in vivo*-Vergleichs als Quotienten ausgedrückt. Die ermittelten  $t_{1/2}$ -Quotienten ( $\pm$  Standardfehler) von CBX:CPFPX, MCBX:CPFPX und CBX:MCBX betragen  $3.1 \pm 0.11$ ,  $1.4 \pm 0.029$  und  $2.2 \pm 0.033$ . Die metabolische *in vivo* Stabilität der <sup>18</sup>F-markierten Verbindungen wurde an narkotisierten Ratten mittels Blutanalyse bestimmt. Die individuellen Plasma Clearance (CL)-Werte der Radiotracer wurden berechnet und als inverse Quotienten ausgedrückt, um einen direkte Vergleich mit den *in vitro*  $t_{1/2}$ -Quotienten zu ermöglichen. Die inversen CL-Quotienten ( $\pm$  Standardfehler) von [<sup>18</sup>F]CBX:[<sup>18</sup>F]CPFPX, [<sup>18</sup>F]MCBX:[<sup>18</sup>F]CPFPX und [<sup>18</sup>F]CBX:[<sup>18</sup>F]MCBX betragen  $2.6 \pm 0.12$ ,  $0.82 \pm 0.019$  und  $3.1 \pm 0.15$ . Die Abweichung der *in vitro*  $t_{1/2}$ -Quotienten von den inversen CL-Quotienten lag zwischen 19 und 71%. In Anbetracht der reduzierte Komplexität des Mikrosomenmodells und der Vielzahl physiologischer Parameter, welche die *in vivo*-Pharmakokinetik einer Substanz beeinflussen, können diese

Abweichungen als geringfügig erachtet werden. Der visuelle Vergleich der *in vitro*- und *in vivo*-Metabolitenprofile erbrachte einen hohen Grad an Übereinstimmung. Zusammenfassend lässt sich sagen, dass anhand der Daten aus Mikrosomenstudien sowohl quantitative als auch qualitative Aspekte des Metabolismus der Radiotracer mit angemessener Genauigkeit vorhergesagt werden konnten. Dieses Ergebnis ermutigt zur generellen Einbeziehung von *in vitro*-Metabolismusstudien in den Prozess der PET-Radiotracer-Entwicklung.

---

## List of abbreviations

[ <sup>18</sup> F]FBA	4-[ <sup>18</sup> F]fluorobenzoic acid
[ <sup>18</sup> F]FBAM	<i>N</i> -[6-(4-[ <sup>18</sup> F]fluorobenzylidene)aminoxyhexyl]maleimide
[ <sup>18</sup> F]FBEM	<i>N</i> -[2-(4-[ <sup>18</sup> F]fluorobenzamido)ethyl]maleimide
[ <sup>18</sup> F]FDG	2-deoxy-2-[ <sup>18</sup> F]fluoro-D-glucose
[ <sup>18</sup> F]SFB	<i>N</i> -succinimidyl 4-[ <sup>18</sup> F]fluorobenzoate
[L]	concentration of free ligand
[LR]	concentration of ligand-receptor complex
[R]	concentration of free (unbound) receptor
1TCM	one-tissue compartment model
2TCM	two-tissue compartment model
A <sub>1</sub> AR	adenosine A <sub>1</sub> receptor
A <sub>2A</sub> AR	adenosine A <sub>2A</sub> receptor
ABC	ATP-binding cassette
ACD	annihilation coincidence detection
ACN	acetonitrile
ADME	absorption, distribution, metabolism and excretion
ANOVA	analysis of variance
AR	Adenosine receptor
ATP	Adenosine triphosphate
AUC	area under the curve
BBB	blood-brain barrier
B <sub>max</sub>	maximum binding capacity
BP <sub>ND</sub>	binding potential
Bq	becquerel (unit of radioactivity)
CAT	catalase
cbl	cerebellar cortex
CBX	8-cyclobutyl-3-(3-fluoropropyl)-1-propylxanthine
CCPA	2-chloro-N <sup>6</sup> -cyclopentyladenosine
CL	clearance (plasma)
CNS	central nervous system
C <sub>p</sub>	plasma compartment
CPA	N <sup>6</sup> -cyclopentyladenosine
CPFPX	8-cyclopentyl-3-(3-fluoropropyl)-1-propylxanthine

CPR	cytochrome P450 reductase
CRS	cofactor regeneration system
CT	computed tomography
ctx	neocortex
CYP	Cytochrome P450 enzyme
Da	Dalton (unified atomic mass unit)
DCE-MRI	dynamic contrast-enhanced magnetic resonance imaging
DLM	dog liver microsomes
DMF	<i>N,N</i> -dimethylformamide
DMSO	dimethyl sulfoxide
DPCPX	8-cyclopentyl-1,3-dipropylxanthine
DPI	diphenyleneiodonium chloride
EDTA	ethylenediamine-tetraacetic acid
eV	electronvolt
FMO	flavin-containing monooxygenase
G6P	glucose-6-phosphate
G6P-DH	glucose-6-phosphate dehydrogenase
GMP	good manufacturing practices
GPCR	G protein-coupled receptor
GTP	guanosine-5'-triphosphate
HAc	acetic acid
HEPES	4-(2-hydroxyethyl)-1-piperazineethanesulfonic acid
hg	Harderian gland
hip	hippocampus
HLM	human liver microsomes
HPLC	high-performance liquid chromatography
HPLC-MS	HPLC coupled with mass spectrometry
HPLC-UV/Vis	HPLC coupled with ultraviolet and visible spectroscopy
i.v.	intravenous
IC50	half maximal inhibitory concentration
k	retention factor
$K_1$ - $k_4$	transfer/fractional rate constants
$K_D$	equilibrium dissociation constant
$K_i$	inhibition constant
$k_{off}$	dissociation rate constant

---

$k_{on}$	association rate constant
log D	distribution coefficient
log P	octanol-water partition coefficient
MCBX	3-(3-fluoropropyl)-8-(1-methylcyclobutyl)-1-propylxanthine
MeOH	methanol
MLM	mouse liver microsomes
MOPS	4-morpholinepropanesulfonic acid
MPLM	mini pig liver microsomes
MRS	magnetic resonance spectroscopy
MRT	mean residence time
MW	molecular weight
n.c.a.	no-carrier-added
NADP <sup>+</sup>	$\beta$ -nicotinamide adenine dinucleotide 2'-phosphate (oxidised form)
NADPH	$\beta$ -nicotinamide adenine dinucleotide 2'-phosphate (reduced form)
NaOH	sodium hydroxide
NCA	non-compartmental analysis
NMR	nuclear magnetic resonance
NOS	nitric oxide synthase
NOX	NADPH oxidase
p.i.	post injection
P450	Cytochrome P450 enzyme
PET	positron emission tomography
P-gp	P-glycoprotein
PK	pharmacokinetics
R <sup>2</sup>	coefficient of determination
rcf	relative centrifugal force
R <sub>f</sub>	retardation factor
RLM	rat liver microsomes
RMLM	rhesus monkey liver microsomes
ROI	region of interest
ROS	reactive oxygen species
R-PIA	( <i>R</i> )-N <sup>6</sup> -(2-phenylisopropyl)adenosine
rpm	revolutions per minute
SAR	structure–activity relationship
SD	standard deviation

SE	standard error
$S_N2$	nucleophilic substitution (bimolecular)
$S_NAr$	aromatic nucleophilic substitution
SOD	superoxide dismutase
SPECT	single photon emission computed tomography
SUV	standardised uptake value
$t_0$	dead time
$t_{1/2}$	half-life
TAC	time-activity curve
TBAB	tetra-n-butylammonium bromide
th	thalamus
TLC	thin-layer chromatography
TPSA	topological polar surface area
$t_R$	retention time
TRIS	2-amino-2-(hydroxymethyl)propane-1,3-diol
UGT	UDP-glucuronosyltransferase
$v_0$	initial velocity
$V_d$	volume of distribution (plasma)
$V_{ND}$	distribution volume of non-displaceable uptake (brain)
$V_S$	specific distribution volume in brain
$V_T$	total distribution volume in brain

---

# Contents

<b>1</b>	<b>Introduction.....</b>	<b>1</b>
1.1	Molecular imaging in neuroscience .....	1
1.2	Principles of positron emission tomography .....	2
1.3	Radiolabelling with <sup>18</sup> F .....	4
1.4	PET radiotracers for molecular neuroimaging.....	8
1.4.1	Radiotracer development process .....	8
1.4.2	Key criteria for PET radiotracers targeting neuroreceptors .....	11
1.5	Evaluation of radiotracer metabolism.....	14
1.5.1	Metabolism of xenobiotics .....	14
1.5.2	<i>In vitro</i> metabolism studies.....	15
1.5.3	<i>In vivo</i> pharmacokinetic studies.....	19
1.6	Neuroreceptor imaging .....	24
1.6.1	Adenosine receptors.....	24
1.6.2	Ligand-receptor interactions.....	26
1.6.3	<i>In vitro</i> radioligand binding studies .....	27
1.6.4	<i>In vivo</i> radiotracer binding studies .....	29
1.6.5	Compartmental models for <i>in vivo</i> radiotracer binding studies .....	29
1.6.6	Logan graphical analysis .....	32
<b>2</b>	<b>Aims and Objectives.....</b>	<b>33</b>
<b>3</b>	<b>Materials and Methods.....</b>	<b>36</b>
3.1	Chemicals.....	36
3.2	Substrates, reference standards and precursors .....	36
3.3	<i>In vitro</i> metabolism .....	38
3.3.1	Microsomes .....	38
3.3.2	General microsomal incubation procedures .....	39
3.3.3	Evaluation of incubation conditions.....	39
3.3.4	Stability assessment of NADPH .....	42
3.3.5	<i>In vitro</i> microsomal half-life determination.....	42
3.3.6	Species differences in microsomal metabolism .....	43
3.3.7	Enone metabolite formation.....	44

---

<b>3.4</b>	<b>Radiotracer production.....</b>	<b>44</b>
<b>3.5</b>	<b><i>In vitro</i> autoradiography.....</b>	<b>45</b>
<b>3.6</b>	<b><i>In vivo</i> pharmacokinetics.....</b>	<b>45</b>
3.6.1	Animals.....	45
3.6.2	Blood sampling and analysis .....	46
3.6.3	Plasma protein binding.....	47
3.6.4	Brain PET imaging.....	47
3.6.5	Analysis of brain PET data.....	48
<b>3.7</b>	<b>Statistical methods.....</b>	<b>48</b>
3.7.1	Independent t-test.....	49
3.7.2	One-way ANOVA .....	49
<b>4</b>	<b><i>Results and Discussion</i>.....</b>	<b>51</b>
<b>4.1</b>	<b><i>In vitro</i> microsomal metabolism.....</b>	<b>51</b>
4.1.1	Influence of incubation conditions on substrate depletion .....	51
4.1.2	Enzyme stability <i>in vitro</i> .....	58
4.1.3	<i>In vitro</i> metabolic stability of CBX, MCBX and CPFPX.....	65
4.1.4	Species differences in microsomal metabolism .....	68
<b>4.2</b>	<b><i>In vivo</i> pharmacokinetics.....</b>	<b>83</b>
4.2.1	Plasma kinetics .....	83
4.2.2	Plasma protein binding.....	86
4.2.3	<i>In vitro-in vivo</i> comparison of tracer metabolism .....	87
4.2.4	Metabolite analysis .....	89
<b>4.3</b>	<b>Brain kinetics.....</b>	<b>94</b>
4.3.1	<i>In vitro</i> autoradiography .....	94
4.3.2	Brain PET images.....	96
4.3.3	<i>In vivo</i> cerebral kinetics .....	96
4.3.4	Graphical and compartmental analysis of brain PET data .....	99
<b>5</b>	<b><i>Summary and Conclusion</i> .....</b>	<b>103</b>
<b>6</b>	<b><i>References</i> .....</b>	<b>109</b>
<b>7</b>	<b><i>Appendix</i> .....</b>	<b>135</b>
7.1	Definite integral of $C(t)dt$ (Eq. 4) .....	135
7.2	Definite integral of $tC(t)dt$ (Eq. 5) .....	136

# 1 Introduction

## 1.1 Molecular imaging in neuroscience

Since the 1970s, nuclear imaging techniques such as X-ray computed tomography (CT), single photon emission computed tomography (SPECT) and positron emission tomography (PET) revolutionised the field of neuroscience in that they provided the opportunity to visualise brain structure and function in the living, intact organism. Whereas CT is restricted to anatomical imaging, SPECT and PET allow for the detection and characterisation of molecular processes underlying physiological function, which is why they are also referred to as molecular imaging techniques.

Molecular imaging is targeted at biological processes such as gene expression and regulation, signal transduction and protein-protein interactions. Nowadays, a variety of high-affinity, high-selectivity molecular probes are available for visualising diverse molecular targets. Common examples are receptor ligands, enzyme inhibitors, transporter substrates, monoclonal antibodies and recombinant proteins. In addition to the classical nuclear techniques SPECT and PET, several novel molecular imaging approaches were introduced during the past few years, for example nuclear magnetic resonance (NMR)-based techniques such as dynamic contrast-enhanced magnetic resonance imaging (DCE-MRI) and magnetic resonance spectroscopy (MRS), optical techniques such as fluorescence and bioluminescence imaging and sophisticated ultrasound techniques. A number of comprehensive reviews addressing molecular imaging techniques and applications have been published recently [1–9].

In neuroscience, the various receptor systems of the brain represent valuable targets for molecular imaging approaches. High-affinity receptor ligands, equipped with a suitable label for external detection, can be utilised to study *in vivo* receptor expression in normal, healthy subjects as well as changes in receptor density due to pathophysiological conditions. Positron- or gamma-emitting radionuclides (PET/SPECT nuclides) are particularly suitable for labelling ligands aimed at visualising cerebral receptors due to their penetrating radiating which is capable of traversing the skull bone. Although being introduced more than 40 years ago, SPECT and PET still represent the cornerstone of molecular imaging in the field of neuroscience.

When comparing both modalities, PET offers several advantages compared to SPECT, for example higher sensitivity (approx. 2-3 orders of magnitude), higher spatial and temporal resolution and an improved image quality [10]. In addition, generation of quantitative data is technically less challenging with PET than with SPECT [11]. Consequently, PET represents a powerful tool for molecular neuroimaging with increasing importance in basic and clinical neuroscience as well as in pharmacology and drug development [12–22].

## 1.2 Principles of positron emission tomography

PET uses imaging probes (tracers) which are labelled with positron-emitting radionuclides. These radionuclides decay by converting a proton into a neutron while ejecting a positron and an electron neutrino ( $\beta^+$ -decay). The emitted positron travels a short distance in matter (e.g. tissue), losing its kinetic energy by collision and scattering events with electrons and nuclei of the surrounding atoms. After thermalisation, the positron annihilates with an electron resulting in the formation of two 511 keV photons which are emitted simultaneously in nearly opposite directions (Fig. 1A). Near-simultaneous detection of these photons via a circular array of radiation detectors (usually scintillation detectors) indicates the original site of annihilation, which is located on the connecting line between the two hit detectors (Fig. 1B). This technique is referred to as annihilation coincidence detection (ACD). Acquisition of numerous coincidence events provides the basis for a three-dimensional reconstruction of the radiotracer distribution inside the subject's body.

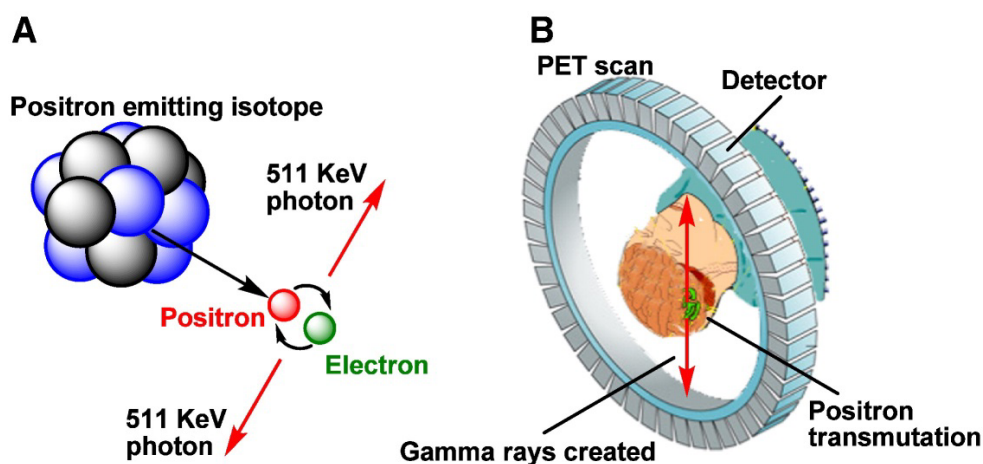


Fig. 1. Principle of PET imaging. (A) Electron-positron annihilation following  $\beta^+$ -decay of a radionuclide. Two 511 keV photons are generated and emitted in opposite directions. (B) Coincidence detection of the two annihilation photons via a circular detector array [23].

An important prerequisite for accurate quantification of radiotracer concentration in various tissues is attenuation correction of the PET raw data. This correction is usually based on separate transmission scans using external  $^{68}\text{Ga}$  sources or CT. Additional data processing steps inevitable for good PET image quality include corrections for scattered radiation, random coincidences and detector dead time. A comprehensive summary on PET image data correction is given in [24].

The spatial resolution achievable in PET imaging is fundamentally limited by two physical aspects of positron decay [25, 26]. First, the emitted positron travels a finite distance in tissue before annihilation occurs. This distance is denoted as positron range and depends on the positron's kinetic energy and the density of the tissue. For commonly used PET nuclides, mean positron ranges in water are in the range of 0.6-3 mm [27]. As a consequence of positron travelling, the exact position of the parent nucleus in the body cannot be localised precisely, resulting in blurring of the PET images. In terms of image quality, radionuclides emitting low-energy positrons are thus preferable. Second, annihilation photons are frequently not emitted at exactly  $180^\circ$  to each other, which is due to a residual momentum of the positron at the moment of annihilation. This effect, known as non-collinearity or acollinearity, results in image blurring that is proportional to the diameter of the detector ring. These inherent effects can be significant for special PET applications such as high-resolution brain imaging or small-animal imaging, however, the main factor that determines spatial resolution of conventional human whole-body PET systems is the size of the individual detector elements [28].

Positron-emitting radionuclides are generally produced with cyclotrons by bombardment of a suitable target material with accelerated charged particles (e.g. protons, deuterons or  $^3\text{He}$  particles). Some commonly used positron emitters are listed in Table 1, along with their decay characteristics. The positron-emitting isotopes of carbon, nitrogen and oxygen ( $^{11}\text{C}$ ,  $^{13}\text{N}$ ,  $^{15}\text{O}$ ) provide the opportunity of isotopic labelling of biomolecules, thus allowing for radiosynthesis of PET radiotracers which exhibit almost identical (bio)chemical characteristics as their non-labelled counterparts (except for minor kinetic isotope effects). However, the extremely short half-lives of these nuclides limit their applicability. Currently,  $^{18}\text{F}$  represents the most important and most widely used positron emitter for PET. The low positron energy of  $^{18}\text{F}$  provides high spatial resolution in imaging and its relatively long half-life of 110 min allows for complex, multi-step radiosynthesis procedures, extended PET protocols and commercial distribution of ready-to-use PET radiotracers. Generally,  $^{18}\text{F}$ -labelled PET radiotracers represent analogous fluoro derivatives of biomolecules in

which a hydrogen atom or a hydroxyl group was substituted by  $^{18}\text{F}$  [29]. In the following section, methods for  $^{18}\text{F}$ -production and  $^{18}\text{F}$ -radiolabelling are discussed in more detail.

Table 1. Properties of some frequently used positron emitters (from [30–32])

Nuclide	Half-life	Positron branching	$E_{\text{max}}$ of positron	Max. positron range in water
		%	keV	mm
$^{11}\text{C}$	20.4 min	99.8	960	3.9
$^{13}\text{N}$	9.97 min	100	1198	5.1
$^{15}\text{O}$	2.03 min	99.9	1732	8.0
$^{18}\text{F}$	109.8 min	97	635	2.3
$^{64}\text{Cu}$	12.7 h	18	653	2.4
$^{68}\text{Ga}$	68 min	88	1899	8.9
$^{89}\text{Zr}$	78.4 h	23	897	3.6
$^{124}\text{I}$	4.17 d	23	2138	10.2

### 1.3 Radiolabelling with $^{18}\text{F}$

Numerous radiochemical techniques are currently known for the radiofluorination of organic target molecules. These methods can be divided into electrophilic and nucleophilic labelling strategies, depending on the chemical form of the  $^{18}\text{F}$ -fluorination reagent involved. For electrophilic  $^{18}\text{F}$ -labelling, either gaseous  $[^{18}\text{F}]\text{F}_2$  or several less reactive  $[^{18}\text{F}]\text{F}_2$  derivatives such as acetyl  $[^{18}\text{F}]\text{hypofluorite}$  [33, 34], xenon  $[^{18}\text{F}]\text{difluoride}$  [35, 36] or  $N$ - $[^{18}\text{F}]\text{fluorosulfonamides}$  [37] can be used.  $[^{18}\text{F}]\text{F}_2$  is usually produced by bombardment of neon gas with deuterons via the  $^{20}\text{Ne}(d,\alpha)^{18}\text{F}$  reaction. A major drawback of this production method is the adsorption of the produced fluorine-18 on the target walls which necessitates the addition of carrier  $[^{19}\text{F}]\text{F}_2$  to the target gas to recover radioactivity by isotopic exchange [38]. Consequently, specific activities of fluorine-18 obtainable by this production route are relatively low (0.03-0.4 GBq/ $\mu\text{mol}$  [39]) which precludes radiosynthesis of PET radiotracers with high specific activity. Electrophilic radiofluorination methods are thus generally restricted to tracer applications which are not particularly sensitive to larger amounts of fluorine-19 carrier, for example ADME (absorption, distribution, metabolism and excretion) studies. However, given the lack of alternative  $^{18}\text{F}$ -labelling strategies, several radiotracers of clinical importance are still produced via electrophilic radiofluorination, the most

prominent example being 6- $^{18}\text{F}$ fluoro-L-3,4-dihydroxyphenylalanine (6- $^{18}\text{F}$ fluoro-L-DOPA) [40, 41].

For imaging low-abundance brain receptors *in vivo*, radiotracers with high specific activity are required, since the presence of significant amounts of tracer molecules labelled with the stable isotope can seriously affect the validity of the data. Nucleophilic  $^{18}\text{F}$ -fluorination starting from no-carrier-added (n.c.a.)  $^{18}\text{F}$ fluoride ( $^{18}\text{F}\text{F}^-$ ) is the method of choice for synthesis of radiotracers with high specific activity. N.c.a.  $^{18}\text{F}\text{F}^-$  is obtained by proton irradiation of  $^{18}\text{O}$ -enriched water according to the  $^{18}\text{O}(\text{p},\text{n})^{18}\text{F}$  reaction. Since carrier addition is dispensable with this production method, specific activities of more than 5000 GBq/ $\mu\text{mol}$  [39] can be attained. In aqueous solution, the fluoride ion is a weak nucleophile due to its strong solvation. Accordingly, nucleophilic  $^{18}\text{F}$ -labelling reactions routinely involve an azeotropic drying step with acetonitrile to remove the residual water followed by redissolution of the dry  $^{18}\text{F}$ fluoride in a dipolar aprotic solvent such as acetonitrile, dimethyl sulfoxide or *N,N*-dimethylformamide. To further enhance nucleophilic reactivity of  $^{18}\text{F}\text{F}^-$ , phase transfer catalysts such as the aminopolyether Kryptofix 2.2.2 (in combination with potassium carbonate)[42, 43] or tetrabutylammonium salts [44, 45] are commonly applied as anion activators. After the drying procedure,  $^{18}\text{F}\text{F}^-$  is present as almost naked, highly nucleophilic anion in polar aprotic solvents. Recently, several nucleophilic  $^{18}\text{F}$ -labelling strategies have been described which do not require a drying step, for example procedures using electrochemical deposition of  $^{18}\text{F}\text{F}^-$  [46], ionic liquids [47, 48] or direct elution of  $^{18}\text{F}\text{F}^-$  from an anion exchange sorbent with alcoholic solutions of iodonium precursors [49]. However, nucleophilic radiofluorinations are still most frequently performed with dried  $^{18}\text{F}\text{F}^-$  in dipolar aprotic media. Under these conditions, aliphatic nucleophilic substitution reactions proceed via an  $\text{S}_{\text{N}}2$  reaction mechanism. High radiochemical yields can be obtained with precursors carrying good leaving groups such as halides (Br, I) or sulfonates (triflate, mesylate, tosylate). As a consequence of the stereospecific  $\text{S}_{\text{N}}2$  mechanism, displacement of the leaving group by  $^{18}\text{F}\text{F}^-$  involves inversion of the stereochemical configuration of the molecule (Walden inversion). A prominent example of aliphatic nucleophilic  $^{18}\text{F}$ -labelling is the synthesis of n.c.a. 2-deoxy-2- $^{18}\text{F}$ fluoro-D-glucose ( $^{18}\text{F}$ FDG) which proceeds via replacement of the triflate leaving group of an acetyl-protected mannose precursor by  $^{18}\text{F}\text{F}^-$  and subsequent hydrolysis to yield the final product (Fig. 2) [42]. With this method, radiochemical yields of 50-70% and specific activities of about 300-500 GBq/ $\mu\text{mol}$  are achievable [50].

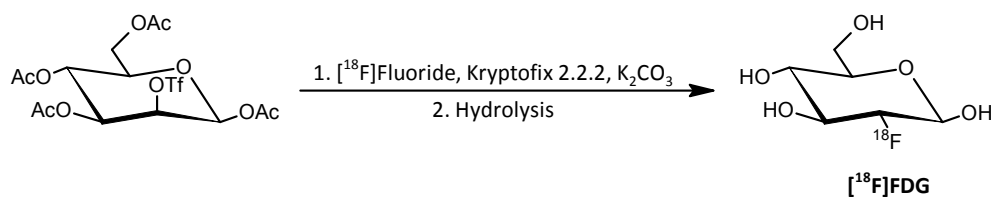


Fig. 2. Radiosynthesis of n.c.a.  $[^{18}\text{F}]\text{FDG}$  via nucleophilic  $^{18}\text{F}$ -for-triflate exchange [42]. Deprotection can be accomplished by either acid hydrolysis (with hydrochloric acid) or base hydrolysis (with sodium hydroxide)[51].

Aromatic nucleophilic substitution ( $\text{S}_{\text{N}}\text{Ar}$ ) reactions require arene precursors which are activated by strong electron-withdrawing substituents such as nitro, cyano or carbonyl groups in *ortho* or *para* position to the leaving group (Fig. 3). Typical leaving groups are nitro and trimethylammonium functional groups or halides [29, 50]. Electron deficient heteroaromatic systems (e.g. pyridines) frequently allow for nucleophilic  $^{18}\text{F}$ -labelling without further activation by electron-withdrawing groups [52]. Radiofluorination of electron rich (deactivated) arenes requires more complex synthesis approaches. Various innovative strategies have been described to date, for example the use of diaryliodonium [53–55] and triarylsulfonium salts [56, 57] as precursors or the application of palladium-mediated fluoride umpolung which converts the nucleophilic  $[^{18}\text{F}]\text{fluoride}$  to an electrophilic  $^{18}\text{F}$ -fluorination reagent [58, 59]. Several detailed reviews on current developments in  $^{18}\text{F}$ -labelling of aromatic compounds have been published recently [60–62].

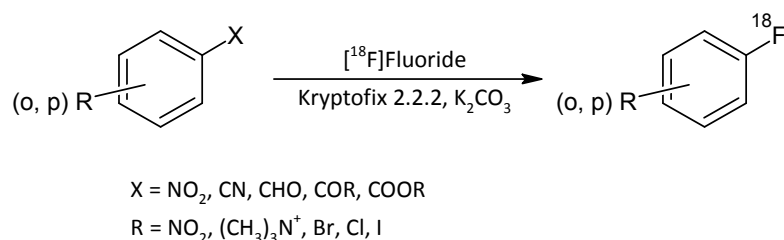


Fig. 3.  $^{18}\text{F}$ -labelling of activated arenes via nucleophilic aromatic substitution [50].

Although direct  $^{18}\text{F}$ -labelling of target molecules at the final stage of the radiosynthesis procedure is desirable in order to maximise the radiochemical yield and to simplify process automation, it is frequently inappropriate for complex molecules bearing multiple reactive functional groups or for biomolecules such as proteins or peptides which are sensitive to the relatively harsh reaction conditions involved in direct radiofluorination. For these target substrates, indirect labelling techniques are available which are based on small  $^{18}\text{F}$ -labelled organic molecules ( $^{18}\text{F}$ -labelled intermediates) that can be coupled to the desired target

structure. Depending on whether they are used for build-up radiosynthesis of small monomeric radiotracers or for radiolabelling of macromolecular biomolecules, these  $^{18}\text{F}$ -labelled intermediates are called synthons (in the former case) or prosthetic groups (in the latter case) [50]. Typically, synthons and prosthetic groups are prepared by direct nucleophilic n.c.a. radiofluoridation of activated, bifunctionalised organic molecules and, in a second step, attached to the target structure by, for example, acylation, alkylation, amidation or thiol-coupling reactions. Versatile synthons for radiochemical build-up synthesis are 4- $^{18}\text{F}$ fluorobenzaldehyde [63–65], 4- $^{18}\text{F}$ fluoroaniline [66, 67], 4- $^{18}\text{F}$ fluorobenzylamine [68, 69], 4- $^{18}\text{F}$ fluoroiodobenzene [70–72], 4- $^{18}\text{F}$ fluorobromobenzene [73–75] and 4- $^{18}\text{F}$ fluorophenol [76–79]. For  $^{18}\text{F}$ -labelling of peptides and proteins, the amine reactive compounds *N*-succinimidyl 4- $^{18}\text{F}$ fluorobenzoate ( $^{18}\text{F}$ SFB) [80–85] and 4- $^{18}\text{F}$ fluorobenzoic acid ( $^{18}\text{F}$ FBA) [86–88] as well as the thiol reactive groups *N*-[6-(4- $^{18}\text{F}$ fluorobenzylidene)aminoxyhexyl]maleimide ( $^{18}\text{F}$ FBAM) [89, 90] and *N*-[2-(4- $^{18}\text{F}$ fluorobenzamido)ethyl]maleimide ( $^{18}\text{F}$ FBEM) [91, 92] are valuable prosthetic groups [60]. The structural formulas of these compounds are shown in Fig. 4. Detailed summaries on the application of synthons and prosthetic groups for  $^{18}\text{F}$ -labelling of complex molecules can be found in [93–99].

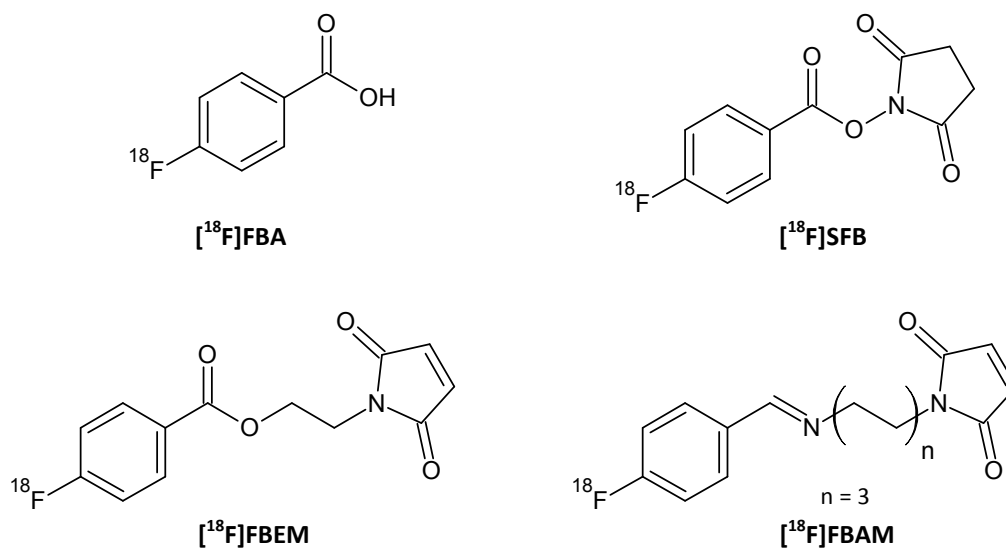


Fig. 4. Common prosthetic groups for  $^{18}\text{F}$ -labelling of biomolecules [60].

## 1.4 PET radiotracers for molecular neuroimaging

### 1.4.1 Radiotracer development process

The development of PET radiotracers for molecular imaging of the brain is a multidisciplinary process which comprises a number of complex, and often iterative, steps (Fig. 5). Initially, a specific biomedical question will be posed by physicians, scientists or pharmaceutical companies. This question may arise from unmet needs in diagnosis and treatment of patients or, more frequently, from basic scientific issues in brain research [100, 101]. Once a biomedical question has been chosen, a suitable molecular target needs to be selected. Classical targets for molecular neuroimaging include neuroreceptors [102-105] and neurotransmitter transporters [106-108], but also enzymes involved in epigenetic modification of gene expression [109-111] or specific protein structures such as amyloid plaques [112-116] have recently been targeted. Key criteria for choosing a suitable molecular target are target expression and localisation, both of which strongly influence later selection of potential lead compounds. Low-abundance targets, for example, demand for radiotracers possessing high affinity and high specific activity and nuclear targets require penetration of the cell nucleus by the tracer. For identification of lead compounds, different strategies can be pursued, including structure-activity relationship (SAR) analysis [117] and compound library screening [118, 119]. In many cases, endogenous substances or established drugs serve as starting point for lead development. Following identification, lead compounds are evaluated and optimised with regard to their physicochemical properties (e.g. solubility, lipophilicity, ionisation constants, passive permeability), their affinity and selectivity towards the molecular target and their *in vitro* metabolic stability. Once a promising candidate has emerged, strategies to radiolabel this compound are developed. Starting from the choice of a suitable radionuclide, a radiosynthesis scheme is designed which includes precursor synthesis, incorporation of the radioisotope into the molecule, purification of the product, quality control as well as development of an injectable formulation of the radiotracer. After successful completion of the radiosynthesis step, extensive *in vitro* and *in vivo* studies are conducted to evaluate the target binding characteristics and pharmacokinetic properties of the novel imaging agent. *In vitro* studies frequently include autoradiographic assessment of radiotracer distribution in brain slices and estimation of non-specific binding to cerebral proteins and lipids. *In vivo* PET imaging is carried out in rodents to evaluate blood-brain barrier (BBB) permeability, cerebral distribution and cerebral kinetics of the candidate radiotracer. Typically, PET imaging sessions involve blood analysis to determine plasma pharmacokinetics of the radiotracer

and *in vivo* metabolite formation. Promising candidates are then taken to non-human primate studies to verify the results obtained in rodent experiments. If the novel compound shows poor performance in preclinical investigations, especially with regard to brain uptake, cerebral kinetics and formation of BBB-penetrant radiometabolites, the process of radiotracer design and evaluation has to be iterated. The last stage of radiotracer development is the evaluation of the novel agent in humans. Before approval for clinical studies is granted, a multitude of regulatory issues must be covered (e.g. radiation protection, toxicological safety, good manufacturing practices (GMP) regulations) [120–124]. Since the regulative requirements became increasingly restrictive during the last 20 years, the time span between the first successful radiosynthesis of a novel PET radiotracer and initial human trials is at least 5-10 years [125].

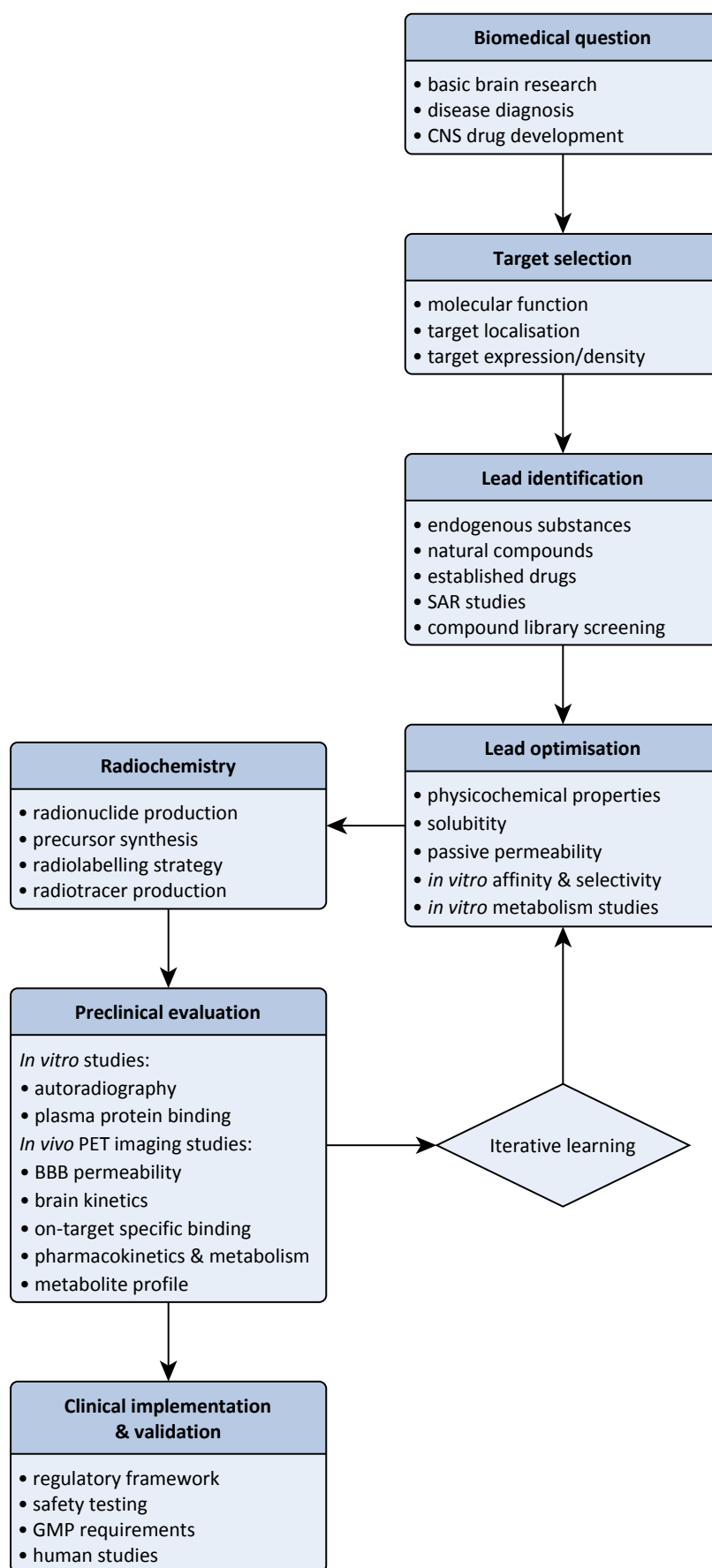


Fig. 5. Stages in the development of novel PET radiotracers for molecular neuroimaging.

## 1.4.2 Key criteria for PET radiotracers targeting neuroreceptors

In order to develop a PET radiotracer which is useful for imaging neuronal receptors *in vivo* (especially with regard to quantitative assessment of receptor expression), a number of demanding criteria have to be met. In addition to the radiochemical requirements discussed above (feasibility of high-specific-activity labelling with an appropriate radionuclide), there are also various biochemical and physiological prerequisites which are essential for good *in vivo* performance of a candidate radiotracer [126, 127]:

- High affinity (<10 nM)
- Target selectivity
- Adequate BBB permeability
- Lack of BBB efflux transporter affinity
- Suitable brain kinetics
- Low non-specific binding in brain
- Low plasma protein binding
- Adequate pharmacokinetics & metabolism
- Lack of BBB-penetrant radiometabolites

Optimisation of these factors primarily aims to ensure a high signal-to-noise ratio (or target-to-background ratio) which is crucial for the reliable quantification of receptor expression *in vivo*. Several articles have been published in which the influence of the abovementioned parameters on PET image quality is discussed in great detail [127–129]. In the following, the most important aspects are outlined briefly.

### 1.4.2.1 Affinity

Binding affinity refers to the strength of the binding interactions between a ligand (e.g. radiotracer) and its binding site (e.g. neuroreceptor). Since affinity of radioligand binding is the reciprocal of the equilibrium dissociation constant  $K_D$  [130], high-affinity radiotracers are characterised by small  $K_D$  values. Binding affinity is a key factor which strongly influences the specific-to-non-displaceable binding ratio and thus the image quality in PET. Because this ratio also depends on the number of binding sites available in a particular region ( $B_{max}$ ), low-abundant target receptors require tracers with especially high affinity to ensure adequate quantification of receptor parameters. Radiotracers used in neuroreceptor

imaging typically display affinities between 1 and 0.01 nM [128]. High affinity is generally considered advantageously for brain receptor studies, however, extremely high affinity values may result in undesirable slow dissociation kinetics which necessitates long acquisition times to reliably quantify receptor parameters [131]. This is particularly problematic if  $^{11}\text{C}$ -labelled tracers are to be used which only allow for short scan durations. Consequently, in radiotracer design, the affinity of a novel tracer should be attuned to the expected target density in the region(s) of interest.

#### 1.4.2.2 BBB penetration

The BBB represents a highly selective regulatory interface which restricts and controls the exchange of substances between the central nervous system (CNS) and the peripheral circulation [132, 133]. It is formed by brain microvascular endothelial cells which are closely connected to each other via tight junctions, thus restricting paracellular diffusion of polar substances [134]. A variety of specific carriers and transporters are expressed at the BBB which facilitate uptake of nutrients and hormones into the brain or allow for active efflux transport of metabolites and xenobiotics out of the brain capillary endothelial cells [135, 136]. Important examples of active transporters expressed at the BBB are the members of the ATP-binding cassette (ABC) transporter family, a group of transmembrane proteins which hydrolyse adenosine triphosphate (ATP) to gain energy for the transport of various substrates across cellular membranes [137–139]. The ABC efflux transporter P-glycoprotein (P-gp) is of particular interest with regard to the development of CNS drugs, as it shows a remarkably broad substrate spectrum and high expression levels at the BBB [140–142].

Brain entry of a radiotracer is governed by its ability to cross the BBB via passive diffusion on the one hand and its affinity for efflux transporters on the other hand. Transmembrane diffusion is promoted by low molecular weight (less than 400-500 Da), low hydrogen bonding capacity (less than 8-10 hydrogen bonds) and lack of negative charge [143–147]. Lipophilicity substantially influences the ability of a tracer to cross cellular membranes via diffusion. In general, a high degree of lipid solubility enhances membrane diffusion of a compound [148], however, it usually also increases efflux transporter affinity, plasma protein binding and metabolic clearance of this compound, which may result in an overall reduction of brain uptake. Frequently, a parabolic relationship between lipophilicity and *in vivo* brain uptake could be demonstrated, where compounds with moderate lipophilicity ( $\log P/\log D$  of about 2.0-3.5) often showed highest uptake values [149]. Owing to the large number of diverse brain efflux transporters expressed at the BBB and the broad substrate

specificity of individual efflux pumps – in particular P-gp - the susceptibility of a novel radiotracer to brain efflux transport is difficult to predict on the basis of its molecular characteristics. Typically, P-gp substrates are neutral or positively charged lipophilic or amphiphilic molecules which often contain planar aromatic domains [140, 142, 150, 151].

#### 1.4.2.3 Radiotracer metabolism

*In vivo* performance of a radiotracer is influenced by both qualitative and quantitative aspects of radiotracer metabolism. A major obstacle to brain PET imaging is the appearance of radiolabelled metabolites in the brain, either as a result of cerebral metabolism or of peripheral generation of brain-penetrant radiometabolites. Brain radiometabolites which exhibit considerable affinity for the target receptor seriously confound quantification of receptor parameters since the measured PET signal represents specific binding of two species with different kinetics. Brain radiometabolites without target affinity contribute to the radioactive background and decrease the signal-to-noise ratio. Although kinetic models have been developed which account for the non-specific accumulation of radiometabolites in brain [152–154], it is generally preferable to avoid formation of troublesome metabolites by rational tracer design.

Metabolism is the main route of elimination for the majority of radiotracers. Fast clearance of radiotracer and radiolabelled metabolites from blood decreases the radioactive background and thus improves the signal-to-noise ratio. Additionally, since the rate of passive diffusion of a radiotracer through the BBB is influenced by the concentration gradient across the cellular membrane, rapid decline in plasma radiotracer concentration results in accelerated radiotracer washout from brain which facilitates measurement of all relevant kinetic parameters in a shorter scanning time [128, 155]. However, if the radiotracer is metabolized too excessively, the extent of brain exposure might be insufficient, especially if longer acquisition times are required for proper imaging of the molecular target. Consequently, metabolic stability of lead compounds should be precisely adjusted during the development process to produce promising radiotracers for *in vivo* PET imaging. In the following section, various methods for *in vitro* and *in vivo* evaluation of radiotracer metabolism are presented.

## 1.5 Evaluation of radiotracer metabolism

### 1.5.1 Metabolism of xenobiotics

Almost immediately after intravenous administration, radiotracers undergo metabolic conversion catalysed by a variety of enzymes located mainly in the liver but also in various extrahepatic tissues. This process, designated as xenobiotic biotransformation, gives rise to metabolites which exhibit physicochemical and physiological characteristics different from those of the parent compound. Biotransformation of xenobiotics is subdivided into phase I and phase II reactions. Phase I reactions (also referred to as functionalisation reactions) include hydrolysis, reduction and oxidation processes which introduce or expose polar functional groups (e.g.  $-OH$ ,  $-COOH$ ,  $-NH_2$ ). Functionalisation usually results in a moderate increase in hydrophilicity of the xenobiotic compound and facilitates the second phase of metabolism in which the functionalised compound is coupled to an endogenous substrate such as glucuronic acid or glutathione. Phase II conjugation reactions typically increase hydrophilicity of the xenobiotic by a large amount, hence promoting its excretion from the body. Although the liver has the highest expression levels of most phase I and II enzymes, significant enzyme concentrations can also be found in pancreas, gastrointestinal tract, spleen, lung, brain and nasal mucosa [156]. On the subcellular level, the major fraction of these enzymes is located in the endoplasmic reticulum and in the cytosol, but smaller quantities have also been detected in mitochondria, lysosomes and nucleus [157].

#### 1.5.1.1 Cytochrome P450

Cytochrome P450 enzymes (P450s or CYPs) are haem-containing proteins that are present in all three domains of life. They play a critical role in the metabolism of endogenous and exogenous substrates. In mammals, hepatic P450 isoforms of families CYP1, CYP2 and CYP3 mediate phase I biotransformation of most xenobiotic compounds [158]. Human P450s, for example, account for the metabolism of about 75% of marketed drugs [159]. Mammalian P450s are membrane-bound enzymes which are expressed in a variety of tissues, with the highest concentration levels found in the endoplasmic reticulum of the liver. P450s predominantly catalyse oxidation reactions, although other reaction types have also been observed, for example reduction, desaturation, dehydration, ring formation and coupling reactions [160, 161].

Molecular oxygen ( $O_2$ ) is activated at the haem-iron centre of the P450 enzyme, resulting in the insertion of a single oxygen atom into an organic substrate and concomitant reduction of

the other oxygen atom to water. The electrons required for this reaction are derived from nicotinamide adenine dinucleotide phosphate (NADPH) and supplied via a redox partner such as the flavoprotein cytochrome P450 reductase (CPR) [162]. The catalytic cycle of P450 (Fig. 6) involves a number of subsequent steps [163]: (1) substrate binding followed by conformational change of the P450 molecule, (2) transfer of the first electron by CPR and reduction of haem-Fe<sup>3+</sup> to haem-Fe<sup>2+</sup>, (3) O<sub>2</sub> binding to haem-Fe<sup>2+</sup>, (4) transfer of the second electron by CPR or cytochrome b5, (5) protonation of the Fe<sup>3+</sup>O<sub>2</sub> intermediate to yield an Fe<sup>3+</sup>OOH intermediate, (6) second protonation and generation of a highly reactive oxo-Fe<sup>4+</sup>-species (referred to as Compound 1), (7) oxygen insertion into the substrate, dissociation of the oxidised substrate (product) from P450.

Interruption (uncoupling) of the catalytic cycle leads to the generation of reactive oxygen species (ROS). The decay of the Fe<sup>3+</sup>O<sub>2</sub> intermediate gives rise to the release of oxygen as superoxide anion (O<sub>2</sub><sup>-</sup>) whereas protonation of the Fe<sup>3+</sup>OOH intermediate entails formation of hydrogen peroxide (H<sub>2</sub>O<sub>2</sub>). In eukaryotes, the P450 cycle is poorly coupled, resulting in continuous ROS production which causes oxidative stress [164].

### 1.5.2 *In vitro* metabolism studies

The use of *in vitro* metabolism models allows for determination of the metabolic properties of a candidate radiotracer at an early stage in the development process. Information on metabolic stability and metabolite formation gained *in vitro* provide guidance for lead optimisation and selection of candidates for further *in vivo* studies. Generally, *in vitro* metabolism studies are relatively inexpensive, time effective and do not require regulatory approval which facilitates flexible study design and fast implementation. Several *in vitro* metabolism models are available to date, all of which have their advantages and disadvantages (Table 2). Because numerous comprehensive reviews have been published on the pros and cons of the individual models [165–173], the following discussion will be limited to the microsomal model which was used in the present work.

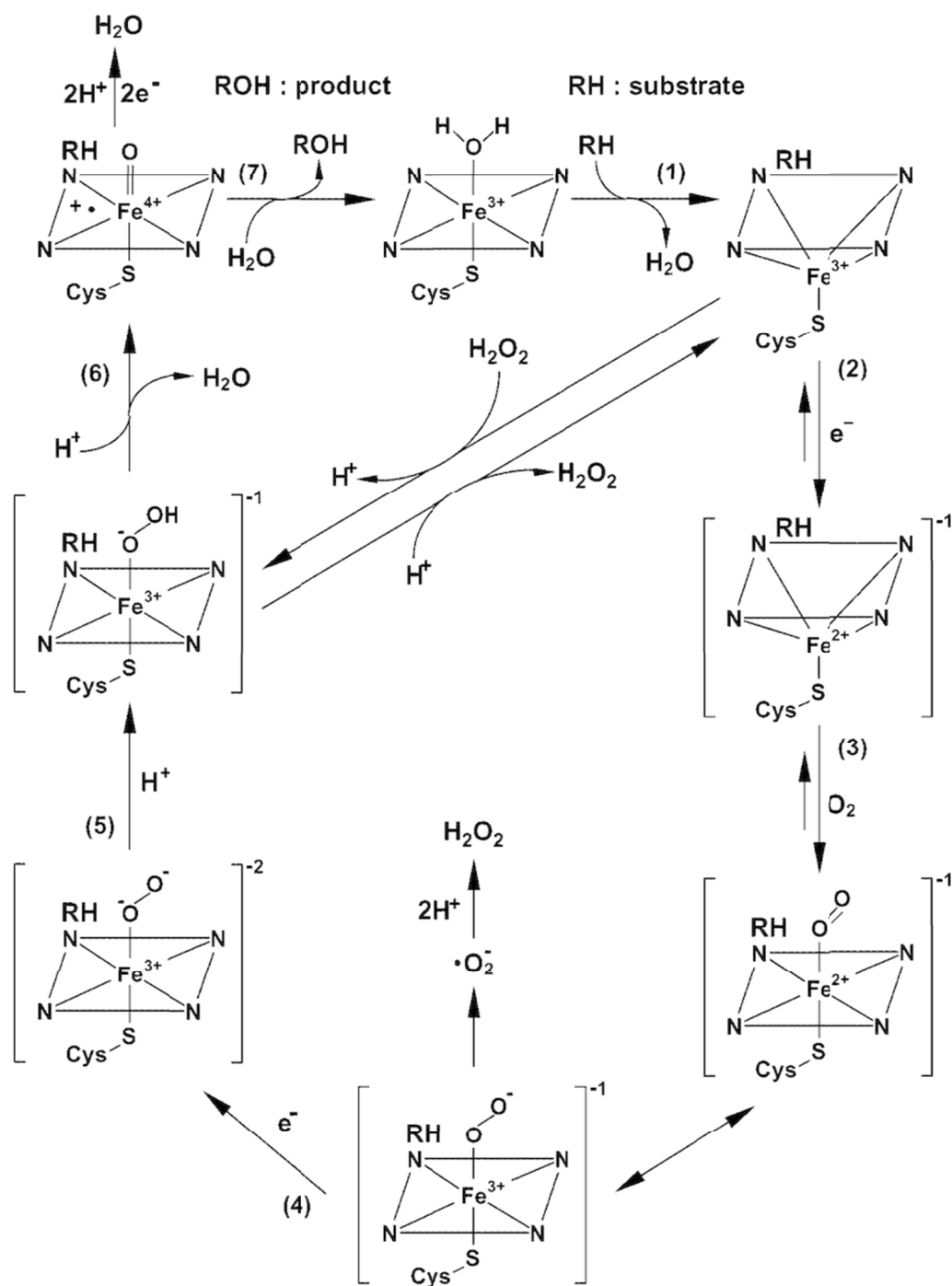


Fig. 6. Catalytic cycle of P450 for monooxygenase reactions. Uncoupling pathways resulting in ROS formation are indicated. The porphyrin macrocycle of the haem is represented as parallelogram with nitrogen at each corner (figure adapted from [163]).

Table 2. Comparison of different *in vitro* metabolism models employed in preclinical research (from [167–169])

<i>In vitro</i> model	Advantages	Disadvantages
Recombinant CYP enzymes	High throughput system Useful for mechanistic studies Commercially available High enzyme activities	Study of only one enzyme at a time <i>In vivo</i> relevance questionable
Microsomes	High throughput system Useful for intrinsic clearance and drug inhibition studies Relatively inexpensive Minimal loss of enzyme activity during storage Commercially available	Only CYP, FMO and UGT enzymes Cofactor addition necessary Incomplete representation of <i>in vivo</i> hepatic function
Primary hepatocytes	Full ensemble of phase I & II enzymes at <i>in vivo</i> levels Whole-cell system Normal cellular levels of cofactors Potential for use in toxicity, drug-drug interaction and induction studies Cryopreservation possible Commercially available	Limited viability Decrease in enzyme expression & activity during culture Restricted availability of human hepatocytes Special equipment required
Liver slices	Intact cellular architecture Cell-cell connections are preserved Complete set of functional enzymes and transporters Morphological studies possible	Limited viability Limited availability (human tissue) Complicated technique
Isolated perfused liver	Preserved hepatic architecture Bile formation Study of hepatobiliary drug disposition	Limited viability Limited availability (human tissue) Complicated technique Poor reproducibility Low throughput, not suitable for routine use

CYP, cytochrome P450; FMO, flavin-containing monooxygenase; UGT, UDP-glucuronosyltransferase

### 1.5.2.1 Microsomes

Microsomes are vesicular structures derived from the endoplasmic reticulum of eukaryotic cells. They are prepared from tissues involved in xenobiotic biotransformation (most often liver tissue) by differential centrifugation [174]. Hepatic microsomes contain P450s, flavin-containing monooxygenases (FMOs) and UDP-glucuronosyltransferases (UGTs). Since P450s and UGTs are responsible for the metabolism of about 90% of marketed drugs [175], liver microsomes are widely used to study *in vitro* drug metabolism at the lead optimisation stage. Compared to more complex *in vitro* models such as hepatocytes or liver slices, microsomes are relatively inexpensive, easy to use and can be stored at -80°C for several

years with minimal loss of enzyme activity [176, 177]. However, the reduced complexity of the microsomal model also limits its physiological relevance. As liver microsomes lack the full complement of hepatic enzymes, metabolic pathways observed with microsomes may differ from *in vivo* metabolism. Intracellular compartmentalisation, which is an important characteristic of eukaryotic cells, is no longer present in microsomal preparations, thus resulting in unrestricted contact of enzymes and substrates which does not reflect the *in vivo* situation. Metabolism studies in microsomes require addition of cofactors such as NADPH to support enzyme activity. Addition of excess amounts of cofactor in order to maintain stable concentration levels during incubation creates unphysiological conditions, whereas *in situ* cofactor regeneration may influence reaction kinetics and complicate interpretation of results. Finally, since microsomes lack the defence mechanisms of vital cells, reactive oxygen species generated as a byproduct of oxidative metabolism rapidly damage the microsomal enzyme systems which leads to a fast decline of enzyme activity during incubation procedures [178]. These factors often hamper *in vitro-in vivo* extrapolation, especially of quantitative data. Nevertheless, liver microsomes are a valuable tool for rapid screening of compound libraries and for lead optimisation studies during drug development. Additionally, they can be used to produce specific metabolites in sufficiently large quantities to enable spectroscopic structure determination.

Microsomes from different donors are usually pooled to reflect mean enzyme expression and activity levels encountered in human or animal populations. Due to the ease of preparation, microsomes isolated from hepatic tissue of numerous toxicologically relevant species (human, rodent, rabbit, dog, mini pig, monkey) and also extrahepatic microsomes (lung, intestine, kidney, skin) are now commercially available, allowing for study of extrahepatic metabolism and interspecies comparison. Microsomal assays generally involve incubation of the test compound with diluted microsomal protein and required cofactor for a certain period of time, followed by termination of the enzymatic reaction and precipitation of microsomal protein by addition of organic solvent or trichloroacetic acid. Samples are subsequently analysed by HPLC-UV/Vis or HPLC-MS to monitor either loss of parent compound (substrate depletion approach) or formation of metabolites (product formation approach) [179, 180]. Metabolic stability of a test substrate can be described in terms of initial reaction velocity, metabolic half-life or derived parameters such as intrinsic clearance which are obtained from the concentration versus time data by linear or non-linear (usually exponential) regression.

In order to produce *in vitro* metabolism data which are relevant for the *in vivo* situation, microsomal assay conditions must be evaluated and carefully controlled. Parameters such

as enzyme and substrate concentration, buffer composition and pH, type and concentration of substrate solvent, incubation time and temperature can influence qualitative and quantitative aspects of microsomal metabolism of a test compound [181]. Generally, incubation parameters should mimic the physiological conditions encountered *in vivo* as closely as possible. With regard to radiotracer evaluation, selection of an appropriate substrate concentration to be used in the microsomal assay is particularly problematic. In a typical PET study, the average body concentration of a tracer is in the subnanomolar range (about 0.1-0.3 nM) [182]. Detection of such low concentrations is often not feasible with the classical analytical techniques usually employed in *in vitro* metabolism studies, especially if structure determination of metabolites is required. Consequently, in radiotracer development, *in vitro* metabolism data are often generated using substrate concentrations that do not reflect the *in vivo* scenario, which raises concerns about the relevance of these data.

### 1.5.3 *In vivo* pharmacokinetic studies

Although *in vitro* metabolism studies provide a fast and simple means of investigating specific aspects of radiotracer metabolism, they cannot resemble the complexity of the whole organism (at least at present). Metabolism is only one of the many factors influencing overall pharmacokinetics (PK) of a radiotracer *in vivo*, others being distribution and excretion processes. *In vivo* PK studies conducted with laboratory animals are required to gain insight into the complex interplay of physicochemical, biochemical and physiological parameters which determine the fate of a radiotracer in the body.

#### 1.5.3.1 Fundamental PK processes

*In vivo* PK of a compound is influenced by four interrelated processes, namely absorption, distribution, metabolism and excretion (ADME). With regard to the development of radiotracers intended for molecular imaging in basic research, absorption is of subordinate importance since these tracers are generally administered intravenously. Once injected into the systemic circulation, the radiotracer rapidly distributes throughout the body. The extent of extravascular distribution depends on the ability of the compound for passive diffusion across cellular membranes, its affinity for active uptake and efflux transporters and its binding to plasma and tissue proteins and lipids [183]. Metabolism is a major pathway for elimination of xenobiotics from the body, although direct renal/biliary excretion of the unchanged molecule may also play an important role for several compounds. As already stated above, metabolism of xenobiotic compounds involves phase I functionalisation and

phase II conjugation reactions and occurs predominantly in the liver. Excretion of xenobiotics and their metabolites proceeds via two major routes: (1) renal excretion through urine and (2) biliary excretion through faeces. Minor pathways are excretion via saliva, milk, tears, respiration and perspiration [184, 185].

### 1.5.3.2 Pharmacokinetic data analysis

*In vivo* pharmacokinetic evaluation of a novel radiotracer involves the quantitative assessment of tracer concentration in various tissues/organs as a function of time. The tracer is usually administered as intravenous bolus and the time course of radioactivity in the target organs (for CNS tracers especially plasma and brain) is measured either *ex vivo* via tissue sampling or *in vivo* via PET. From the resulting activity-time (or concentration-time) data, pharmacokinetic parameters can be estimated via non-compartmental or compartmental analysis.

#### Non-compartmental analysis

In non-compartmental analysis (NCA), the time course of plasma concentration following single bolus administration of a radiotracer (or a drug) is regarded as statistical distribution curve. NCA uses statistical moment theory to derive PK parameters from this concentration-time profile [186]. The most important moments for PK analysis, the zero moment (area under the curve, AUC) and the first normal moment (mean residence time, MRT), are defined as follows:

$$AUC = \int_0^{\infty} C(t)dt \quad \text{Eq. 1}$$

$$MRT = \int_0^{\infty} tC(t)dt / \int_0^{\infty} C(t)dt \quad \text{Eq. 2}$$

where  $t$  is the time since administration of the radiotracer and  $C(t)$  is the plasma concentration of the tracer at time  $t$ .

AUC and MRT can be calculated from the plasma concentration-time data either by numerical integration using the trapezoidal formula or by fitting the data to polyexponential functions of the general form:

$$C(t) = \sum_{i=1}^n A_i e^{-\lambda_i t} \quad \text{Eq. 3}$$

Integration of Eq. 3 yields:

$$\int_0^{\infty} C(t)dt = \sum_{i=1}^n \frac{A_i}{\lambda_i} \quad \text{Eq. 4}$$

and

$$\int_0^{\infty} tC(t)dt = \sum_{i=1}^n \frac{A_i}{\lambda_i^2} \quad \text{Eq. 5}$$

The detailed calculations of these two definite integrals are given in the appendix.

Substituting Eq. 4 into Eq. 1:

$$AUC = \int_0^{\infty} C(t)dt = \sum_{i=1}^n \frac{A_i}{\lambda_i} \quad \text{Eq. 6}$$

Substituting Eq. 5 into Eq. 2:

$$MRT = \int_0^{\infty} tC(t)dt / \int_0^{\infty} C(t)dt = \frac{\sum_{i=1}^n \frac{A_i}{\lambda_i^2}}{\sum_{i=1}^n \frac{A_i}{\lambda_i}} \quad \text{Eq. 7}$$

In Eq. 3-7,  $A_i$  represent the zero-time intercepts of each exponential and  $\lambda_i$  the individual elimination rate constants (macro rate constants).

The basic pharmacokinetic parameters applied in NCA to describing plasma kinetics of a tracer following bolus administration can be estimated from the polyexponential fits of the concentration-time data using the definitions of AUC and MRT given above [187]:

1. Total clearance  $CL$  (represents the volume of plasma from which the tracer is completely removed per unit time; unit: ml/min)

$$CL = \frac{D}{\int_0^{\infty} C(t)dt} = \frac{D}{\sum_{i=1}^n \frac{A_i}{\lambda_i}} \quad \text{Eq. 8}$$

where  $D$  is injected radioactivity.

2. Volume of distribution  $V_d$  (proportionality constant between tracer concentration in plasma and the amount of tracer in the body; unit: ml/g)

$$V_d = \frac{CL}{\lambda_{el}} \quad \text{Eq. 9}$$

where  $\lambda_{el}$  is the smallest of the rate constants  $\lambda_i$

3. Terminal half-life  $t_{1/2\gamma}$  (time required for the tracer concentration in plasma to fall by 50% during the terminal phase; unit: min)

$$t_{1/2\gamma} = \frac{\ln(2)}{\lambda_{el}} \quad \text{Eq. 10}$$

Non-compartmental analysis is largely independent of *a priori* assumptions concerning the structure of the physiological system (model-independent) and thus a robust, versatile and straightforward approach to interpret experimental data. However, NCA is of limited use for predictive and explanatory purposes since it provides little to no information on the underlying biological and physiological processes which determine disposition of a compound in the body. To understand mechanism of tracer pharmacokinetics in the body, application of compartmental models is advantageous.

### Compartmental analysis

In compartmental analysis (or compartmental modelling), disposition of a compound (drug/tracer) is described in terms of transfer processes between interconnected, pharmacokinetically distinct compartments which constitute the body. Each compartment represents a specific chemical state of the compound (e.g. metabolic form or binding state) in a particular physical location (e.g. interstitial space, plasma)[188]. Within an individual compartment, the concentration of the chemical species is assumed to be homogeneous. The rate of exchange of the compound between individual compartments can be described by first order kinetics. Accordingly, compartment models can be mathematically represented by polyexponential terms or sets of ordinary differential equations.

Typically, compartment models applied in PK analysis comprise two or more compartments, although disposition of several drugs can be accurately characterised by one-compartment models. Of the numerous model configurations described in literature, only those which were used in the context of the present work will be discussed in more detail in this introduction. In the following, the mammillary three-compartment model which was applied to interpret the plasma profiles of the evaluated radiotracers is presented. The specific compartment models which were used for analysis of the brain PET data are described in section 1.6.5.

The mammillary three-compartment model is characterised by a central compartment connected to two peripheral compartments (Fig. 7). Tracer (or drug) is introduced into and eliminated from the system via the central compartment. All transfer processes occur via the central compartment, there is no direct exchange between the two peripheral compartments. Following intravenous (i.v.) injection, tracer is reversibly transferred from the central compartment to both peripheral compartments. The peripheral compartments differ with regard to their transport kinetics, so that the time required for equilibration with the central compartment varies. These variations result in complex intercompartmental distribution and redistribution processes which lead to a triphasic plasma concentration-time profile with two distinct distribution phases preceding the terminal elimination phase. Although the compartments of the model may not have precise physiological correlates, common interpretations associate the central compartment with blood and highly perfused organs/tissues (e.g. liver), the rapidly equilibrating ("shallow") compartment with well perfused organs/tissues (e.g. kidneys, muscles) and the slowly equilibrating ("deep") compartment with poorly perfused organs/tissues (e.g. fat tissue, skin). The mammillary three-compartment model can be described by the sum of three exponentials:

$$C(t) = A_1e^{-\lambda_1t} + A_2e^{-\lambda_2t} + A_3e^{-\lambda_3t} \quad \text{Eq. 11}$$

where  $t$  is the time since bolus injection,  $C(t)$  is the tracer concentration in plasma at time  $t$  and  $A_1$ - $A_3$  and  $\lambda_1$ - $\lambda_3$  are the model parameters.

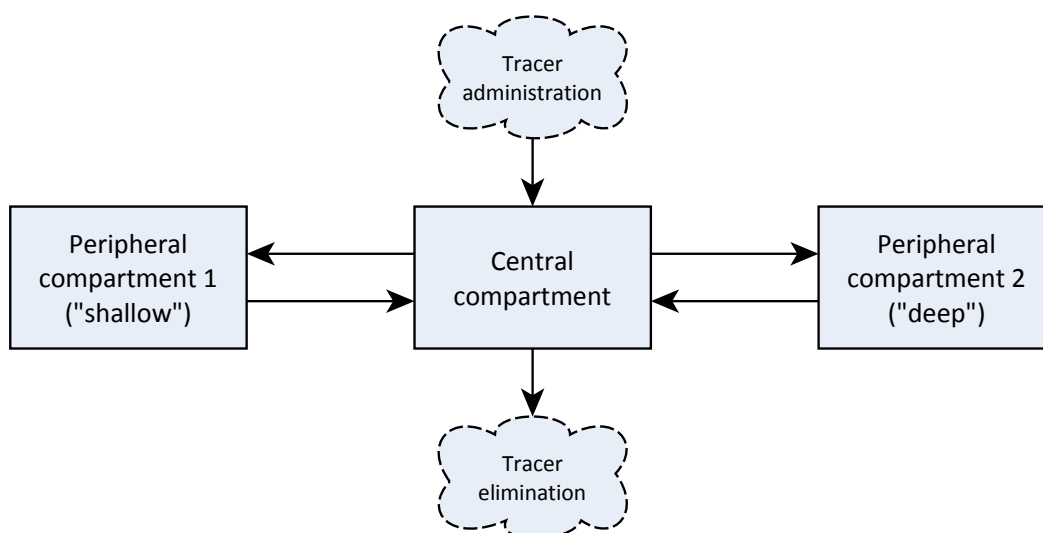


Fig. 7. Schematic of a mammillary three-compartment model. Tracer enters and leaves the system only via the central compartment. Peripheral compartments 1 and 2 differ with respect to their tracer exchange kinetics. The shallow peripheral compartment equilibrates rapidly with the central compartment, whereas the deep peripheral compartment equilibrates slowly.

Multi-compartment mammillary models and their application in pharmacokinetics are discussed in detail in [189–192]. A comprehensive summary of the underlying mathematics can be found in [187, 193].

## 1.6 Neuroreceptor imaging

In biology and pharmacology, the term receptor generally denotes a protein structure on the surface of a cell or inside a cell that selectively binds to a specific compound and acts as a transducer of a physiological signal or mediator of a physiological effect [194]. In molecular neuroscience, the diverse postsynaptic transmembrane neurotransmitter receptors (neuroreceptors) constitute important objects of investigation. Neuroreceptors can be subdivided into two classes, (1) ionotropic receptors (ligand-gated ion channels) which contain an ion channel in their structure that opens in response to the binding of a ligand, and (2) metabotropic receptors (G protein-coupled receptors, GPCRs) which activate internal signalling pathways upon ligand binding. In the context of the present work, radiotracers targeted at the adenosine  $A_1$  receptor ( $A_1AR$ ), a member of the GPCR family, have been investigated. In the following section, the adenosine receptor system is thus outlined briefly.

### 1.6.1 Adenosine receptors

Adenosine receptors (ARs) are a family of GPCRs which mediate the physiological actions of the purine nucleoside adenosine. To date, four AR subtypes have been identified, denoted as  $A_1$ ,  $A_{2A}$ ,  $A_{2B}$  and  $A_3$  [195]. These subtypes have different signal transduction pathways and distinct, but often overlapping, distribution patterns in tissue. Adenosine is involved in the modulation of numerous physiological processes such as sleep and arousal [196–203], but also in the development of pathophysiological conditions, for example Alzheimer's disease [204, 205], Parkinson's disease [206–208], schizophrenia [209] and epilepsy [210, 211]. In the CNS,  $A_1$  and  $A_{2A}$  are the most abundant AR subtypes. In most species, expression of  $A_{2A}$  receptors is mainly restricted to the striatum and olfactory bulb while  $A_1$  receptors are widely expressed throughout the brain. In rodents, high  $A_1AR$  levels can be found in cerebral cortex, cerebellum, hippocampus, striatum and thalamus [212–217]. In the human brain,  $A_1AR$  densities are high in hippocampus, striatum, thalamus and cerebral cortex, but low in cerebellar cortex [218–220].

By now, numerous subtype-selective ligands have been described which can be used to study AR expression and distribution *in vitro* and *in vivo*. AR agonists have been derived

from the endogenous ligand adenosine by modification of the 5'-position of the ribose and the C2- and N<sup>6</sup>-position of the purine heterocycle (Fig. 8). N<sup>6</sup>-substituted adenosine derivatives such as (*R*)-N<sup>6</sup>-(2-phenylisopropyl)adenosine (*R*-PIA)[221], N<sup>6</sup>-cyclopentyladenosine (CPA)[222] and 2-chloro-N<sup>6</sup>-cyclopentyladenosine (CCPA)[223, 224] are potent and selective A<sub>1</sub>AR agonists which are also available as tritiated radioligands.

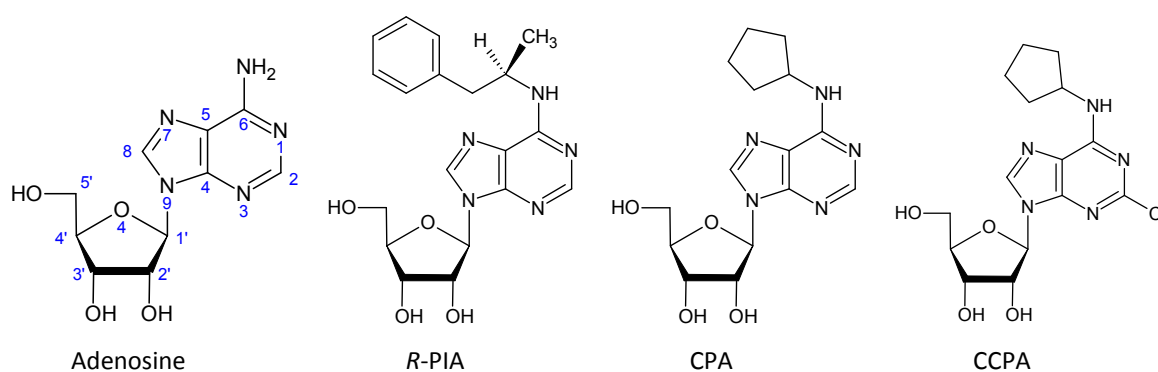


Fig. 8. Structural formulas of adenosine and selective A<sub>1</sub>AR agonists derived from adenosine.

Most AR antagonists reported to date are based on the xanthine structure (Fig. 9). The naturally occurring xanthine derivative caffeine represents the prototypical AR antagonist, however, since caffeine lacks affinity and subtype selectivity, this compound is of limited interest as a tool for the investigation of ARs. Modification of the xanthine structure at C8, N1, N3 (and sometimes N7) led to selective and highly affine A<sub>1</sub>AR and A<sub>2A</sub>AR antagonists. Two important xanthine-type A<sub>1</sub>AR antagonists are shown in Fig. 9, 8-cyclopentyl-1,3-dipropylxanthine (DPCPX)[225] and its <sup>18</sup>F-labelled analogue, 8-cyclopentyl-3-(3-[<sup>18</sup>F]fluoropropyl)-1-propylxanthine ([<sup>18</sup>F]CPFPX)[226]. A comprehensive overview of xanthine-based AR antagonist can be found in [227].

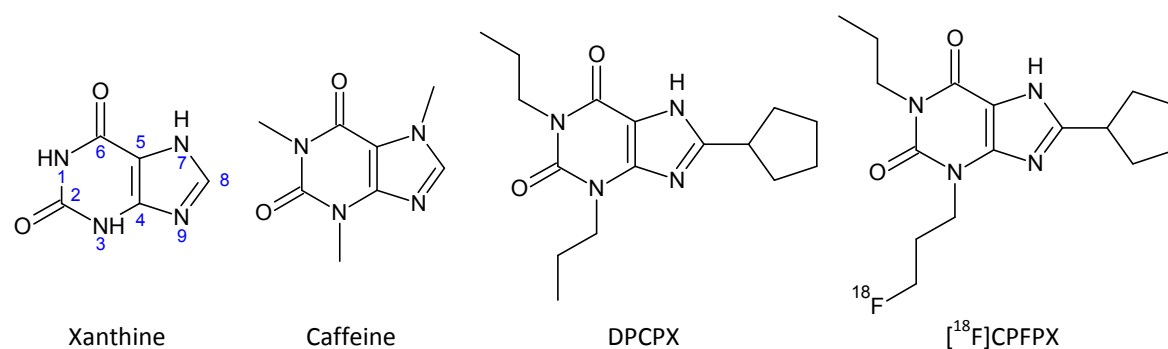


Fig. 9. Structural formulas of xanthine, the non-selective AR antagonist caffeine and the selective A<sub>1</sub>AR antagonists DPCPX and [<sup>18</sup>F]CPFPX.

In addition to the aforementioned xanthine derivatives, several classes of non-xanthine AR antagonists have been developed, including triazoloquinoxalines, triazoloquinazolines, imidazoquinolines and 7-deazaadenine derivatives. Characteristics and application potential of these compounds have been review for example in [228–232].

### 1.6.2 Ligand-receptor interactions

The specific binding of a (radio)ligand to its target receptor can be described by a bimolecular reaction scheme which involves the reversible association of a ligand L and a receptor R to form a ligand-receptor complex LR [233]:



where  $k_{on}$  is the association rate constant and  $k_{off}$  is the dissociation rate constant. Squared brackets indicate molar concentrations.

According to the law of mass action, the rate at which free ligand reversibly binds to free (unbound) receptor can be described by:

$$\text{Rate of association} = k_{on}[L][R] \quad \text{Eq. 13}$$

The rate at which ligand-receptor complex breaks down is described by:

$$\text{Rate of dissociation} = k_{off}[LR] \quad \text{Eq. 14}$$

At equilibrium (steady state), the rates of association and dissociation are equal:

$$k_{on}[L][R] = k_{off}[LR] \quad \text{Eq. 15}$$

Eq. 15 can be rearranged to:

$$\frac{k_{off}}{k_{on}} = \frac{[L][R]}{[LR]} = K_D \quad \text{Eq. 16}$$

Consequently, the equilibrium dissociation constant  $K_D$  can be defined both by the ratio of dissociation and association rate constants and by the concentration ratio of free species to ligand-receptor complex.  $K_D$  is an intrinsic characteristic of each individual ligand-receptor pair and a measure of binding affinity. A low  $K_D$  value designates high binding affinity.

Ligands are typically classified according to the effects they provoke on their corresponding receptors. Ligands which cause changes in the activity of the receptor upon binding are called agonists. Full agonists are capable of activating the receptor to a maximal extent whereas partial agonists produce a submaximal response. Inverse agonists reduce the intrinsic activity of a receptor. Ligands which bind to a receptor and inhibit the action of an agonist without activating the receptor themselves are referred to as antagonists. Antagonists are subdivided into several groups depending on their site of binding to the receptor (agonist binding site or allosteric site) and on the reversibility of their binding (reversible or irreversible)[234]. For radioligand binding studies, antagonists are usually favoured over agonists since antagonist binding is generally less affected by confounding factors such as pH or local concentrations of nucleotides and mono or divalent cations [235].

### 1.6.3 *In vitro* radioligand binding studies

Various *in vitro* techniques are available to study receptor distribution in tissue or binding properties of ligands. One commonly used approach involves the assessment of radioligand binding to tissue receptors under equilibrium binding conditions (equilibrium binding analysis). Equilibrium binding can be studied either directly via saturation binding assays or indirectly via competition binding experiments. In a typical saturation binding assay, a fixed concentration of a receptor-containing tissue preparation (e.g. homogenate, membrane suspension, tissue section) is incubated with increasing concentrations of a radioligand. Once binding equilibrium is achieved, bound ligand is separated from free ligand by filtration, centrifugation or washing with buffer and quantified by means of radioactivity measurement. Because the radioligand usually does not only bind to its target receptor (specific binding), but also to other components of the tissue preparation or the assay equipment (non-specific binding), additional measurements have to be conducted in order to correct for this non-specific binding. Generally, the level of non-specific binding is determined in the presence of high concentrations of an unlabelled competitor. Specific binding is then calculated as the difference between total and non-specific binding. One possible graphical representation of the results obtained from a saturation binding assay is shown in Fig. 10. The specific binding curve asymptotically approaches a plateau value which represents the total number of specific binding sites (maximum binding capacity,  $B_{\max}$ ). The equilibrium dissociation constant  $K_D$  of the radioligand can be determined as the concentration of radioligand at which half of these binding sites are occupied.

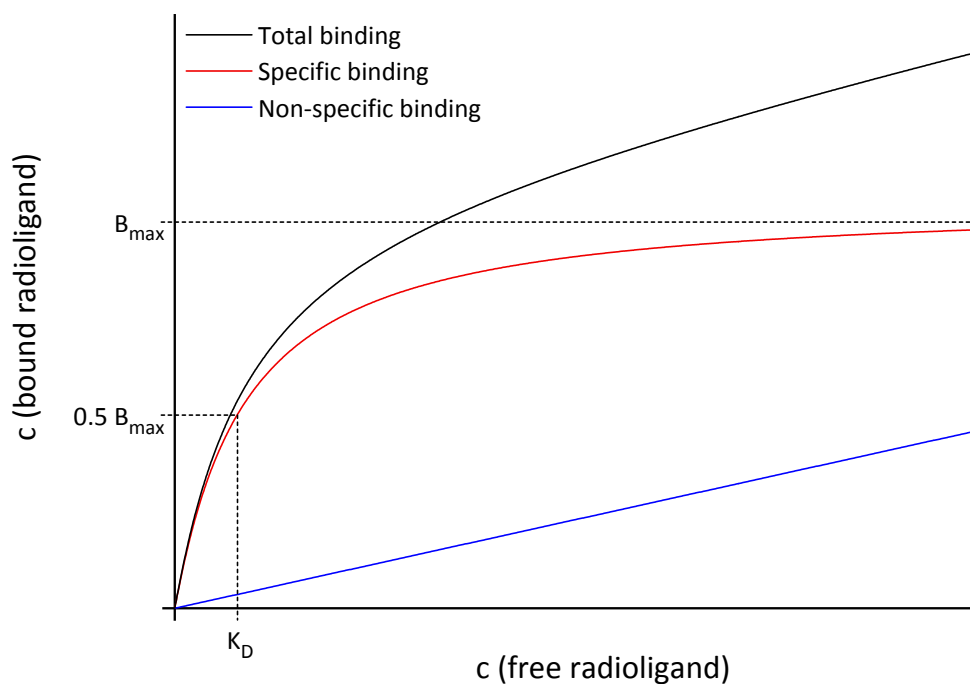


Fig. 10. Generalised saturation binding plot. Receptor-containing tissue preparations are incubated with various concentrations of a radioligand, either in absence (total binding) or presence (non-specific binding) of a competitor. The concentration of bound radioligand is determined and plotted against initial radioligand concentration. Specific binding is calculated as the difference between total and non-specific binding.

Mathematically, the saturation curve can be derived from Eq. 16 using the following definition of  $B_{max}$ :

$$B_{max} = [R] + [LR] \quad \text{Eq. 17}$$

Substitution for  $[R]$  in Eq. 16 and rearrangement yields:

$$[LR] = \frac{B_{max}[L]}{[L] + K_D} \quad \text{Eq. 18}$$

This equation, which describes a rectangular hyperbola, represents a special case of the general Hill equation where the Hill coefficient has been set to one (i.e. non-cooperative binding is assumed).

In competition binding experiments, the ability of an unlabelled ligand to compete with a radioligand for binding sites is used to examine ligand-receptor interactions. Typically, receptor-containing tissue preparations are incubated with a low, fixed concentration of a radioligand with known  $K_D$  for the specific binding site and increasing concentrations of the competing ligand. The amount of specifically bound radioligand is determined and plotted against competitor concentration. An important parameter which can be derived from these

plots is the  $IC_{50}$ , i.e. the concentration of unlabelled competitor that inhibits 50% of the specific radioligand binding. Based on the  $IC_{50}$ , the affinity of the competitor for the binding site can be estimated using the Cheng-Prusoff equation [236]:

$$K_i = \frac{IC_{50}}{\left(1 + \frac{[L]}{K_D}\right)} \quad \text{Eq. 19}$$

where  $K_i$  is the dissociation constant of the competitor,  $[L]$  is the concentration of free radioligand and  $K_D$  is the dissociation constant of the radioligand. Apart from the evaluation of novel ligands, competition binding assays may also be used to study receptor subtypes and conformations. Further information regarding the conduct and analysis of equilibrium binding assays can be found in [233, 235, 237–241].

#### 1.6.4 *In vivo* radiotracer binding studies

Generally, *in vivo* imaging of neuroreceptors involves intravenous administration of a suitable radiotracer followed by dynamic measurement of radioactivity in the brain. In order to extract quantitative information on physiological processes from these imaging data, tracer kinetic models are applied. Compartmental models are the most widely used approach to analyse time-radioactivity data obtained from brain PET scans. These models provide information on the temporal changes in cerebral radiotracer distribution, but not on spatial concentration gradients as do complex distributed models [188]. Nevertheless, the limited complexity of common compartmental models may also be beneficial with regard to the accuracy and reliability of model parameter estimation. As with *in vitro* radiotracer binding studies, the specific binding interactions between radiotracer and receptor are of major interest in PET neuroreceptor imaging, however, several additional factors have to be taken into consideration, for example the extent of radiotracer delivery to the brain or the rate of radiotracer uptake and washout. The specific compartment models applied to *in vivo* radiotracer binding studies usually account for these factors.

#### 1.6.5 Compartmental models for *in vivo* radiotracer binding studies

Two basic compartmental model configurations which are widely applied to PET radiotracer-receptor studies are shown in Fig. 11. In these models, a plasma compartment and either one or two tissue compartments are arranged in series (catenary models). The plasma compartment ( $C_p$ ) represents the concentration of free radiotracer in arterial plasma. Strictly speaking, plasma radiotracer concentration is not a compartment of the

model since this parameter is measured independently (via blood sampling) and applied to the compartment model as a known input function. However, in PET literature, radiotracer concentration in plasma is most often denoted as compartment and drawn as a box in graphical representations of compartmental models [242]. In the one-tissue compartment model (1TCM), only one uniform tissue compartment ( $C_2$ ) is postulated which represents cerebral radiotracer concentration. In the two-tissue compartment model (2TCM), the first tissue compartment ( $C_2$ ) represents the intracerebral concentration of free and non-specifically bound tracer (also referred to as non-displaceable compartment) and the second tissue compartment ( $C_3$ ) the concentration of specifically bound tracer, i.e. tracer bound to its receptor. The intercompartmental transfer of tracer is described by two (1TCM) or four (2TCM) rate constants (transfer or fractional rate constants, denoted as  $K_1$ - $k_4$ ), which reflect the fraction of tracer molecules moving from one compartment to another per unit of time. In the 1TCM, there is no differentiation between free, non-specifically and specifically bound tracer, thus only the exchange of tracer between plasma and brain is modelled. Occasionally, the 1TCM is chosen in preference to the 2TCM although specific receptor-ligand interactions are anticipated. This might be the case, for example, if transfer kinetics between  $C_2$  and  $C_3$  become so fast that the two compartments cannot be distinguished from one another [242] or if radioactivity concentration in brain tissue is very low so that background noise interferes substantially with the measurement signal.

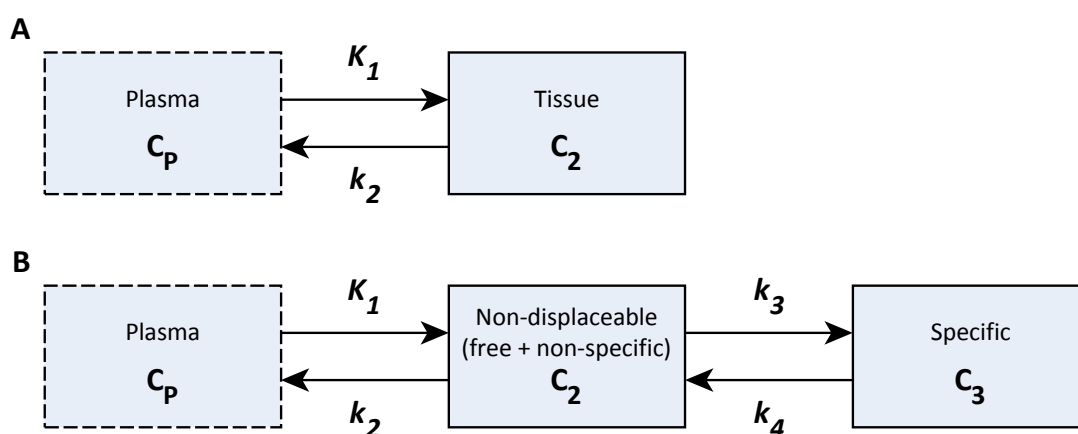


Fig. 11. Configuration of the 1TCM (A) and the 2TCM (B).  $C_p$  is the concentration of tracer in arterial plasma,  $C_2$  and  $C_3$  are the tracer concentrations in the respective tissue compartments and  $K_1$ - $k_4$  are the rate constants which describe the reversible transfer of tracer between the compartments. In the 1TCM, tracer in brain tissue is treated as a single compartment ( $C_2$ ). The 2TCM discriminates between intracerebral free and non-specifically bound tracer (non-displaceable compartment  $C_2$ ) and tracer specifically bound to the receptor (specific compartment  $C_3$ ).

The rate of change in radioactivity concentration in the tissue compartments can be described mathematically by ordinary differential equations.

For the 1TCM:

$$\frac{dC_2}{dt} = K_1 C_P(t) - k_2 C_2(t) \quad \text{Eq. 20}$$

For the 2 TCM:

$$\frac{dC_2}{dt} = K_1 C_P(t) - (k_2 + k_3) C_2(t) + k_4 C_3(t) \quad \text{Eq. 21}$$

$$\frac{dC_3}{dt} = k_3 C_2(t) - k_4 C_3(t) \quad \text{Eq. 22}$$

where  $C_P$  is the time-varying concentration of tracer in arterial plasma (the input function),  $C_2$  and  $C_3$  are the time-varying concentrations of tracer in the two tissue compartments and  $K_1$ - $k_4$  are the fractional rate constants which define the rate of tracer transfer between the compartments.

From the individual kinetic rate constants (micro parameters), additional pharmacokinetic system parameters (macro parameters) can be derived:

1. Total distribution volume  $V_T$  (defined as the ratio of the tracer concentration in tissue to the tracer concentration in plasma at equilibrium)

$$\text{1TCM} \quad V_T = \frac{K_1}{k_2} \quad \text{Eq. 23}$$

$$\text{2TCM} \quad V_T = \frac{K_1}{k_2} \left( 1 + \frac{k_3}{k_4} \right) \quad \text{Eq. 24}$$

2. Specific distribution volume  $V_S$  (defined as the concentration ratio of specifically bound tracer in tissue to tracer in plasma at equilibrium)

$$\text{2TCM} \quad V_S = \frac{K_1 k_3}{k_2 k_4} \quad \text{Eq. 25}$$

3. Distribution volume of non-displaceable uptake  $V_{ND}$  (concentration ratio of non-specifically bound tracer in tissue compartment  $C_2$  to tracer in plasma at equilibrium)

$$2\text{TCM} \quad V_{ND} = \frac{K_1}{k_2} \quad \text{Eq. 26}$$

for the 1TCM,  $V_{ND}$  equals  $V_T$

4. Binding potential  $BP_{ND}$  (concentration ratio of specifically bound to non-displaceable tracer at equilibrium)

$$2\text{TCM} \quad BP_{ND} = \frac{k_3}{k_4} \quad \text{Eq. 27}$$

The theoretical foundations of the outlined models and the mathematical solutions of the model equations are discussed in detail in [188, 242–245].

### 1.6.6 Logan graphical analysis

Graphical analysis methods are based on mathematical transformation of the PET data into a linear plot whose slope and y-intercept represent pharmacokinetic parameters. An important graphical technique developed for determination of the total distribution volume  $V_T$  of reversibly binding radiotracers is Logan graphical analysis (or Logan plot)[246, 247]. The Logan relationship can be derived from the differential equation defining the 1TCM (Eq. 20) by integration [188]:

$$C_2(t) = K_1 \int_0^t C_P(u) du - k_2 \int_0^t C_2(u) du \quad \text{Eq. 28}$$

Dividing by  $k_2$  and  $C_2(t)$  and rearranging yields:

$$\frac{\int_0^t C_2(u) du}{C_2(t)} = V_T * \frac{\int_0^t C_P(u) du}{C_2(t)} - \frac{1}{k_2} \quad \text{Eq. 29}$$

In Eq. 28 and 29,  $C_P$  refers to the radiotracer concentration in arterial plasma (input function) and  $C_2$  to the radiotracer concentration in brain tissue. The integration variable  $u$  relates to the continuous input function. The slope of this relationship equals  $V_T$  in the 1TCM. If the measured data are not consistent with the 1TCM, the Logan plot becomes linear after a certain time. Linear regression is then performed for those later data points and the slope represents an estimate of  $V_T$ . Logan graphical analysis is independent of any particular model structure and computationally more robust than iterative non-linear compartmental model fits [248, 249]. In the present work,  $V_T$  values derived from Logan plots served as comparison to assess reliability of  $V_T$  values estimated via compartmental analysis.

## 2 Aims and Objectives

The development of PET radiotracers is a multidisciplinary process which involves a series of iterative steps ranging from molecular target identification to clinical evaluation studies in humans. One important stage in this process is the structural modification of promising compounds in order to optimise relevant physicochemical and pharmacological parameters such as water solubility, target affinity and specificity, non-specific protein binding, blood-brain barrier permeability and *in vivo* pharmacokinetics. Adequate pharmacokinetic properties are a decisive prerequisite for the successful application of a novel radiotracer in neuroimaging studies. Metabolism is one important factor contributing to *in vivo* pharmacokinetics of a radiotracer. Metabolic lability of a candidate radiotracer may result in rapid decrease of plasma radiotracer concentration and thus in insufficient brain exposure. This is particularly problematic if longer scan durations are required to properly image the molecular target. Additionally, fast radiotracer metabolism increases the risk that brain-penetrant radiolabelled metabolites are generated in sufficient amounts to compromise the PET signal. However, metabolic degradation also supports fast clearance of radioactivity from the blood pool which, on the one hand, improves the signal-to-noise ratio obtainable during the PET scan and thus the image contrast, and, on the other hand, allows for shorter scan duration. These aspects illustrate the importance of a precise adjustment of the metabolic properties of lead compounds during the development process to produce promising imaging agents for *in vivo* application. Various *in vitro* techniques are available to evaluate metabolic stability of novel compounds during the preclinical stage. The potential and the limitations of these methods have been extensively evaluated in the field of drug discovery and development, however, with regard to the development of radiotracers, studies on the physiological relevance of *in vitro* metabolism models are rare. Since *in vivo* application of PET radiotracers differs greatly from the application of classical drugs in terms of the amount of administered substance (picomoles to nanomoles versus millimoles) and the period of time during which the fate of the substance in the body is monitored, the question rises whether the conclusions on the physiological relevance and predictive power of *in vitro* metabolism models reached in the context of drug evaluation studies are applicable to the field of radiotracer development.

The aim of this work was to assess the relevance and validity of one of the most commonly applied models of *in vitro* drug metabolism, the microsomal stability assay, as a tool for the development of PET radiotracers. This central question should be investigated by

comparison of the *in vitro* metabolic stability and the *in vivo* pharmacokinetic properties of three xanthine-derived adenosine A<sub>1</sub> receptor ligands in the rat model. One of these ligands, 8-cyclopentyl-3-(3-fluoropropyl)-1-propylxanthine (CPFPX), has already been established as PET radiotracer for imaging A<sub>1</sub>AR *in vivo* in animals and humans. However, since this compound is rapidly metabolised *in vivo*, considerable efforts have been made to develop metabolically stable structural analogues which may exhibit higher plasma levels and, as a possible consequence, also enhanced brain uptake. Two recently synthesised cyclobutyl-substituted analogues of CPFPX, 8-cyclobutyl-3-(3-fluoropropyl)-1-propylxanthine (CBX) and 3-(3-fluoropropyl)-8-(1-methylcyclobutyl)-1-propylxanthine (MCBX) were chosen for comparative evaluation in the context of this work.

The first objective was to investigate the influence of *in vitro* assay conditions (incubation matrix composition, concentration of microsomal protein, preincubation time) on the rate of metabolism of CBX, MCBX and CPFPX by rat liver microsomes with a particular focus on potential changes in the stability rank order of the three test compounds. Based on the results of these studies, the microsomal stability assay should be optimised in such a way as to provide physiological relevant metabolism data which are only marginally influenced by *in vitro* artefacts or bias. The optimised microsomal assay configuration should then be used to determine the *in vitro* metabolic stability of the test compounds.

The next step was to evaluate the *in vivo* pharmacokinetic properties of CBX, MCBX and CPFPX in the rat model. For this purpose, the <sup>18</sup>F-labelled compounds had to be administered to the animals and the time-course of plasma concentration measured invasively. From these data, suitable PK parameters had to be derived which enable the comparison of *in vitro* and *in vivo* metabolic stability of the test compounds.

Subsequently, microsomal stability data and *in vivo* pharmacokinetic data should be compared in a suitable way and the possibilities and limitations of predicting *in vivo* radiotracer metabolism from *in vitro* metabolism data should be discussed. Special emphasis should be laid on the potential influence of confounding physiological factors such as plasma protein binding on the accuracy and reliability of prediction. In addition to the quantitative aspects of radiotracer metabolism, the utility of *in vitro* metabolism studies as predictive tool regarding the occurrence and relevance of individual metabolic pathways *in vivo* should be assessed. For this purpose, *in vitro* and *in vivo* metabolite profiles of CBX, MCBX and CPFPX generated in the rat model should be compared.

In order to gain further insights into the qualitative and quantitative aspects of the metabolism of the test compounds, additional *in vitro* metabolism studies should be conducted using liver microsomes obtained from humans and various preclinical animal

species. These investigations should also provide a basis for selecting the most appropriate animal species for future *in vitro* and *in vivo* evaluation of novel xanthine-derived A<sub>1</sub>AR ligands.

As a final point, cerebral distribution and kinetics of the three radiotracers should be comparatively evaluated using both *in vitro* autoradiography and *in vivo* PET. The results of these examinations should be discussed with special focus on the potential correlation between *in vivo* metabolic stability and cerebral kinetics of the test compounds.

## 3 Materials and Methods

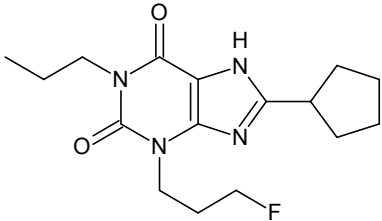
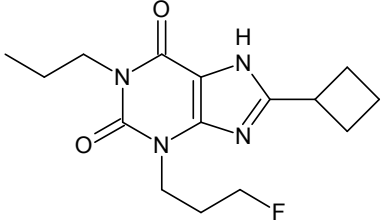
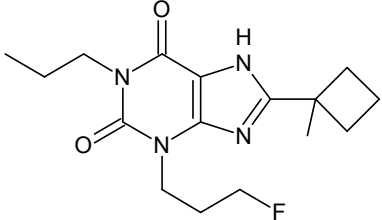
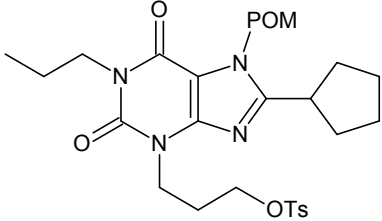
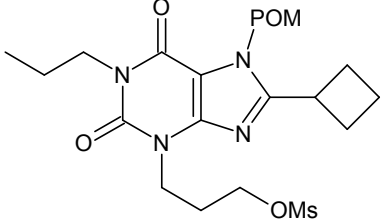
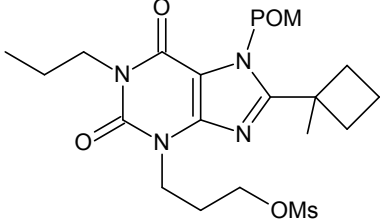
### 3.1 Chemicals

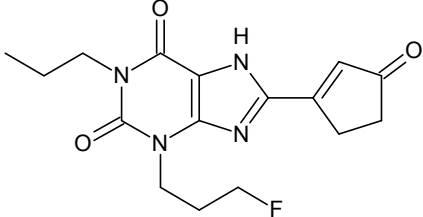
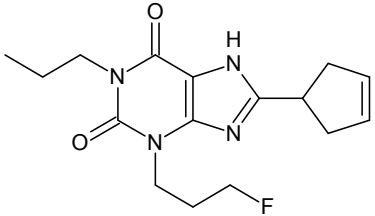
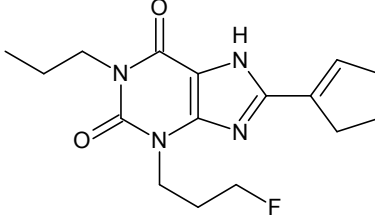
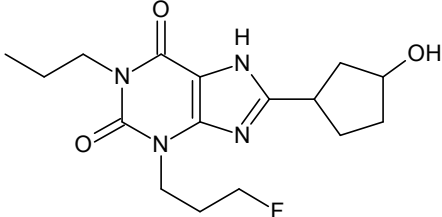
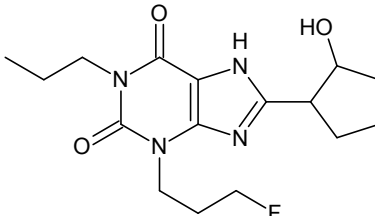
Reduced  $\beta$ -nicotinamide adenine dinucleotide 2'-phosphate (NADPH) was purchased from Roche Diagnostics (Mannheim, Germany).  $\beta$ -Nicotinamide adenine dinucleotide 2'-phosphate (oxidised form, NADP<sup>+</sup>), glucose-6-phosphate (G6P), glucose-6-phosphate dehydrogenase (G6P-DH), magnesium chloride (MgCl<sub>2</sub>), superoxide dismutase (SOD), catalase (CAT), plumbagin, diphenyliodonium chloride (DPI), 4-(2-hydroxyethyl)-1-piperazineethanesulfonic acid (HEPES), 4-morpholinepropanesulfonic acid (MOPS), 2-amino-2-(hydroxymethyl)propane-1,3-diol (TRIS), potassium phosphate, tetra-n-butylammonium bromide (TBAB), guanosine-5'-triphosphate (GTP), *N,N*-dimethylformamide (DMF), dimethyl sulfoxide (DMSO), 8-cyclopentyl-1,3-dipropylxanthine (DPCPX), ethylenediamine-tetraacetic acid (EDTA), acetic acid (HAc) and sodium hydroxide (NaOH) were purchased from Sigma-Aldrich (Steinheim, Germany). Reagent grade acetonitrile (ACN), methanol (MeOH), ethyl acetate, hexane and isopentane were obtained from Merck (Darmstadt, Germany). For preparation of eluents and buffers, aqua ad iniectabilia (water for injection) from B. Braun Melsungen (Melsungen, Germany) was used. Isoflurane for anaesthesia was purchased from CP-Pharma (Burgdorf, Germany).

### 3.2 Substrates, reference standards and precursors

All substrates, reference standards and precursors listed in Table 3 were synthesised and characterised in our laboratories except for CFPX precursor which was purchased from ABX GmbH (Radeberg, Germany).

Table 3. Substrates, reference standards and precursors used in this work. TPSA and log P values were calculated with Molinspiration Property Calculator (Molinspiration Cheminformatics).

Structural formula, numbering	Name, physicochemical properties
<b>1</b> 	8-Cyclopentyl-3-(3-fluoropropyl)-1-propylxanthine (CPFPX) MW: 322.38 g/mol Log P: 2.93 TPSA: 72.69 Å <sup>2</sup>
<b>2</b> 	8-Cyclobutyl-3-(3-fluoropropyl)-1-propylxanthine (CBX) MW: 308.35 g/mol Log P: 2.19 TPSA: 72.69 Å <sup>2</sup>
<b>3</b> 	3-(3-Fluoropropyl)-8-(1-methylcyclobutyl)-1-propylxanthine (MCBX) MW: 322.38 g/mol Log P: 2.82 TPSA: 72.69 Å <sup>2</sup>
<b>4</b> 	8-Cyclopentyl-3-(3-tosyloxypropyl)-7-pivaloyloxymethyl-1-propylxanthine (CPFPX precursor) MW: 588.72 g/mol
<b>5</b> 	8-Cyclobutyl-3-(3-mesyloxypropyl)-7-pivaloyloxymethyl-1-propylxanthine (CBX precursor) MW: 498.59 g/mol
<b>6</b> 	3-(3-Mesyloxypropyl)-8-(1-methylcyclobutyl)-7-pivaloyloxymethyl-1-propylxanthine (MCBX precursor) MW: 512.62 g/mol

Structural formula, numbering	Name, physicochemical properties
<p>7</p> 	<p>3-(3-Fluoropropyl)-8-(3-oxocyclopent-1-en-1-yl)-1-propyl-xanthine (CPFPX metabolite) MW: 334.35 g/mol</p>
<p>8</p> 	<p>8-(Cyclopent-3-en-1-yl)-3-(3-fluoropropyl)-1-propyl-xanthine (CPFPX metabolite) MW: 320.36 g/mol</p>
<p>9</p> 	<p>8-(Cyclopent-1-en-1-yl)-3-(3-fluoropropyl)-1-propyl-xanthine (CPFPX metabolite) MW: 320.36 g/mol</p>
<p>10</p> 	<p>3-(3-Fluoropropyl)-8-(3-hydroxycyclopentyl)-1-propyl-xanthine (CPFPX metabolite) MW: 338.38 g/mol</p>
<p>11</p> 	<p>3-(3-Fluoropropyl)-8-(2-hydroxycyclopentyl)-1-propyl-xanthine (CPFPX metabolite) MW: 338.38 g/mol</p>

MW, molecular weight; log P, octanol-water partition coefficient; TPSA, topological polar surface area

### 3.3 *In vitro* metabolism

#### 3.3.1 Microsomes

Human liver microsomes (HLM, total P450 content: 0.286 nmol/mg protein), dog (Beagle) liver microsomes (DLM), mini pig (Göttingen) liver microsomes (MPLM), mouse (CD-1) liver microsomes (MLM), monkey (rhesus) liver microsomes (RMLM) and rat (Sprague Dawley) liver microsomes (RLM) were purchased from Thermo Fisher Scientific/Life Technologies (Darmstadt, Germany).

### 3.3.2 General microsomal incubation procedures

All microsomal incubations were conducted at 37°C with continuous gentle agitation (300 rpm) using a thermomixer device (Thermomixer Comfort, Eppendorf, Hamburg, Germany). Cofactor NADPH was added either directly (protocol A) or generated *in situ* using a cofactor regeneration system (CRS) consisting of NADP<sup>+</sup>, G6P and G6P-DH (protocol B). Total incubation volume was 500 µl (single time point assays) or 1000 µl (multiple time point assays). 10 mM stock solutions of CBX, MCBX and CFPX were prepared in DMSO or DMF and stored in the dark and at 4°C up to one year. 1 mM working solutions were freshly prepared every month and stored in the dark at room temperature (21°C). Generally, liver microsomes (0.4 mg/ml microsomal protein), substrate (8 µM), MgCl<sub>2</sub> (3.3 mM) and, for protocol B, G6P (3.3 mM) and G6P-DH (0.4 U/ml) were mixed with buffer and preincubated for 5 min at 37°C. Reaction was initiated by addition of preheated (37°C) NADPH (1.3 mM, protocol A) or NADP<sup>+</sup> (1.3 mM, protocol B). Aliquots (100 µl) were removed at appropriate time points (including one sample removed directly after cofactor addition, i.e.  $t = 0$  min) and added to an equal volume of methanol/acetonitrile (50:50, v/v, -20°C) to terminate the reaction. The samples were homogenised on a vortex mixer (1 min, 21°C) and centrifuged (20,000 rcf, 10 min, 21°C) to sediment precipitated protein. The supernatants were analysed on a Knauer smartline HPLC-UV/VIS system (Knauer, Berlin, Germany) equipped with a manual sample injector (Rheodyne type 7125) and a 500 µl sample loop. Isocratic elution was performed using a Kromasil 100-5 C18 (4.6x250 mm) analytical column (AkzoNobel, Bohus, Sweden) and a mobile phase composed of ACN/H<sub>2</sub>O/HAc 48:52:0.2 (v/v/v). Injection volume was 50 µl, flow rate 1 ml/min and detection wavelength 275 nm. Specific incubation conditions and deviations from the general procedures are listed in the following sections. Substrate depletion was calculated from the area ratios of the analyte peak, using the value at  $t = 0$  min as 100%.

### 3.3.3 Evaluation of incubation conditions

#### 3.3.3.1 Influence of buffer medium, substrate solvent and cofactors

CBX, MCBX and CFPX (8 µM) were incubated with RLM (0.4 mg/ml microsomal protein) for 30 min in a final volume of 500 µl according to either protocol A or B. For individual assays, buffer composition (buffer substance, concentration, pH), substrate solvent (substance, final concentration), and cofactor supply (NADPH, CRS) were varied according to Table 4. Aliquots sampled at 0 and 30 min were processed as described above. Incubations were conducted in quadruplicate. The data were analysed for statistically

significant differences between incubation parameter sets by performing one-way ANOVA ( $p < 0.05$ ) with *post-hoc* Tukey test.

Table 4. Individual composition of microsomal assays used for evaluation of incubation conditions. Assays were conducted as described in general incubation procedures.

Incubation No.	Buffer			Substrate Solvent		Protocol*	NADPH Final Conc.
	Substance	Concentration	pH	Substance	Final Conc.		
		<i>mM</i>			<i>vol %</i>		<i>mM</i>
1	Phosphate	100	7.4	DMF	0.8	B	
2	MOPS	100	7.4	DMF	0.8	B	
3	HEPES	100	7.4	DMF	0.8	B	
4	HEPES	200	7.4	DMF	0.8	B	
5	HEPES	500	7.4	DMF	0.8	B	
6	HEPES	50	7.4	DMF	0.8	B	
7	HEPES	100	6.8	DMF	0.8	B	
8	HEPES	100	8.2	DMF	0.8	B	
9	HEPES	100	7.4	DMF	0.8	A	1.3
10	HEPES	100	6.8	DMF	0.8	A	1.3
11	HEPES	100	8.2	DMF	0.8	A	1.3
12	HEPES	100	7.4	DMF	1.5	B	
13	HEPES	100	7.4	DMF	2.0	B	
14	HEPES	100	7.4	DMSO	0.08	B	
15	HEPES	100	7.4	DMSO	0.8	B	
16	HEPES	100	7.4	DMSO	1.5	B	
17	HEPES	100	7.4	DMSO	2.0	B	
18	HEPES	100	7.4	DMSO	0.08	A	1.3
19	HEPES	100	7.4	DMSO	0.8	A	1.3
20	HEPES	100	7.4	DMSO	2.0	A	1.3
21	HEPES	100	7.4	DMSO	0.8	A	1.0
22	HEPES	100	7.4	DMSO	0.8	A	0.78
23	HEPES	100	7.4	DMSO	0.8	A	0.26

\* protocol A, direct addition of NADPH; protocol B, addition of CRS

### 3.3.3.2 Influence of enzyme concentration

CPFPX (8  $\mu$ M, stock solution in DMSO) was preincubated with RLM (0.2, 0.4 or 0.8 mg/ml microsomal protein) in HEPES buffer (100 mM, pH 7.4, 3.3 mM  $MgCl_2$ ) for 3 min at 37°C. Reaction was commenced by addition of preheated NADPH (1.3 mM). Aliquots were

sampled at 0 and 3 min and processed as described in general procedures. Incubations were conducted in quadruplicate. An external calibration curve (see below) was used to quantify the concentration of CPF PX in the samples. Initial velocities ( $v_0$ ) were derived from the slopes of the concentration-time graphs, plotted against the concentration of microsomal protein and analysed via linear regression analysis.

### External calibration curve

Seven CPF PX calibration standards (1-12  $\mu\text{M}$ ) were prepared from the CPF PX stock solution by dilution with eluent and injected into the HPLC (single injection). The chromatographic conditions were analogous to those applied to regular microsomal samples (see general procedures). The resulting peak area versus concentration data were fitted to a linear regression model (Fig. 12).

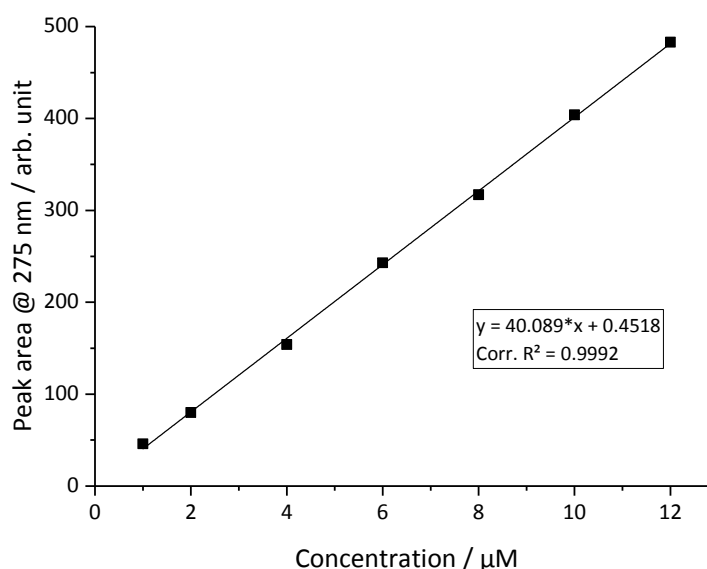


Fig. 12. External calibration curve for quantification of CPF PX in microsomal extracts. Chromatographic conditions were the same as described in general microsomal incubation procedures. Each calibration standard was injected once.

### 3.3.3.3 Influence of preincubation time

RLM (0.4 mg/ml microsomal protein),  $\text{MgCl}_2$  (3.3 mM) and NADPH (1.3 mM) were mixed with HEPES buffer (100 mM, pH 7.4) and preincubated for 2, 10, 30, 60 and 120 min at 37°C. Addition of CPF PX (8  $\mu\text{M}$ , stock solution in DMSO) initiated the enzymatic reaction which was allowed to proceed for 5 min. CAT (1 U/ml, 1500 U/ml), SOD (100 U/ml, 1000 U/ml) or a mixture of both CAT and SOD (1000 U/ml each) was added to several incubations to

evaluate the effect of ROS scavengers on enzyme lability. Samples taken at 0 and 5 min were processed and analysed as described above. Incubations were conducted in triplicate.

### 3.3.4 Stability assessment of NADPH

Stability of NADPH during incubation was examined using procedures that resembled microsomal incubation protocols A and B. NADPH (1.3 mM) was incubated at 37°C either in buffer alone (HEPES, 100 mM, pH 7.4, 3.3 mM MgCl<sub>2</sub>) or in buffer containing microsomal protein (0.4 mg/ml RLM). EDTA (5 mM), DPI (25 μM, 100 μM), or plumbagin (1 μM) was added to some incubations to test for potential effects on NADPH stability. Aliquots sampled from the incubation mixture at appropriate time points were quenched by rapid dilution (1:100) with cold (-20°C) potassium phosphate buffer (100 mM, pH 9.0) containing 10 mM TBAB. Quenched samples were kept at -20°C until HPLC analysis. The suitability of the quenching protocol was evaluated via repeated analysis of samples within a time interval of 24 h. Isocratic HPLC elution was performed using a Kromasil C18 column (see general procedures), a mobile phase consisting of MeOH/potassium phosphate buffer (100 mM, pH 6.0, 10 mM TBAB) 25:75 (v/v) and a flow rate of 1 ml/min. Detection wavelengths were 340 and 260 nm to monitor both NADPH and NADP<sup>+</sup>. Incubations were conducted in triplicate.

Additionally, the time-course of NADPH regeneration from CRS was studied. RLM (0.4 mg/ml microsomal protein), MgCl<sub>2</sub> (3.3 mM), G6P (3.3 mM) and G6P-DH (0.4 U/ml) were mixed with buffer and preincubated for 5 min at 37°C. Enzymatic reaction was initiated by addition of preheated NADP<sup>+</sup> (1.3 mM). Aliquots were removed at appropriate time points and processed as described above.

### 3.3.5 *In vitro* microsomal half-life determination

For determination of *in vitro* microsomal  $t_{1/2}$ , depletion-time profiles of CBX, MCBX and CPF PX in RLM and HLM were generated using incubation protocol A with optimised parameters.

CBX, MCBX and CPF PX (8 μM, stock solutions in DMSO, final DMSO concentration 0.8%) were incubated with either RLM (0.5 mg/ml) or HLM (3.0 mg/ml) in HEPES buffer (100 mM, pH 7.4, 3.3 mM MgCl<sub>2</sub>). After 5 min of preincubation, the reaction was initiated by addition of NADPH (1.3 mM, preheated to 37°C). Final incubation volume was 1 ml. Aliquots were removed at 0, 2, 5, 10, 15, 20, 25 and 30 min (RLM) or 0, 5, 10, 15, 20, 30 min (HLM)

and processed as described in general procedures. RLM assays were conducted in triplicate, HLM assays in duplicate. Data were analysed via non-linear curve fitting.

### 3.3.6 Species differences in microsomal metabolism

To assess interspecies variations in microsomal activity, CBX, MCBX and CPF PX (8  $\mu$ M, stock solutions in DMSO) were incubated with 0.4 mg/ml RLM, MLM, DLM and MPLM, 0.4 and 2.0 mg/ml HLM and 0.04 mg/ml RMLM according to protocol A. Incubation time was 30 min, total volume 500  $\mu$ l. All incubations were conducted in quadruplicate.

To generate species-specific *in vitro* metabolite profiles, CBX, MCBX and CPF PX (10  $\mu$ M) were incubated with liver microsomes according to protocol A (1 ml total incubation volume). The respective incubation times and microsomal protein concentrations are given in Table 5. Blank samples were included containing all matrix components except for substrate. Following incubation, samples were quenched with 2 volumes of ACN/MeOH (50:50, v/v, -20°C), vortexed (1 min, 21°C), centrifuged (20,000 rcf, 10 min, 21°C) and evaporated to dryness using a centrifugal vacuum concentrator (Concentrator 5301, Eppendorf) set to 45°C. Samples were subsequently reconstituted with 160  $\mu$ l HPLC eluent consisting of ACN/H<sub>2</sub>O/HAc 35:65:0.1 (v/v/v) and centrifuged for 3 min at 20,000 rcf (21°C). 25  $\mu$ l of the clear supernatant was injected onto a Kromasil C18 column (see general procedures) equipped with a 3 mm NH<sub>2</sub> guard column (OPTI-GUARD, Optimize Technologies). Flow rate was 1 ml/min, detection wavelength 275 nm. Peaks in the chromatograms were distinguished from matrix components by visual comparison with the blank samples. Retention factors (*k*) of the metabolites were calculated as

$$k = \frac{t_R - t_0}{t_0} \quad \text{Eq. 30}$$

with  $t_R$ , retention time and  $t_0$ , dead time.

Table 5. Species-specific microsomal incubation conditions for generation of *in vitro* metabolite profiles. All other parameters are specified in the general incubation procedures (protocol A).

Microsomes	Substrate	Microsomal protein concentration	Incubation time
		<i>mg/ml</i>	<i>min</i>
HLM	CBX, MCBX, CPFPPX	0.8	180
RLM	CBX, MCBX, CPFPPX	0.4	30
MLM	CBX, MCBX, CPFPPX	0.4	30
DLM	CBX, MCBX, CPFPPX	0.8	45
MPLM	CBX	0.8	45
	MCBX, CPFPPX	0.8	30
RMLM	CBX	0.04	45
	MCBX, CPFPPX	0.04	30

### 3.3.7 Enone metabolite formation

In preliminary studies, the potential enone precursor species **8-11** (8  $\mu$ M) were incubated with RLM (0.4 mg/ml) and HLM (0.8 mg/ml) for up to 4 h according to protocol A. Multiple samples were taken during incubation and processed as described in general procedures. The samples were analysed with regard to the appearance of **7** in the chromatograms. Peak identities were verified by comparison of the retention times with standard solutions of **7** and by conduction of additional spike experiments.

The time-course of formation of **7** from precursor **9** was assessed by incubation of **9** (4  $\mu$ M) with either 1.0 mg/ml HLM for 150 min or 0.4 mg/ml RLM for 100 min according to protocol A with prolonged centrifugation (15 min) of the quenched samples. Chromatographic separation was performed on a Kromasil C18 column (see general procedures) equipped with a 3 mm NH<sub>2</sub> guard column (OPTI-GUARD, Optimize Technologies) and an eluent composed of ACN/H<sub>2</sub>O/HAc 45:55:0.1 (v/v/v). All other chromatographic parameters were the same as those described in general procedures.

## 3.4 Radiotracer production

[<sup>18</sup>F]CPFPPX was synthesised in-house as described previously [226]. [<sup>18</sup>F]CBX and [<sup>18</sup>F]MCBX were synthesised analogous to [<sup>18</sup>F]CPFPPX with minor adjustments of the chromatographic separation procedure (HPLC column: Kromasil 100-5 C18, 250x10 mm (AkzoNobel, Bohus, Sweden); eluent: MeOH/H<sub>2</sub>O/HAc 60:40:0.2 (v/v/v)). Radiochemical

purity of the first [ $^{18}\text{F}$ ]CBX batches ranged from 95% to 97%. These batches were used exclusively for metabolism studies where radiochemical purity is not a critical parameter. For evaluation of brain kinetics and *in vitro* autoradiography, only batches with radiochemical purity >98% were used.

### 3.5 *In vitro* autoradiography

Whole brains of female Wistar rats were rapidly removed after decapitation of the animals and immediately frozen in isopentane (-50°C). The brains were cut into 20  $\mu\text{m}$  slices using a Leica CM3050 cryostat (Leica Biosystems, Nussloch, Germany) which was set to a temperature of -20°C. Sections were thaw-mounted onto silica-coated object slides, dried for 1 h at 37°C and stored in vacuum-sealed plastic bags at -80°C until use. Slices were preincubated in 50 mM TRIS buffer (pH 7.4) for 10 min (21°C) and subsequently incubated in 50 mM TRIS buffer (pH 7.4) containing 100  $\mu\text{M}$  GTP and 0.4-0.5 nM [ $^{18}\text{F}$ ]CBX, [ $^{18}\text{F}$ ]MCBX or [ $^{18}\text{F}$ ]CPFPX for 120 min (21°C). For estimation of non-specific binding, the competing ligand DPCPX (13  $\mu\text{M}$ ) was added to some incubations. The slices were washed twice in TRIS buffer (21°C) for 1 min, immersed in deionised water (4°C) to remove salt and dried under a stream of dry, warm (30°C) air for about 15 min. Subsequently, the dry slices were exposed to a phosphor imaging plate for 3-5 min, scanned with a phosphor imager (BAS 5000, Fujifilm, Düsseldorf, Germany) and analysed with appropriate software (AIDA Image Analyzer V4.13, Raytest, Straubenhardt, Germany). To estimate total and non-specific binding of the radiotracers, regions of interest (ROIs) were drawn around the entire brain slices and deposited energies within these ROIs were quantified. Specific binding was calculated as the difference between total and non-specific binding. Mean values were determined from 7-8 incubated slices per tracer.

### 3.6 *In vivo* pharmacokinetics

#### 3.6.1 Animals

All animal experiments were conducted in accordance with the German Animal Welfare Act and approved by the governmental authorities (AZ: 84-02.04.2014.A496). Adult male Sprague Dawley rats ( $n = 33$ , body weight =  $505 \pm 43$  g) were housed two to three per cage under standard conditions (12-h light/12-h dark cycle, 22°C) with access to food and water *ad libitum*. Data sets of 26 animals were included in the evaluation.

### 3.6.2 Blood sampling and analysis

The animals were anaesthetised with a mixture of isoflurane/oxygen (5% isoflurane during induction, 1.5–2% during maintenance of anaesthesia). Respiratory rate and body temperature were controlled during anaesthesia and kept within physiological ranges. A catheter was placed in the right femoral artery for blood sampling; another catheter was placed in the tail vein for radiotracer application. [ $^{18}\text{F}$ ]CPFPX, [ $^{18}\text{F}$ ]MCBX or [ $^{18}\text{F}$ ]CBX ( $21 \pm 2.5$  MBq ( $0.44 \pm 0.22$  nmol) in a volume of 1 ml physiological saline solution) was administered over 1 min using a syringe pump (model 44, Harvard Apparatus, Holliston, USA). Arterial blood samples (ca. 200  $\mu\text{l}$ ) were collected at regular time intervals throughout the 180-min measurement. Details on the blood sampling procedure can be found in [215]. Total blood sampling volume was kept below 10% of the circulating blood volume of the animal. The blood samples were weighed and measured in a  $\gamma$ -counter (ISOMED 2100, MED Nuklear-Medizintechnik Dresden GmbH, Dresden, Germany) to calculate whole blood radioactivity concentration. Plasma was separated by centrifugation (3000 rcf, 3 min, 21°C), weighed and measured in the  $\gamma$ -counter to calculate plasma radioactivity concentration. Fractions of unchanged tracer and radiometabolites in plasma were assessed by radio-thin layer chromatography (TLC) analysis. Aliquots (45  $\mu\text{l}$ ) of plasma were mixed with 3 volumes of methanol/acetonitrile (50:50, v/v, 4°C), vortexed (1 min, 21°C) and centrifuged (20,000 rcf, 5 min, 21°C) to sediment precipitated protein. Aliquots (5  $\mu\text{l}$ ) of the supernatants were spotted on a TLC plate (SIL G-25, 10x20 cm, Macherey-Nagel, Düren, Germany). The TLC plate was developed with ethyl acetate/hexane, 75:25 (v/v), dried and subsequently imaged for 50 min with an electronic autoradiography system (InstantImager, Canberra-Packard, Rüsselsheim, Germany). Using the implemented InstantImager software, ROIs were defined for unchanged tracer and metabolites. Radioactivity within these ROIs was quantified and used for calculation of the fraction of unchanged tracer. Retardation factors ( $R_f$ ) of the metabolites were calculated as the ratio of the migration distance of the metabolite (centre of the spot) to the migration distance of the solvent front. To determine the recovery of radioactivity after the extraction step, aliquots (5  $\mu\text{l}$ ) of both supernatant and native plasma were spotted on a separate TLC plate which was not developed. This plate was imaged simultaneously with the first one. Recovery was calculated as the ratio of radioactivity in supernatant to that in plasma, corrected for the dilution factor. Whole blood and plasma time-activity curves (TACs) were generated and decay corrected to the time of tracer injection. Standardised uptake values (SUVs) of whole blood and plasma were calculated according to the following formula [250]:

$$SUV = \frac{r}{(a'/w)} \quad \text{Eq. 31}$$

where  $r$  is the radioactivity concentration,  $a'$  is the amount of injected radioactivity (decay corrected) and  $w$  is the body weight. For both whole blood and plasma, a specific density of 1 g/ml was assumed. Plasma SUV versus time data were fitted to triexponential functions. Total clearance (CL), volume of distribution ( $V_d$ ) and terminal half-life ( $t_{1/2\gamma}$ ) of the tracers were estimated from the fitted parameters via non-compartmental analysis (see section 1.5.3.2).

### 3.6.3 Plasma protein binding

An additional blood sample was taken before tracer injection to assess the plasma protein binding of the tracer. 200–300  $\mu$ l of the separated plasma was spiked with tracer (5–6 kBq) and incubated for 1 h at 37°C and 300 rpm in a thermomixer device (Thermomixer Comfort, Eppendorf, Hamburg, Germany). Plasma proteins were removed via ultrafiltration using Microcon-30 kDa centrifugal filter units (Merck Millipore, Darmstadt, Germany). The filter units were centrifuged for 20 min at 14,000 rcf and 37°C. Radioactivity in equal volumes (50  $\mu$ l) of spiked plasma and filtrate was measured in a  $\gamma$ -counter. Calculated free fractions were used only for comparison of the physicochemical properties of the tracers. For kinetic analyses, a free fraction of 1 was assumed for all tracers.

### 3.6.4 Brain PET imaging

Four animals per tracer received an additional brain PET scan which was performed on a Siemens Inveon PET/CT Multimodality System (Siemens, Erlangen, Germany). The catheterised animals were positioned in the scanner with the brain in the field of view. Prior to tracer administration, a 20-min transmission scan ( $^{57}\text{Co}$  source) was carried out to correct for attenuation. PET acquisition (180 min) started simultaneously with tracer injection. List-mode PET data were reframed into a dynamic sequence of 12x10 s, 6x30 s, 15x60 s, 8x300 s and 12x600 s frames. The data were corrected for random coincidences, scattered radiation and attenuation, rebinned into 2-dimensional sinograms (Fourier Rebinning Algorithm) and reconstructed via filtered backprojection (ramp filter, cutoff: 0.5). The final datasets consisted of 159 slices with an image voxel size (x, y, z) of 0.7764, 0.7764, 0.796 mm (matrix size (x, y, z, t): 128, 128, 159, 53).

### 3.6.5 Analysis of brain PET data

Brain PET data were analysed using the PMOD V 3.4 software package (PMOD Technologies LLC, Zürich, Switzerland). Three-dimensional regions of interest were drawn manually or semi-automatically (iso-contour algorithm) around the entire brain. Whole brain TACs and SUVs were calculated, assuming a specific density of 1 g/mL for brain tissue. Time-weighted average SUV images (time window: 0-60 min post injection (p.i.); SUV maximum set to 5 g/ml) were generated for visual illustration. Cerebral pharmacokinetics of [<sup>18</sup>F]CPFPX, [<sup>18</sup>F]MCBX and [<sup>18</sup>F]CBX were evaluated using both graphical and compartmental analysis. Metabolite corrected arterial plasma TACs served as input functions for kinetic modelling. Logan graphical analysis was used to determine total cerebral distribution volume ( $V_T$ ) of the tracers. Individual transfer rate constants and macro parameters were estimated from two-tissue compartment model fits of dynamic whole brain PET data. For [<sup>18</sup>F]CBX, only  $V_T$  and specific volume of distribution ( $V_S$ ) could be estimated reliably from 2TCM fits of the data, therefore, additional one-tissue compartment model fits were used to derive the influx and efflux rate constants  $K_1$  and  $k_2$ . Iterative fitting was performed using a Levenberg-Marquardt algorithm (non-linear least squares minimisation procedure). Residual weighting took into account frame duration, radioactive decay and, if appropriate, measured uptake. The fractional blood volume was fixed to a value of 3.6% [251]. No correction was applied for the time delay between the blood and tissue activity curves. The applied pharmacokinetic methods and models are described in detail in sections 1.6.5 and 1.6.6.

## 3.7 Statistical methods

Values are given as mean  $\pm$  SD unless stated otherwise. For statistical analyses, OriginPro 2015G (OriginLab, Northampton, USA) and GraphPad Prism 4 (GraphPad Software, La Jolla, USA) were used. Significant differences between the means of individual test groups were assessed by using either an independent two-tailed t-test or a one-way analysis of variance (one-way ANOVA) followed by a *post-hoc* Tukey test. The significance level was set to 0.05. Normal distribution of the data and homogeneity of variances were assumed. In the following, the principles of the applied methods are outlined briefly. A comprehensive summary including the mathematical principles can be found in [252].

### 3.7.1 Independent t-test

The independent t-test is a statistical hypothesis test which is commonly used to determine whether the means of two independent (unrelated) groups differ significantly from each other. It is based on the t-distribution which represents a continuous, bell-shaped probability distribution similar to the normal distribution [253]. The t-distribution is used to estimate population parameters from small samples of populations with (nearly) normal distribution. The independent t-test discriminates between two statistical hypotheses: the null hypothesis which states that there is no difference between the means of the two groups and the alternative hypothesis which states that there is a difference between them. When performing a t-test, the group means, standard deviations and group sizes are used to calculate the t-test statistic (t-value) from which a p-value is derived which represents the probability that the null hypothesis is true, i.e. that the means of the two groups are not significantly different. The p-value is then compared to a pre-set significance level ( $\alpha$ ) which indicates the risk of rejecting the null hypothesis although it is true. If the p-value is less than  $\alpha$ , the null hypothesis is rejected and the two test groups are stated to be significantly different. Typically, the significance level is set to 0.05, this means that a 5%-risk of erroneously rejecting the null hypothesis (type 1 error) is accepted. A t-test can be performed in either one-tailed or two-tailed configuration, depending on the exact formulation of the alternative hypothesis. With the one-tailed t-test, statistical significance is tested in only one direction of interest, i.e. the test determines either if one mean is greater than another mean or if it is less, but not both. In contrast, the two-tailed t-test evaluates significance in both directions simultaneously and thus allows for statements on whether two means are significantly different from each other irrespective of whether the effect is positive or negative.

### 3.7.2 One-way ANOVA

The one-way ANOVA is employed to test for significant differences among three or more group means. ANOVA uses F-tests [254] to determine whether the variability between group means is larger than the variability within the groups. If the ratio of between-group variability to within-group variability (F-value) is high enough, the null hypothesis (which states that the group means are equal) can be rejected. As with the t-test, a p-value (the probability that the null hypothesis is true) is calculated from the F-test statistic and compared to a pre-set significance level  $\alpha$ . The null hypothesis is rejected if the p-value is lower than  $\alpha$ . The one-way ANOVA is the simplest form of ANOVA tests, since it examines

---

the effect of only one factor on a dependent variable [255]. This is equivalent to the t-test. Following a significant ANOVA test result, a *post-hoc* analysis is performed to determine which group means are significantly different. In this work, the Tukey test [256] was applied to compare the individual means. The Tukey test compares each mean to every other mean (all pairwise comparisons) while controlling the increase in type 1 error arising from multiple statistical testing. A concise summary on the principles of the Tukey test can be found in [257].

## 4 Results and Discussion

### 4.1 *In vitro* microsomal metabolism

#### 4.1.1 Influence of incubation conditions on substrate depletion

##### 4.1.1.1 Incubation matrix composition

Generally, evaluation of microsomal incubation conditions was done within physiologically relevant parameter ranges. The effects of changes in incubation matrix composition on the metabolic depletion of CBX, MCBX and CPF PX are summarised in Fig. 13. From these data, the ratios of depletion of CBX and MCBX to CPF PX were calculated (Fig. 14). The results of statistical data analysis (significant group differences) are listed in Table 6.

In order to assess the potential influences of the buffer substance on microsomal degradation of the test compounds, three buffers were compared which are frequently used in enzyme assays: sodium phosphate, MOPS and HEPES buffer. TRIS buffer, although offering a suitable pH range, was excluded from the evaluation, since preliminary tests showed that this buffering agent adversely affects chromatographic performance during sample analysis. Metabolic activity in liver microsomes (as measured by substrate depletion) was about 25% higher in HEPES than in sodium phosphate buffer. With MOPS buffer, comparable increases in metabolic activity were obtained for CBX and MCBX, whereas for CPF PX, depletion in MOPS and sodium phosphate buffer did not differ significantly. Since HEPES buffer provided best support of enzymatic degradation of CBX, MCBX and CPF PX in RLM and exhibited good chromatographic properties, this buffer type was chosen for all further incubations.

The reduced metabolic activity observed with sodium phosphate buffer could possibly be attributed to an inhibitory effect of the phosphate ion towards G6P-DH [258], which may result in a deceleration of NADPH regeneration, or to the complexation of  $Mg^{2+}$  ions which are known to exhibit a stimulatory effect on the microsomal metabolism of several substrates [259]. It is also conceivable that differences in the ionic strength of the buffer preparations [260] may lead to conformational alterations of the enzymes which affect substrate binding and conversion. However, as the influence of the buffer type on metabolic activity was not particularly pronounced, this parameter is not considered critical.

The effect of buffer concentration on substrate depletion was evaluated using HEPES buffers ranging from 50–500 mM. This concentration range reflects physiological intracellular ionic strength which is typically in the range of 150-200 mM [261]. Since buffer molecules are generally the main ionic species in microsomal stability assays, buffer molarity can be considered decisive for *in vitro* ionic strength. Medium buffer concentrations (100 or 200 mM HEPES) proved to be favourable in terms of metabolic activity. Increasing the buffer concentration from 100 to 500 mM caused a significant decrease of CPFPX depletion (by 13%), but not of CBX and MCBX depletion. Decreasing the buffer concentration from 100 to 50 mM resulted in reduced depletion of MCBX and CPFPX (by 14% and 25%, respectively), but also in a marked shift of the pH value of the incubation matrix towards more acidic conditions (approx. pH 7.2), indicating an insufficient buffer capacity. Further studies on the influence of buffer pH on substrate depletion clearly showed an adverse effect of lower pH values on enzyme activity (see below), which suggests that the deceleration of substrate degradation observed with the use of 50 mM HEPES buffer is caused by the pH shift rather than by the lower ionic strength of the medium.

The influence of pH on metabolic activity was quite pronounced. For both protocol A (NADPH) and protocol B (CRS), substrate depletion was highest in microsomal incubations conducted at pH 7.4. At a pH value of 6.8, CBX depletion decreased by 44% (protocol A) or 48% (protocol B), MCBX depletion by 45% (protocol A) or 58% (protocol B) and CPFPX depletion by 51% (protocol A) or 65% (protocol B). When incubations were conducted according to protocol A, an increased pH value of 8.2 resulted in a considerable reduction of CPFPX and MCBX depletion by 29% and 37%, respectively. In contrast, when incubations were conducted using a CRS (protocol B), the more basic conditions only affected CPFPX depletion in a significant way (12% decrease). The varying magnitude of pH dependent decrease in metabolic activity observed when NADPH was supplied either directly or via a CRS might be a consequence of different pH optima of the individual enzymes involved in the catalytic cycle. G6P-DH typically shows maximum catalytic activity at pH values above 7.4 depending on the buffer medium [262]. Enhanced supply of NADPH by G6P-DH could partially compensate negative effects of increased pH values on catalytic activity of cytochrome P450 enzymes or cytochrome P450 reductase, resulting in a less pronounced decline of substrate metabolism.

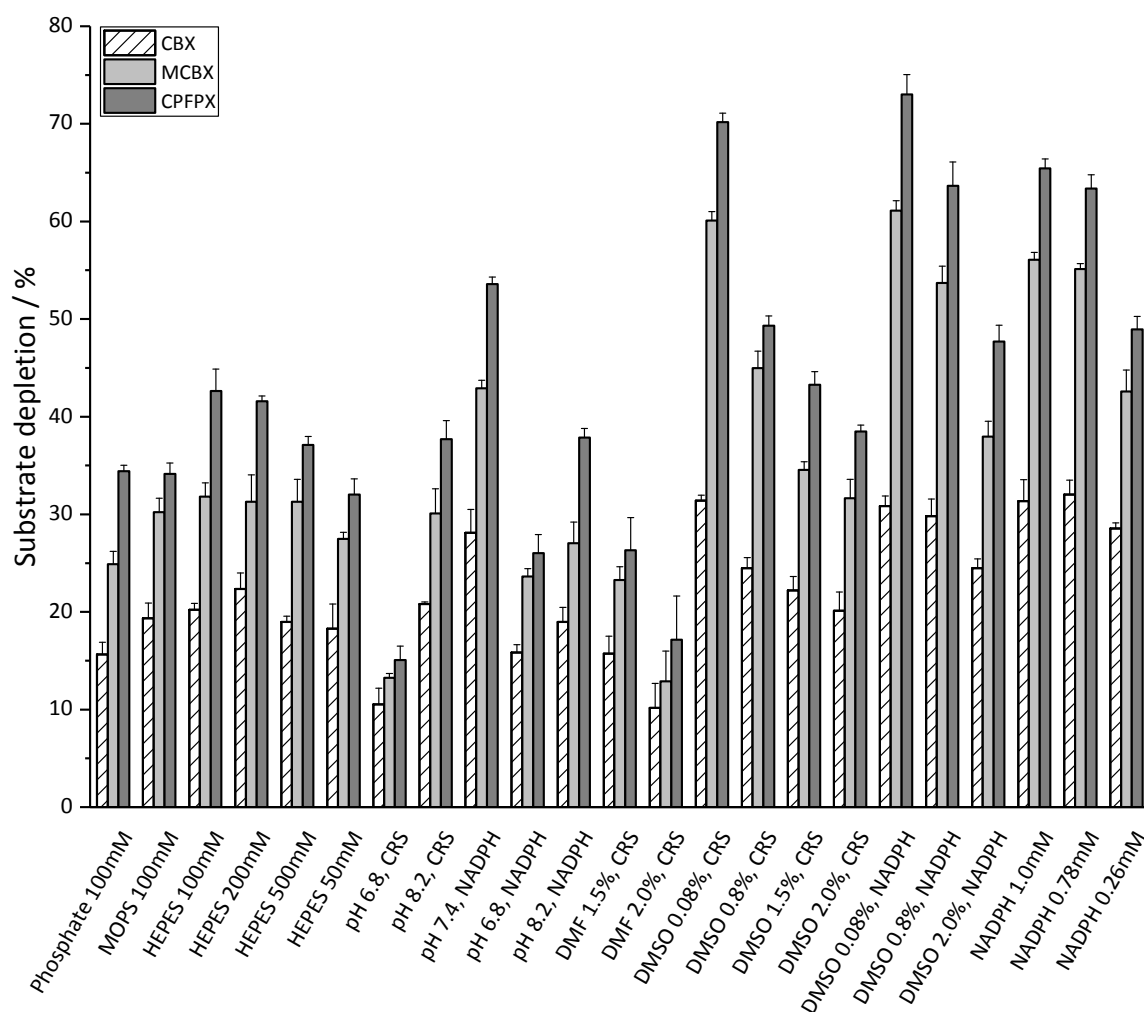


Fig. 13. Influence of incubation matrix composition on depletion of CBX, MCBX and CPFPX in rat liver microsomes. Bars represent the loss of substrate during an incubation period of 30 min. For every data set, the detailed composition of the incubation matrix is given in Table 4. Data represent the mean  $\pm$  SD of four independent experiments. Results of statistical evaluation are given in Table 6.

Studies on the effect of organic solvents on enzyme activities were limited to DMF and DMSO due to the inadequacy of other frequently used solvents (alcohols, alkanes, ketones, tetrahydrofuran) to dissolve sufficient quantities of the xanthine derivatives. DMF exhibited considerably higher inhibitory potential than DMSO. Depletion of the test compounds was 16–42% lower when incubations contained 0.8% DMF instead of 0.8% DMSO and 97–145% lower when incubations contained 2.0% DMF instead of 2.0% DMSO. Since DMSO proved to be favourable in terms of enzyme activity, investigations concerning the influence of cofactor supply (NADPH vs. CRS) were conducted exclusively with DMSO. At DMSO concentrations above 0.08%, direct addition of NADPH resulted in a marked enhancement of metabolic activity. Substrate depletion was increased by 19–29% compared to incubations using a CRS. However, at 0.08% DMSO, direct addition of NADPH did not result in considerable differences in metabolic activity.

Table 6. Results of statistical evaluation of the data visualised in Fig. 13. Evaluation was performed using one-way ANOVA with *post-hoc* Tukey test.  $P < 0.05$  was considered statistically significant.

Parameter	Means comparison	Significant difference
Buffer type	MOPS vs. Phosphate	CBX, MCBX
	HEPES vs. Phosphate	CBX, MCBX
	HEPES vs. MOPS	CPFPX
Buffer concentration	HEPES 200 mM vs. 100 mM	-
	HEPES 500 mM vs. 100 mM	CPFPX
	HEPES 500 mM vs. 200 mM	CBX, CPFPX
	HEPES 50 mM vs. 100 mM	MCBX, CPFPX
	HEPES 50 mM vs. 200 mM	CBX, CPFPX
	HEPES 50 mM vs. 500 mM	CPFPX
pH (CRS)	pH 6.8 vs. pH 7.4 (CRS)	CBX, MCBX, CPFPX
	pH 8.2 vs. pH 7.4 (CRS)	CPFPX
	pH 8.2 vs. pH 6.8 (CRS)	CBX, MCBX, CPFPX
pH (NADPH)	pH 6.8 vs. pH 7.4 (NADPH)	CBX, MCBX, CPFPX
	pH 8.2 vs. pH 7.4 (NADPH)	CBX, MCBX, CPFPX
	pH 8.2 vs. pH 6.8 (NADPH)	MCBX, CPFPX
DMF concentration	DMF 1.5% vs. 0.8%	CBX, MCBX, CPFPX
	DMF 2.0% vs. 1.5%	CBX, MCBX, CPFPX
	DMF 2.0% vs. 0.8%	CBX, MCBX, CPFPX
DMSO concentration (CRS)	DMSO 0.8% vs. 0.08% (CRS)	CBX, MCBX, CPFPX
	DMSO 1.5% vs. 0.08% (CRS)	CBX, MCBX, CPFPX
	DMSO 1.5% vs. 0.8% (CRS)	MCBX, CPFPX
	DMSO 2.0% vs. 0.08% (CRS)	CBX, MCBX, CPFPX
	DMSO 2.0% vs. 0.8% (CRS)	CBX, MCBX, CPFPX
	DMSO 2.0% vs. 1.5% (CRS)	CPFPX
DMSO concentration (NADPH)	DMSO 0.8% vs. 0.08% (NADPH)	MCBX, CPFPX
	DMSO 2.0% vs. 0.08% (NADPH)	CBX, MCBX, CPFPX
	DMSO 2.0% vs. 0.8% (NADPH)	CBX, MCBX, CPFPX
NADPH concentration	NADPH 1.0 mM vs. 1.3 mM	-
	NADPH 0.78 mM vs. 1.3 mM	-
	NADPH 0.78 mM vs. 1.0 mM	-
	NADPH 0.26 mM vs. 1.3 mM	MCBX, CPFPX
	NADPH 0.26 mM vs. 1.0 mM	MCBX, CPFPX
	NADPH 0.26 mM vs. 0.78 mM	CBX, MCBX, CPFPX

With regard to the enzyme-substrate systems evaluated in the present study, DMF showed considerably stronger inhibitory effects on microsomal metabolism than DMSO. By contrast, Hickman et al. observed only slight inhibition of caffeine N<sup>3</sup>-demethylation in HLM by DMF but substantial inhibition by DMSO [263]. The insufficient transferability of results obtained with quite similar enzyme-substrate systems becomes even more apparent when comparing the extent of inhibition produced by a particular solvent. The inhibitory effect of DMSO on P450 1A2 has been the subject of numerous studies with sometimes controversial results. Some authors reported only slight inhibition of biotransformation at DMSO concentrations of up to 2% [264–266], whereas others observed a medium to high inhibitory potential even at concentrations as low as 0.2% [263, 267, 268]. The test systems used in these studies differed with regard to enzyme preparation (microsomes, isoenzymes, hepatocytes), species from which the enzymes originated (human, rat), test substrate/test reaction (phenacetin O-deethylation, caffeine N<sup>3</sup>-demethylation) and composition of the incubation medium. These widely varying results illustrate that the inhibitory potential of organic solvents on a given enzyme-substrate system cannot be predicted reliably on the basis of published studies which used slightly different experimental setups, but has to be investigated experimentally.

Increasing DMSO concentrations had more pronounced effects on metabolic activity when NADPH was supplied indirectly via a CRS. Apparently, DMSO did not only inhibit the CYP/CPR system, but also G6P-DH, resulting in further reduction of substrate depletion rates. Only at very low DMSO concentrations (0.08%), this additional effect becomes negligible, so that no significant difference could be observed between incubations conducted according to either protocol A or B. Although DMSO concentrations below 0.1% proved to be advantageous in terms of enzyme activity, pipetting minimum liquid volumes (0.4 µl) did result in poor assay precision. Final concentrations of substrate and DMSO in the incubation matrix varied considerably between repeated assays (regardless of the pipetting technique used). Additionally, preliminary tests showed that the addition of an adequate amount of DMSO helps to stabilise the poorly water soluble xanthine derivatives in aqueous solution. Hence, a final DMSO concentration of 0.8% was considered acceptable for further microsomal assays. Although this concentration appears quite low, it greatly exceeds the amount of organic solvents applied *in vivo* in the context of a typical PET scan (adjuvants or residual impurities in the tracer injection solution). This difference between *in vitro* and *in vivo* situations, which is difficult, if not impossible, to overcome (at least for the hydrophobic compounds used in this work), may account for discrepancies in *in vitro-in vivo* comparisons.

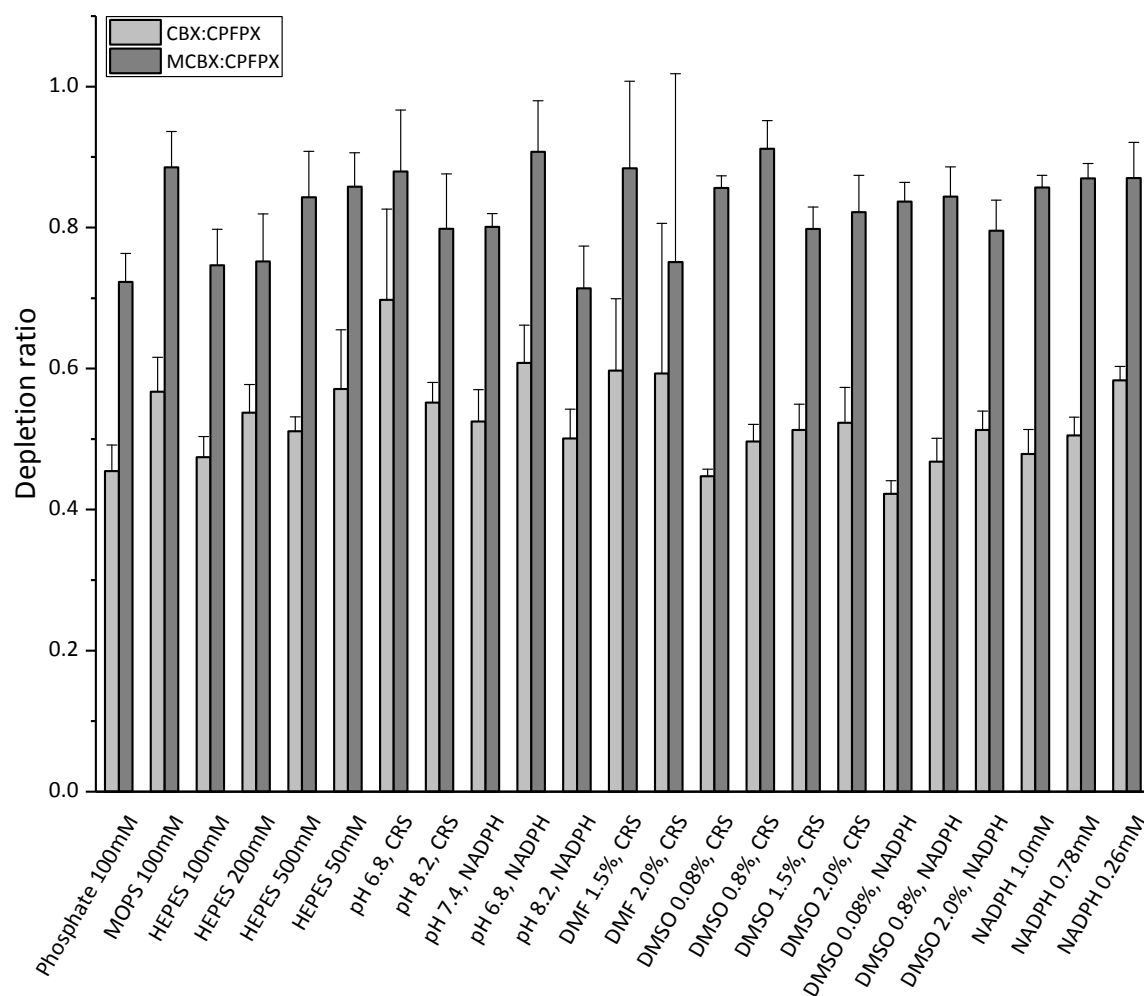


Fig. 14. Influence of incubation matrix composition on depletion ratios of CBX and MCBX to CFPFX in rat liver microsomes. Bars represent the quotient of percentage degradation of CBX and CFPFX and MCBX and CFPFX, respectively. Note that the depletion ratios are only slightly affected by changes in the composition of the incubation matrix. Ratios were calculated from the mean values ( $n=4$ ) of substrate depletion, error bars represent the SD estimated via error propagation.

A reduction of the NADPH concentration from 1.3 mM (standard assay condition) to 0.78 mM did not affect microsomal metabolism of CBX, MCBX and CFPFX significantly. Further reduction to 0.26 mM diminished MCBX and CFPFX depletion by about 20%, whereas CBX depletion was not affected in a significant way. These results clearly indicate that small to medium variations in NADPH concentration caused by depletion or incomplete reduction of  $\text{NADP}^+$  via G6P/G6P-DH do not influence substrate degradation to a relevant extent, since NADPH is present in high excess in the microsomal assay (millimolar concentration of NADPH, micromolar concentration of substrate).

In summary, modification of incubation matrix composition resulted in variations in substrate depletion of up to 300% for the slowly metabolised CBX and up to 500% for the quickly metabolised MCBX and CFPFX. In contrast, depletion ratios (CBX to CFPFX and

MCBX to CPFPPX) proved to be highly constant. The mean values were  $0.53 \pm 0.06$  (CBX:CPFPPX) and  $0.83 \pm 0.06$  (MCBX:CPFPPX). These figures illustrate that a relative quantification approach such as the calculation of depletion ratios allows for statements on metabolic stability that are rather insensitive to variations of the test conditions.

#### 4.1.1.2 Concentration of microsomal protein

The impact of varying concentrations of microsomal protein on substrate depletion kinetics was studied by measuring initial velocities of CPFPPX metabolism in rat liver microsomes. Since most microsomal incubations carried out in this work were done at concentrations of 0.2 to 0.8 mg/ml microsomal protein, this range was used for evaluation. As can be seen in Fig. 15, the initial velocity tracked almost linearly with increasing protein concentration. A weighted linear regression model could be fitted to the dataset with an adjusted  $R^2$  of 0.9917. A doubling of the protein concentration resulted in an approximate doubling of the initial velocity. It can thus be anticipated that, within the concentration range evaluated, sufficient comparability of initial velocity data measured at different concentrations of microsomal protein is ensured. Given the high degree of physicochemical similarity between the test compounds, it seems reasonable to assume that these findings can be transferred to CBX and MCBX.

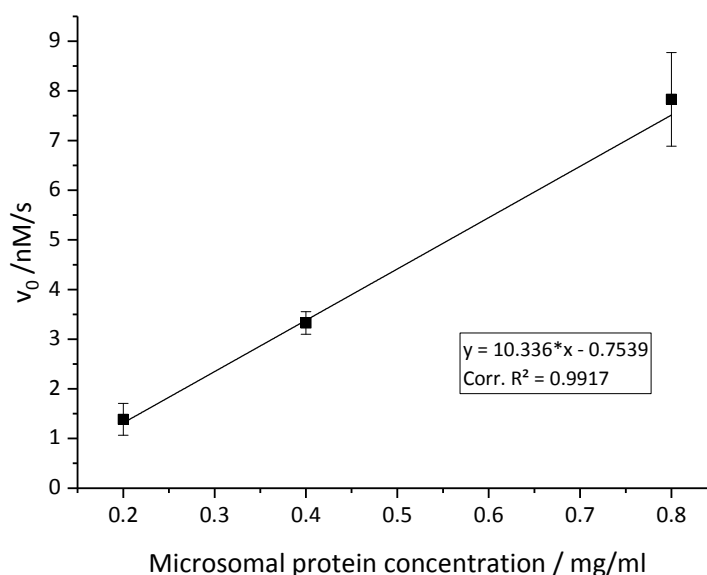


Fig. 15. Dependence of the initial reaction velocity on the concentration of microsomal protein. A weighted linear model was fitted to the data. Each data point represents the mean  $\pm$  SD of four independent determinations.

## 4.1.2 Enzyme stability *in vitro*

### 4.1.2.1 Effect of preincubation

Prolonged preincubation of microsomal matrix with NADPH resulted in a rapid decrease of metabolic activity (Fig. 16). After 30 min of preincubation, depletion of added CPF PX was reduced by 34% compared to the value obtained with a preincubation time of only 2 min. After 120 min, metabolic activity was diminished by 89% and CPF PX degradation could hardly be observed. No significant differences in CPF PX depletion could be observed when preincubation (60 min) was conducted in the presence of both medium and high concentrations of the antioxidant enzymes catalase and superoxide dismutase.

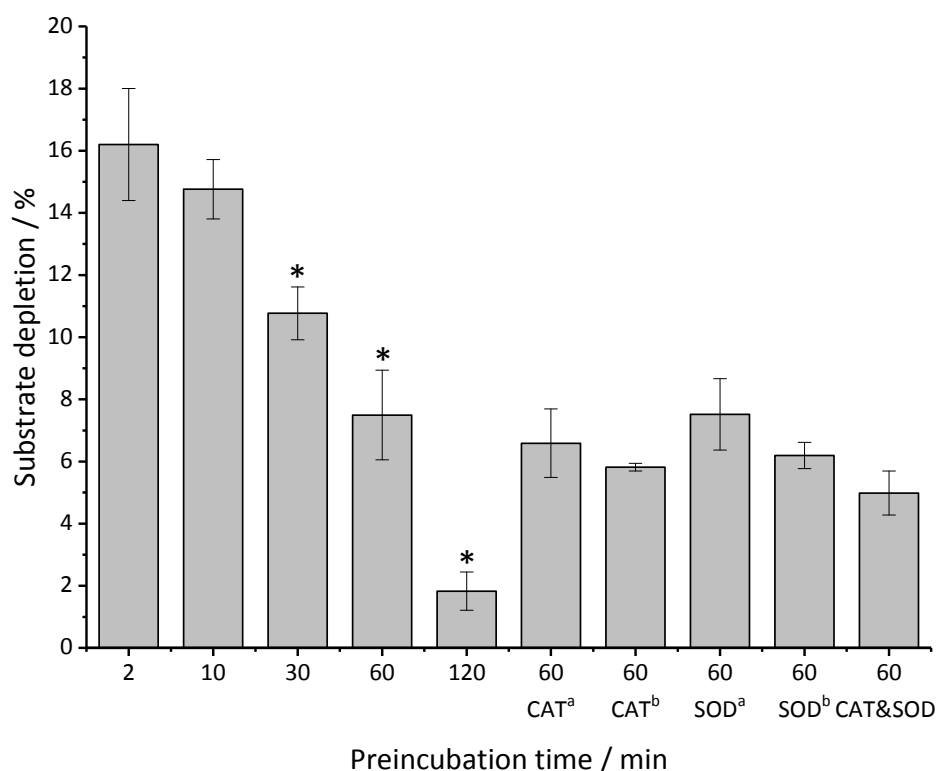


Fig. 16. Decrease of microsomal activity as a consequence of prolonged preincubation periods. CPF PX depletion was assayed in RLM following preincubation of microsomal protein with NADPH. Concentrations of CAT and SOD were as follows: CAT<sup>a</sup> = 1 U/ml, CAT<sup>b</sup> = 1500 U/ml, SOD<sup>a</sup> = 100 U/ml, SOD<sup>b</sup> = 1000 U/ml, CAT&SOD = 1000 U/ml (each). Data represent the mean  $\pm$  SD of three independent experiments. \*Significant difference from 2 min ( $p < 0.05$ , two-tailed t-test)

Inactivation of P450 enzymes in microsomal assays is a frequently observed phenomenon the causes of which are still controversially discussed. In addition to mechanism-based inhibition occurring during catalytic turnover of substrates which form active intermediates that bind covalently to the enzyme, inactivation processes have also been observed in the

absence of any substrate. The formation of reactive oxygen species was identified as a key factor for P450 inactivation, although there still remain some uncertainties regarding the influence of the particular sources of ROS production in the microsomal system. Generation of ROS is an inevitable side effect of the catalytic cycle of P450, resulting from uncoupling of the electron transfer chain [164, 269, 270]. P450 dependent generation of ROS is considered a major cause of enzyme inactivation and lipid peroxidation in hepatic tissue. Alternatively, ROS formation due to NADPH oxidase (NOX) activity in microsomal preparations has been proposed by several authors [271–273].

Addition of CAT and SOD to the microsomal incubation matrix was reported to prevent hydrogen peroxide formation [274], microsomal lipid peroxidation [271] and P450 inactivation [178]. However, in the present study, no restoring effect of CAT and SOD could be observed (Fig. 16). Since the mechanisms of ROS action on microsomal targets are not yet fully understood, the effectiveness of incubation additives is likely to vary largely from one particular system to another. Different effects of ROS formed either directly at the active site of the P450 enzyme or accumulating in the surrounding matrix were reported [275], as well as variations in ROS action in dependence of the source of the enzyme and the composition of the incubation matrix [270, 276]. It might also be possible that CAT and SOD exhibit an inhibitory effect on several P450 isoenzymes which counteracts the potential benefits of ROS detoxification.

In view of the pivotal role of NADPH in the process of enzyme inactivation, further studies on the fate of NADPH in microsomal assays were conducted in order to determine incubation conditions that allow for minimisation of undesired side effects. The results of these investigations are presented in the following section.

#### **4.1.2.2 Stability of NADPH during incubation**

The stability of NADPH in buffer and in microsomal incubation matrix with or without specific additives is shown in Fig. 17. NADPH proved to be quite stable in HEPES buffer (100 mM, pH 7.4, 3.3 mM MgCl<sub>2</sub>). After 3 h of incubation at 37°C, the concentration of NADPH dropped by only 17%. When NADPH was incubated in the presence of microsomal protein (0.4 mg/ml RLM), a steep, monoexponential decrease in concentration could be observed. After 3 h, the concentration of NADPH dropped by almost 77%. UV detection at 260 nm revealed a simultaneous increase of the NADP<sup>+</sup> peak, indicating an oxidation of NADPH rather than decomposition (Fig. 18). Addition of EDTA (5 mM) could not prevent the fast loss of NADPH. Addition of plumbagin (1 μM) even accelerated NADPH loss. However, addition of DPI could prevent consumption of NADPH even at low concentrations (25 μM).

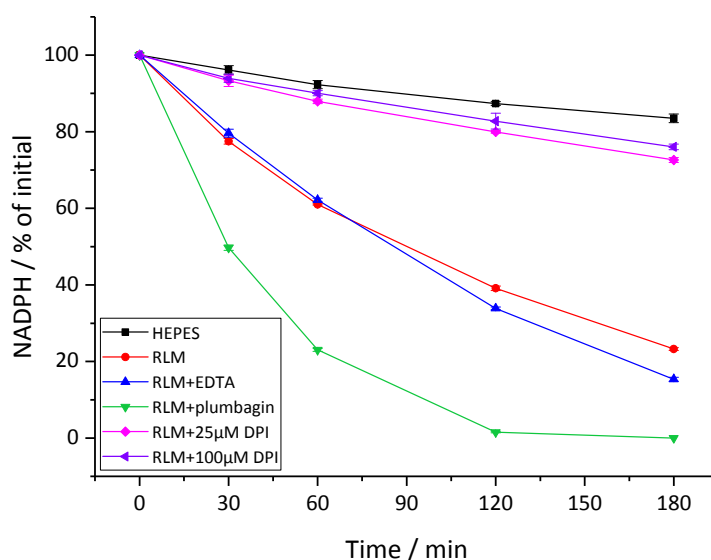


Fig. 17. Time course of NADPH loss during incubation in buffer or microsomal incubation matrix. Incubations were conducted at 37°C. Data points represent the mean  $\pm$  SD of three independent experiments.

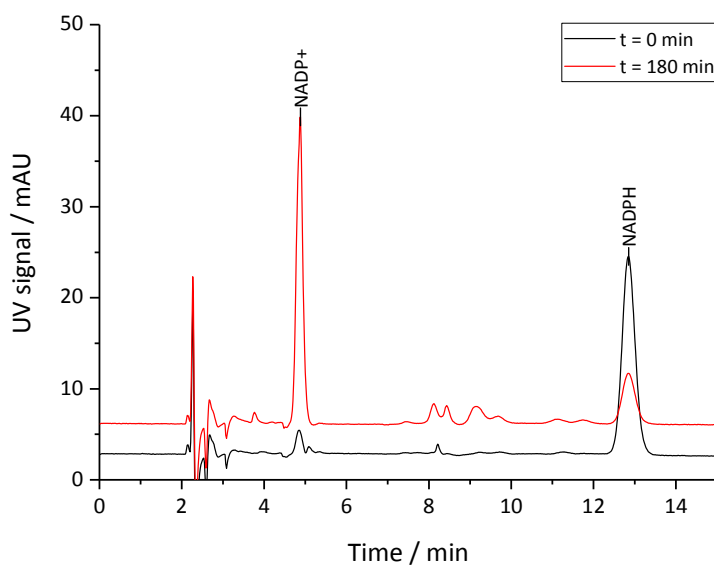


Fig. 18. NADPH consumption in RLM. NADPH was incubated in buffer containing microsomal protein. One sample was analysed directly after mixing of all components (black chromatogram), another after an incubation period of 3 h (red chromatogram). The decrease of the peak area of the NADPH peak is accompanied by an increase of the peak area of the NADP<sup>+</sup> peak, indicating oxidative consumption of NADPH in the microsomal matrix. Detection wavelength was 260 nm.

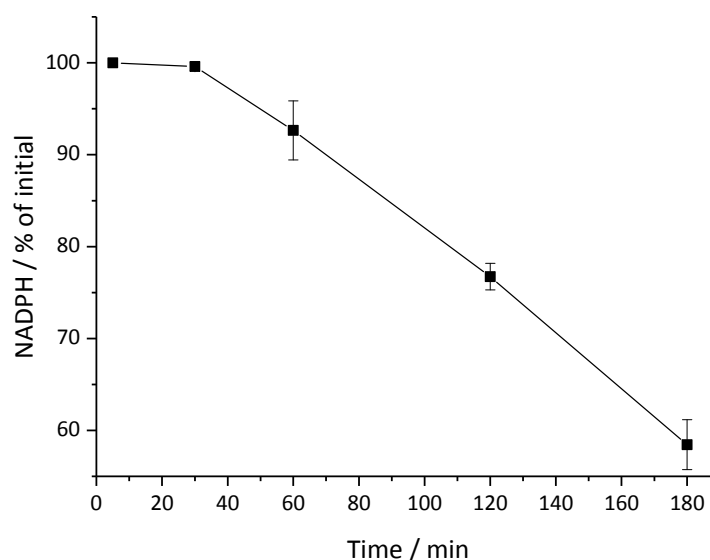


Fig. 19. Time-course of *in situ* NADPH regenerated via G6P/G6P-DH. The value obtained from the first sample taken at 5 min was set at 100% (initial value). Data points represent the mean  $\pm$  SD of three independent experiments.

*In situ* cofactor regeneration via the G6P/G6P-DH system resulted in a stable NADPH level during the first 30 min (Fig. 19). After 60 min, the concentration of NADPH was still above 90% of the initial value. When incubation times were extended, NADPH concentration decreased in an almost linear manner, resulting in a 42% reduction of NADPH after 3 h.

It is well-known that the chemical stability of NADPH in solution is adversely affected by low pH values (below pH 8) and by the presence of several ionic species such as phosphate and acetate ions [277, 278]. While the buffer system chosen for the present study proved to be favourable in terms of NADPH stability, the addition of microsomal protein led to a dramatic acceleration of NADPH loss. Nevertheless, it seems unlikely that the mere reduction of the NADPH concentration accounts for the decrease in enzymatic activity observed with prolonged preincubation periods (section 4.1.2.1). The loss of NADPH in microsomal matrix was about 23% after 30 min (compare Fig. 17), hence the remaining NADPH concentration in the incubation matrix was about 1.0 mM. As discussed in section 4.1.1.1, reduction of the NADPH concentration from 1.3 mM to 1.0 or even 0.78 mM did not result in a significant reduction of substrate metabolism in microsomal assays. This strengthens the hypothesis that the actual reason for the loss of metabolic activity is enzyme inactivation rather than shortage of the cofactor.

Complementary to the previously described studies concerning the influence of antioxidant enzymes on metabolic activity (section 4.1.2.1), the potential of several non-enzymatic additives to prevent NADPH loss (and thus NADPH-dependent ROS formation) during incubation was investigated.

It has been reported that addition of EDTA to microsomal incubations could prevent NADPH-dependent lipid peroxidation, probably by chelating non-haem iron which may act as a catalyst in the formation of the highly reactive hydroxyl radical [279–282]. This pathway does not appear relevant for the system used in the present study, since addition of 5 mM EDTA did not result in a considerable change of NADPH loss. It is possible that, in the studies cited above, the lack of high purity chemicals and sophisticated technical equipment led to a higher content of iron in the microsomal incubations than usually encountered today. This might be an explanation for the ineffectiveness of metal chelating agents observed in the present study as well as in other studies conducted in the recent past [276, 283]. Another explanation might be that the iron-mediated formation of lipid peroxides represents only a small proportion of the overall processes triggered by the ongoing consumption of NADPH in the microsomal matrix. Since the present study focused on the loss of NADPH, not on lipid peroxide formation, the contradictory observations concerning the effect of EDTA become understandable.

The naphthoquinone derivative plumbagin has been shown to inhibit NADPH-dependent ROS generation in cells expressing NOX4 [284] and to prevent lipid peroxidation in microsomal assays [271]. In terms of NADPH consumption, addition of plumbagin to the incubation matrix led to an accelerated decline of the NADPH concentration (Fig. 17). It is most probable that plumbagin served as a substrate for P450 and thus provoked the utilisation of NADPH in the catalytic cycle. On the basis of this result, it cannot be ruled out that plumbagin is effective in inhibiting ROS generation and P450 inactivation in the model system studied in this work, but since the presence of a competing substrate would adulterate the result of a microsomal stability assay, plumbagin proved not to be an appropriate incubation additive.

Addition of DPI, on the other hand, nearly abolished enhanced NADPH loss (Fig. 17). Since the diphenyleneiodonium cation acts as a potent uncompetitive inhibitor of flavoenzymes such as NOX, CPR, nitric oxide synthase (NOS), xanthine oxidase, NADH ubiquinone oxidoreductase, NADH dehydrogenase, G6P-DH and also P450 [285–287], these results clearly confirm that the loss of NADPH in microsomal incubations is a consequence of enzyme activity and not of mere chemical degradation. However, due to the lack of specificity of DPI, the relative contribution of the individual enzyme systems to NADPH consumption and ROS formation cannot be clearly differentiated. Moreover, the inhibitory potential of DPI on P450 and CPR precludes the use of this agent in regular microsomal stability assays. Since the main goal of the present study was the optimisation of microsomal incubation conditions rather than the elucidation of the molecular mechanisms underlying

enzyme inactivation, no additional investigations on ROS production and ROS actions were conducted.

The final aspect of the investigations on NADPH stability in microsomal assays was the potential benefit of using a CRS instead of adding NADPH directly to the incubation matrix. The depletion profile displayed in Fig. 19 shows that *in situ* NADPH regeneration allows for a stable NADPH level only during the first 30 min of incubation, followed by a steep concentration decline. It is highly likely that G6P-DH is also adversely affected by ROS generated during incubation, resulting in a deceleration of NADP<sup>+</sup> reduction. The presumed advantage of using a CRS in order to maintain a constant NADPH level during long term microsomal incubations could therefore not be confirmed.

To summarise, neither antioxidant enzymes nor enzyme inhibitors or metal chelators proved to be suitable additives for microsomal stability assays in terms of preventing the fast decrease of enzymatic activity *in vitro*. Although some of these agents might have been successful in preventing formation of ROS or impeding the deleterious actions of ROS on the P450 system, these agents also interfered unfavourably with other components of the microsomal assay. The defence mechanism that viable cells use to protect themselves from the actions of ROS cannot be readily mimicked in the microsomal model system. The addition of one or two antioxidant agents does not reflect the complex interplay of a multitude of enzymes and substances present in the cell, many of which may not even be known at present. Additionally, the different magnitude of compartmentalisation in the microsomal model system and in intact, viable cells may contribute to differences in ROS formation and action as well as to differences in the efficacy of antioxidants. Therefore, the most promising strategy to avoid misleading data seems to be the shortening of the incubation periods used in microsomal stability assays. Short incubation periods that nevertheless ensure sufficient substrate depletion for adequate quantification and kinetic modelling can be realised by adjusting the microsomal protein concentration used in the assay. However, this approach can be limited by high protein binding of the substrate, oxygen diffusion limitation in highly protein-rich matrices, problems in sample preparation or economic considerations. An alternative concept could be the correction of depletion data by previously measured enzyme inactivation rates, as suggested by Foti and Fisher [178].

#### **4.1.2.3 Criteria for the choice of optimal incubation conditions**

Evaluation and optimisation of microsomal assay conditions were aimed at providing an optimal basis for *in vitro-in vivo* comparison of metabolism data. In order to determine a set of optimal incubation conditions, the individual parameters were adjusted according to the

following aspects: (1) physiologically relevant size/level, (2) maximum substrate depletion (i.e. maximum catalytic activity).

For parameters such as pH value, buffer molarity (i.e. ionic strength) and concentration of cofactors, literature data on the physiologically relevant levels are either varying or incomplete. These parameters were optimised with regard to maximum catalytic activity within the ranges reported in literature. Maximum catalytic activity was considered as decisive criterion since it reflects absence (or low extent) of *in vitro* enzyme inhibition.

Several parameters (e.g. incubation temperature, substrate concentration) have not been subjected to evaluation but instead set to a fixed value since the physiological levels of these parameters are known or because of technical and analytical restrictions. The body temperature of the anaesthetised rats used in the *in vivo* experiments of the present study was held at about 37°C, hence this temperature was also chosen for microsomal incubations, regardless of the actual temperature optimum of the particular enzymes. The initial substrate concentration was set to 8 µM since this value represented a reasonable compromise between analytical requirements (e.g. limit of quantification) and the limited solubility of the substrates in aqueous media.

The pronounced inhibition and degradation of microsomal enzymes caused by organic solvents or NADPH-dependent ROS formation in the incubation matrix were considered as *in vitro* artefacts without equivalent in the intact organism. Thus, incubation conditions were adjusted so as to minimise these negative effects. Although ROS formation is a natural phenomenon occurring in the living cell, the consequences on enzyme integrity are not the same as in a simplified *in vitro* system. Living cells contain large concentrations of antioxidants that protect cellular components from the damaging effects of ROS. Additionally, vital cells can replace corrupted enzymes by newly synthesised ones and hence maintain a constant level of metabolic activity over a prolonged period of time. Since both tactics cannot be adequately simulated *in vitro*, the effects of ROS formation on microsomal enzymes were minimised by reduction of the incubation periods rather than addition of radical scavengers.

The choice of a suitable organic solvent was hampered by the difficult solubility characteristics of the three xanthine derivatives. Solvents which proved to be capable of dissolving sufficient amounts of substrate (DMF & DMSO) also exhibited an inhibitory effect on the respective enzymes. Since enzyme inhibition was less pronounced with DMSO than with DMF, DMSO was chosen as standard solvent for all further assays. The optimal concentration of DMSO in the final incubation mixture was determined by balancing

negative (enzyme inhibitory) and positive (substrate solubility improving) effects of the organic solvent on the system.

The concentration of microsomal protein (i.e. the enzyme concentration) for *in vitro*  $t_{1/2}$  assays (see following section) was adjusted as to ensure depletion of 30 – 70% substrate during an incubation period of maximal 30 min. These conditions allow for a comprehensive evaluation of the kinetic characteristics of the substrate-enzyme system (initial lag phase, linear phase, plateau phase) as well as for non-linear curve fitting. In order to ensure good comparability of the data, microsomal protein concentrations used in the *in vitro*  $t_{1/2}$  assays were the same for all three substrates.

#### 4.1.3 *In vitro* metabolic stability of CBX, MCBX and CFPX

Following evaluation of incubation conditions, a set of optimal conditions was determined for examination of substrate depletion kinetics in RLM. Incubations were conducted in 100 mM HEPES buffer at pH 7.4 and 37°C using a microsomal protein concentration of 0.5 mg/ml and a substrate concentration of 8  $\mu$ M. NADPH (1.3 mM) was added directly to the incubation matrix and DMSO concentration was kept below 1%. The incubation time was limited to 30 min to minimise the effect of enzyme degradation.

The depletion-time profiles of CBX, MCBX and CFPX in RLM are shown in Fig. 20. With all three substrates, an initial lag phase could be observed, resulting in a sigmoidal shape of the depletion profiles. Consequently, a logistic regression model of the following general form (a variant of the Hill equation) was applied for data analysis:

$$y = \frac{A_1 - A_2}{1 + \left(\frac{x}{x_0}\right)^p} + A_2 \quad \text{Eq. 32}$$

with  $A_1$ , initial value;  $A_2$ , final value;  $x_0$ , centre and  $p$ , power.

$A_1$  and  $A_2$  were fixed at 100 and 0 (percentage substrate remaining). This gave the final fitting equation:

$$y = \frac{100}{1 + \left(\frac{x}{x_0}\right)^p} \quad \text{Eq. 33}$$

In this equation, the centre value  $x_0$  represents the time point at which the substrate concentration has dropped down to 50% of the initial value. Thus,  $x_0$  is equivalent to the half-life  $t_{1/2}$ .

The fitted curves are displayed in Fig. 20. In order to evaluate parameter stability, additional fits were carried out with reduced data sets in which the last sampling points were omitted. Adjusted  $R^2$  values, reduced  $\chi^2$  values and derived half-lives are listed in Table 7.

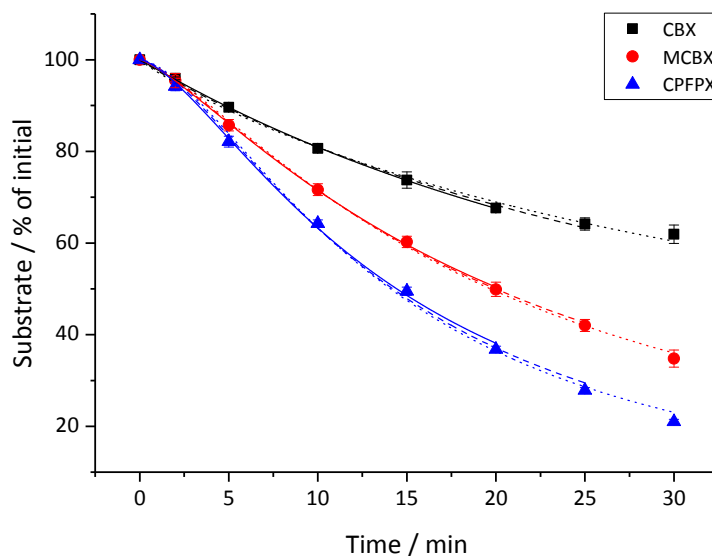


Fig. 20. Kinetics of CBX, MCBX and CPFPPX depletion in RLM. Data were fitted to a logistic model. Dotted curve: all data points were included into the fit. Dashed curve: the last data point ( $t = 30$  min) was excluded from the fit. Solid curve: the last two data points ( $t = 25$  min,  $30$  min) were excluded from the fit. Data points represent the mean  $\pm$  SD of three independent experiments.

*In vitro* half-lives of MCBX and CPFPPX were insensitive to restrictions of the fitted data range. Relative standard deviations of  $t_{1/2}$  were  $\leq 1.4\%$ . CBX was more affected by changes in data set size; the relative standard deviation of  $t_{1/2}$  was  $7.3\%$ . Goodness-of-fit criteria and visual inspection of the fitting curves and residual plots were decisive for the exclusion of the last data point ( $t = 30$  min) for all substrates. The *in vitro* half-lives derived from this shortened depletion curves were used to calculate *in vitro*  $t_{1/2}$  ratios. The *in vitro*  $t_{1/2}$  ratio ( $\pm$  SE) of CBX to CPFPPX was  $3.1 \pm 0.11$ , that of MCBX to CPFPPX  $1.4 \pm 0.029$  and that of CBX to MCBX  $2.2 \pm 0.033$ . These ratios were used for *in vitro-in vivo* comparison (see section 4.2.3).

Table 7. Results of non-linear regression analysis of the data visualised in Fig. 20. The data sets selected for calculation of *in vitro*  $t_{1/2}$  ratios are marked in bold.

Substrate	Number of fitted data points	Adjusted R <sup>2</sup>	Reduced $\chi^2$	$t_{1/2}$ (SE)
				<i>min</i>
CBX	8	0.99535	1.00334	47.2 (2.2)
MCBX	8	0.99895	0.64237	19.7 (0.22)
CPFPX	8	0.99724	2.55596	14.1 (0.28)
<b>CBX</b>	<b>7</b>	<b>0.99832</b>	<b>0.32810</b>	<b>43.6 (1.4)</b>
<b>MCBX</b>	<b>7</b>	<b>0.99944</b>	<b>0.28287</b>	<b>20.0 (0.18)</b>
<b>CPFPX</b>	<b>7</b>	<b>0.99770</b>	<b>1.83781</b>	<b>14.2 (0.26)</b>
CBX	6	0.99978	0.03541	40.9 (0.56)
MCBX	6	0.99951	0.19568	20.2 (0.22)
CPFPX	6	0.99820	1.14559	14.4 (0.25)

R<sup>2</sup>, coefficient of determination;  $t_{1/2}$ , *in vitro* half-life; SE, standard error of the parameter

Common approaches to describe and compare the kinetics of enzymatic reactions are to derive initial velocities from the initial linear phases of the reaction progress curves or to fit the experimental data to an exponential model in order to derive the metabolic half-life. The latter procedure is equally suitable for *in vitro* metabolism data and *in vivo* pharmacokinetic data. In the present study, an alternative approach was chosen to account for the unusual kinetic characteristics of CBX, MCBX and CPFPX metabolism in RLM. As a consequence of an initial lag phase, the depletion profiles of these substrates were markedly sigmoidal in shape. This effect occurred independently of incubation conditions, substrate and enzyme concentrations or NADPH supply. Similar observations were made during *in vitro* evaluation of other xanthine derivatives synthesised at INM-5 (unpublished results). A critical assessment of the physiological relevance of this phenomenon is crucial for deciding which fitting model is the most appropriate for the data. The observed lag phase could possibly be attributed to a delayed reconstitution of the P450/CPR/NADPH/substrate system after mixing all components together. Since component mixing is an artificial process that does not occur in the living cell in a comparable manner, lag phases caused by this effect would clearly be *in vitro* artefacts which do not reflect intrinsic properties of the enzyme-substrate system under examination. Consequently, inclusion of the lag phase into kinetic modelling would not be appropriate. On the other hand, the initial lag phase could also be due to the interaction of multiple catalytic pathways with different kinetics. In this case, similar kinetic behaviour can be anticipated *in vivo*, hence inclusion of the lag phase into the model fit appears reasonable. Two observations indicate that the latter assumption is more likely to

be valid. First, the sigmoidal shape of the depletion curves could be observed independently of the specific conditions and procedures used in the assay (initiating and mixing procedures, NADPH supply, enzyme-substrate concentration ratios, preincubation time). If reconstitution processes would be causal for the shape of the depletion curve, variations in assay conditions and procedures would be likely to affect this shape. Second, *in vitro* and *in vivo* metabolite profiles of the prototypical xanthine derivative CPF PX revealed numerous catalytic pathways including metabolite species resulting from multiple attacks of P450 1A2 (and potentially other P450 isoforms) on the parent structure [288–290]. It is thus quite probable that the initial lag phase results from the unequal kinetic characteristics of the various catalytic pathways and hence is a consequence of the intrinsic properties of the enzyme-substrate system rather than an *in vitro* artefact. Since analogous processes can be postulated *in vivo* with reasonable certainty, the initial lag phase was included in the model fit. As a consequence of this decision, derivation of initial velocities was considered inappropriate since the initial lag phase did not represent all kinetic aspects of substrate metabolism. Fitting the data to the logistic function (Eq. 33) provided better results in terms of goodness-of-fit criteria than a biexponential fit. Moreover, the combination of two half-lives derived from the biexponential fit complicates the comparison between different substrates as well as the comparison between *in vitro* and *in vivo* data. In contrast, application of the logistic fitting equation results in only one half-life that characterises the progress of the whole depletion curve and thus facilitates quick and simple comparison and ranking of metabolic stability data.

#### 4.1.4 Species differences in microsomal metabolism

Although this work focused on the metabolism of CBX, MCBX and CPF PX in the rat model, additional *in vitro* studies were conducted using liver microsomes of several other species, including humans. The objectives of these additional studies were, first, to elucidate the causal mechanisms leading to the qualitative differences between *in vitro* and *in vivo* metabolite profiles as observed with rodents, but not with humans [288] and second, to assess the suitability of common preclinical animal species for evaluation of xanthine-derived A<sub>1</sub>AR tracers.

In the first part of this section, metabolic activity towards the test compounds is compared among species (quantitative metabolic differences) and in the second part, variations in metabolite profiles are discussed (qualitative metabolic differences). Since human microsomal metabolism deviated substantially from that of non-human animals, additional

quantitative and qualitative studies were conducted using human liver microsomes. The results of these investigations are presented in the last part of the section.

#### 4.1.4.1 Quantitative differences

Interspecies differences in the microsomal metabolism of CBX, MCBX and CPFPPX were studied using human, rat, mouse, dog, mini pig and rhesus monkey liver microsomes. The results of the quantitative depletion studies are shown in Fig. 21.

Metabolic activities (as measured by substrate depletion) varied widely across species. Highest metabolic activity was measured in rhesus microsomes. Percentage substrate depletion obtained with 0.04 mg/ml rhesus microsomes was in the same range as with 0.4 mg/ml rodent microsomes. On the other hand, substrate depletion in human microsomes was extremely low. Using a standard assay concentration of 0.4 mg/ml microsomal protein, percentage substrate depletion of CBX, MCBX and CPFPPX was less than 10% during 30 min of incubation. In order to increase the statistical power of the experiment, incubations were repeated using 2.0 mg/ml human microsomal protein. The metabolic activities of mini pig and dog microsomes were comparable to each other. Percentage substrate depletion measured in microsomes of these relatively large species was about 50% lower than in rodent microsomes, but significantly higher than in human microsomes (with the exception of CBX depletion in mini pig and human microsomes, which were of comparable magnitude).

Depletion ratios and rank order of metabolic stability of the test compounds were less variable across species than total metabolic activity. Again, metabolism in human microsomes was a noticeable exception. Whereas the microsomal stability ranking of CBX, MCBX and CPFPPX was comparable among non-human animal species (CBX being the most stable and CPFPPX the least stable compound), a different ranking was observed with human liver microsomes. When incubated with 2.0 mg/ml human microsomal protein, MCBX was the most stable and CBX the least stable compound. Incubations conducted at 0.4 mg/ml human microsomal protein were not used for evaluation of the ranking order since the statistical power was insufficient due to the very low depletion rates.

To further investigate the deviating kinetics of human microsomal metabolism of the test compounds, additional time-course studies were conducted which allowed for determination of *in vitro*  $t_{1/2}$ . The results of these studies are presented in section 4.1.4.4.

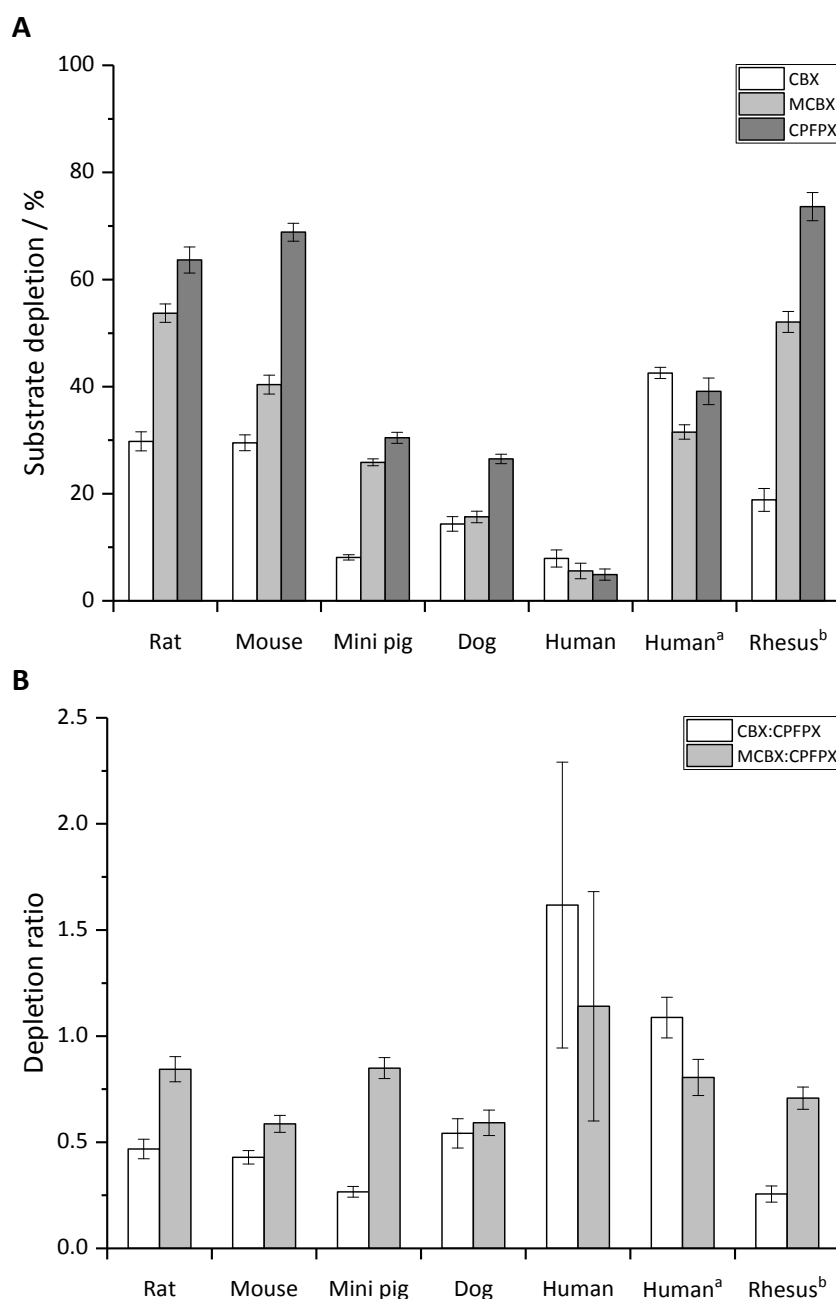


Fig. 21. Quantitative species differences in microsomal metabolism of CBX, MCBX and CFPFX. (A) Percentage substrate depletion in liver microsomes of various species during an incubation period of 30 min. Concentration of microsomal protein was 0.4 mg/ml, except for Human<sup>a</sup> (2.0 mg/ml) and Rhesus<sup>b</sup> (0.04 mg/ml). Data represent the mean  $\pm$  SD of four independent experiments. (B) Depletion ratios of CBX and MCBX to CFPFX, calculated from the data visualised in A. Bars represent the quotient of percentage degradation of CBX and CFPFX and MCBX and CFPFX, respectively.

Species-dependent differences in microsomal metabolism can be attributed to the following main factors: (1) different levels of total microsomal P450, (2) different levels of individual P450 isoforms, (3) variations in the functional characteristics of individual P450 isoforms (catalytic activity, substrate specificity, preferred reaction pathways).

Quantitative differences in microsomal metabolism resulting from different levels of total or individual P450 enzymes can often be dealt with by application of scaling factors or by adjustment of the protein concentration used in the microsomal assay. In contrast, interspecies differences in the functional characteristics of an enzyme may result in fundamental quantitative and qualitative metabolic differences which may render a particular animal species unsuitable as predictive model for e.g. the human metabolism.

Since manufacturer's data on total P450 content were only available for the human microsomes used in the present study, but not for the non-human animal species, literature data on total microsomal P450 content reported for these species (see Table 8) were used as reference values for discussion.

Table 8. Total microsomal P450 content reported for various species

Species	Total microsomal P450 content <i>nmol/mg microsomal protein</i>				
	[291]	[292]	[293]	[294]	[295]
Human	0.307 ± 0.160	0.231 ± 0.013	0.31 ± 0.09	n.d.	0.29 ± 0.06
Rat	0.673 ± 0.050	0.444 ± 0.016	0.58 ± 0.02	n.d.	n.d.
Mouse	n.d.	0.719 ± 0.041	0.48 ± 0.04	n.d.	n.d.
Mini pig	n.d.	n.d.	n.d.	0.798 ± 0.145	n.d.
Dog	0.385 ± 0.036	0.685 ± 0.031	n.d.	n.d.	n.d.
Monkey	1.030 ± 0.106 <sup>a</sup>	1.195 ± 0.089 <sup>b</sup>	0.74 ± 0.02 <sup>a</sup>	n.d.	0.95 ± 0.08 <sup>b</sup>

n.d., not determined; <sup>a</sup> cynomolgus monkey, <sup>b</sup> rhesus monkey

In the following discussion of interspecies differences in expression levels and functional characteristics of individual P450 isoforms, the focus is on P450 1A2, which is considered the main enzyme involved in phase I metabolism of CPF PX and its analogues [289]. At present, information on hepatic P450 1A2 levels is not available for all species used in this study. In humans, P450 1A2 accounts for about 13% of the total P450 content [296], in rats for about 2% [297] and in dogs for about 4% [298]. Basal hepatic levels of P450 1A2 in macaques are generally reported to be low or even undetectable [299–303], however, Shimada et al. measured comparable levels of P450 1A2 in liver microsomes of cynomolgus macaques and humans [291].

Obviously, interspecies differences in total and isoform specific P450 content cannot fully account for the large variations in metabolic activity towards the tested xanthine derivatives. Microsomal P450 levels reported in Table 8 are about 2-3 times higher in rodents and about 3 times higher in rhesus and cynomolgus monkeys than in humans. By

contrast, depletion of MCBX and CPFPX measured in rodent microsomes was 7-14 times higher than in human microsomes. In rhesus monkey microsomes, depletion of CBX, MCBX and CPFPX was about 24, 93 and 150 times higher than in human microsomes. This is particularly noteworthy since, as mentioned above, the constitutive hepatic expression of P450 1A2 in rhesus monkeys is questionable. It is probable that P450 isoforms other than 1A2 are responsible for degradation of the test substrates in macaques, rendering this animal model less useful for prediction of the pharmacokinetic characteristics of xanthine-derived A<sub>1</sub>AR ligands in humans.

Numerous studies on interspecies variations in catalytic activity of P450 1A2 toward various marker substrates have been published so far, revealing large differences not only in enzymatic activity of the homologues 1A2 enzymes, but also in substrate specificity [291, 304–310]. Interestingly, the rate of caffeine metabolism, which was studied by Berthou and colleagues, was two times higher in human liver microsomes than in rat liver microsomes and 1.4 times higher than in monkey liver microsomes [304]. Despite the high degree of structural similarity between caffeine and the xanthine-derived compounds evaluated in the present study, species-specific metabolism of these substances seems to differ substantially. However, it is important to note that the apparent differences in depletion kinetics may be partially attributed to the different qualities of the microsomal material used in both studies. In the present study, pooled microsomes prepared from liver tissue of 50 donors were used in order to minimise the effect of interindividual variations in enzyme concentration and activity. The microsomes used by Berthou et al. were prepared from tissue of a single donor and showed exceptionally high values for P450 content and caffeine biotransformation [311]. This experimental aspect may have led to a deviating assessment of the metabolic activity of human microsomes relative to other species.

To summarise, interspecies differences in metabolic activities towards CBX, MCBX and CPFPX are pronounced and not readily surmountable by simple scaling approaches. The metabolic stability ranking observed with human microsomes did not match any of the tested animal species. Based on these results, the relevance of animal microsomes as a model for human pharmacokinetics of the test compounds must be doubted. However, it should be considered that metabolism data generated using human liver tissue preparations might be biased as a result of the specific conditions encountered during sampling and preparation of human tissue. First, human liver tissue obtained from diagnostic biopsies might be pathologically changed which could lead to altered functional characteristics. Second, *post-mortem* times preceding actual tissue preparation are generally longer for human than for animal autopsy tissue (due to regulatory requirements, for example). It has

been shown by various authors that enzyme activity decreases rapidly in *post-mortem* liver tissue as a result of autolysis [312–316], especially if the liver tissue is left *in situ* at room temperature. The consequences of *post-mortem* enzyme stability on the results obtained by microsomal stability assays have not yet been definitively clarified.

#### 4.1.4.2 Qualitative differences

Metabolite profiles resulting from biotransformation of CBX, MCBX and CPF PX by human, rat, mouse, dog, mini pig and rhesus monkey liver microsomes are shown in Fig. 22 - Fig. 24. Peaks were assigned as metabolites only if they were clearly distinguishable from matrix components (by comparison with blank samples) and if the peak areas were of considerable size in the chromatogram of at least one species. Minor components eluting in close vicinity to the injection peak were disregarded. The assigned metabolite peaks are listed in Table 9 together with their retention times and retention factors. Since mass-spectrometric data were not hitherto available to clarify peak identities, peaks were matched solely by comparison of the retention times. The main goal was a straightforward assessment of qualitative differences in number and relative abundance of metabolites in liver microsomes of different species in order to identify the most promising preclinical species for evaluation of xanthine-derived A<sub>1</sub>AR tracers.

Microsomal metabolism of CBX produced at least 8 metabolites of which A1 and A5 were dominant in all species. Regarding human *in vitro* biotransformation of CBX, metabolite profiles generated by rhesus monkey and mini pig microsomes exhibited the highest degree of similarity. Biotransformation of MCBX produced at least 10 metabolites. Metabolite B3 was dominant in the profiles of all species, whereas peak area ratios of metabolites B5-B7 were highly variable. Human microsomal metabolism of MCBX was most closely approximated by rodent microsomes. Biotransformation of CPF PX by human and rodent microsomes has been extensively studied by Bier et al. [288]. As a supplement, microsomes of three common non-rodent preclinical species were used in the present study in order to select the most predictive animal species for human metabolism of CPF PX and its analogues. Species-specific microsomal biotransformation of CPF PX resulted in at least 12 metabolites. Of particular interest was the *in vitro* formation of the enone metabolite **7**, which was hitherto considered to occur only in human microsomes. Since this compound was available as reference standard, the corresponding peak in the human chromatogram could be identified by its retention time (C9, 9.8 min). As can be seen in Fig. 24, the dog metabolite profile also shows a peak eluting at 9.8 min, suggesting formation of **7** in dog microsomes. An initial mass spectrometric analysis indicated the presence of the expected [M+H]<sup>+</sup> quasi-

molecular ion, but since the signal was relatively low, further analyses are to be conducted in order to verify the chemical identity of the metabolite.

In summary, no single animal species could accurately predict qualitative human microsomal metabolism of all three substrates. Regarding CBX and MCBX, comparison of the metabolite profiles suggests that microsomal metabolism of these substrates generates similar metabolites in all species, but in varying relative amounts. In the case of CFPFX, formation of the enone metabolite **7**, a dominant species in the human metabolite profile, could only be observed in dog microsomes (with reservations regarding the final spectroscopic identification). Because it would be impracticable to evaluate the most predictive animal species for every single test substrate, a reasonable approach could be a combined analysis of *in vitro* metabolic data obtained from at least two different animal species. This concept may help to recognise species differences in metabolic pathways in an early stage of development and to assess the impacts of these differences on the desired characteristics of the new chemical entity. Regarding the evaluation of CFPFX analogues, the beagle dog appears to be a promising species for *in vitro* metabolic stability studies (and possibly also for *in vivo* pharmacokinetic testing), complementing standard rodent studies.

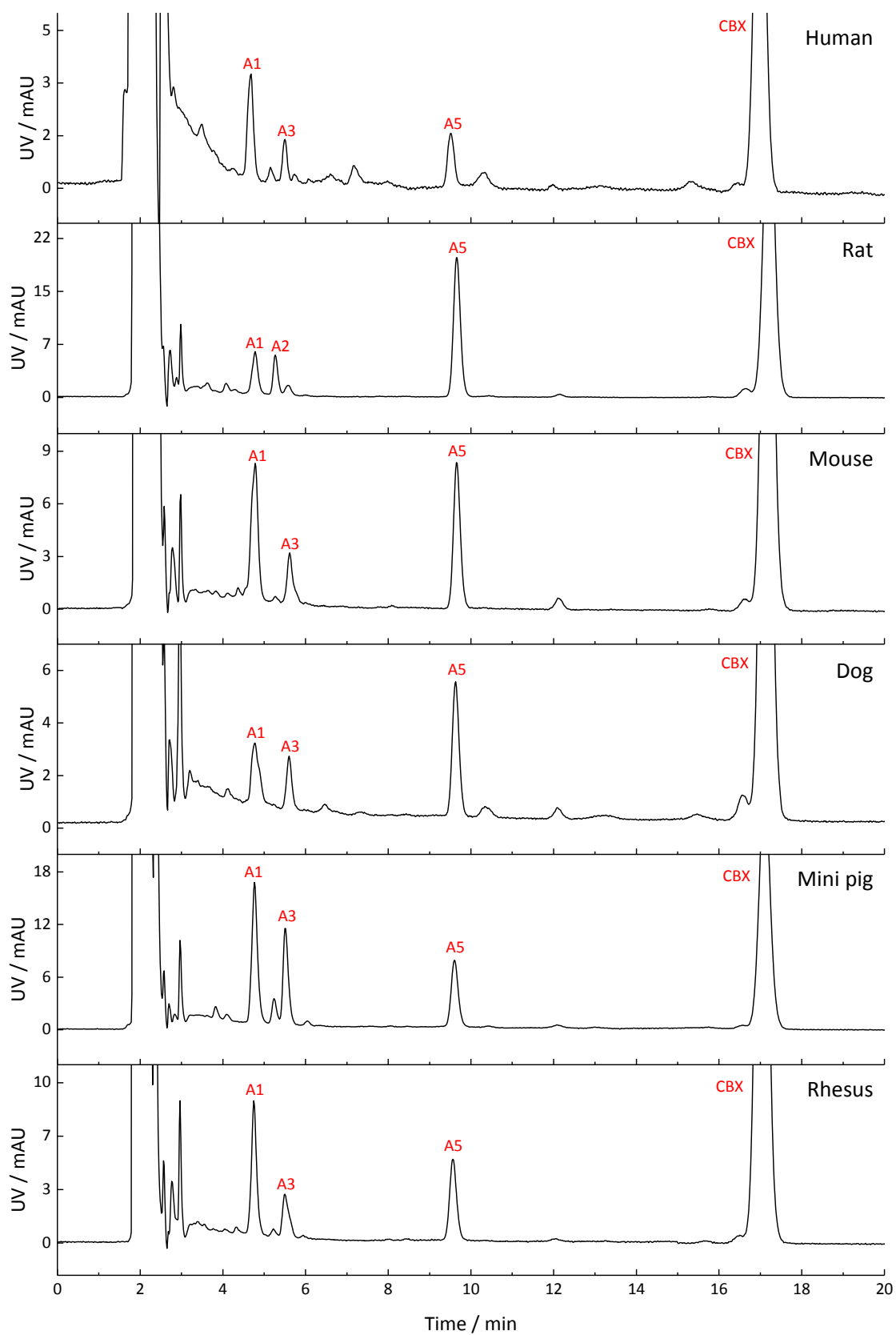


Fig. 22. Biotransformation of CBX in liver microsomes of various species. HPLC-UV chromatograms were generated at 275 nm. For reasons of clarity, only metabolite peaks which account for at least 10% of the total metabolite peak area were labelled in the chromatograms. A full list of metabolites is given in Table 9.

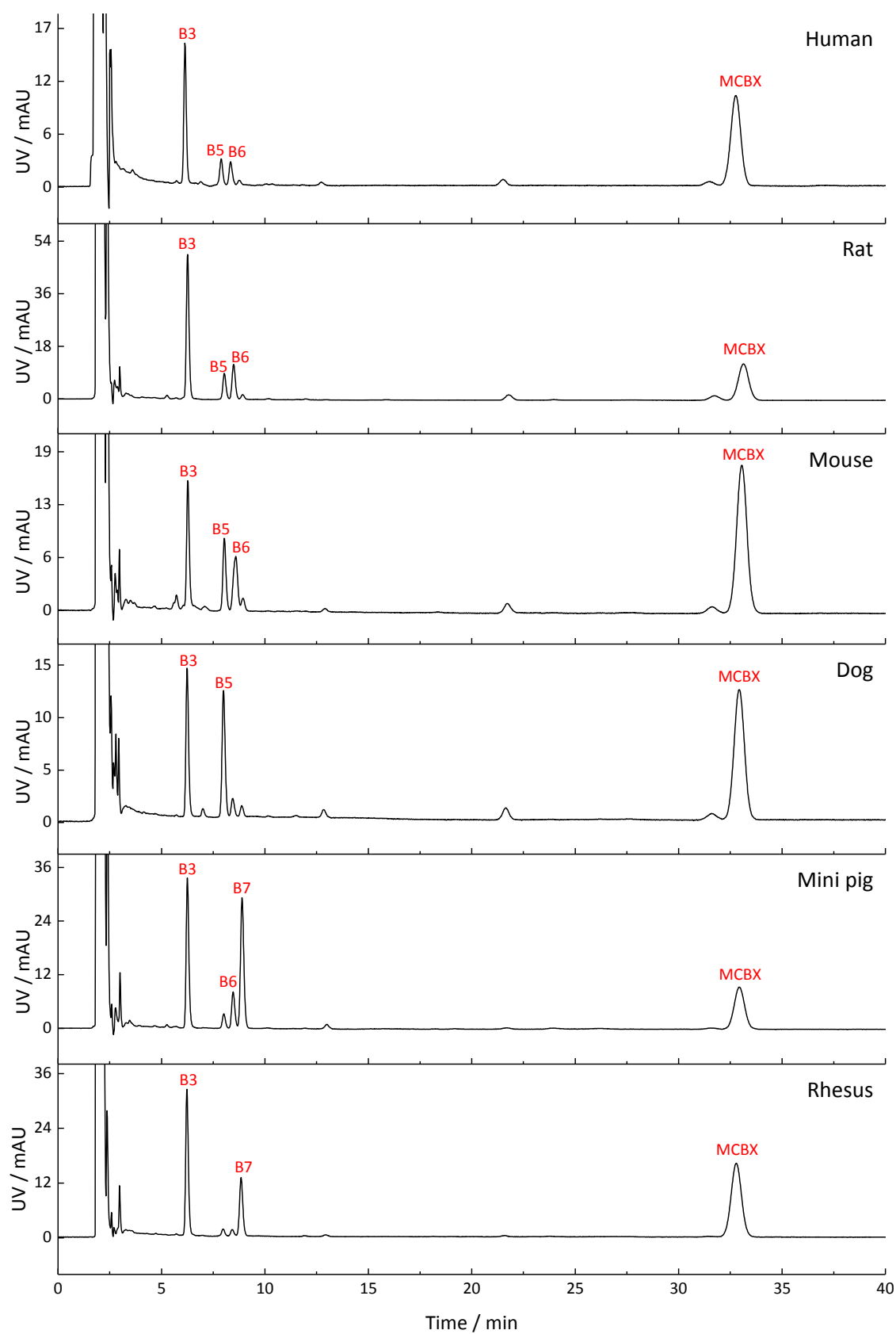


Fig. 23. Biotransformation of MCBX in liver microsomes of various species. HPLC-UV chromatograms were generated at 275 nm. For reasons of clarity, only metabolite peaks which account for at least 10% of the total metabolite peak area were labelled in the chromatograms. A full list of metabolites is given in Table 9.

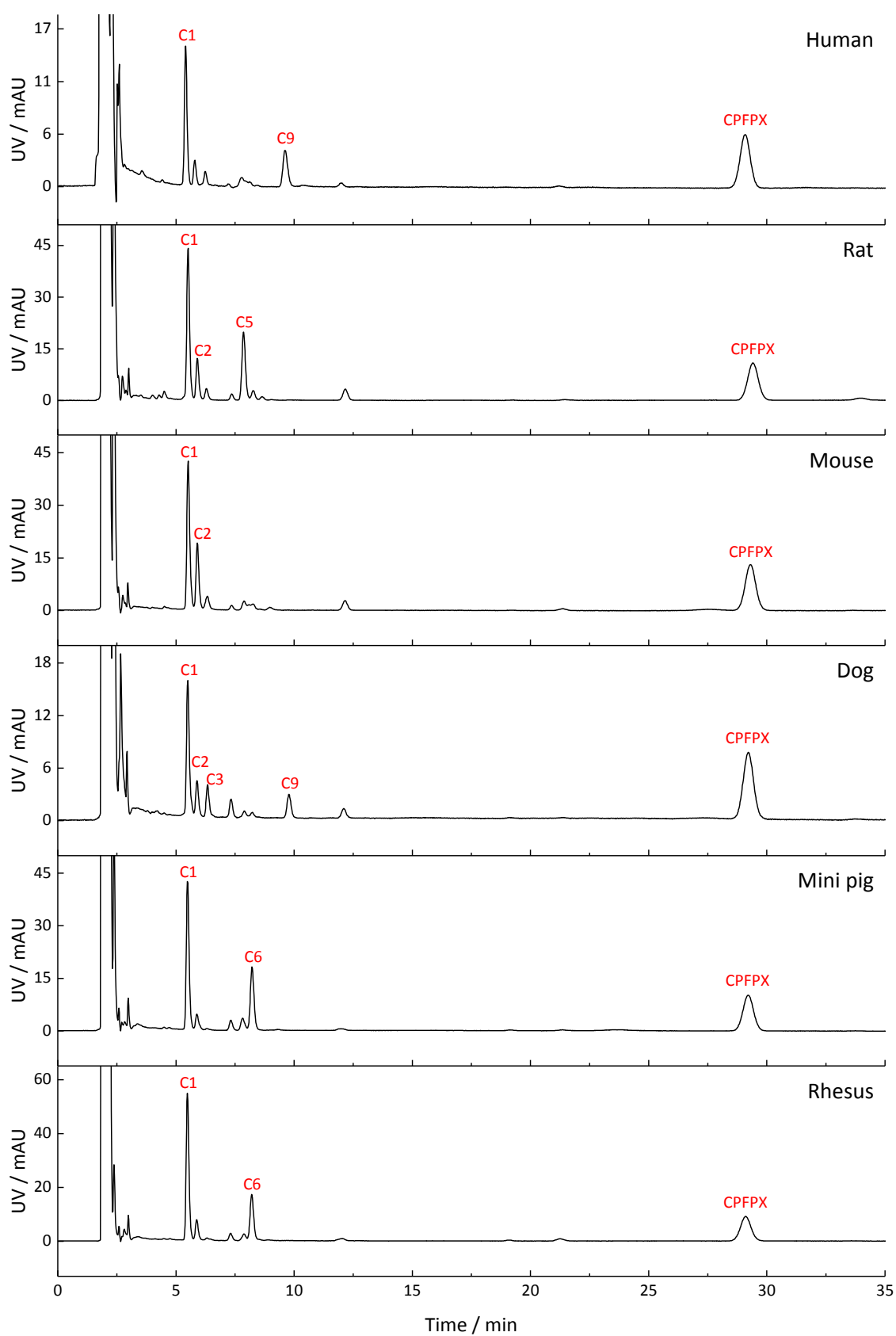


Fig. 24. Biotransformation of CPFPPX in liver microsomes of various species. HPLC-UV chromatograms were generated at 275 nm. For reasons of clarity, only metabolite peaks which account for at least 10% of the total metabolite peak area were labelled in the chromatograms. A full list of metabolites is given in Table 9.

Table 9. Metabolites of CBX, MCBX and CFPFX generated in liver microsomes of various species

Substrate	Peak fraction	Retention time	Retention factor	Species
		<i>min</i>		
CBX	A1	4.8	0.9	h, r, m, d, mp, rh
	A2	5.3	1.1	(h), r, (m), mp, rh
	A3	5.6	1.2	h, r, m, d, mp, rh
	A4	6.0	1.4	(r), (m), mp, (rh)
	A5	9.6	2.9	h, r, m, d, mp, rh
	A6	10.4	3.2	(h), (r), d, (mp)
	A7	12.1	3.9	(h), r, m, d, (mp), (rh)
	A8	16.6	5.7	(h), r, m, d, (mp), rh
	CBX	17.2	5.9	h, r, m, d, mp, rh
MCBX	B1	5.3	1.1	r, mp
	B2	5.7	1.3	(r), m, (d), (mp), (rh)
	B3	6.3	1.5	h, r, m, d, mp, rh
	B4	7.1	1.8	(h), m, d, (rh)
	B5	8.0	2.2	h, r, m, d, mp, rh
	B6	8.6	2.4	h, r, m, d, mp, rh
	B7	8.9	2.6	h, r, m, d, mp, rh
	B8	12.9	4.2	(h), m, d, mp, (rh)
	B9	21.7	7.7	h, r, m, d, (mp), (rh)
	B10	31.6	11.7	h, r, m, d, (mp), (rh)
MCBX	33.1	12.3	h, r, m, d, mp, rh	
CFPFX	C1	5.5	1.2	h, r, m, d, mp, rh
	C2	5.9	1.4	h, r, m, d, mp, rh
	C3	6.3	1.5	h, r, m, d, (mp), (rh)
	C4	7.4	2.0	(h), r, m, d, mp, rh
	C5	7.9	2.2	h, r, m, d, mp, rh
	C6	8.3	2.3	h, r, m, d, mp, rh
	C7	8.7	2.5	(h), r, (m), (d), (rh)
	C8	9.0	2.6	(r), m, (d), (rh)
	C9	9.8	2.9	h, d
	C10	12.2	3.9	h, r, m, d, mp, rh
	C11	21.4	7.6	(h), r, m, (mp), rh
	C12	34.0	12.6	r, (m), (d)
CFPFX	29.4	10.8	h, r, m, d, mp, rh	

h, human; r, rat; m, mouse; d, dog; mp, mini pig; rh, rhesus  
brackets indicate minor peaks

#### 4.1.4.3 Enone metabolite formation in liver microsomes

Formation of the enone metabolite **7** represents a major metabolic pathway in human *in vivo* and *in vitro* CFPX metabolism [288–290]. Thus, blockage of this pathway is considered a promising approach to enhance metabolic stability of CFPX analogues. Remarkably, in rodents, **7** is generated exclusively in the living animal, but not in liver microsomes [288]. To elucidate the potential causes of this phenomenon and to assess its relevance for both *in vitro-in vivo* comparison and comparison among species, microsomal metabolism studies were conducted in both rat and human liver microsomes using four potential precursor species (**8-11**) which were all found to be present in the human microsomal metabolite profile. Of these primary metabolites, only **9** served as precursor for the formation of **7** in human liver microsomes. This biotransformation passed via an intermediate which could be separated chromatographically (Fig. 25). Mass spectrometric analyses supported the hypothesis that this intermediate may contain a cyclopentenol moiety instead of the cyclopentenone moiety of **7**, thus being most probable 3-(3-fluoropropyl)-8-(3-hydroxycyclopent-1-en-1-yl)-1-propylxanthine (**12**).

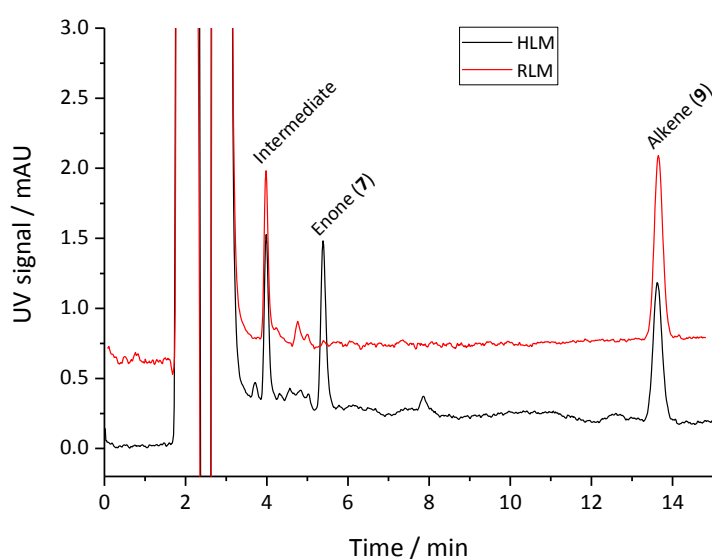


Fig. 25. Biotransformation of **9** in HLM (black chromatogram) and RLM (red chromatogram). Enone (**7**) formation can only be observed in HLM. Chromatograms were smoothed by applying a moving average algorithm (filter width 2). Detection wavelength was 275 nm.

The time course of formation of **7** and **12** in human liver microsomes is shown in Fig. 26A. It can be seen that (1) the formation of **7** still proceeded after **9** was completely depleted and that (2) the concentration of **12** started declining after a certain incubation period. Both observations confirm a pathway that proceeds from **9** via **12** to **7** (Fig. 27). In comparison,

the time course of metabolism of **9** in rat liver microsomes is given in Fig. 26B. Apparently, formation of **12** proceeded as previously observed in human liver microsomes, but the final oxidation step which converts the hydroxy compound into a ketone did not take place. No enone peak could be detected in the respective chromatograms (Fig. 25). Consequently, the concentration of **12** increased until **9** was completely depleted, but then stayed at the same level throughout the remaining incubation period.

It seems plausible that the ability of oxidising **12** is a special feature of human (and potentially dog) P450 1A2. Previous studies on CFPX biotransformation using recombinant human 1A2 isoenzyme preparations [289] clearly indicated that all reaction steps leading from CFPX to **7** can be catalysed by human P450 1A2 alone, i.e. no further enzymes are required for this complex multi-oxidation reaction pathway. In contrast, rodent microsomal P450 1A2 enzymes are seemingly unable to catalyse the last oxidation step leading to the ketone (or at least not to a significant extent). This is readily explainable by species differences in the active site structures of the particular enzymes, resulting in different functional characteristics (substrate specificity, reaction pathways). The formation of **7** in the living rodent, which might seem paradoxical at first sight, could be a consequence of the catalytic action of enzymes other than hepatic P450 1A2. Since intermediate metabolites are subjected to systemic circulation in the living animal, they will be exposed to a multitude of hepatic and extrahepatic enzyme systems. It is conceivable that extrahepatic P450 isoenzymes or alcohol oxidoreductases complete the reaction pathway by oxidising **12**. The exact mechanism of *in vivo* formation of **7** in rodents remains to be elucidated in future studies.

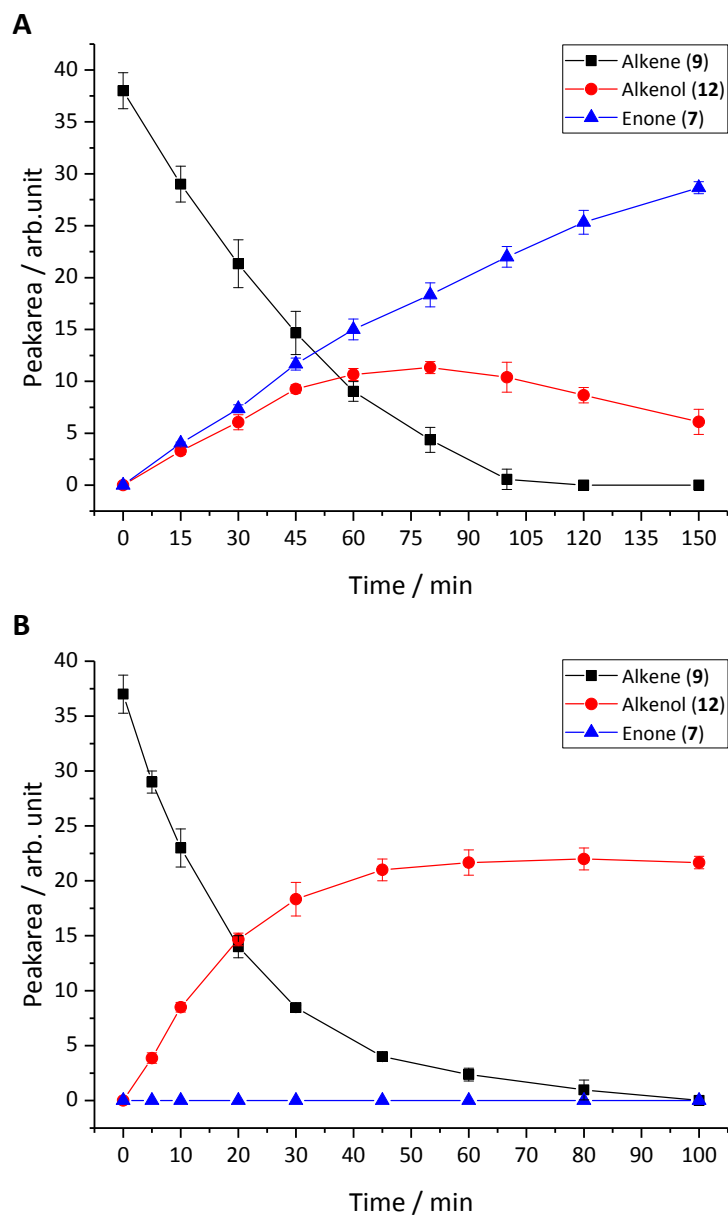


Fig. 26. Kinetics of biotransformation of **9** in HLM (A) and RLM (B). In both HLM and RLM, degradation of **9** (black curve) results in the formation of an intermediate alkenol compound (red curve). In HLM, this intermediate is subsequently metabolised to **7** (blue curve). Formation of **7** cannot be observed in RLM. Data points represent the mean  $\pm$  SD of three independent experiments.

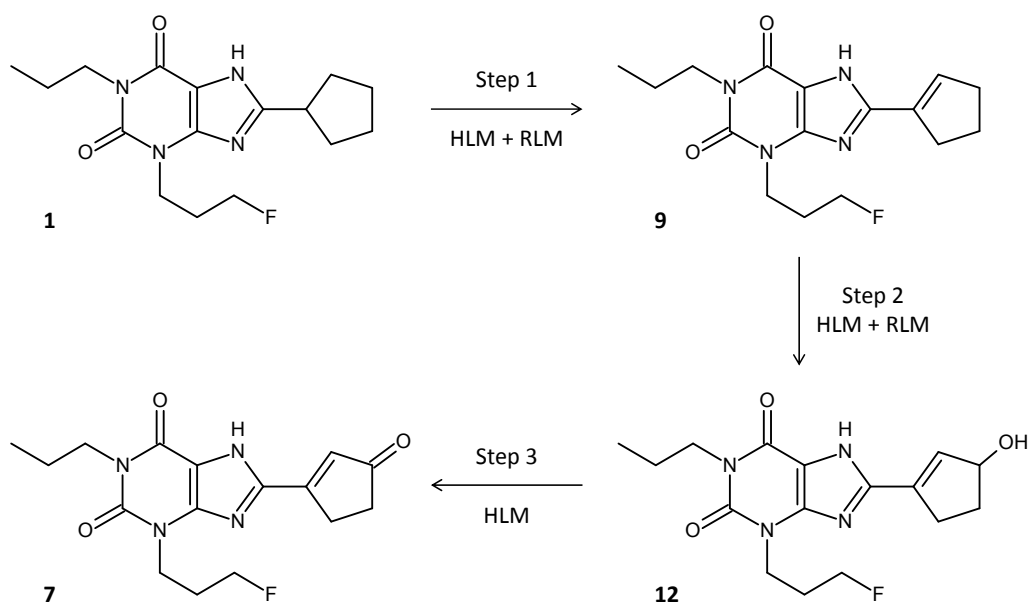


Fig. 27. Proposed mechanism of enone (7) formation in HLM. Three distinct biotransformation steps are necessary to convert CPFPX (1) into the enone metabolite (7). Steps 1 and 2 occur in both RLM and HLM, whereas step 3, the final oxidation of the hydroxy intermediate (12) to the carbonyl compound, can only be observed in HLM.

#### 4.1.4.4 Time-course of CBX, MCBX and CPFPX metabolism in HLM

As apparent from the preceding sections, human microsomal metabolism of CPFPX and its analogues shows noticeable qualitative and quantitative deviations from any other species. Since tracer development in most cases pursues the goal of human application, kinetics of human *in vitro* metabolism of the test substances is of special interest. In addition to the fixed-time experiments presented in section 4.1.4.1, microsomal time-course studies were performed in order to assess the kinetic characteristics of substrate metabolism in human liver microsomes. These data were fitted to the logistic model described in section 4.1.3. The resulting depletion curves are shown in Fig. 28. *In vitro*  $t_{1/2}$  of CBX, CPFPX and MCBX were 25, 34 and 43 min, respectively. Interestingly, the depletion curves of MCBX and CPFPX intersected at about 13 min, resulting in a change of the stability rank order. This might be a consequence of an overlap of different catalytic pathways realised at one and the same substrate species. However, the physiological relevance of this phenomenon is difficult to assess. Enzyme inactivation resulting from prolonged incubation periods or enzyme inhibition caused by accumulation of metabolites in the incubation matrix may affect the course of the depletion curves at later time points. Since, as a consequence of the low depletion rates of the xanthine derivatives in HLM, extended incubation periods are almost inevitable in order to fully assess depletion kinetics, these problems are far from easy to

resolve. Further investigations are required to determine whether the observed behaviour is an intrinsic property of the particular enzyme-substrate system or an *in vitro* artefact.

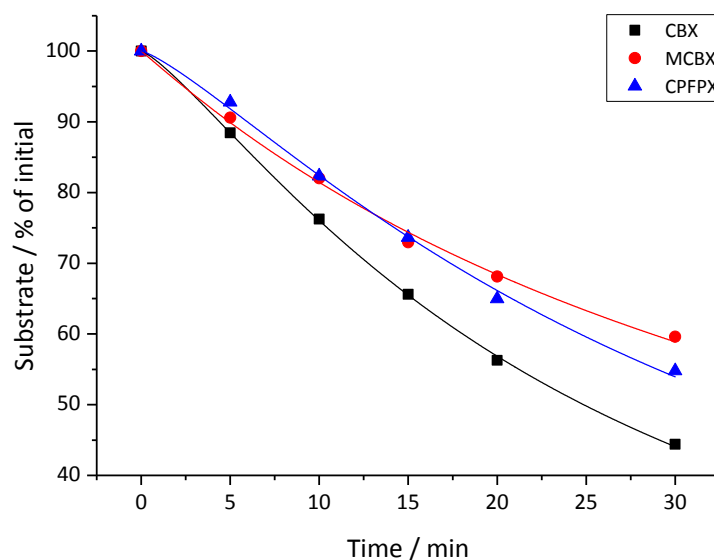


Fig. 28. Kinetics of CBX, MCBX and CPFPX depletion in HLM. Data were fitted to the same logistic model that was applied for depletion kinetics in RLM (see section 4.1.3). Data points represent the mean of two independent experiments.

## 4.2 *In vivo* pharmacokinetics

### 4.2.1 Plasma kinetics

Kinetics of [ $^{18}\text{F}$ ]CBX, [ $^{18}\text{F}$ ]MCBX and [ $^{18}\text{F}$ ]CPFPX in rat plasma following i.v. bolus administration are compared in Fig. 29. Since inter-individual variations in plasma kinetics within the test groups were relatively small, mean data sets were used for pharmacokinetic analysis. Plasma kinetics of the three tracers could not be adequately described by the simple biexponential model frequently applied in pharmacokinetic analysis [317–319]. Examination of the semi-logarithmic SUV versus time plots (not shown) revealed three distinctive kinetic phases associated with the decline of tracer concentration in plasma. Consequently, a triexponential model was chosen for curve fitting. Plasma clearance, volume of distribution and terminal half-life were estimated from the fitted parameters via non-compartmental PK analysis (Table 10). Highest clearance was observed with [ $^{18}\text{F}$ ]CBX, lowest clearance with [ $^{18}\text{F}$ ]MCBX. Clearance ratios ( $\pm$  SE) were as follows: [ $^{18}\text{F}$ ]CBX:[ $^{18}\text{F}$ ]CPFPX= $0.39 \pm 0.019$ , [ $^{18}\text{F}$ ]MCBX:[ $^{18}\text{F}$ ]CPFPX= $1.2 \pm 0.028$ , [ $^{18}\text{F}$ ]CBX:[ $^{18}\text{F}$ ]MCBX= $0.32 \pm 0.016$ . Terminal half-life of [ $^{18}\text{F}$ ]CBX was 1.8 times longer than that of [ $^{18}\text{F}$ ]CPFPX and 1.6 times longer than that of [ $^{18}\text{F}$ ]MCBX. Half-lives of [ $^{18}\text{F}$ ]CPFPX and [ $^{18}\text{F}$ ]MCBX did not

differ in a statistically significant way. Volumes of distribution varied only slightly (190-362 ml), thus comparable distribution of the tracers throughout the body can be presumed.

Table 10. Pharmacokinetic parameters derived from triexponential fits of the plasma activity versus time data visualised in Fig. 29. Values were calculated according to Eq. 8-10 given in section 1.5.3.2. Absolute errors were estimated from SEs of the individual fitting parameters via error propagation.

Tracer	Number of animals	$V_d$ (SE)	CL (SE)	$t_{1/2\gamma}$ (SE)
		<i>ml</i>	<i>ml/min</i>	<i>min</i>
[ <sup>18</sup> F]CBX	8	190 (21) <sup>b</sup>	1.50 (0.068) <sup>bc</sup>	88.1 (8.8) <sup>bc</sup>
[ <sup>18</sup> F]MCBX	9	362 (24) <sup>ac</sup>	4.65 (0.081) <sup>ac</sup>	54.0 (3.4) <sup>a</sup>
[ <sup>18</sup> F]CPFPX	8	263 (23) <sup>b</sup>	3.81 (0.057) <sup>ab</sup>	47.8 (4.1) <sup>a</sup>

$V_d$ , volume of distribution; CL, total clearance,  $t_{1/2\gamma}$ , terminal half-life; SE, standard error; <sup>a</sup> significantly different from [<sup>18</sup>F]CBX; <sup>b</sup> significantly different from [<sup>18</sup>F]MCBX; <sup>c</sup> significantly different from [<sup>18</sup>F]CPFPX ( $p < 0.05$ , one-way ANOVA with *post-hoc* Tukey test)

With all tracers, metabolic degradation started immediately after i.v. injection (Fig. 29B). At 1 min p.i., parent fractions had already declined to 98-99%. At 2 and 3 min p.i., parent fractions were in the range of 91-94% and 81-88%, respectively. At the end of the measurement (180 min p.i.), authentic tracer accounted for about 7% ([<sup>18</sup>F]CPFPX), 13% ([<sup>18</sup>F]MCBX) and 25% ([<sup>18</sup>F]CBX) of the total plasma radioactivity.

Plasma kinetics of [<sup>18</sup>F]CPFPX and its analogues exhibited a triphasic profile. Although basic pharmacokinetic parameters can be derived from the triexponential equations without further physiological interpretation of this behaviour, application of a distinct pharmacokinetic model may help to elucidate the physiological correlates of the three exponential terms and thus to understand the fate of the test compounds in the body. The observed triphasic plasma profiles of the evaluated tracers can be well explained by a three-compartment mammillary PK model in which a central plasma compartment is connected to two peripheral tissue compartments with distinct kinetic properties [187, 189]. Intercompartmental transfer processes account for an initial rapid distribution phase followed by a second slower distribution phase. These phases are described by the first two terms of the exponential equation. The third exponential corresponds to the final elimination phase which is characterised by a shallow decline of the plasma concentration-time curve. Application of this model appears reasonable with regard to the physicochemical properties of the tested tracers. Being small, non-ionic, polar molecules of medium lipophilicity, [<sup>18</sup>F]CPFPX and similar xanthine derivatives can be assumed to cross biological membranes readily and to distribute throughout body tissues [320, 321]. This

assumption is supported by the estimated  $V_d$ -values which suggest distribution in total body water (data on total body water of rats can be found in [322, 323]). Given the fact that the main transport vehicle of tracer in the body is blood and that tissues differ with regard to blood perfusion, the hypothesis of a central plasma compartment and two distinct tissue compartments with individual transport and equilibration kinetics seems appropriate.

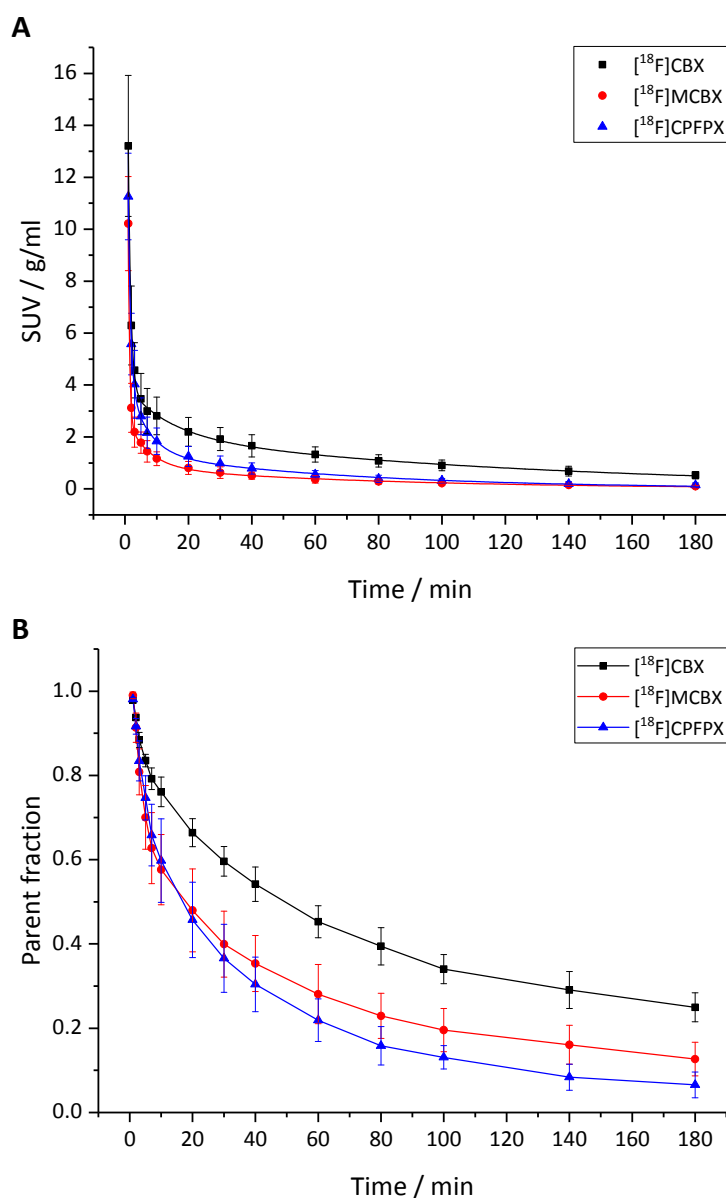


Fig. 29. Plasma kinetics of  $[^{18}\text{F}]\text{CBX}$ ,  $[^{18}\text{F}]\text{MCBX}$  and  $[^{18}\text{F}]\text{CPFPX}$  following i.v. bolus injection of  $21 \pm 3$  MBq into male Sprague Dawley rats. (A) Metabolite-corrected arterial plasma time-activity curves. SUVs were calculated by normalising plasma radioactivity concentration to amount of injected radioactivity and body weight. Values were fit to a triexponential model (solid lines). (B) Fraction of plasma radioactivity representing authentic (unchanged) tracer. Solid lines are a guide to the eye. Data (mean  $\pm$  SD) were obtained from 8 ( $[^{18}\text{F}]\text{CBX}$ ,  $[^{18}\text{F}]\text{CPFPX}$ ) or 9 animals ( $[^{18}\text{F}]\text{MCBX}$ ).

### 4.2.2 Plasma protein binding

According to the free drug hypothesis [324], which is still widely applied in pharmacology, only drug molecules which are not bound to plasma proteins are able to cross biological membranes and to interact with biomolecules such as enzymes or receptors. Thus, the extent of plasma protein binding of a drug may affect its metabolic fate as well as its efficacy at biological targets. In order to assess whether or not variations in plasma protein binding might lead to differences in metabolism of the evaluated tracers, the free fraction of tracer in rat plasma was determined during each PET scan.

Measured free fractions of the three tracers in rat plasma ranged from 0.02 to 0.04 (Fig. 30). Due to the pronounced inter-individual variability in plasma protein binding, statistical significance could only be demonstrated for the difference between [ $^{18}\text{F}$ ]MCBX and [ $^{18}\text{F}$ ]CPFPX. Despite the high extent of plasma protein binding, all tracers were suspected to extensive metabolism almost immediately after i.v. injection (compare Fig. 29B), suggesting fast uptake into hepatocytes. In recent years, the impact of plasma protein binding on physiological processes and thus the validity of the free drug hypotheses is being increasingly questioned [325], since numerous studies reported apparent discrepancies between predicted and observed uptake and clearance rates especially of highly bound drugs [326–330]. Regarding [ $^{18}\text{F}$ ]CPFPX and its analogues, plasma and brain kinetics indicated that tracer uptake into cells was not as restricted by plasma protein binding as anticipated from the assumption that cellular uptake is solely driven by the unbound fraction of a drug. In light of these observations and as a consequence of the unsolved questions concerning the role of plasma protein binding in pharmacokinetics, measured free fractions of [ $^{18}\text{F}$ ]CBX, [ $^{18}\text{F}$ ]MCBX and [ $^{18}\text{F}$ ]CPFPX were used only for comparison of the tracers' physicochemical properties and not for kinetic analyses. As measured free fractions were in a comparable range, this parameter was not assumed to account for fundamental differences in the physiological behaviour of the tracers.

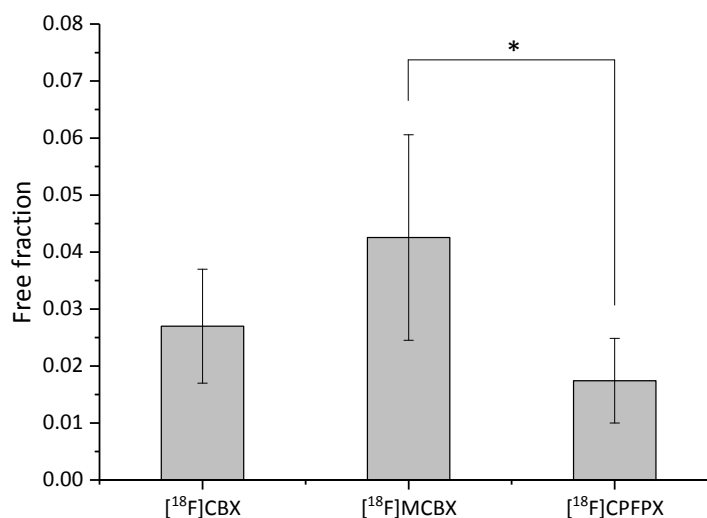


Fig. 30. Free fractions of tracer in rat plasma. Unbound fractions were assessed via ultrafiltration of plasma samples spiked with the respective tracer. Data (mean  $\pm$  SD) were obtained from 4 [<sup>18</sup>F]CPFPX, 6 [<sup>18</sup>F]CBX or 7 animals [<sup>18</sup>F]MCBX). \*significantly different ( $p < 0.05$ , one-way ANOVA with *post-hoc* Tukey test)

#### 4.2.3 *In vitro-in vivo* comparison of tracer metabolism

One of the main difficulties encountered when correlating *in vitro* metabolic stability data to *in vivo* pharmacokinetics is the almost impossible task of isolating one single aspect from the multitude of physiological interactions that constitute the *in vivo* behaviour of a drug. Whereas the microsomal stability assays used in this work provide data only on the intrinsic metabolic lability of the test compounds, pharmacokinetic plasma profiles reflect processes of distribution, metabolism and elimination occurring in various organs/tissues with different kinetic characteristics. Due to the low molecular weight and the non-ionic nature of the substances evaluated in the current study, direct renal or biliary excretion (i.e. excretion of the unchanged molecule) seems unlikely [331–333]. Consequently, a high correlation between metabolism and elimination can be assumed. From plasma time-activity curves, information on tracer elimination can be extracted in form of total (plasma) clearance and terminal half-life. Because terminal half-life is a hybrid parameter depending on both clearance and volume of distribution [334], total clearance was chosen as predictive parameter and basis for *in vitro-in vivo* comparison. Total clearance ratios reported above were inversed to facilitate direct comparison with *in vitro* microsomal half-life ratios (reported in section 4.1.3). The results of *in vitro-in vivo* comparison are summarised in Table 11. For the sake of simplicity, the terms CBX, MCBX and CPFPX are used for both radiolabelled and cold compound in the following discussion.

Table 11. Comparison of *in vivo* total clearance ratios (inversed) and *in vitro* microsomal half-life ratios. For reasons of clarity, both radiolabelled and cold compound are summarised under the same term.

Tracers compared	<i>In vivo</i> total clearance ratio, inversed (SE)	<i>In vitro</i> microsomal half-life ratio (SE)	Deviation <i>in vitro</i> from <i>in vivo</i>
			%
CBX:CPFPX	2.6 (0.12)	3.1 (0.11)*	19
MCBX:CPFPX	0.82 (0.019)	1.4 (0.029)*	71
CBX:MCBX	3.1 (0.15)	2.2 (0.072)*	29

\* significantly different from inverse *in vivo* total clearance ratio ( $p < 0.05$ , two-tailed t-test)  
SE, standard error (estimated from SEs of the individual ratios via error propagation)

Despite the relatively straightforward approach chosen for kinetic parameter estimation and the limitations of the applied PK model, *in vitro* metabolic stability data obtained from microsomal stability assays proved to be predictive for *in vivo* pharmacokinetics of the xanthine-derived A<sub>1</sub>AR ligands. *In vitro* half-life ratios deviated between 19 and 71% from inverse *in vivo* clearance ratios. *In vitro* metabolic stability ranking correlated well with *in vivo* clearance ranking. CBX exhibited considerable higher metabolic stability *in vitro* and lower clearance *in vivo* as compared to CPFPX and MCBX. Comparing MCBX and CPFPX, *in vitro* metabolic stability of MCBX was slightly higher than that of CPFPX ( $t_{1/2}$  ratio of 1.4). By contrast, MCBX was cleared somewhat faster from plasma than CPFPX. Although the difference between half-life ratio and inverse clearance ratio was statistically significant, this discrepancy has no practical relevance for the development of second generation radiotracers with improved metabolic properties since a marginal enhancement of metabolic stability would not justify further labour and cost intensive evaluation of a novel compound.

To summarise, for the substances investigated in this study, *in vitro* microsomal stability data (expressed as half-life ratios) proved to be a good predictive tool for pharmacokinetic behaviour *in vivo*, even without extensive kinetic analyses and complex *in vitro-in vivo* extrapolation procedures. This might be, at least partially, due to the favourable physicochemical characteristics of this substance class. Intrinsic molecular properties such as very high or very low lipophilicity, acidic/basic character and high molecular weight frequently entail poor membrane permeability, direct renal/biliary excretion or susceptibility to active transport mechanisms which all impede estimation of *in vivo* pharmacokinetics from *in vitro* data [169, 328, 335–337]. Since the xanthine-based A<sub>1</sub>AR ligands examined in the current study are characterised by low molecular weight, moderate lipophilicity and neutral character, the abovementioned interfering biochemical and

physiological effects are less likely to occur. Additionally, the approach of relative comparison (comparison of ratios) used throughout this work may have contributed to the good comparability of *in vitro* and *in vivo* behaviour of the test compounds, because several obstructive attributes shared by all three tracers may have cancelled out. The predictive value of this approach (quantified by the percentage deviation of *in vitro*  $t_{1/2}$  ratios to inverse *in vivo* clearance ratios; see Table 11) was comparably to sophisticated *in vitro-in vivo* extrapolation strategies which are based on complex model assumptions or empirically determined scaling factors [336, 338–347]. A drawback of using comparative approaches to evaluate novel candidate radiotracers is the need for a well-characterised reference compound which allows for quantitative statements on the biochemical and pharmacological behaviour of new chemical entities. Nevertheless, since analytical comparison of structurally modified analogues of established drugs with the original compound is a common procedure in the development of (radio)pharmaceuticals (analogue design) [348, 349], a general acceptance of comparative evaluation approaches can be expected.

#### 4.2.4 Metabolite analysis

##### 4.2.4.1 Extraction efficiency

With all three tested tracers, the applied extraction protocol yielded recoveries that slightly exceeded 100% throughout the whole measurement period (Fig. 31). For individual times of measurement, calculated recoveries of [ $^{18}\text{F}$ ]CBX, [ $^{18}\text{F}$ ]MCBX and [ $^{18}\text{F}$ ]CPFPX were in the range of 100 - 111%, 103 - 109% and 105 - 117%, respectively. The decrease in total volume of the supernatant, which is a consequence of both volume contraction resulting from mixing aqueous plasma with extraction solvent and the precipitation of plasma protein, amounted to  $8 \pm 1\%$ . Recovery of radioactivity from plasma can thus be regarded as essentially quantitative for the three tracers. On the basis of these results, it can be anticipated that radio-TLC detected all metabolite species formed *in vivo*.

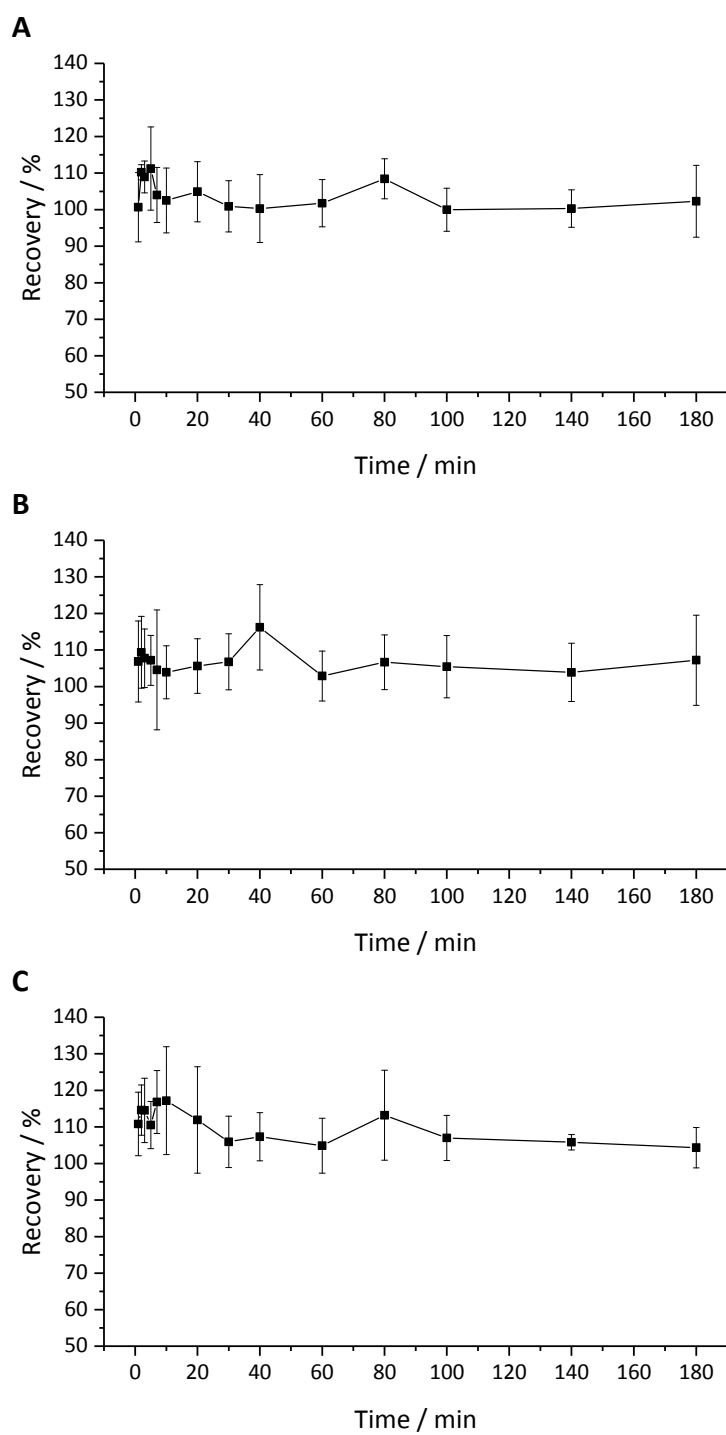


Fig. 31. Recovery of radioactivity from plasma samples after i.v. administration of [ $^{18}\text{F}$ ]CBX (A), [ $^{18}\text{F}$ ]MCBX (B) and [ $^{18}\text{F}$ ]CPFPX (C). Plasma was extracted with 3 volumes of a mixture of ACN/MeOH (50:50, v/v). Data (mean  $\pm$  SD) were obtained from 7-8 animals per tracer.

#### 4.2.4.2 *In vivo* metabolite profiles

Metabolite profiles obtained from rat plasma after administration of [ $^{18}\text{F}$ ]CBX, [ $^{18}\text{F}$ ]MCBX and [ $^{18}\text{F}$ ]CPFPX are shown in Fig. 32 (radio-TLC images and densitometer scans). Since spectroscopic identification of the individual molecules could not yet be performed, *in vivo* metabolite profiles were only visually compared to the rat *in vitro* metabolite profiles presented in section 4.1.4.2.

Radio-TLC of [ $^{18}\text{F}$ ]CBX (Fig. 32A) resolved a dominant, relatively lipophilic (low retention on the silica TLC plate) metabolite species ( $M_{A4}$ ,  $R_f$  0.71) and three less abundant metabolites of lower lipophilicity ( $M_{A1}$ ,  $R_f$  0.17;  $M_{A2}$ ,  $R_f$  0.24;  $M_{A3}$ ,  $R_f$  0.31). The  $R_f$  value of authentic [ $^{18}\text{F}$ ]CBX was 0.71. At later time-points, accumulation of non-migrating compounds at the origin was observed, which might indicate the appearance of hydrophilic phase II metabolites in plasma. The *in vivo* metabolite profiles of [ $^{18}\text{F}$ ]CBX corresponded well to the *in vitro* metabolite profiles which also showed a dominant metabolite with high retention on the C18 stationary phase (A5) and three smaller metabolite peaks eluting shortly after the injection peak (A1-A3).

Radio-TLC of [ $^{18}\text{F}$ ]MCBX (Fig. 32B) showed a major metabolite ( $M_{B1}$ ,  $R_f$  0.29) exhibiting high retention on silica (low lipophilicity). Two smaller activity spots are clearly visible ( $M_{B2}$ ,  $R_f$  0.40;  $M_{B3}$ ,  $R_f$  0.48), and a fourth spot ( $M_{B4}$ ) can be recognised at  $R_f$  0.62, in close vicinity to the authentic tracer ( $R_f$  0.79). This is in good agreement with microsomal metabolite profiles showing an early eluting major compound (B3) followed by two smaller peaks (B5-B7). The third activity spot on the TLC plate might correspond to peak B9 or B10 in the rat microsomal profile.

*In vivo* and *in vitro* metabolite profiles of [ $^{18}\text{F}$ ]CPFPX in rodents have been extensively compared in [288]. Bier et al. first recognised the discrepancies between *in vitro* and *in vivo* metabolism of [ $^{18}\text{F}$ ]CPFPX in rodents. One major metabolite, the enone species **7**, was generated exclusively in the living animal and not in liver microsomes. In the current study, microsomal incubation procedures and HPLC analyses had been slightly modified, thus qualitative *in vitro-in vivo* comparison was repeated. At least four metabolites ( $M_{C1}$ - $M_{C4}$ ) could be detected in rat plasma after [ $^{18}\text{F}$ ]CPFPX administration (Fig. 32C).  $R_f$  values of the compounds were as follows: [ $^{18}\text{F}$ ]CPFPX, 0.82;  $M_{C1}$ , 0.21;  $M_{C2}$ , 0.32;  $M_{C3}$ , 0.43;  $M_{C4}$ , 0.50. The most hydrophilic species,  $M_{C1}$ , represented the main metabolite during the first 60 min after tracer injection. Later, intensity of the  $M_{C1}$  spot decreased continuously, suggesting fast clearance of this metabolite from blood. At later time points, the least hydrophilic metabolite,  $M_{C4}$ , became the dominant species in plasma. A comparison of the rat metabolite

profile shown in Fig. 32C and the human metabolite pattern of [<sup>18</sup>F]CPFPX published in the abovementioned paper of Bier et al. (which was generated using comparable chromatographic conditions) suggests that M<sub>C4</sub> represents the enone metabolite. As discussed in section 4.1.4.3, the discrepancy between *in vitro* and *in vivo* metabolite pattern of CPFPX in rodents could possibly be attributed to the action of extrahepatic P450 isoforms or non-P450 enzymes. Except for the absence of the enone metabolite, the microsomal *in vitro* metabolite profiles matched their *in vivo* counterparts: a major, hydrophilic metabolite (C1) and two slightly more lipophilic metabolites (C2, C5) of sufficient peak size to represent potential candidates for *in vivo* metabolites M<sub>C2</sub> and M<sub>C3</sub>.

Although a conclusive statement on the comparability of *in vitro* and *in vivo* metabolite profiles cannot yet be made due to the lack of spectroscopic data, a high degree of similarity was observed between HPLC analyses of microsomal extracts and radio-TLC analyses of plasma. For CBX and MCBX, the number of peaks detected in microsomal extracts (which were of considerable peak size) and their chromatographic properties corresponded closely to the radio-TLCs obtained from plasma extracts. It can therefore be assumed that the *in vitro* metabolite profiles are comparable to the *in vivo* metabolite profiles. In the case of CPFPX, the observations of Bier et al. regarding the differences between *in vitro* and *in vivo* metabolic pathways could be confirmed. However, since the formation of **7** *in vivo* in rodents is most probably governed by enzyme systems not contained in liver microsomal preparations, the observed discrepancies do not necessarily indicate a lack of validity of microsomal data, but might rather illustrate the intrinsic limitations of the reduced microsomal model. With regard to the utilisation of liver microsomes for the biosynthesis of specific metabolites on the macroscopic scale (quantities large enough for spectroscopic identification), the results of the studies on species differences in microsomal metabolism reported in section 4.1.4.2 showed that it might be promising to compare the *in vitro* metabolite profiles of several animal species, since a specific metabolic pathway observed *in vivo* in one species might be realised *in vitro* in another species (e.g. *in vitro* enone formation in humans and beagle dogs). Alternatively, the use of a more complex *in vitro* metabolism model such as hepatocytes might be advisable.

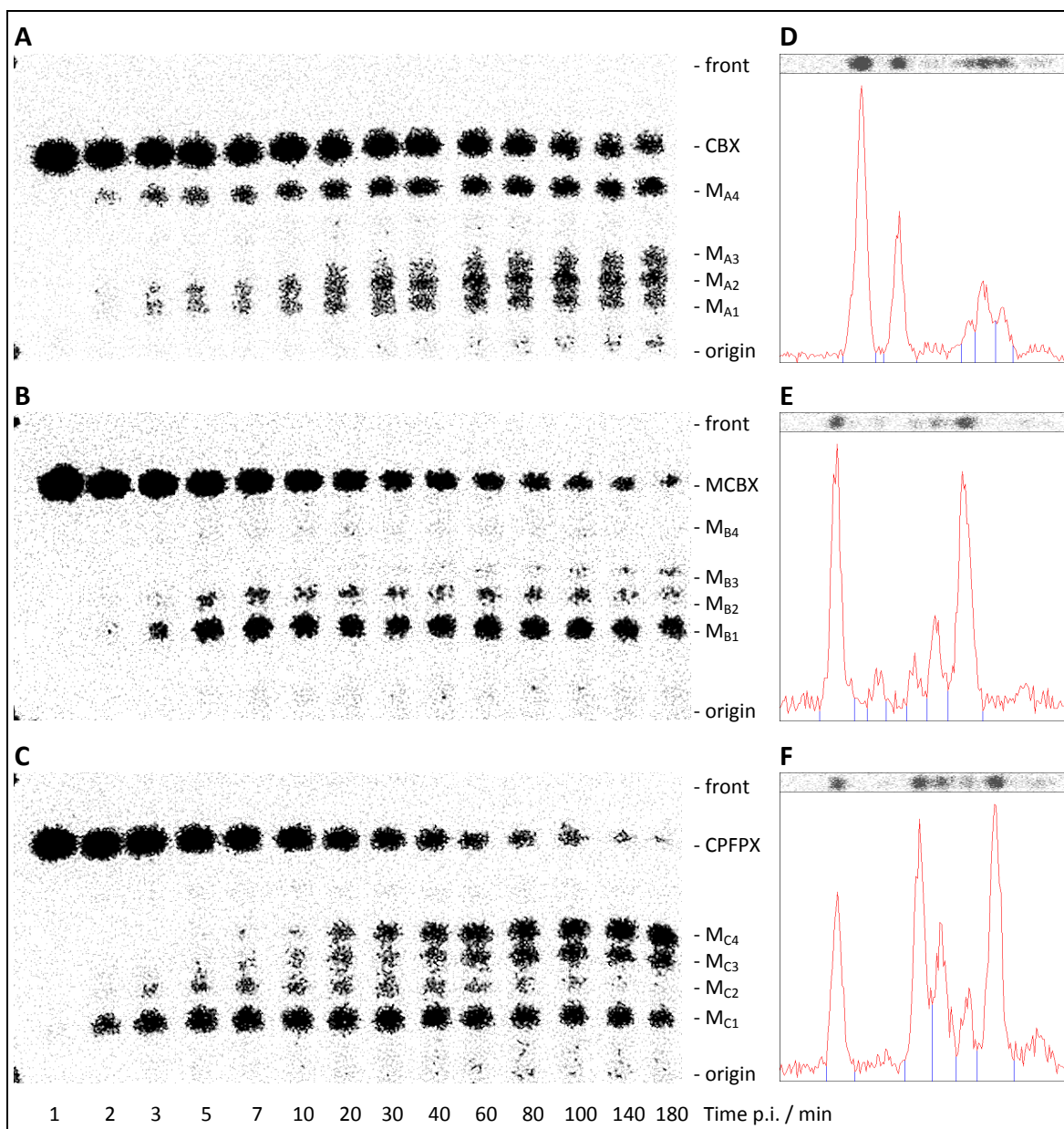


Fig. 32. Typical *in vivo* metabolite profiles obtained from rat plasma after administration of  $[^{18}\text{F}]$ CBX (A+D),  $[^{18}\text{F}]$ MCBX (B+E) and  $[^{18}\text{F}]$ CPFPX (C+F). Figures on the left side show the radio-TLC images, figures on the right side the corresponding densitometer scans at 60 min p.i. For  $R_f$  values of authentic tracers and metabolites, see text.

### 4.3 Brain kinetics

In order to be useful for PET brain imaging, a newly developed tracer must exhibit adequate cerebral pharmacokinetics. Candidate tracers may fail due to poor passive brain entry or active rejection from brain via efflux transporters [127]. Even if a tracer is able to cross the BBB readily, accumulation in the brain may be insufficient for imaging. The amount of tracer entering the brain depends on both the ability of the tracer to cross the BBB and the amount of tracer delivered to the brain via the blood stream [350]. Extensive peripheral metabolism which rapidly decreases tracer concentration in blood may prevent entry of sufficient amounts of tracer into the brain. Exemplary for this problem is [ $^{18}\text{F}$ ]CPFPX, which is rapidly metabolised in rodents as well as in humans [213, 220, 226, 288]. A study of Matusch et al. [289] showed that cerebral uptake of [ $^{18}\text{F}$ ]CPFPX was significantly higher in patients with impaired metabolism of the tracer resulting from liver cirrhosis or fluvoxamine treatment (a selective serotonin reuptake inhibitor which also inhibits P450 1A2, the major enzyme responsible for [ $^{18}\text{F}$ ]CPFPX degradation). Consequently, the development of metabolically stable structural analogues of [ $^{18}\text{F}$ ]CPFPX is one approach to improve PET imaging of A<sub>1</sub>AR.

In the current study, pharmacokinetics of two recently synthesised [ $^{18}\text{F}$ ]CPFPX analogues, [ $^{18}\text{F}$ ]CBX and [ $^{18}\text{F}$ ]MCBX, were evaluated in the rat model. [ $^{18}\text{F}$ ]CBX actually showed noticeably delayed metabolic clearance and increased plasma levels *in vivo* as compared to [ $^{18}\text{F}$ ]CPFPX (see section 4.2.1). In order to examine the influence of enhanced tracer delivery to brain via plasma, cerebral kinetics of [ $^{18}\text{F}$ ]CBX and [ $^{18}\text{F}$ ]CPFPX were measured by *in vivo* PET. Additionally, cerebral kinetics of [ $^{18}\text{F}$ ]MCBX were also investigated and used for comparison, although this compound did not show higher *in vivo* metabolic stability than [ $^{18}\text{F}$ ]CPFPX. Prior to PET measurements, a supplementary *in vitro* autoradiographic study was conducted to gain information on the cerebral binding characteristics of the novel tracers.

#### 4.3.1 *In vitro* autoradiography

*In vitro* autoradiography served primarily for analysis of cerebral tracer distribution and estimation of non-specific binding to brain tissue. *In vitro* autoradiographic binding of [ $^{18}\text{F}$ ]CBX, [ $^{18}\text{F}$ ]MCBX and [ $^{18}\text{F}$ ]CPFPX in rat brain is presented in Fig. 33. With all tracers, comparable cerebral distribution patterns were obtained. Highest activity accumulation was observed in hippocampus, thalamus, cerebellar cortex and neocortex, lowest in midbrain and brain stem. This pattern corresponds well with cerebral A<sub>1</sub>AR distribution as described in the literature [212-217]. The fraction of non-specific binding of [ $^{18}\text{F}$ ]CBX, [ $^{18}\text{F}$ ]MCBX and

[<sup>18</sup>F]CPFPX in rat brain amounted to  $1.7 \pm 0.25\%$ ,  $1.9 \pm 0.24\%$  and  $1.0 \pm 0.09\%$ , respectively. Considering this relatively narrow range, no fundamental variations in cerebral *in vivo* pharmacokinetics are likely to result from this parameter.

Additionally, *in vitro* binding affinities of CBX, MCBX, CPFPX toward rat cortical A<sub>1</sub>AR were recently determined in our laboratories via competitive radioligand binding assays (experimental procedure as described in [351]). Measured K<sub>i</sub> values (mean  $\pm$  SD, n  $\geq$  3) were  $0.33 \pm 0.06$  nM for CPFPX,  $1.4 \pm 0.05$  nM for CBX and  $1.4 \pm 0.1$  nM for MCBX. Affinities of the novel cyclobutyl-substituted xanthine derivatives for the A<sub>1</sub>AR were thus about four times lower than that of CPFPX.

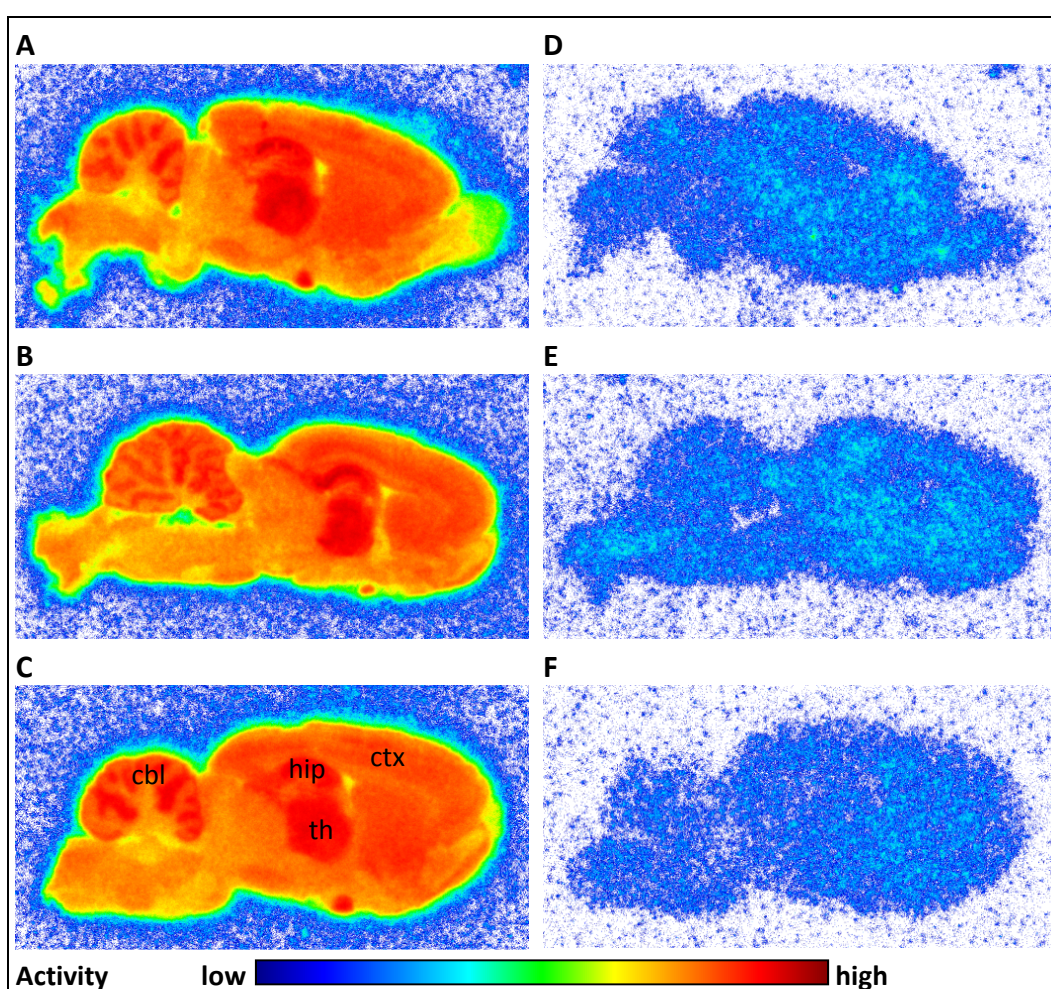


Fig. 33. Representative autoradiographs of sagittal rat brain slices after incubation with 0.4-0.5 nM [<sup>18</sup>F]CBX (A+D), [<sup>18</sup>F]MCBX (B+E) and [<sup>18</sup>F]CPFPX (C+F). Figures on the left side show total binding of the tracer, figures on the right side show non-specific binding in the presence of 13  $\mu$ M DPCPX. High accumulation of radioactivity (warm colours) can be recognised in hippocampus (hip), thalamus (th), cerebellar cortex (cbl) and neocortex (ctx).

### 4.3.2 Brain PET images

PET images acquired after administration of [ $^{18}\text{F}$ ]CBX, [ $^{18}\text{F}$ ]MCBX and [ $^{18}\text{F}$ ]CPFPX are presented in Fig. 34. With [ $^{18}\text{F}$ ]CPFPX and [ $^{18}\text{F}$ ]MCBX, the rat brain could be clearly visualised. High accumulation of radioactivity was observed in  $A_1$ AR-rich structures such as thalamus, hippocampus, neocortex and cerebellar cortex. Average SUVs of [ $^{18}\text{F}$ ]MCBX within the selected time window (0-60 min p.i.) were markedly lower than those of [ $^{18}\text{F}$ ]CPFPX. These differences in cerebral kinetics are further discussed in the following sections. Compared with the two other tracers, cerebral accumulation of [ $^{18}\text{F}$ ]CBX was marginal. Brain contours and cerebral structures were hardly identifiable. Only thalamus, hippocampus, cerebellar cortex and neocortex showed noticeable accumulation of radioactivity. Further kinetic analyses were conducted in order to identify possible physiological causes for this unexpected result (see following sections).

### 4.3.3 *In vivo* cerebral kinetics

Kinetics of [ $^{18}\text{F}$ ]CBX, [ $^{18}\text{F}$ ]MCBX and [ $^{18}\text{F}$ ]CPFPX in the rat brain are compared in Fig. 35. Despite the higher concentration of tracer in plasma, cerebral uptake of [ $^{18}\text{F}$ ]CBX was considerably lower than uptake of [ $^{18}\text{F}$ ]CPFPX. The brain SUV curve of [ $^{18}\text{F}$ ]CBX remained below the plasma SUV curve during the entire measurement period, indicating cerebral efflux of tracer rather than accumulation. To gain more insight into the mechanisms underlying this phenomenon, additional kinetic analyses were performed (see following section).

Cerebral kinetics of [ $^{18}\text{F}$ ]MCBX deviated noticeable from that of [ $^{18}\text{F}$ ]CPFPX. Whole brain SUV curves of [ $^{18}\text{F}$ ]MCBX peaked earlier (4 min) than SUV curves of [ $^{18}\text{F}$ ]CPFPX (12 min) and dropped more steeply. However, peak SUV values were comparable for both tracers (about 4 g/ml). These observations suggest that brain uptake of [ $^{18}\text{F}$ ]MCBX and [ $^{18}\text{F}$ ]CPFPX is comparable, but transfer kinetics of [ $^{18}\text{F}$ ]MCBX is faster, resulting in a compressed SUV versus time curve. Rapid tracer wash-out also explains the differences in average SUVs between [ $^{18}\text{F}$ ]MCBX and [ $^{18}\text{F}$ ]CPFPX as depicted in Fig. 34. These PET images were generated by averaging activity data measured from the time point of tracer injection up to 60 min p.i. (time-weighted average). Within this time window, a much higher fraction of [ $^{18}\text{F}$ ]MCBX than of [ $^{18}\text{F}$ ]CPFPX has already left the brain, implying lower average activity values. This assumption was substantiated by reanalysis of the [ $^{18}\text{F}$ ]MCBX PET data set with a shortened averaging period (0-30 min p.i.). Cerebral SUVs of [ $^{18}\text{F}$ ]MCBX averaged from 0-30 min p.i. were almost similar to cerebral SUVs of [ $^{18}\text{F}$ ]CPFPX averaged from 0-60 min p.i.

(data not shown). A more detailed analysis of cerebral transfer kinetics of [ $^{18}\text{F}$ ]MCBX based on compartmental modelling is presented in the following section.

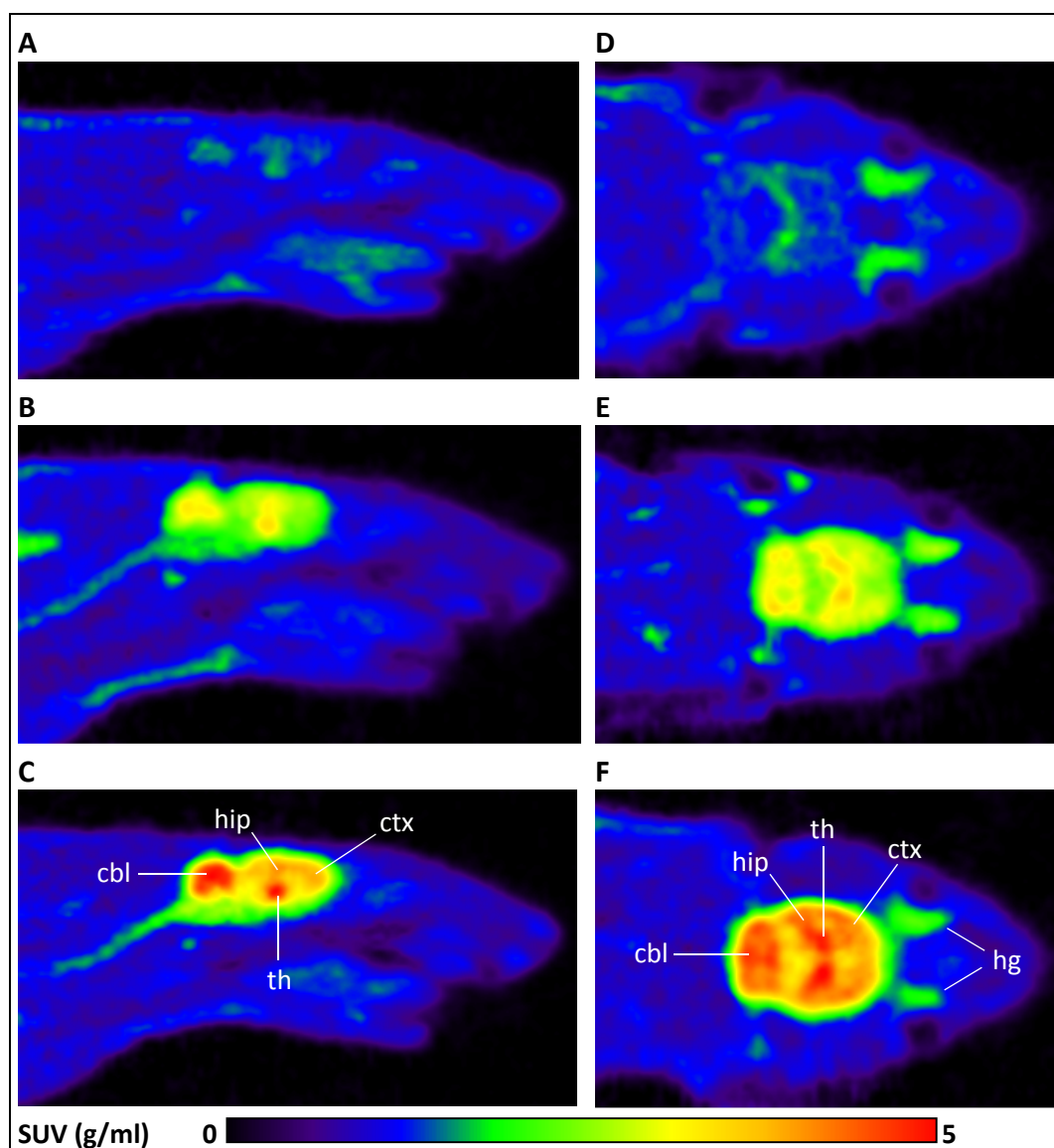


Fig. 34. Representative PET images of rat brain after i.v. bolus administration of 20-22 MBq [ $^{18}\text{F}$ ]CBX (A+D), [ $^{18}\text{F}$ ]MCBX (B+E) and [ $^{18}\text{F}$ ]CPFPX (C+F). Activity concentration values registered 0-60 min p.i. were averaged (time-weighted average) and normalised to body weight and amount of injected radioactivity. SUV maximum was set to 5 g/ml (left side: sagittal plane, right side: horizontal plane; cbl, cerebellar cortex; ctx, neocortex; hip, hippocampus; hg, Harderian gland; th, thalamus).

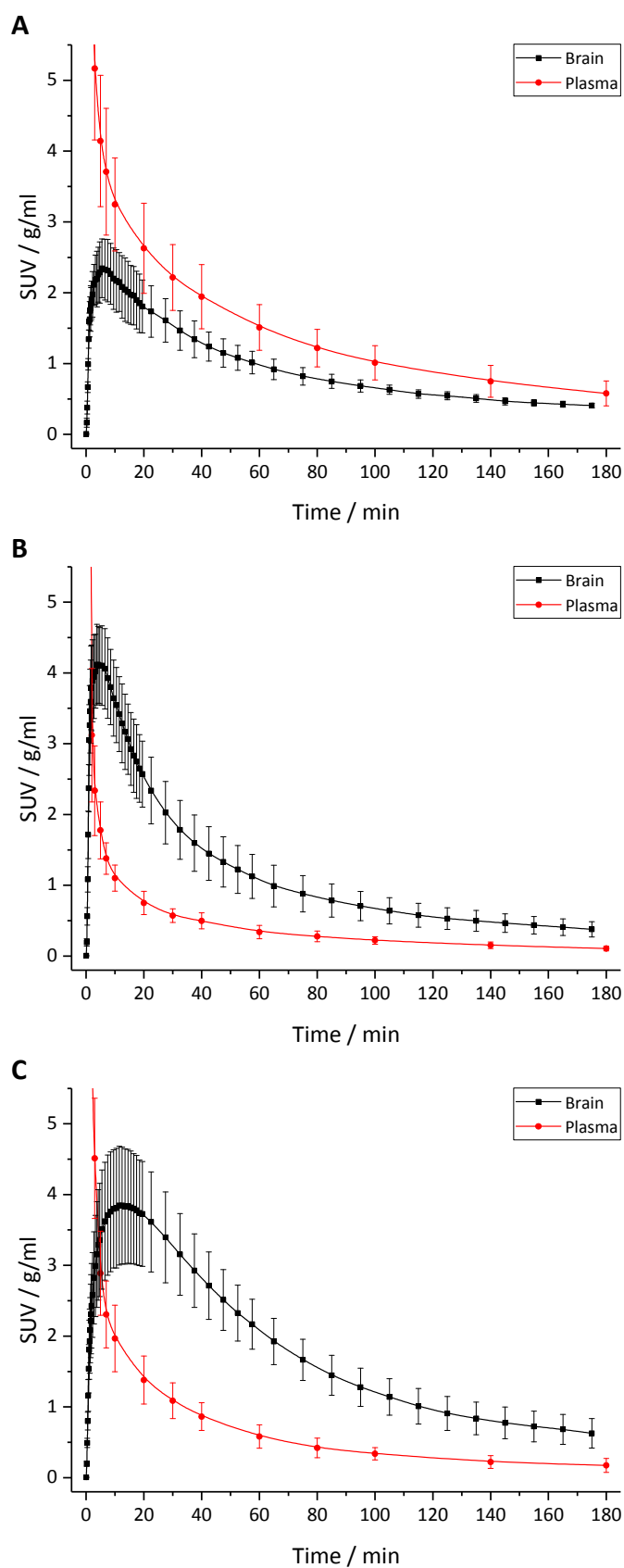


Fig. 35. Kinetics of  $[^{18}\text{F}]\text{CBX}$  (A),  $[^{18}\text{F}]\text{MCBX}$  (B) and  $[^{18}\text{F}]\text{CPF PX}$  (C) in rat brain (whole brain) and arterial plasma following single bolus injection. SUVs were calculated by normalising radioactivity concentration to amount of injected radioactivity and body weight. Plasma data were corrected for metabolites. Data (mean  $\pm$  SD) were obtained from 4 animals per tracer.

#### 4.3.4 Graphical and compartmental analysis of brain PET data

Kinetic parameters describing cerebral tracer uptake and distribution were determined either graphically (Logan plot, Fig. 36D-F) or via compartmental modelling (Fig. 36A-C). A 2TCM could be readily fitted to whole brain TACs of [<sup>18</sup>F]MCBX and [<sup>18</sup>F]CPFPX. For these two tracers, the 2TCM was clearly superior to the 1TCM, as proved by significantly lower Akaike information criterion values. In the case of [<sup>18</sup>F]CBX, the low accumulation of tracer in brain and the resulting unfavourable signal-to-noise ratio hampered fitting of the four rate constants describing tracer transfer in the 2TCM. A reliable estimation of individual rate constants was difficult, therefore only the robust compound parameters  $V_T$  and  $V_S$  (calculated from all four rate constants) were derived from 2TCM fits of the [<sup>18</sup>F]CBX PET data. Additional 1TCM fits were used to derive the rate constants  $K_1$  and  $k_2$  which characterise the rate of influx and efflux across the blood brain barrier. Results of compartmental modelling and graphical analysis are given in Table 12.

Table 12. Results of graphical analysis and compartmental modelling of cerebral PET data (whole brain ROI).  $K_1$  and  $k_2$  were derived either from 1TCM fits ([<sup>18</sup>F]CBX) or 2TCM fits ([<sup>18</sup>F]MCBX, [<sup>18</sup>F]CPFPX).

Kinetic parameter	Model	[ <sup>18</sup> F]CBX	[ <sup>18</sup> F]MCBX	[ <sup>18</sup> F]CPFPX
$V_T / ml/cm^3$	LGA	0.641 (0.184) <sup>bc</sup>	2.648 (0.717) <sup>a</sup>	2.678 (0.980) <sup>a</sup>
$V_T / ml/cm^3$	2TCM	0.621 (0.192) <sup>bc</sup>	2.716 (0.791) <sup>a</sup>	2.703 (1.015) <sup>a</sup>
$V_S / ml/cm^3$	2TCM	0.469 (0.174)	0.496 (0.205)	0.653 (0.262)
$K_1 / ml/cm^3/min$	1TCM/2TCM	0.124 (0.039) <sup>b</sup>	0.366 (0.097) <sup>ac</sup>	0.172 (0.059) <sup>b</sup>
$k_2 / 1/min$	1TCM/2TCM	0.202 (0.022)	0.170 (0.040)	0.093 (0.037)
$k_3 / 1/min$	2TCM	n.d.	0.027 (0.044)	0.025 (0.039)
$k_4 / 1/min$	2TCM	n.d.	0.075 (0.093)	0.039 (0.030)
$K_1/k_2 / ml/cm^3$	1TCM/2TCM	0.621 (0.192)*	2.219 (0.740)	2.049 (0.998)
$k_3/k_4 / 1/1$	2TCM	n.d.	0.239 (0.136)	0.418 (0.383)

LGA, Logan graphical analysis; 1TCM, one-tissue compartment model; 2TCM, two-tissue compartment model;  $V_T$ , total distribution volume;  $V_S$ , specific distribution volume;  $K_1$ - $k_4$ , transfer rate constants; n.d., not determined; \* $K_1/k_2$  equals  $V_T$  in 1TCM; <sup>a</sup> significantly different from [<sup>18</sup>F]CBX; <sup>b</sup> significantly different from [<sup>18</sup>F]MCBX; <sup>c</sup> significantly different from [<sup>18</sup>F]CPFPX ( $p < 0.05$ , one-way ANOVA with *post-hoc* Tukey test) mean (SD),  $n = 4$

Total distribution volumes were determined via Logan graphical analysis and compartmental modelling.  $V_T$  of [<sup>18</sup>F]MCBX and [<sup>18</sup>F]CPFPX were nearly identical whereas  $V_T$  of [<sup>18</sup>F]CBX was about 4 times lower.  $V_T$  values acquired via compartmental modelling corresponded closely to the values obtained graphically. Differences in  $V_S$  between the tracers did not reach statistical significance. Values of  $K_1$  and  $k_2$  were significantly higher for

[<sup>18</sup>F]MCBX than for [<sup>18</sup>F]CPFPX, whereas  $K_1/k_2$  was nearly constant. This indicates that influx and efflux kinetics of [<sup>18</sup>F]MCBX are faster compared with [<sup>18</sup>F]CPFPX, but that the extent of tracer uptake into the brain is similar. These results support the assumption that the different shapes of the brain SUV curves of the two tracers are caused by variations in transport kinetics. Potential causes for these variations may be the faster peripheral clearance observed with [<sup>18</sup>F]MCBX, more rapid diffusion across the BBB (due to the somewhat higher lipophilicity of [<sup>18</sup>F]MCBX) or faster drug–receptor binding kinetics (resulting from the lower affinity of [<sup>18</sup>F]MCBX for the A<sub>1</sub>AR). Most likely, the observed differences in cerebral kinetics of [<sup>18</sup>F]MCBX are attributed to a combination of all of the above mentioned factors.

The most apparent characteristic of [<sup>18</sup>F]CBX brain kinetics was the minimal to non-existent cerebral accumulation. Tissue to plasma ratio was <1 throughout the whole measurement. In view of the multiple factors affecting brain uptake and washout of a radiotracer, the deviating cerebral kinetics of [<sup>18</sup>F]CBX are not readily explainable. The results of *in vitro* competitive binding assay and *in vitro* autoradiography showed that the affinity of [<sup>18</sup>F]CBX for the rat A<sub>1</sub>AR (as measured by  $K_i$ ) is lower than the affinity of [<sup>18</sup>F]CPFPX (by a factor of 4) but similar to that of [<sup>18</sup>F]MCBX, and that the extent of non-specific binding to brain tissue and plasma proteins of [<sup>18</sup>F]CBX is comparable to both [<sup>18</sup>F]CPFPX and [<sup>18</sup>F]MCBX. Although differences in  $V_s$  of the tracers were not statistically significant, the lower affinity of [<sup>18</sup>F]CBX (compared to [<sup>18</sup>F]CPFPX) will certainly influence specific binding and therefore also  $V_s$  and  $V_T$ . However, it is questionable whether affinity is the only cause for inadequate cerebral kinetics of [<sup>18</sup>F]CBX, since  $V_T$  of [<sup>18</sup>F]MCBX, which exhibited similar affinity for rat A<sub>1</sub>ARs and similar protein binding as [<sup>18</sup>F]CBX, did not decrease in comparable manner. Another potential reason for low cerebral accumulation of [<sup>18</sup>F]CBX could be insufficient brain entry of the tracer. As [<sup>18</sup>F]CBX is less lipophilic than the other two tracers, it is likely that its ability to diffuse across the BBB will also be diminished. The small  $K_1$  value of [<sup>18</sup>F]CBX points to this direction, although the difference in  $K_1$  between [<sup>18</sup>F]CBX and [<sup>18</sup>F]CPFPX did not reach statistical significance. Values of  $k_2$  must be interpreted with caution, because  $k_2$  is defined as the ration of  $K_1$  and the distribution volume of the tracer in the first tissue compartment ( $k_2 = K_1/V_1$ ). In the 2TCM,  $V_1$  not only depends on the transfer of tracer from plasma to  $V_1$  and back, but also on the transfer of tracer from  $V_1$  to  $V_2$  (the receptor compartment) and back, which is strongly influenced by the affinity of the tracer for its receptor. Since affinities of both [<sup>18</sup>F]CBX and [<sup>18</sup>F]MCBX were significantly lower than that of [<sup>18</sup>F]CPFPX, direct comparison of  $k_2$  values does not seem appropriate. Comparison of  $k_2$  values of [<sup>18</sup>F]CBX and [<sup>18</sup>F]MCBX might be justified because of the comparable affinities of these two tracers, but the difference in  $k_2$  did not reach statistical significance, hence no

clear statement can be made about differences in the unidirectional transport of tracer back from tissue to blood. A possible explanation for poor brain entry of [ $^{18}\text{F}$ ]CBX might be the involvement of drug efflux transporters which actively transport tracer molecules out of the brain capillary endothelial cells that form the BBB. With regard to the relatively broad substrate specificity of many efflux transporters [136, 142], it is conceivable that also [ $^{18}\text{F}$ ]CPFPX, [ $^{18}\text{F}$ ]MCBX and other structurally similar  $A_1$ AR tracers are susceptible to brain efflux, but to a varying extent, which might lead to differences in cerebral tracer uptake.

However, it is important to note that the significance of the kinetic parameters reported in Table 12 is limited due to the small number of animals used, the high inter-individual variations in cerebral kinetics and the difficulty of estimating accurate parameters from complicated multi-parameter models. Therefore, these data can only serve as an indication regarding the potential causes of variations in brain kinetics of the individual tracers. Although the underlying mechanisms which cause inadequate brain entry of [ $^{18}\text{F}$ ]CBX cannot be conclusively assessed on the basis of the data acquired in the current study, the results provide evidence that delivery of the tracer across the BBB might be an important factor. Further *in vitro* and *in vivo* studies on brain penetration of [ $^{18}\text{F}$ ]CBX and similar xanthine-derived  $A_1$ AR tracers appear promising. With regard to future human application of  $A_1$ AR tracers, particular attention should be paid to potential species-differences in the ability of a tracer to cross the BBB. These differences can be particularly pronounced in the case of uptake/efflux transporter substrates, impeding translation of a tracer from preclinical to clinical phase [352–354].

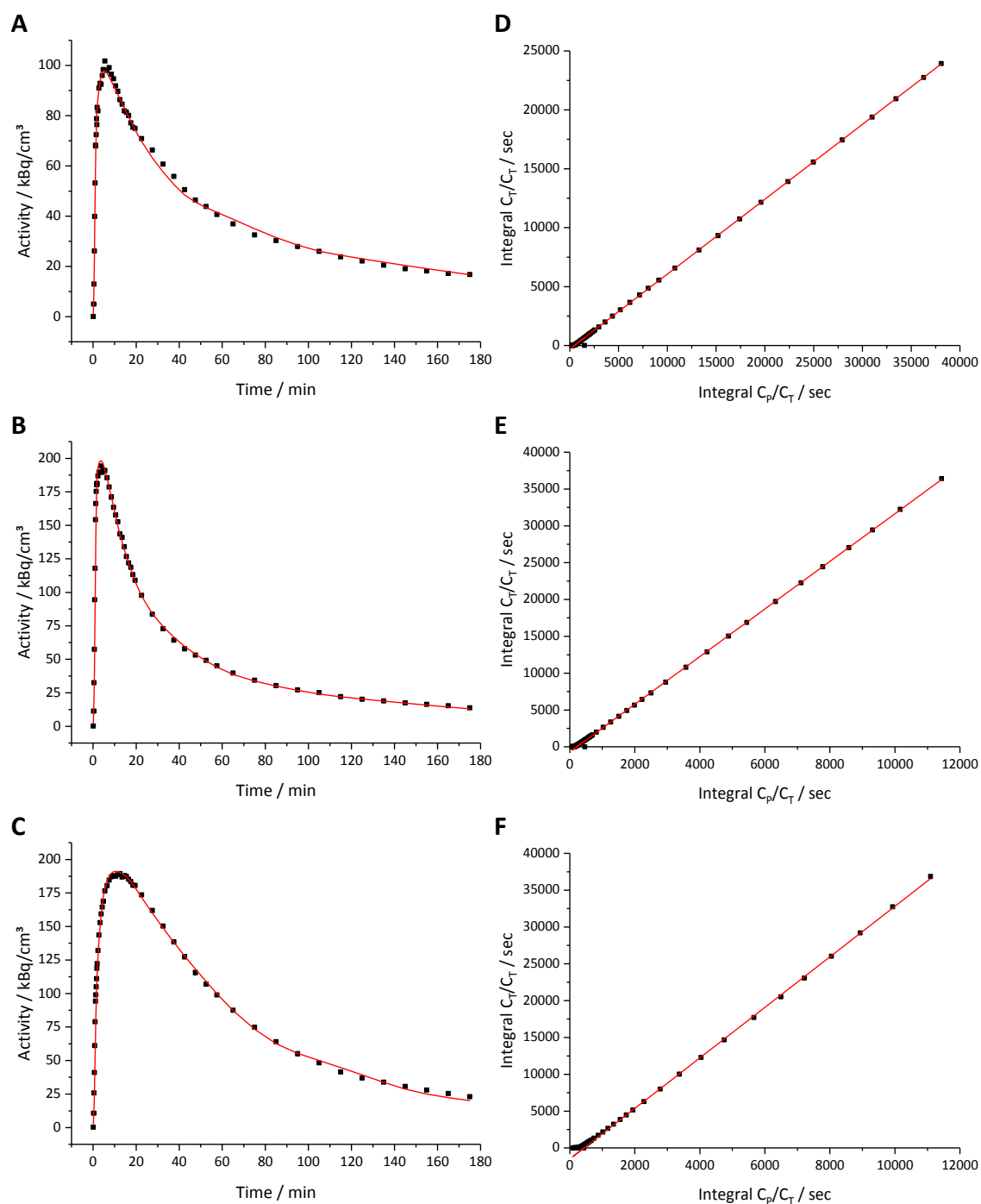


Fig. 36. Representative 2TCM fits (left row) and Logan plots (right row) of brain activity data acquired after i.v. bolus injection of 21-22 MBq  $[^{18}\text{F}]\text{CBX}$  (A+D),  $[^{18}\text{F}]\text{MCBx}$  (B+E) and  $[^{18}\text{F}]\text{CPFPX}$  (C+F). Black symbols represent measured data, red solid lines represent model fits ( $C_p$ , plasma time-activity curve;  $C_T$ , tissue time-activity curve).

## 5 Summary and Conclusion

The development of PET radiotracers for *in vivo* imaging of molecular targets in the brain is an enormous challenge given the large number of physicochemical and pharmacological criteria that must be met by these compounds. Metabolism is one important factor determining the *in vivo* performance of a candidate radiotracer. Inadequate metabolic stability or formation of brain-penetrant radiolabelled metabolites may render a novel compound unsuitable for PET imaging. An initial assessment of the metabolic properties of a candidate at an early stage in the development process is therefore essential. In the pharmaceutical sector, numerous *in vitro* metabolism models have been developed for the evaluation of drug candidates prior to first animal studies, but little information is available concerning the relevance of these models in the context of radiotracer development.

In this work, the utility of *in vitro* metabolism data for predicting *in vivo* metabolic properties of PET radiotracers was evaluated using three xanthine-derived A<sub>1</sub>AR ligands, namely 8-cyclopentyl-3-(3-fluoropropyl)-1-propylxanthine (CPFPX), 8-cyclobutyl-3-(3-fluoropropyl)-1-propylxanthine (CBX) and 3-(3-fluoropropyl)-8-(1-methylcyclobutyl)-1-propylxanthine (MCBX), as model compounds. *In vivo* pharmacokinetics and metabolite patterns of the three compounds were studied in the rat model and compared to *in vitro* data generated in rat liver microsomes (RLM).

Since the choice of incubation conditions may influence the results of *in vitro* studies, the effect of critical assay parameters on substrate depletion was extensively studied prior to the actual kinetic characterisation of the microsomal metabolism of the test compounds. For the enzyme-substrate systems investigated in the current study, strong influence on metabolic activity was exerted by (1) the pH of the incubation medium and (2) the type and concentration of the organic solvent used to solubilise the substrate. The effects of changes in buffer type, buffer molarity and concentration of the cofactor NADPH were less pronounced (although measurable). Alteration of the incubation matrix composition resulted in variations in substrate depletion of up to 300% (CBX) or 500% (MCBX, CPFPX). On the other hand, the ratios of substrate depletion (CBX to CPFPX and MCBX to CPFPX) proved to be highly constant, as well as the *in vitro* metabolic stability rank order of the three compounds (CBX>MCBX>CPFPX). These results suggest that a relative quantification approach such as the calculation of depletion ratios allows for quantitative statements on *in vitro* metabolic stability which are rather insensitive to variations of assay conditions.

Enzyme inactivation during microsomal incubations proved to be a considerable problem which may limit the validity of the results obtained from microsomal assays. Preincubation of microsomal protein in the presence of NADPH for 30 min reduced microsomal metabolism of CPF PX by 34%. An extended preincubation period of 120 min resulted in almost complete (89%) loss of metabolic activity. This phenomenon, which has been frequently described in the literature, is generally attributed to the NADPH-dependent formation of reactive oxygen species (ROS) in the microsomal matrix. The addition of antioxidant enzymes to the incubation matrix was reported beneficial by several authors, however, in the present study, addition of catalase and superoxide dismutase did not prevent enzyme inactivation. Further investigations on the role of NADPH in enzyme inactivation revealed that the concentration of NADPH remained stable during incubation at 37°C in HEPES buffer containing only MgCl<sub>2</sub>, but rapidly decreased when incubations were conducted in the presence of microsomal protein. It could be demonstrated chromatographically that NADPH loss was a consequence of oxidative consumption in the microsomal matrix rather than of chemical decomposition. Addition of diphenyleneiodonium chloride (DPI), a non-selective inhibitor of numerous flavoenzymes, could prevent accelerated loss of NADPH. These observations supported the assumption that, even in the absence of P450 substrates, enzymatic processes take place in the microsomal matrix which account for the formation of ROS and thus for enzyme inactivation. However, the use of DPI as incubation additive for microsomal assays is precluded by the inhibitory potential of this compound against P450 and cytochrome P450 reductase. Since other additives (EDTA, plumbagin) proved equally inadequate to maintain enzyme activity in microsomal incubations, the most promising strategy to avoid misleading *in vitro* stability data seems to be the shortening of the incubation period.

Based on the results of these investigations, the microsomal stability assay was optimised to allow for physiological relevant data. Most importantly, the concentration of DMSO in the assay was restricted to a level of less than 1% and the concentration of microsomal protein was adjusted to a value of 0.5 mg/ml in order to allow for sufficient substrate depletion during an maximum incubation period of 30 min. Using this optimised microsomal assay, the depletion kinetics of CBX, MCBX and CPF PX in RLM were assessed. Since the depletion profiles of all compounds exhibited sigmoidal shapes, Hill-type logistic regression models were used to analyse the data. From the logistic fits, *in vitro* metabolic half-lives of the substrates were deduced. Generally, microsomal half-life depends on the concentration of both substrate and microsomal protein. In order to derive a parameter which is independent of the assay conditions and thus suitable for *in vitro-in vivo* comparison of tracer metabolism, *in vitro* half-life ratios were calculated from the individual half-lives of

the radiotracers. The  $t_{1/2}$  ratios ( $\pm$  SE) of CBX:CPFPX, MCBX:CPFPX and CBX:MCBX were as follows:  $3.1 \pm 0.11$ ,  $1.4 \pm 0.029$  and  $2.2 \pm 0.033$ .

*In vivo* plasma kinetics of the  $^{18}\text{F}$ -labelled test compounds were assessed in anaesthetised rats via arterial blood sampling following intravenous bolus injection of the tracer. Standardised uptake value (SUV) versus time profiles were generated and fitted to triexponential models. From the triexponential fits, volume of distribution ( $V_d$ ), total clearance (CL) and terminal half-life ( $t_{1/2\gamma}$ ) were derived. Unlike  $t_{1/2\gamma}$ , CL is independent of  $V_d$  and therefore more suitable as predictive parameter for *in vitro-in vivo* comparison. CL values ( $\pm$  SE) for  $[^{18}\text{F}]\text{CBX}$ ,  $[^{18}\text{F}]\text{MCBX}$  and  $[^{18}\text{F}]\text{CPFPX}$  amounted to  $1.50 \pm 0.068$  ml/min,  $4.65 \pm 0.081$  ml/min and  $3.81 \pm 0.057$  ml/min. As with *in vitro* microsomal half-life, CL ratios were calculated from the individual values. Since, in contrast to *in vitro* microsomal  $t_{1/2}$ , smaller CL values correspond to higher metabolic stability, the *in vivo* CL ratios were inversed to facilitate direct comparison. The inversed CL ratios ( $\pm$  SE) of  $[^{18}\text{F}]\text{CBX}:[^{18}\text{F}]\text{CPFPX}$ ,  $[^{18}\text{F}]\text{MCBX}:[^{18}\text{F}]\text{CPFPX}$ , and  $[^{18}\text{F}]\text{CBX}:[^{18}\text{F}]\text{MCBX}$  were as follows:  $2.6 \pm 0.12$ ,  $0.82 \pm 0.019$  and  $3.1 \pm 0.15$ . *In vitro*  $t_{1/2}$  ratios deviated between 19 and 71% from inverse CL ratios. In view of the reduced complexity of the microsomal model and the multitude of physiological parameters affecting *in vivo* pharmacokinetics of a substance, these deviations can be considered as small. Free fractions of  $[^{18}\text{F}]\text{CBX}$ ,  $[^{18}\text{F}]\text{MCBX}$  and  $[^{18}\text{F}]\text{CPFPX}$  in rat plasma ranged from 0.02 to 0.04, with only  $[^{18}\text{F}]\text{MCBX}$  and  $[^{18}\text{F}]\text{CPFPX}$  being significantly different. Since the extent of plasma protein binding of the tracers was in a comparable range, this parameter is not assumed to account for substantial differences in individual pharmacokinetics. Volumes of distribution of the evaluated tracers were in the range of 190-362 ml. These values indicate similar distributions of the tracers throughout the body of the rat (namely distribution in total body water). Consequently, it seems unlikely that the individual distribution characteristics of the three compounds represent a confounding factor which may bias the results of pharmacokinetic analysis.

Visual comparison of *in vitro* and *in vivo* metabolite profiles of CBX and MCBX revealed a high degree of similarity regarding both number of metabolites and their relative abundance. Although spectroscopic identification of the metabolites could not yet be performed, the consistent chromatographic properties of metabolites generated *in vivo* and their potential counterparts formed *in vitro* suggest that *in vitro* and *in vivo* metabolite profiles of CBX and MCBX are comparable. *In vitro* and *in vivo* metabolite profiles of CPFPX differed significantly from each other. One major metabolite generated *in vivo* ( $M_{C4}$ ) did not correspond to any peak in the microsomal profile. This mismatch has already been described by Bier et al. [288], which identified the respective metabolite as

3-(3-fluoropropyl)-8-(3-oxocyclopent-1-en-1-yl)-1-propylxanthine (“enone metabolite”). In rodents, this metabolite is generated in the living animal, but not in the microsomal model. In the present work, further investigations on this phenomenon were conducted in order to permit an assessment of the suitability of the microsomal model to predict metabolic pathways *in vivo*. It could be demonstrated that *in vitro* formation of the enone metabolite proceeds via an intermediate species (most probably the corresponding alkenol) which is finally oxidised to yield the enone. This last reaction step is catalysed by human liver microsomes, but not by rodent liver microsomes. However, in the living animal, the intermediate metabolite is subjected to systemic circulation and hence exposed to a variety of enzyme systems other than hepatic P450 which might be able to oxidise the alkenol and complete the metabolic pathway (e.g. alcohol oxidoreductases or extrahepatic P450 isoforms). The observed differences between *in vitro* and *in vivo* metabolite profiles of CPF PX in rodents might therefore be an indicator for the intrinsic limitations of the microsomal model rather than for the insufficient validity of microsomal data.

Microsomal metabolism of the test compounds varied considerably among species, both in terms of metabolic rates and metabolic pathways. Substrate depletion measured in liver microsomes of rats and mice were roughly comparable, as well as those measured in mini pig and beagle dog microsomes. In the latter, relatively large, preclinical species, *in vitro* metabolic activity was about 50% lower than in rodents. Metabolic activities observed with rhesus monkey microsomes were exceptionally high, exceeding rodent values by a factor of 10. This is particularly surprising since the constitutive hepatic expression of P450 1A2 in macaques has been questioned frequently. Human liver microsomes (HLM), on the other hand, showed conspicuously low metabolic activity towards the test substrates. For example, depletion of CPF PX in HLM was about 6 times lower than in mini pig and dog microsomes, 14 times lower than in rodent microsomes and even 150 times lower than in rhesus microsomes. The *in vitro* metabolic stability rank order of the test compounds was well conserved among non-human animal species (CBX>MCBX>CPF PX), but differed in the case of human microsomes (MCBX>CPF PX>CBX). The results of these investigations do not yet allow for a definitive conclusion on whether the deviating metabolic kinetics observed with HLM are an intrinsic property (and yet an indication of significant species differences) or an *in vitro* artefact resulting from variations in *post-mortem* tissue preparation.

Interspecies comparison of *in vitro* metabolite profiles revealed considerable qualitative differences in microsomal metabolism of the evaluate compounds. Biotransformation of CBX and MCBX led to similar metabolites in all species, but the relative importance of the individual metabolic pathways varied markedly. Regarding CPF PX, *in vitro* formation of the

enone metabolite in non-human animals was of special interest. In beagle dog microsomes, one metabolite was generated which exhibited an identical retention time as the enone reference standard. Although the definitive identification of the chemical structure has not been accomplished yet, initial mass spectrometric analyses supported the assumption that this metabolite represents the enone species. In summary, none of the investigated animal species could accurately predict biotransformation of all three evaluated compounds. With regard to future evaluation of novel CPFPPX analogues, the beagle dog appears a promising preclinical species which could complement standard rodent studies.

The cerebral binding characteristics of the novel cyclobutyl-substituted  $A_1AR$  ligands [ $^{18}F$ ]CBX and [ $^{18}F$ ]MCBX were evaluated in the rat model by means of *in vitro* autoradiography and *in vivo* PET and compared with the corresponding data of [ $^{18}F$ ]CPFPPX. Autoradiographic images demonstrated identical binding patterns of the three tracers in rat brain. Highest accumulation of radioactivity was observed in brain regions generally associated with high  $A_1AR$  density such as hippocampus, thalamus, neocortex and cerebellar cortex. For all tracers, the fraction of non-specific binding to brain tissue amounted to less than 2%. Dynamic brain PET studies revealed substantial differences in cerebral kinetics of [ $^{18}F$ ]CBX, [ $^{18}F$ ]MCBX and [ $^{18}F$ ]CPFPPX. Whole brain SUV curves of [ $^{18}F$ ]MCBX peaked much earlier and dropped more steeply than SUV curves of [ $^{18}F$ ]CPFPPX, although peak SUV values of both tracers were comparable. Compartmental data analysis substantiated the assumption that this behaviour might be a consequence of similar brain uptake but faster transfer kinetics of [ $^{18}F$ ]MCBX as compared to [ $^{18}F$ ]CPFPPX, resulting from the slightly higher lipophilicity and lower  $A_1AR$  affinity of [ $^{18}F$ ]MCBX. With [ $^{18}F$ ]CBX, on the other hand, virtually no brain uptake could be observed (tissue to plasma SUV ratio < 1). A closer analysis of the cerebral kinetics of [ $^{18}F$ ]CBX suggested that these deviating kinetics might be attributable to the combined effect of the lower affinity of [ $^{18}F$ ]CBX (as compared to [ $^{18}F$ ]CPFPPX) and insufficient brain entry. The latter effect is of particular interest with regard to the design of novel xanthine-based  $A_1AR$  tracers. Although the exact mechanism underlying this phenomenon has not yet been completely elucidated, the results of the present work suggest that poor brain entry of [ $^{18}F$ ]CBX might be a consequence of both hampered diffusion through the BBB arising from lower lipophilicity and active efflux transport. Further investigations should be conducted in order to assess the impact of the specific molecular structure of xanthine-derived  $A_1AR$  ligands on brain penetration which might reveal new strategies for radiotracer optimisation.

In conclusion, the results of the present work indicate that metabolism data obtained from liver microsomal assays are a suitable tool for predicting both qualitative and quantitative

aspects of *in vivo* radiotracer metabolism. Despite the discrepancy between radiotracer concentrations occurring *in vitro* and *in vivo* and the intrinsic limitations of the simple microsomal model system, a reasonable degree of predictive accuracy can be achieved if several points are considered. First, on the basis of the molecular structure of the candidate compound, it should be estimated whether direct renal/biliary excretion or metabolism via non-P450 enzymes are likely to occur which may reduce the significance of *in vitro* metabolism data. Second, microsomal assay conditions should be carefully evaluated and adjusted to produce physiologically relevant results. Third, the approach of relative comparison (comparison of ratios) might offer advantages in terms of simplicity and robustness and could therefore represent an alternative to classical *in vitro-in vivo* extrapolation methods if suitable reference compounds are available for the respective substance class. Fourth, combined *in vitro* studies using liver microsomes of several different species might help to elucidate potential metabolic pathways of the candidate radiotracer.

This work demonstrated the application potential of hepatic microsomes in PET radiotracer development. The data encourage the implementation of microsomal assays as an integral part of preclinical evaluation of novel PET radiotracers and suggest additional studies on the ability of human liver microsomes to *a priori* predict human radiotracer metabolism.

## 6 References

- [1] James, M.L.; Gambhir, S.S. A Molecular Imaging Primer: Modalities, Imaging Agents, and Applications. *Physiological Reviews*, **2012**, *92*(2), 897–965.
- [2] Kemp, R.A. de; Epstein, F.H.; Catana, C.; Tsui, B.M.W.; Ritman, E.L. Small-Animal Molecular Imaging Methods. *Journal of Nuclear Medicine*, **2010**, *51*(Suppl 1), 18S–32S.
- [3] Kuchmiy, A.A.; Efimov, G.A.; Nedospasov, S.A. Methods for *in vivo* molecular imaging. *Biochemistry Moscow*, **2012**, *77*(12), 1339–1353.
- [4] Massoud, T.F.; Gambhir, S.S. Molecular imaging in living subjects: seeing fundamental biological processes in a new light. *Genes & Development*, **2003**, *17*(5), 545–580.
- [5] Levin, C.S. Primer on molecular imaging technology. *European Journal of Nuclear Medicine and Molecular Imaging*, **2005**, *32*(Suppl 2), S325–S345.
- [6] Pysz, M.A.; Gambhir, S.S.; Willmann, J.K. Molecular imaging: current status and emerging strategies. *Clinical Radiology*, **2010**, *65*(7), 500–516.
- [7] Weissleder, R.; Mahmood, U. Molecular imaging. *Radiology*, **2001**, *219*(2), 316–333.
- [8] Rudin, M.; Weissleder, R. Molecular imaging in drug discovery and development. *Nature Reviews Drug Discovery*, **2003**, *2*(2), 123–131.
- [9] Cassidy, P.J.; Radda, G.K. Molecular imaging perspectives. *Journal of The Royal Society Interface*, **2005**, *2*(3), 133–144.
- [10] Herzog, H. *In vivo* functional imaging with SPECT and PET. *Radiochimica Acta*, **2001**, *89*(4-5), 203–214.
- [11] Bailey, D.L.; Willowson, K.P. Quantitative SPECT/CT: SPECT joins PET as a quantitative imaging modality. *European Journal of Nuclear Medicine and Molecular Imaging*, **2014**, *41*(Suppl 1), S17–S25.
- [12] Aboagye, E.O.; Price, P.M.; Jones, T. *In vivo* pharmacokinetics and pharmacodynamics in drug development using positron-emission tomography. *Drug Discovery Today*, **2001**, *6*(6), 293–302.
- [13] Gambhir, S.S. Molecular imaging of cancer with positron emission tomography. *Nature Reviews Cancer*, **2002**, *2*(9), 683–693.
- [14] Gupta, N.; Price, P.M.; Aboagye, E.O. PET for *in vivo* pharmacokinetic and pharmacodynamic measurements. *European Journal of Cancer*, **2002**, *38*(16), 2094–2107.
- [15] Jacobs, A.H.; Li, H.; Winkeler, A.; Hilker, R.; Knoess, C.; Rüger, A.; Galldiks, N.; Schaller, B.; Sobesky, J.; Kracht, L.; Monfared, P.; Klein, M.; Vollmar, S.; Bauer, B.; Wagner, R.; Graf, R.; Wienhard, K.; Herholz, K.; Heiss, W.D. PET-based molecular imaging in neuroscience. *European Journal of Nuclear Medicine and Molecular Imaging*, **2003**, *30*(7), 1051–1065.

- [16] Klimas, M.T. Positron emission tomography and drug discovery: contributions to the understanding of pharmacokinetics, mechanism of action and disease state characterization. *Molecular Imaging and Biology*, **2002**, 4(5), 311–337.
- [17] Lee, C.-M.; Farde, L. Using positron emission tomography to facilitate CNS drug development. *Trends in Pharmacological Sciences*, **2006**, 27(6), 310–316.
- [18] Schnöckel, U.; Hermann, S.; Stegger, L.; Law, M.; Kuhlmann, M.; Schober, O.; Schäfers, K.; Schäfers, M. Small-animal PET: A promising, non-invasive tool in pre-clinical research. *European Journal of Pharmaceutics and Biopharmaceutics*, **2010**, 74(1), 50–54.
- [19] Matthews, P.M.; Rabiner, E.A.; Passchier, J.; Gunn, R.N. Positron emission tomography molecular imaging for drug development. *British Journal of Clinical Pharmacology*, **2012**, 73(2), 175–186.
- [20] Nasrallah, I.; Dubroff, J. An Overview of PET Neuroimaging. *Seminars in Nuclear Medicine*, **2013**, 43(6), 449–461.
- [21] Virdee, K.; Cumming, P.; Caprioli, D.; Jupp, B.; Rominger, A.; Aigbirhio, F.I.; Fryer, T.D.; Riss, P.J.; Dalley, J.W. Applications of positron emission tomography in animal models of neurological and neuropsychiatric disorders. *Neuroscience & Biobehavioral Reviews*, **2012**, 36(4), 1188–1216.
- [22] Wagner, C.C.; Langer, O. Approaches using molecular imaging technology — use of PET in clinical microdose studies. *Advanced Drug Delivery Reviews*, **2011**, 63(7), 539–546.
- [23] Li, Z.; Conti, P.S. Radiopharmaceutical chemistry for positron emission tomography. *Advanced Drug Delivery Reviews*, **2010**, 62(11), 1031–1051.
- [24] Meikle, S.R.; Badawi, R.D. Quantitative Techniques in PET. In: *Positron Emission Tomography*. Bailey, D.L., Townsend, D.W., Valk, P.E., Maisey, M.N., Eds.; Springer-Verlag: London, **2005**; pp. 93–126.
- [25] Moses, W.W. Fundamental limits of spatial resolution in PET. *Nuclear Instruments and Methods in Physics Research Section A: Accelerators, Spectrometers, Detectors and Associated Equipment*, **2011**, 648(Suppl 1), S236-S240.
- [26] Partridge, M.; Spinelli, A.; Ryder, W.; Hindorf, C. The effect of  $\beta^+$  energy on performance of a small animal PET camera. *Nuclear Instruments and Methods in Physics Research Section A: Accelerators, Spectrometers, Detectors and Associated Equipment*, **2006**, 568(2), 933–936.
- [27] Bailey, D.L.; Karp, J.S.; Surti, S. Physics and Instrumentation in PET. In: *Positron Emission Tomography*. Bailey, D.L., Townsend, D.W., Valk, P.E., Maisey, M.N., Eds.; Springer-Verlag: London, **2005**; pp. 13–39.
- [28] Rahmim, A.; Zaidi, H. PET versus SPECT: strengths, limitations and challenges. *Nuclear medicine communications*, **2008**, 29(3), 193–207.
- [29] Coenen, H.H. Fluorine-18 Labeling Methods: Features and Possibilities of Basic Reactions. In: *PET Chemistry*. Schubiger, P.A., Lehmann, L., Friebe, M., Eds.; Springer Berlin Heidelberg, **2007**; Vol. 64; pp. 15–50.

- [30] Serdons, K.; Verbruggen, A.; Bormans, G.M. Developing new molecular imaging probes for PET. *Methods*, **2009**, *48*(2), 104–111.
- [31] Coenen, H.H. Radiopharmazeutische Chemie: Grundlagen zur in vivo Untersuchung molekularer Vorgänge mit PET. *Der Nuklearmediziner*, **1994**, *17*, 203–214.
- [32] Zhang, Y.; Hong, H.; Cai, W. PET Tracers Based on Zirconium-89. *Current radiopharmaceuticals*, **2011**, *4*(2), 131–139.
- [33] Shiue, C.Y.; Salvadori, P.A.; Wolf, A.P.; Fowler, J.S.; MacGregor, R.R. A New Improved Synthesis of 2-Deoxy-2-[<sup>18</sup>F]Fluoro-D-Glucose from <sup>18</sup>F-Labeled Acetyl Hypofluorite. *The Journal of Nuclear Medicine*, **1982**, *23*(10), 899–903.
- [34] Chaly, T.; Diksic, M. High Yield Synthesis of 6-[<sup>18</sup>F]Fluoro-L-Dopa by Regioselective Fluorination of Protected L-Dopa with [<sup>18</sup>F]Acetylhypofluorite. *The Journal of Nuclear Medicine*, **1986**, *27*(12), 1896–1901.
- [35] Chirakal, R.; Firnau, G.; Schrobilgen, G.J.; McKay, J.; Garnett, E.S. The Synthesis of [<sup>18</sup>F]Xenon Difluoride from [<sup>18</sup>F]Fluoride Gas. *The International Journal of Applied Radiation and Isotopes*, **1984**, *35*(5), 401–404.
- [36] Sood, S.; Firnau, G.; Garnett, E.S. Radiofluorination with Xenon Difluoride: A New High Yield Synthesis of [<sup>18</sup>F]2-Fluoro-2-deoxy-D-glucose. *The International Journal of Applied Radiation and Isotopes*, **1983**, *34*(4), 743–745.
- [37] Satyamurthy, N.; Bida, G.T.; Phelps, M.E.; Barrio, J.R. N-[<sup>18</sup>F]Fluoro-N-alkylsulfonamides: Novel Reagents for Mild and Regioselective Radiofluorination. *International Journal of Radiation Applications and Instrumentation. Part A. Applied Radiation and Isotopes*, **1990**, *41*(8), 733–738.
- [38] Qaim, S.M.; Clark, J.C.; Crouzel, C.; Guillaume, M.; Helmeke, H.J.; Nebeling, B.; Pike, V.W.; Stöcklin, G. PET Radionuclide Production. In: *Radiopharmaceuticals for Positron Emission Tomography*. Stöcklin, G., Pike, V.W., Eds.; Springer Netherlands: Dordrecht, **1993**; pp. 1–43.
- [39] Guillaume, M.; Luxen, A.; Nebeling, B.; Argentini, M.; Clark, J.C.; Pike, V.W. Recommendations for Fluorine-18 Production. *International Journal of Radiation Applications and Instrumentation. Part A. Applied Radiation and Isotopes*, **1991**, *42*(8), 749–762.
- [40] Luxen, A.; Guillaume, M.; Melega, W.P.; Pike, V.W.; Solin, O.; Wagner, R. Production of 6-[<sup>18</sup>F]Fluoro-L-DOPA and its Metabolism *In Vivo*—a Critical Review. *International Journal of Radiation Applications and Instrumentation. Part B. Nuclear Medicine and Biology*, **1992**, *19*(2), 149–158.
- [41] Namavari, M.; Bishop, A.; Satyamurthy, N.; Bida, G.; Barrio, J.R. Regioselective Radiofluorodestannylation with [<sup>18</sup>F]F<sub>2</sub> and [<sup>18</sup>F]CH<sub>3</sub>COOF: a High Yield Synthesis of 6-[<sup>18</sup>F]Fluoro-L-dopa. *International Journal of Radiation Applications and Instrumentation. Part A. Applied Radiation and Isotopes*, **1992**, *43*(8), 989–996.
- [42] Hamacher, K.; Coenen, H.H.; Stöcklin, G. Efficient Stereospecific Synthesis of No-Carrier-Added 2-[<sup>18</sup>F]-Fluoro-2-Deoxy-D-Glucose Using Aminopolyether Supported Nucleophilic Substitution. *The Journal of Nuclear Medicine*, **1986**, *27*(2), 235–238.

- [43] Coenen, H.H.; Klatte, B.; Knöchel, A.; Schüller, M.; Stöcklin, G. Preparation of N.C.A. [17-<sup>18</sup>F]-Fluoroheptadecanoic Acid in High Yields via Aminopolyether Supported, Nucleophilic Fluorination. *Journal of Labelled Compounds and Radiopharmaceuticals*, **1986**, *23*(5), 455–466.
- [44] Chi, D.Y.; Kilbourn, M.R.; Katzenellenbogen, J.A.; Brodack, J.W.; Welch, M.J. Synthesis of No-Carrier-Added N-([<sup>18</sup>F]Fluoroalkyl)Spiperone Derivatives. *International Journal of Radiation Applications and Instrumentation. Part A. Applied Radiation and Isotopes*, **1986**, *37*(12), 1173–1180.
- [45] Brodack, J.W.; Dence, C.S.; Kilbourn, M.R.; Welch, M.J. Robotic Production of 2-Deoxy-2-[<sup>18</sup>F]Fluoro-D-Glucose: A Routine Method of Synthesis Using Tetrabutylammonium [<sup>18</sup>F]Fluoride. *International Journal of Radiation Applications and Instrumentation. Part A, Applied Radiation and Isotopes*, **1988**, *39*(7), 699–703.
- [46] Hamacher, K.; Hirschfelder, T.; Coenen, H.H. Electrochemical cell for separation of [<sup>18</sup>F]fluoride from irradiated <sup>18</sup>O-water and subsequent no carrier added nucleophilic fluorination. *Applied Radiation and Isotopes*, **2002**, *56*(3), 519–523.
- [47] Kim, D.W.; Choe, Y.S.; Chi, D.Y. A new nucleophilic fluorine-18 labeling method for aliphatic mesylates: Reaction in ionic liquids shows tolerance for water. *Nuclear Medicine and Biology*, **2003**, *30*(4), 345–350.
- [48] Kim, H.W.; Jeong, J.M.; Lee, Y.-S.; Chi, D.Y.; Chung, K.-H.; Lee, D.S.; Chung, J.-K.; Lee, M.C. Rapid synthesis of [<sup>18</sup>F]FDG without an evaporation step using an ionic liquid. *Applied Radiation and Isotopes*, **2004**, *61*(6), 1241–1246.
- [49] Richarz, R.; Krapf, P.; Zarrad, F.; Urusova, E.A.; Neumaier, B.; Zlatopolskiy, B.D. Neither azeotropic drying, nor base nor other additives: a minimalist approach to <sup>18</sup>F-labeling. *Organic & Biomolecular Chemistry*, **2014**, *12*(40), 8094–8099.
- [50] Roß, T.L.; Ametamey, S.M. PET Chemistry: An Introduction. In: *Basic Sciences of Nuclear Medicine*. Khalil, M.M., Ed.; Springer Berlin Heidelberg: Berlin, Heidelberg, **2011**; pp. 65–101.
- [51] Füchtner, F.; Steinbach, J.; Mäding, P.; Johannsen, B. Basic Hydrolysis of 2-[<sup>18</sup>F]Fluoro-1,3,4,6-tetra-O-acetyl-D-glucose in the Preparation of 2-[<sup>18</sup>F]Fluoro-2-deoxy-D-glucose. *Applied Radiation and Isotopes*, **1996**, *47*(1), 61–66.
- [52] Dollé, F. Fluorine-18-Labelled Fluoropyridines: Advances in Radiopharmaceutical Design. *Current pharmaceutical design*, **2005**, *11*(25), 3221–3235.
- [53] Pike, V.W.; Aigbirhio, F.I. Reactions of Cyclotron-produced [<sup>18</sup>F]Fluoride with Diaryliodonium Salts—a Novel Single-step Route to No-carrier-added [<sup>18</sup>F]Fluoroarenes. *J. Journal of the Chemical Society, Chemical Communications*, **1995**, *16*(21), 2215–2216.
- [54] Ross, T.L.; Ermert, J.; Hocke, C.; Coenen, H.H. Nucleophilic <sup>18</sup>F-Fluorination of Heteroaromatic Iodonium Salts with No-Carrier-Added [<sup>18</sup>F]Fluoride. *Journal of the American Chemical Society*, **2007**, *129*(25), 8018–8025.
- [55] Zhang, M.-R.; Kumata, K.; Suzuki, K. A practical route for synthesizing a PET ligand containing [<sup>18</sup>F]fluorobenzene using reaction of diphenyliodonium salt with [<sup>18</sup>F]F<sup>-</sup>. *Tetrahedron Letters*, **2007**, *48*(49), 8632–8635.

- [56] Mu, L.; Fischer, C.R.; Holland, J.P.; Becaude, J.; Schubiger, P.A.; Schibli, R.; Ametamey, S.M.; Graham, K.; Stellfeld, T.; Dinkelborg, L.M.; Lehmann, L.  $^{18}\text{F}$ -Radiolabeling of Aromatic Compounds Using Triarylsulfonium Salts. *European Journal of Organic Chemistry*, **2012**, 2012(5), 889–892.
- [57] Sander, K.; Gendron, T.; Yiannaki, E.; Cybulska, K.; Kalber, T.L.; Lythgoe, M.F.; Årstad, E. Sulfonium Salts as Leaving Groups for Aromatic Labelling of Drug-like Small Molecules with Fluorine-18. *Scientific Reports*, **2015**, 5, 9941.
- [58] Lee, E.; Kamlet, A.S.; Powers, D.C.; Neumann, C.N.; Boursalian, G.B.; Furuya, T.; Choi, D.C.; Hooker, J.M.; Ritter, T. A Fluoride-Derived Electrophilic Late-Stage Fluorination Reagent for PET Imaging. *Science*, **2011**, 334(6056), 639–642.
- [59] Gouverneur, V. Radiochemistry: Flipping fluoride's reactivity. *Nature Chemistry*, **2012**, 4(3), 152–154.
- [60] Preshlock, S.; Tredwell, M.; Gouverneur, V.  $^{18}\text{F}$ -Labeling of Arenes and Heteroarenes for Applications in Positron Emission Tomography. *Chemical Reviews*, **2016**, 116(2), 719–766.
- [61] Tredwell, M.; Gouverneur, V.  $^{18}\text{F}$  Labeling of Arenes. *Angewandte Chemie Internationale Edition*, **2012**, 51(46), 11426–11437.
- [62] Coenen, H.H.; Ermert, J. Direct Nucleophilic  $^{18}\text{F}$ -Fluorination of Electron Rich Arenes: Present Limits of No-Carrier-Added Reactions. *Current Radiopharmaceuticals*, **2010**, 3(3), 163–173.
- [63] Wilson, A.A.; Dannals, R.F.; Ravert, H.T.; Wagner, H.N. Reductive Amination of [ $^{18}\text{F}$ ]Fluorobenzaldehydes: Radiosyntheses of [2- $^{18}\text{F}$ ]- and [4- $^{18}\text{F}$ ]Fluorodexetimides. *Journal of Labelled Compounds and Radiopharmaceuticals*, **1990**, 28(10), 1189–1199.
- [64] Mäding, P.; Füchtner, F.; Johannsen, B.; Steinbach, J.; Hilger, C.S.; Friebe, M.; Halks-Miller, M.; Horuk, R.; Mohan, R.  $^{18}\text{F}$ -labelling of a potent nonpeptide CCR1 antagonist: synthesis of 1-(5-chloro-2-{2-[(2R)-4-(4-[ $^{18}\text{F}$ ]fluorobenzyl)-2-methylpiperazin-1-yl]-2-oxoethoxy}phenyl)urea in an automated module. *Journal of Labelled Compounds and Radiopharmaceuticals*, **2006**, 49(3), 253–262.
- [65] Li, L.; Hopkinson, M.N.; Yona, R.L.; Bejot, R.; Gee, A.D.; Gouverneur, V. Convergent  $^{18}\text{F}$  radiosynthesis: A new dimension for radiolabelling. *Chemical Science*, **2011**, 2(1), 123–131.
- [66] Olma, S.; Ermert, J.; Coenen, H.H. 4-[ $^{18}\text{F}$ ]fluorophenyl ureas via carbamate-4-nitrophenyl esters and 4-[ $^{18}\text{F}$ ]fluoroaniline. *Journal of Labelled Compounds and Radiopharmaceuticals*, **2006**, 49(12), 1037–1050.
- [67] Collins, M.; Lasne, M.-C.; Barré, L. Rapid Synthesis of  $N,N'$ -Disubstituted Piperazines. Application to the Preparation of No Carrier Added 1-(4-[ $^{18}\text{F}$ ]Fluorophenyl)piperazine and of an [ $^{18}\text{F}$ ]-Selective Ligand of Serotonergic Receptors (5HT<sub>2</sub> antagonist). *Journal of the Chemical Society, Perkin Transactions 1*, **1992**, 43(23), 3185–3188.
- [68] Koslowsky, I.; Mercer, J.; Wuest, F. Synthesis and application of 4-[ $^{18}\text{F}$ ]fluorobenzylamine: A versatile building block for the preparation of PET radiotracers. *Organic & Biomolecular Chemistry*, **2010**, 8(20), 4730–4735.

- [69] Way, J.; Wuest, F. Fully automated synthesis of 4-[<sup>18</sup>F]fluorobenzylamine based on borohydride/NiCl<sub>2</sub> reduction. *Nuclear Medicine and Biology*, **2013**, *40*(3), 430–436.
- [70] Wüst, F.R.; Kniess, T. Synthesis of 4-[<sup>18</sup>F]fluoroiodobenzene and its application in sonogashira cross-coupling reactions. *Journal of Labelled Compounds and Radiopharmaceuticals*, **2003**, *46*(8), 699–713.
- [71] Wüst, F.R.; Kniess, T. No-carrier added synthesis of <sup>18</sup>F-labelled nucleosides using Stille cross-coupling reactions with 4-[<sup>18</sup>F]fluoroiodobenzene. *Journal of Labelled Compounds and Radiopharmaceuticals*, **2004**, *47*(8), 457–468.
- [72] Way, J.D.; Bergman, C.; Wuest, F. Sonogashira cross-coupling reaction with 4-[<sup>18</sup>F]fluoroiodobenzene for rapid <sup>18</sup>F-labelling of peptides. *Chemical Communications*, **2015**, *51*(18), 3838–3841.
- [73] Ermert, J.; Hocke, C.; Ludwig, T.; Gail, R.; Coenen, H.H. Comparison of pathways to the versatile synthon of no-carrier-added 1-bromo-4-[<sup>18</sup>F]fluorobenzene. *Journal of Labelled Compounds and Radiopharmaceuticals*, **2004**, *47*(7), 429–441.
- [74] Ermert, J.; Ludwig, T.; Gail, R.; Coenen, H.H. [<sup>18</sup>F]Fluorophenyl organometallics as intermediates of no-carrier-added <sup>18</sup>F-fluoroarylation reactions. *Journal of Organometallic Chemistry*, **2007**, *692*(19), 4084–4092.
- [75] Forngren, T.; Andersson, Y.; Lamm, B.; Långström, B. Synthesis of [4-<sup>18</sup>F]-1-Bromo-4-fluorobenzene and its Use in Palladium-Promoted Cross-Coupling Reactions with Organostannanes. *Acta Chemica Scandinavica*, **1998**, *52*, 475–479.
- [76] Ekaeva, I.; Barre, L.; Lasne, M.-C.; Gourand, F. 2- and 4-[<sup>18</sup>F]Fluorophenols from Baeyer-Villiger Oxidation of [<sup>18</sup>F]Fluorophenylketones and [<sup>18</sup>F]Fluorobenzaldehydes. *Applied Radiation and Isotopes*, **1995**, *46*(8), 777–782.
- [77] Ludwig, T.; Ermert, J.; Coenen, H.H. 4-[<sup>18</sup>F]Fluoroarylalkylethers via an improved synthesis of n.c.a. 4-[<sup>18</sup>F]fluorophenol. *Nuclear Medicine and Biology*, **2002**, *29*(2), 255–262.
- [78] Stoll, T.; Ermert, J.; Oya, S.; Kung, H.F.; Coenen, H.H. Application of n.c.a. 4-[<sup>18</sup>F]fluorophenol in diaryl ether syntheses of 2-(4-[<sup>18</sup>F]fluorophenoxy)-benzylamines. *Journal of Labelled Compounds and Radiopharmaceuticals*, **2004**, *47*(7), 443–455.
- [79] Ross, T.L.; Ermert, J.; Coenen, H.H. Synthesis of No-Carrier-Added 4-[<sup>18</sup>F]Fluorophenol from 4-Benzyloxyphenyl-(2-thienyl)iodonium Bromide. *Molecules*, **2011**, *16*(12), 7621–7626.
- [80] Vaidyanathan, G.; Zalutsky, M.R. Labeling proteins with fluorine-18 using *N*-succinimidyl 4-[<sup>18</sup>F]fluorobenzoate. *International journal of radiation applications and instrumentation. Part B, Nuclear medicine and biology*, **1992**, *19*(3), 275–281.
- [81] Vaidyanathan, G.; Zalutsky, M.R. Synthesis of *N*-succinimidyl 4-[<sup>18</sup>F]fluorobenzoate, an agent for labeling proteins and peptides with <sup>18</sup>F. *Nature protocols*, **2006**, *1*(4), 1655–1661.

- [82] Tang, G.; Zeng, W.; Yu, M.; Kabalka, G. Facile synthesis of *N*-succinimidyl 4-<sup>18</sup>F-fluorobenzoate ([<sup>18</sup>F]SFB) for protein labeling. *Journal of Labelled Compounds and Radiopharmaceuticals*, **2008**, *51*(1), 68–71.
- [83] Jahan, M.; Nag, S.; Krasikova, R.; Weber, U.; Muhs, A.; Pfeifer, A.; Spenger, C.; Willbold, D.; Gulyás, B.; Halldin, C. Fluorine-18 labeling of three novel D-peptides by conjugation with *N*-succinimidyl-4-<sup>18</sup>F-fluorobenzoate and preliminary examination by postmortem whole-hemisphere human brain autoradiography. *Nuclear Medicine and Biology*, **2012**, *39*(3), 315–323.
- [84] Mäding, P.; Füchtner, F.; Wüst, F. Module-assisted synthesis of the bifunctional labelling agent *N*-succinimidyl 4-<sup>18</sup>F-fluorobenzoate ([<sup>18</sup>F]SFB). *Applied Radiation and Isotopes*, **2005**, *63*(3), 329–332.
- [85] Johnström, P.; Clark, J.C.; Pickard, J.D.; Davenport, A.P. Automated synthesis of the generic peptide labelling agent *N*-succinimidyl 4-<sup>18</sup>F-fluorobenzoate and application to <sup>18</sup>F-label the vasoactive transmitter urotensin-II as a ligand for positron emission tomography. *Nuclear Medicine and Biology*, **2008**, *35*(6), 725–731.
- [86] Sutcliffe-Goulden, J.L.; O'Doherty, M.J.; Bansal, S.S. Solid Phase Synthesis of [<sup>18</sup>F]Labelled Peptides for Positron Emission Tomography. *Bioorganic & Medicinal Chemistry Letters*, **2000**, *10*(14), 1501–1503.
- [87] Sutcliffe-Goulden, J.L.; O'Doherty, M.J.; Marsden, P.K.; Hart, I.R.; Marshall, J.F.; Bansal, S.S. Rapid solid phase synthesis and biodistribution of <sup>18</sup>F-labelled linear peptides. *European Journal of Nuclear Medicine*, **2002**, *29*(6), 754–759.
- [88] Marik, J.; Sutcliffe, J.L. Fully automated preparation of n.c.a. 4-<sup>18</sup>F-fluorobenzoic acid and *N*-succinimidyl 4-<sup>18</sup>F-fluorobenzoate using a Siemens/CTI chemistry process control unit (CPCU). *Applied Radiation and Isotopes*, **2007**, *65*(2), 199–203.
- [89] Berndt, M.; Pietzsch, J.; Wuest, F. Labeling of low-density lipoproteins using the <sup>18</sup>F-labeled thiol-reactive reagent *N*-[6-(4-<sup>18</sup>F-fluorobenzylidene)aminoxyhexyl]-maleimide. *Nuclear Medicine and Biology*, **2007**, *34*(1), 5–15.
- [90] Kniess, T.; Kuchar, M.; Pietzsch, J. Automated radiosynthesis of the thiol-reactive labeling agent *N*-[6-(4-<sup>18</sup>F-fluorobenzylidene)aminoxyhexyl]maleimide ([<sup>18</sup>F]FBAM). *Applied Radiation and Isotopes*, **2011**, *69*(9), 1226–1230.
- [91] Cai, W.; Zhang, X.; Wu, Y.; Chen, X. A Thiol-Reactive <sup>18</sup>F-Labeling Agent, *N*-[2-(4-<sup>18</sup>F-Fluorobenzamido)ethyl]maleimide, and Synthesis of RGD Peptide-Based Tracer for PET Imaging of  $\alpha_v\beta_3$  Integrin Expression. *The Journal of Nuclear Medicine*, **2006**, *47*(7), 1172–1180.
- [92] Kiesewetter, D.O.; Jacobson, O.; Lang, L.; Chen, X. Automated radiochemical synthesis of [<sup>18</sup>F]FBEM: A thiol reactive synthon for radiofluorination of peptides and proteins. *Applied Radiation and Isotopes*, **2011**, *69*(2), 410–414.
- [93] Ermert, J. <sup>18</sup>F-Labelled Intermediates for Radiosynthesis by Modular Build-Up Reactions: Newer Developments. *BioMed Research International*, **2014**, *2014*, Article ID 812973, 1–15.
- [94] Wuest, F. Fluorine-18 Labeling of Small Molecules: The Use of <sup>18</sup>F-Labeled Aryl Fluorides Derived from No-Carrier-Added [<sup>18</sup>F]Fluoride as Labeling Precursors. In:

- PET Chemistry*. Schubiger, P.A., Lehmann, L., Friebe, M., Eds.; Springer Berlin Heidelberg, **2007**; Vol. 64; pp. 51–78.
- [95] Richter, S.; Wuest, F.  $^{18}\text{F}$ -Labeled Peptides: The Future Is Bright. *Molecules*, **2014**, *19*(12), 20536–20556.
- [96] Wuest, F. Aspects of positron emission tomography radiochemistry as relevant for food chemistry. *Amino Acids*, **2005**, *29*(4), 323–339.
- [97] Wu, Z.; Kandeel, F.  $^{18}\text{F}$ -Labeled Proteins. *Current Pharmaceutical Biotechnology*, **2010**, *11*(6), 572–580.
- [98] Olberg, D.E.; Hjelstuen, O.K. Labeling Strategies of Peptides with  $^{18}\text{F}$  for Positron Emission Tomography. *Current Topics in Medicinal Chemistry*, **2010**, *10*(16), 1669–1679.
- [99] Wester, H.J.; Schottelius, M. Fluorine-18 Labeling of Peptides and Proteins. In: *PET Chemistry*. Schubiger, P.A., Lehmann, L., Friebe, M., Eds.; Springer Berlin Heidelberg, **2007**; Vol. 64; pp. 79–111.
- [100] Van de Bittner, G.C.; Ricq, E.L.; Hooker, J.M. A Philosophy for CNS Radiotracer Design. *Accounts of chemical research*, **2014**, *47*(10), 3127–3134.
- [101] Wong, D.F.; Gründer, G.; Brašić, J.R. Brain imaging research: Does the science serve clinical practice? *International Review of Psychiatry*, **2007**, *19*(5), 541–558.
- [102] Ametamey, S.M.; Schubinger, P.A. PET radiopharmaceuticals for neuroreceptor imaging. *Nuclear Science and Techniques*, **2006**, *17*(3), 143–147.
- [103] Heiss, W.-D.; Herholz, K. Brain Receptor Imaging. *The Journal of Nuclear Medicine*, **2006**, *47*(2), 302–312.
- [104] Burns, H.D.; Hamill, T.G.; Eng, W.-s.; Francis, B.; Fioravanti, C.; Gibson, R.E. Positron emission tomography neuroreceptor imaging as a tool in drug discovery, research and development. *Current Opinion in Chemical Biology*, **1999**, *3*(4), 388–394.
- [105] Savitz, J.B.; Drevets, W.C. Neuroreceptor imaging in depression. *Neurobiology of Disease*, **2013**, *52*, 49–65.
- [106] Kilbourn, M.R. *In Vivo* Radiotracers for Vesicular Neurotransmitter Transporters. *Nuclear Medicine & Biology*, **1997**, *24*(7), 615–619.
- [107] Brooks, D.J. Molecular imaging of dopamine transporters. *Ageing Research Reviews*, **2016**, *30*, 114–121.
- [108] Schou, M.; Pike, V.W.; Halldin, C. Development of Radioligands for Imaging of Brain Norepinephrine Transporters *In Vivo* with Positron Emission Tomography. *Current Topics in Medicinal Chemistry*, **2007**, *7*(18), 1806–1816.
- [109] Wang, C.; Schroeder, F.A.; Hooker, J.M. Visualizing Epigenetics: Current Advances and Advantages in HDAC PET Imaging Techniques. *Neuroscience*, **2014**, *264*, 186–197.
- [110] Seo, Y.J.; Muench, L.; Reid, A.; Chen, J.; Kang, Y.; Hooker, J.M.; Volkow, N.D.; Fowler, J.S.; Kim, S.W. Radionuclide labeling and evaluation of candidate radioligands for PET imaging of histone deacetylase in the brain. *Bioorganic & Medicinal Chemistry Letters*, **2013**, *23*(24), 6700–6705.

- [111] Yeh, H.-H.; Tian, M.; Hinz, R.; Young, D.; Shavrin, A.; Mukhapadhyay, U.; Flores, L.G.; Balatoni, J.; Soghomonyan, S.; Jeong, H.J.; Pal, A.; Uthamanthil, R.; Jackson, J.N.; Nishii, R.; Mizuma, H.; Onoe, H.; Kagawa, S.; Higashi, T.; Fukumitsu, N.; Alauddin, M.; Tong, W.; Herholz, K.; Gelovani, J.G. Imaging epigenetic regulation by histone deacetylases in the brain using PET/MRI with  $^{18}\text{F}$ -FAHA. *NeuroImage*, **2013**, *64*, 630–639.
- [112] Nordberg, A. PET imaging of amyloid in Alzheimer's disease. *The Lancet Neurology*, **2004**, *3*(9), 519–527.
- [113] Ono, M. Development of Positron-Emission Tomography/Single-Photon Emission Computed Tomography Imaging Probes for *in Vivo* Detection of  $\beta$ -Amyloid Plaques in Alzheimer's Brains. *Chemical and Pharmaceutical Bulletin*, **2009**, *57*(10), 1029–1039.
- [114] Nordberg, A. Amyloid imaging in Alzheimer's disease. *Neuropsychologia*, **2008**, *46*(6), 1636–1641.
- [115] Neumaier, B.; Deisenhofer, S.; Fürst, D.; von Arnim, C.A.F.; Thees, S.; Buck, A.K.; Glatting, G.; Landwehrmeyer, G.B.; Krause, B.J.; Müller, H.D.; Sommer, C.; Reske, S.N.; Mottaghy, F.M. Radiosynthesis and evaluation of [ $^{11}\text{C}$ ]BTA-1 and [ $^{11}\text{C}$ ]3'-Me-BTA-1 as potential radiotracers for *in vivo* imaging of  $\beta$ -amyloid plaques. *Nuklearmedizin*, **2007**, *46*(6), 271–280.
- [116] Neumaier, B.; Deisenhofer, S.; Sommer, C.; Solbach, C.; Reske, S.N.; Mottaghy, F. Synthesis and evaluation of  $^{18}\text{F}$ -fluoroethylated benzothiazole derivatives for *in vivo* imaging of amyloid plaques in Alzheimer's disease. *Applied Radiation and Isotopes*, **2010**, *68*(6), 1066–1072.
- [117] McKinney, J.D.; Richard, A.; Waller, C.; Newman, M.C.; Gerberick, F. The Practice of Structure Activity Relationships (SAR) in Toxicology. *Toxicological Sciences*, **2000**, *56*(1), 8–17.
- [118] Langer, T.; Krovat, E.M. Chemical feature-based pharmacophores and virtual library screening for discovery of new leads. *Current opinion in drug discovery & development*, **2003**, *6*(3), 370–376.
- [119] Hou, T.; Xu, X. Recent Development and Application of Virtual Screening in Drug Discovery: An Overview. *Current Pharmaceutical Design*, **2004**, *10*(9), 1011–1033.
- [120] Lange, R.; ter Heine, R.; Decristoforo, C.; Peñuelas, I.; Elsinga, P.H.; van der Westerlaken, M.M.L.; Hendrikse, N.H. Untangling the web of European regulations for the preparation of unlicensed radiopharmaceuticals: a concise overview and practical guidance for a risk-based approach. *Nuclear medicine communications*, **2015**, *36*(5), 414–422.
- [121] Aerts, J.; Ballinger, J.R.; Behe, M.; Decristoforo, C.; Elsinga, P.H.; Faivre-Chauvet, A.; Mindt, T.L.; Kolenc Peitl, P.; Todde, S.C.; Kozirowski, J. Guidance on current good radiopharmacy practice for the small-scale preparation of radiopharmaceuticals using automated modules: a European perspective. *Journal of Labelled Compounds and Radiopharmaceuticals*, **2014**, *57*(10), 615–620.
- [122] Verbruggen, A.; Coenen, H.H.; Deverre, J.-R.; Guilloteau, D.; Langstrom, B.; Salvadori, P.A.; Halldin, C. Guideline to regulations for radiopharmaceuticals in early phase

- clinical trials in the EU. *European Journal of Nuclear Medicine and Molecular Imaging*, **2008**, *35*(11), 2144–2151.
- [123] De Vos, F.J.; De Decker, M.; Dierckx, R.A. The good laboratory practice and good clinical practice requirements for the production of radiopharmaceuticals in clinical research. *Nuclear medicine communications*, **2005**, *26*(7), 575–579.
- [124] Harapanhalli, R.S. Food and Drug Administration Requirements for Testing and Approval of New Radiopharmaceuticals. *Seminars in Nuclear Medicine*, **2010**, *40*(5), 364–384.
- [125] Brust, P.; van den Hoff, J.; Steinbach, J. Development of  $^{18}\text{F}$ -labeled radiotracers for neuroreceptor imaging with positron emission tomography. *Neuroscience bulletin*, **2014**, *30*(5), 777–811.
- [126] Barth, V.; Need, A. Identifying Novel Radiotracers for PET Imaging of the Brain: Application of LC-MS/MS to Tracer Identification. *ACS Chemical Neuroscience*, **2014**, *5*(12), 1148–1153.
- [127] Pike, V.W. PET radiotracers: crossing the blood–brain barrier and surviving metabolism. *Trends in Pharmacological Sciences*, **2009**, *30*(8), 431–440.
- [128] Laruelle, M.; Slifstein, M.; Huang, Y. Relationships between Radiotracer Properties and Image Quality in Molecular Imaging of the Brain with Positron Emission Tomography. *Molecular Imaging and Biology*, **2003**, *5*(6), 363–375.
- [129] Fumita, M.; Innis, R.B. *In vivo* molecular imaging: ligand development and research applications. In: *Neuropsychopharmacology - The Fifth Generation of Progress*. Davis, K.L.; Charney, D.; Coyle, J.T.; Nemeroff, C., Eds.; Lippincott Williams & Wilkins: Philadelphia, **2002**; pp. 411–425.
- [130] Innis, R.B.; Cunningham, V.J.; Delforge, J.; Fujita, M.; Gjedde, A.; Gunn, R.N.; Holden, J.; Houle, S.; Huang, S.-C.; Ichise, M.; Iida, H.; Ito, H.; Kimura, Y.; Koeppe, R.A.; Knudsen, G.M.; Knuuti, J.; Lammertsma, A.A.; Laruelle, M.; Logan, J.; Maguire, R.P.; Mintun, M.A.; Morris, E.D.; Parsey, R.; Price, J.C.; Slifstein, M.; Sossi, V.; Suhara, T.; Votaw, J.R.; Wong, D.F.; Carson, R.E. Consensus Nomenclature for *in vivo* Imaging of Reversibly Binding Radioligands. *Journal of Cerebral Blood Flow & Metabolism*, **2007**, *27*(9), 1533–1539.
- [131] Olsson, H.; Farde, L. Potentials and Pitfalls Using High Affinity Radioligands in PET and SPET Determinations on Regional Drug Induced D2 Receptor Occupancy—A Simulation Study Based on Experimental Data. *NeuroImage*, **2001**, *14*(4), 936–945.
- [132] Banks, W.A. Blood-Brain Barrier as a Regulatory Interface. *Forum of nutrition*, **2010**, *63*, 102–110.
- [133] Smith, Q.R. A Review of Blood–Brain Barrier Transport Techniques. In: *The Blood-Brain Barrier*. Nag, S., Ed.; Humana Press: New Jersey, **2003**; Vol. 89; pp. 193–208.
- [134] Serlin, Y.; Shelef, I.; Knyazer, B.; Friedman, A. Anatomy and physiology of the blood–brain barrier. *Seminars in Cell & Developmental Biology*, **2015**, *38*, 2–6.
- [135] Cardoso, F.L.; Brites, D.; Brito, M.A. Looking at the blood–brain barrier: Molecular anatomy and possible investigation approaches. *Brain Research Reviews*, **2010**, *64*(2), 328–363.

- [136] Giacomini, K.M.; Huang, S.-M.; Tweedie, D.J.; Benet, L.Z.; Brouwer, K.L.; Chu, X.; Dahlin, A.; Evers, R.; Fischer, V.; Hillgren, K.M.; Hoffmaster, K.A.; Ishikawa, T.; Keppler, D.; Kim, R.B.; Lee, C.A.; Niemi, M.; Polli, J.W.; Sugiyama, Y.; Swaan, P.W.; Ware, J.A.; Wright, S.H.; Wah Yee, S.; Zamek-Gliszczyński, M.J.; Zhang, L. Membrane transporters in drug development. *Nature Reviews Drug Discovery*, **2010**, *9*(3), 215–236.
- [137] Löscher, W.; Potschka, H. Blood-Brain Barrier Active Efflux Transporters: ATP-Binding Cassette Gene Family. *Neurotherapeutics*, **2005**, *2*(1), 86–98.
- [138] Shen, S.; Zhang, W. ABC transporters and drug efflux at the blood-brain barrier. *Reviews in the neurosciences*, **2010**, *21*(1), 29–53.
- [139] Miller, D.S. Regulation of ABC Transporters at the Blood-Brain Barrier. *Clinical Pharmacology & Therapeutics*, **2015**, *97*(4), 395–403.
- [140] Schinkel, A.H. P-Glycoprotein, a gatekeeper in the blood–brain barrier. *Advanced Drug Delivery Reviews*, **1999**, *36*(2-3), 179–194.
- [141] Demeule, M.; Régina, A.; Jodoin, J.; Laplante, A.; Dagenais, C.; Berthelet, F.; Moghrabi, A.; Béliveau, R. Drug transport to the brain: Key roles for the efflux pump P-glycoprotein in the blood–brain barrier. *Vascular Pharmacology*, **2002**, *38*(6), 339–348.
- [142] Sun, H.; Dai, H.; Shaik, N.; Elmquist, W.F. Drug efflux transporters in the CNS. *Advanced Drug Delivery Reviews*, **2003**, *55*(1), 83–105.
- [143] Pardridge, W.M. The Blood-Brain Barrier: Bottleneck in Brain Drug Development. *Neurotherapeutics*, **2005**, *2*(1), 3–14.
- [144] Seelig, A. The Role of Size and Charge for Blood–Brain Barrier Permeation of Drugs and Fatty Acids. *Journal of Molecular Neuroscience*, **2007**, *33*(1), 32–41.
- [145] Pajouhesh, H.; Lenz, G.R. Medicinal Chemical Properties of Successful Central Nervous System Drugs. *Neurotherapeutics*, **2005**, *2*(4), 541–553.
- [146] Clark, D.E. *In silico* prediction of blood–brain barrier permeation. *Drug Discovery Today*, **2003**, *8*(20), 927–933.
- [147] van de Waterbeemd, H.; Camenisch, G.; Folkers, G.; Chretien, J.R.; Raevsky, O.A. Estimation of Blood-Brain Barrier Crossing of Drugs Using Molecular Size and Shape, and H-Bonding Descriptors. *Journal of Drug Targeting*, **1998**, *6*(2), 151–165.
- [148] Pardridge, W.M. CNS Drug Design Based on Principles of Blood-Brain Barrier Transport. *Journal of Neurochemistry*, **1998**, *70*(5), 1781–1792.
- [149] Waterhouse, R. Determination of Lipophilicity and Its Use as a Predictor of Blood–Brain Barrier Penetration of Molecular Imaging Agents. *Molecular Imaging and Biology*, **2003**, *5*(6), 376–389.
- [150] Schinkel, A.H.; Jonker, J.W. Mammalian drug efflux transporters of the ATP binding cassette (ABC) family: an overview. *Advanced Drug Delivery Reviews*, **2003**, *55*(1), 3–29.
- [151] Raub, T.J. P-Glycoprotein Recognition of Substrates and Circumvention through Rational Drug Design. *Molecular Pharmaceutics*, **2006**, *3*(1), 3–25.

- [152] Price, J.C.; Lopresti, B.J.; Mason, N.S.; Holt, D.P.; Huang, Y.; Mathis, C.A. Analyses of [<sup>18</sup>F]Altanserin Bolus Injection PET Data. I: Consideration of Radiolabeled Metabolites in Baboons. *Synapse*, **2001**, *41*(1), 1–10.
- [153] Price, J.C.; Lopresti, B.J.; Meltzer, C.C.; Smith, G.S.; Mason, N.S.; Huang, Y.; Holt, D.P.; Gunn, R.N.; Mathis, C.A. Analyses of [<sup>18</sup>F]Altanserin Bolus Injection PET Data. II: Consideration of Radiolabeled Metabolites in Humans. *Synapse*, **2001**, *41*(1), 11–21.
- [154] Fujita, M.; Seibyl, J.P.; Verhoeff, N.P.; Ichise, M.; Baldwin, R.M.; Zoghbi, S.S.; Burger, C.; Staley, J.K.; Rajeevan, N.; Charney, D.S.; Innis, R.B. Kinetic and Equilibrium Analyses of [<sup>123</sup>I]Epidepride Binding to Striatal and Extrastriatal Dopamine D<sub>2</sub> receptors. *Synapse*, **1999**, *34*(4), 290–304.
- [155] Huang, Y.; Hwang, D.-R.; Narendran, R.; Sudo, Y.; Chatterjee, R.; Bae, S.-A.; Mawlawi, O.; Kegeles, L.S.; Wilson, A.A.; Kung, H.F.; Laruelle, M. Comparative Evaluation in Nonhuman Primates of Five PET Radiotracers for Imaging the Serotonin Transporters: [<sup>11</sup>C]McN 5652, [<sup>11</sup>C]ADAM, [<sup>11</sup>C]DASB, [<sup>11</sup>C]DAPA, and [<sup>11</sup>C]AFM. *Journal of Cerebral Blood Flow & Metabolism*, **2002**, *22*(11), 1377–1398.
- [156] Krishna, D.R.; Klotz, U. Extrahepatic Metabolism of Drugs in Humans. *Clinical Pharmacokinetics*, **1994**, *26*(2), 144–160.
- [157] Parkinson, A. Biotransformation of Xenobiotics. In: *Casarett and Doull's Toxicology*. Klaassen, C.D., Casarett, L.J., Doull, J., Eds., 6<sup>th</sup> ed.; McGraw-Hill: New-York, **2001**; pp. 133–224.
- [158] Lewis, D.F. On the Recognition of Mammalian Microsomal Cytochrome P450 Substrates and Their Characteristics. *Biochemical Pharmacology*, **2000**, *60*(3), 293–306.
- [159] Guengerich, F.P. Cytochrome P450 and Chemical Toxicology. *Chemical Research in Toxicology*, **2008**, *21*(1), 70–83.
- [160] Guengerich, F.P. Common and Uncommon Cytochrome P450 Reactions Related to Metabolism and Chemical Toxicity. *Chemical Research in Toxicology*, **2001**, *14*(6), 611–650.
- [161] Guengerich, F.P.; Munro, A.W. Unusual Cytochrome P450 Enzymes and Reactions. *Journal of Biological Chemistry*, **2013**, *288*(24), 17065–17073.
- [162] Paine, M.J.I.; Scrutton, N.S.; Munro, A.W.; Gutierrez, A.; Roberts, G.C.K.; Wolf, C.R. Electron Transfer Partners of Cytochrome P450. In: *Cytochrome P450*. Ortiz de Montellano, P. R., Ed.; 3<sup>rd</sup> ed.; Springer US: Boston, MA, **2005**; pp. 115–148.
- [163] Yasui, H.; Hayashi, S.; Sakurai, H. Possible Involvement of Singlet Oxygen Species as Multiple Oxidants in P450 Catalytic Reactions. *Drug Metabolism and Pharmacokinetics*, **2005**, *20*(1), 1–13.
- [164] Zangar, R.C.; Davydov, D.R.; Verma, S. Mechanisms that regulate production of reactive oxygen species by cytochrome P450. *Toxicology and Applied Pharmacology*, **2004**, *199*(3), 316–331.
- [165] Baranczewski, P.; Stańczak, A.; Sundberg, K.; Svensson, R.; Wallin, A.; Jansson, J.; Garberg, P.; Postlind, H. Introduction to *in vitro* estimation of metabolic stability and

- drug interactions of new chemical entities in drug discovery and development. *Pharmacological Reports*, **2006**, 58(4), 453–472.
- [166] Crommentuyn, K.M.L.; Schellens, J.H.M.; van den Berg, J.D.; Beijnen, J.H. In-vitro metabolism of anti-cancer drugs, methods and applications: paclitaxel, docetaxel, tamoxifen and ifosfamide. *Cancer Treatment Reviews*, **1998**, 24(5), 345–366.
- [167] Brandon, E.F.A.; Raap, C.D.; Meijerman, I.; Beijnen, J.H.; Schellens, J.H.M. An update on in vitro test methods in human hepatic drug biotransformation research: pros and cons. *Toxicology and Applied Pharmacology*, **2003**, 189(3), 233–246.
- [168] Giron, M.C.; Portolan, S.; Bin, A.; Mazzi, U.; Cutler, C.S. Cytochrome P450 and radiopharmaceutical metabolism. *The Quarterly Journal of Nuclear Medicine and Molecular Imaging*, **2008**, 52(3), 254–266.
- [169] Pelkonen, O.; Turpeinen, M. *In vitro*–*in vivo* extrapolation of hepatic clearance: Biological tools, scaling factors, model assumptions and correct concentrations. *Xenobiotica*, **2007**, 37(10-11), 1066–1089.
- [170] Hariparsad, N.; Sane, R.S.; Strom, S.C.; Desai, P.B. In vitro methods in human drug biotransformation research: Implications for cancer chemotherapy. *Toxicology in Vitro*, **2006**, 20(2), 135–153.
- [171] Jia, L.; Liu, X. The Conduct of Drug Metabolism Studies Considered Good Practice (II): *In Vitro* Experiments. *Current Drug Metabolism*, **2007**, 8(8), 822–829.
- [172] Kramer, M.A.; Tracy, T.S. Studying cytochrome P450 kinetics in drug metabolism. *Expert Opinion on Drug Metabolism & Toxicology*, **2008**, 4(5), 591–603.
- [173] Zhang, D.; Luo, G.; Ding, X.; Lu, C. Preclinical experimental models of drug metabolism and disposition in drug discovery and development. *Acta Pharmaceutica Sinica B*, **2012**, 2(6), 549–561.
- [174] Palade, G.E.; Siekevitz, P. Liver microsomes; an integrated morphological and biochemical study. *The Journal of Biophysical and Biochemical Cytology*, **1956**, 2(2), 171–200.
- [175] Guengerich, F.P. Cytochrome P450s and Other Enzymes in Drug Metabolism and Toxicity. *The AAPS Journal*, **2006**, 8(1), E101-E111.
- [176] Pearce, R.E.; McIntyre, C.J.; Madan, A.; Sanzgiri, U.; Draper, A.J.; Bullock, P.L.; Cook, D.C.; Burton, L.A.; Latham, J.; Nevins, C.; Parkinson, A. Effects of Freezing, Thawing, and Storing Human Liver Microsomes on Cytochrome P450 Activity. *Archives of Biochemistry and Biophysics*, **1996**, 331(2), 145–169.
- [177] Yamazaki, H.; Inoue, K.; Turvy, C.G.; Guengerich, F.P.; Shimada, T. Effects of Freezing, Thawing, and Storage of Human Liver Samples on the Microsomal Contents and Activities of Cytochrome P450 Enzymes. *Drug Metabolism and Disposition*, **1997**, 25(2), 168–174.
- [178] Foti, R.S.; Fisher, M.B. Impact of Incubation Conditions on Bufuralol Human Clearance Predictions: Enzyme Lability and Nonspecific Binding. *Drug Metabolism and Disposition*, **2004**, 32(3), 295–304.

- [179] Obach, R.S.; Reed-Hagen, A.E. Measurement of Michaelis Constants for Cytochrome P450-Mediated Biotransformation Reactions Using a Substrate Depletion Approach. *Drug Metabolism and Disposition*, **2002**, *30*(7), 831–837.
- [180] Nath, A.; Atkins, W.M. A Theoretical Validation of the Substrate Depletion Approach to Determining Kinetic Parameters. *Drug Metabolism and Disposition*, **2006**, *34*(9), 1433–1435.
- [181] Bisswanger, H. Enzyme assays. *Perspectives in Science*, **2014**, *1*(1-6), 41–55.
- [182] Bergström, M.; Grahnén, A.; Långström, B. Positron emission tomography microdosing: a new concept with application in tracer and early clinical drug development. *European Journal of Clinical Pharmacology*, **2003**, *59*(5-6), 357–366.
- [183] Fan, J.; de Lannoy, I.A.M. Pharmacokinetics. *Biochemical Pharmacology*, **2014**, *87*(1), 93–120.
- [184] Benedetti, M.S.; Whomsley, R.; Poggesi, I.; Cawello, W.; Mathy, F.-X.; Delporte, M.-L.; Papeleu, P.; Watelet, J.-B. Drug metabolism and pharmacokinetics. *Drug Metabolism Reviews*, **2009**, *41*(3), 344–390.
- [185] Taft, D.R. Drug Excretion. In: *Pharmacology: Principles and Practice*. Hacker, M., Messer, W., Bachmann, K., Eds.; Academic Press: San Diego, CA, **2009**; pp. 175–199.
- [186] Yamaoka, K.; Nakagawa, T.; Uno, T. Statistical Moments in Pharmacokinetics. *Journal of Pharmacokinetics and Biopharmaceutics*, **1978**, *6*(6), 547–558.
- [187] Källén, A. *Computational Pharmacokinetics*; Chapman & Hall/CRC: Boca Raton, **2008**.
- [188] Carson, R.E. Tracer Kinetic Modeling in PET. In: *Positron Emission Tomography: Basic Sciences*. Bailey, D.L., Townsend, D.W., Valk, P.E., Maisey, M.N., Eds.; Springer-Verlag: London, **2005**; pp. 127–159.
- [189] Cobelli, C.; Foster, D.; Toffolo, G. *Tracer Kinetics in Biomedical Research: From Data to Model*; Kluwer Academic: New York, **2002**.
- [190] Wylie, W.D.; Churchill-Davidson, H.C.; Healy, T. E. J.; Cohen, P.J. *Wylie Churchill-Davidson's a Practice of Anesthesia*, 7<sup>th</sup> ed.; Hodder Education: London, **2003**.
- [191] Barash, P.G. *Clinical anesthesia*, 7<sup>th</sup> ed.; Wolters Kluwer Health/Lippincott Williams & Wilkins: Philadelphia, PA, **2013**.
- [192] Kretz, F.-J. *Anästhesie und Intensivmedizin*; Springer: Berlin, **2006**.
- [193] Macheras, P.; Iliadis, A. *Modeling in Biopharmaceutics, Pharmacokinetics, and Pharmacodynamics: Homogeneous and Heterogeneous Approaches*; Springer: New York, **2006**.
- [194] Nordberg, M.; Duffus, J.; Templeton, D.M. Glossary of Terms Used in Toxicokinetics (IUPAC Recommendations 2003). *Pure and Applied Chemistry*, **2004**, *76*(5).
- [195] Fredholm, B.B.; Ijzerman, A.P.; Jacobson, K.A.; Klotz, K.-N.; Linden, J. International Union of Pharmacology. XXV. Nomenclature and Classification of Adenosine Receptors. *Pharmacological Reviews*, **2001**, *53*(4), 527–552.
- [196] Porkka-Heiskanen, T. Adenosine in sleep and wakefulness. *Annals of Medicine*, **1999**, *31*(2), 125–129.

- [197] Porkka-Heiskanen, T.; Strecker, R.E.; Thakkar, M.; Bjorkum, A.A.; Greene, R.W.; McCarley, R.W. Adenosine: A Mediator of the Sleep-Inducing Effects of Prolonged Wakefulness. *Science*, **1997**, *276*(5316), 1265–1268.
- [198] Portas, C.M.; Thakkar, M.; Rainnie, D.G.; Greene, R.W.; McCarley, R.W. Role of Adenosine in Behavioral State Modulation: A Microdialysis Study in the Freely Moving Cat. *Neuroscience*, **1997**, *79*(1), 225–235.
- [199] Elmenhorst, D.; Meyer, P.T.; Winz, O.H.; Matusch, A.; Ermert, J.; Coenen, H.H.; Basheer, R.; Haas, H.L.; Zilles, K.; Bauer, A. Sleep Deprivation Increases A<sub>1</sub> Adenosine Receptor Binding in the Human Brain: A Positron Emission Tomography Study. *The Journal of Neuroscience*, **2007**, *27*(9), 2410–2415.
- [200] Kim, Y.; Elmenhorst, D.; Weisshaupt, A.; Wedekind, F.; Kroll, T.; McCarley, R.W.; Strecker, R.E.; Bauer, A. Chronic sleep restriction induces long-lasting changes in adenosine and noradrenaline receptor density in the rat brain. *Journal of Sleep Research*, **2015**, *24*(5), 549–558.
- [201] Huang, Z.-L.; Urade, Y.; Hayaishi, O. The Role of Adenosine in the Regulation of Sleep. *Current Topics in Medicinal Chemistry*, **2011**, *11*(8), 1047–1057.
- [202] Basheer, R.; Bauer, A.; Elmenhorst, D.; Ramesh, V.; McCarley, R.W. Sleep deprivation upregulates A<sub>1</sub> adenosine receptors in the rat basal forebrain. *NeuroReport*, **2007**, *18*(18), 1895–1899.
- [203] Elmenhorst, D.; Basheer, R.; McCarley, R.W.; Bauer, A. Sleep deprivation increases A<sub>1</sub> adenosine receptor density in the rat brain. *Brain Research*, **2009**, *1258*, 53–58.
- [204] Maia, L.; de Mendonca, A. Does caffeine intake protect from Alzheimer's disease? *European Journal of Neurology*, **2002**, *9*(4), 377–382.
- [205] Rahman, A. The Role of Adenosine in Alzheimers Disease. *Current Neuropharmacology*, **2009**, *7*(3), 207–216.
- [206] Fuxe, K.; Strömberg, I.; Popoli, P.; Rimondini-Giorgini, R.; Torvinen, M.; Ogren, S.O.; Franco, R.; Agnati, L.F.; Ferré, S. Adenosine receptors and Parkinson's disease. Relevance of antagonistic adenosine and dopamine receptor interactions in the striatum. *Advances in Neurology*, **2001**, *86*, 345–353.
- [207] Cieślak, M.; Komoszyński, M.; Wojtczak, A. Adenosine A<sub>2A</sub> receptors in Parkinson's disease treatment. *Purinergic Signalling*, **2008**, *4*(4), 305–312.
- [208] Morelli, M.; Carta, A.R.; Jenner, P. Adenosine A<sub>2A</sub> Receptors and Parkinson's Disease. *Handbook of Experimental Pharmacology*, **2009**(193), 589–615.
- [209] Ferré, S. Adenosine-dopamine interactions in the ventral striatum. Implications for the treatment of schizophrenia. *Psychopharmacology*, **1997**, *133*(2), 107–120.
- [210] Dragunow, M. Adenosine: the brain's natural anticonvulsant? *Trends in Pharmacological Sciences*, **1986**, *7*, 128–130.
- [211] Ribeiro, J.A.; Sebastião, A.M.; de Mendonça, A. Adenosine receptors in the nervous system: pathophysiological implications. *Progress in Neurobiology*, **2003**, *68*(6), 377–392.

- [212] Fastbom, J.; Pazos, A.; Palacios, J. The Distribution of Adenosine A<sub>1</sub> Receptors and 5'-Nucleotidase in the Brain of Some Commonly Used Experimental Animals. *Neuroscience*, **1987**, *22*(3), 813–826.
- [213] Bauer, A.; Holschbach, M.H.; Cremer, M.; Weber, S.; Boy, C.; Shah, N.J.; Olsson, R.A.; Halling, H.; Coenen, H.H.; Zilles, K. Evaluation of <sup>18</sup>F-CPFPX, a Novel Adenosine A<sub>1</sub> Receptor Ligand: In Vitro Autoradiography and High-Resolution Small Animal PET. *The Journal of Nuclear Medicine*, **2003**, *44*(10), 1682–1689.
- [214] Daval, J.-L.; Werck, M.C.; Nehlig, A.; Pereira de Vasconcelos, A. Quantitative Autoradiographic Study of the Postnatal Development of Adenosine A<sub>1</sub> Receptors and Their Coupling to G Proteins in the Rat Brain. *Neuroscience*, **1991**, *40*(3), 841–851.
- [215] Elmenhorst, D.; Kroll, T.; Wedekind, F.; Weisshaupt, A.; Beer, S.; Bauer, A. In Vivo Kinetic and Steady-State Quantification of <sup>18</sup>F-CPFPX Binding to Rat Cerebral A<sub>1</sub> Adenosine Receptors: Validation by Displacement and Autoradiographic Experiments. *Journal of Nuclear Medicine*, **2013**, *54*(8), 1411–1419.
- [216] Goodman, R.R.; Synder, S.H. Autoradiographic Localization of Adenosine Receptors in Rat Brain Using [<sup>3</sup>H]Cyclohexyladenosine. *The Journal of Neuroscience*, **1982**, *2*(9), 1230–1241.
- [217] Weber, R.G.; Jones, C.R.; Lohse, M.J.; Palacios, J.M. Autoradiographic Visualization of A<sub>1</sub> Adenosine Receptors in Rat Brain with [<sup>3</sup>H]8-Cyclopentyl-1,3-Dipropylxanthine. *Journal of Neurochemistry*, **1990**, *54*(4), 1344–1353.
- [218] Fastbom, J.; Pazos, A.; Probst, A.; Palacios, J. Adenosine A<sub>1</sub> Receptors in the Human Brain: A Quantitative Autoradiographic Study. *Neuroscience*, **1987**, *22*(3), 827–839.
- [219] Svenningsson, P.; Hall, H.; Sedvall, G.; Fredholm, B.B. Distribution of Adenosine Receptors in the Postmortem Human Brain: An Extended Autoradiographic Study. *Synapse*, **1997**, *27*(4), 322–335.
- [220] Bauer, A.; Holschbach, M.H.; Meyer, P.T.; Boy, C.; Herzog, H.; Olsson, R.A.; Coenen, H.H.; Zilles, K. In vivo imaging of adenosine A<sub>1</sub> receptors in the human brain with [<sup>18</sup>F]CPFPX and positron emission tomography. *NeuroImage*, **2003**, *19*(4), 1760–1769.
- [221] Schwabe, U.; Trost, T. Characterization of Adenosine Receptors in Rat Brain by (-)[<sup>3</sup>H]N<sup>6</sup>-Phenylisopropyladenosine. *Naunyn-Schmiedeberg's Archives of Pharmacology*, **1980**, *313*(3), 179–187.
- [222] Williams, M.; Braunwalder, A.; Erickson, T.J. Evaluation of the binding of the A-1 selective adenosine radioligand, cyclopentyladenosine (CPA), to rat brain tissue. *Naunyn-Schmiedeberg's Archives of Pharmacology*, **1986**, *332*(2), 179–183.
- [223] Lohse, M.J.; Klotz, K.-N.; Schwabe, U.; Cristalli, G.; Vittori, S.; Grifantini, M. 2-Chloro-N<sup>6</sup>-cyclopentyladenosine: a highly selective agonist at A<sub>1</sub> adenosine receptors. *Naunyn-Schmiedeberg's Archives of Pharmacology*, **1988**, *337*(6), 687–689.
- [224] Klotz, K.-N.; Lohse, M.J.; Schwabe, U.; Cristalli, G.; Vittori, S.; Grifantini, M. 2-Chloro-N<sup>6</sup>-[<sup>3</sup>H]cyclopentyladenosine ([<sup>3</sup>H]CCPA) - a high affinity agonist radioligand for A<sub>1</sub>

- adenosine receptors. *Naunyn-Schmiedeberg's Archives of Pharmacology*, **1989**, *340*(6), 679–683.
- [225] Lohse, M.J.; Klotz, K.-N.; Lindenborn-Fotinos, J.; Reddington, M.; Schwabe, U.; Olsson, R.A. 8-Cyclopentyl-1,3-dipropylxanthine (DPCPX) - a selective high affinity antagonist radioligand for A<sub>1</sub> adenosine receptors. *Naunyn-Schmiedeberg's Archives of Pharmacology*, **1987**, *336*(2), 204–210.
- [226] Holschbach, M.H.; Olsson, R.A.; Bier, D.; Wutz, W.; Sihver, W.; Schüller, M.; Palm, B.; Coenen, H.H. Synthesis and Evaluation of No-Carrier-Added 8-Cyclopentyl-3-(3-[<sup>18</sup>F]fluoropropyl)-1-propylxanthine ([<sup>18</sup>F]CPFPX): A Potent and Selective A<sub>1</sub>-Adenosine Receptor Antagonist for in Vivo Imaging. *Journal of Medicinal Chemistry*, **2002**, *45*(23), 5150–5156.
- [227] Müller, C.E.; Jacobson, K.A. Xanthines as Adenosine Receptor Antagonists. In: *Methylxanthines*. Fredholm, B.B., Ed.; Springer Berlin Heidelberg: Berlin, Heidelberg, **2011**; pp. 151–199.
- [228] Müller, C.E.; Scior, T. Adenosine receptors and their modulators. *Pharmaceutica Acta Helveticae*, **1993**, *68*(2), 77–111.
- [229] Ralevic, V.; Burnstock, G. Receptors for Purines and Pyrimidines. *Pharmacological Reviews*, **1998**, *50*(3), 413–492.
- [230] Chang, L.C.W.; Brussee, J.; IJzerman, A.P. Non-Xanthine Antagonists for the Adenosine A<sub>1</sub> Receptor. *Chemistry & Biodiversity*, **2004**, *1*(11), 1591–1626.
- [231] Klotz, K.-N. Adenosine receptors and their ligands. *Naunyn-Schmiedeberg's Archives of Pharmacology*, **2000**, *362*(4-5), 382–391.
- [232] Shook, B.C.; Jackson, P.F. Adenosine A<sub>2A</sub> Receptor Antagonists and Parkinson's Disease. *ACS Chemical Neuroscience*, **2011**, *2*(10), 555–567.
- [233] Taylor, P.; Insel, P.A. Molecular Basis of Pharmacologic Selectivity. In: *Principles of drug action: The basis of pharmacology*. Pratt, W.B., Taylor, P., Goldstein, A., Eds., 3<sup>rd</sup> ed.; Churchill Livingstone: New York, **1990**; pp. 1-102.
- [234] Baca, Q.J.; Golan, D.E. Pharmacodynamics. In: *Principles of pharmacology: The pathophysiologic basis of drug therapy*. Golan, D.E., Ed., 3<sup>rd</sup> ed.; Lippincott Williams & Wilkins: Philadelphia, Pa, London, **2011**; pp. 17–26.
- [235] Keen, M.; MacDermot, J. Analysis of receptors by radioligand binding. In: *Receptor autoradiography: Principles and practice*. Wharton, J., Polak, J.M., Eds.; Oxford University Press: Oxford, New York, **1993**; pp. 23-55.
- [236] Cheng, Y.-C.; Prusoff, W.H. Relationship Between the Inhibition Constant ( $K_1$ ) and the Concentration of Inhibitor Which Causes 50 Per Cent Inhibition ( $I_{50}$ ) of an Enzymatic Reaction. *Biochemical Pharmacology*, **1973**, *22*(23), 3099–3108.
- [237] Vauquelin, G.; von Mentzer, B. *G protein-coupled receptors: Molecular pharmacology*; John Wiley: Chichester, **2007**.
- [238] Hulme, E.C.; Trevethick, M.A. Ligand binding assays at equilibrium: validation and interpretation. *British Journal of Pharmacology*, **2010**, *161*(6), 1219–1237.

- [239] McKinney, M.; Raddatz, R. Practical Aspects of Radioligand Binding. In: *Current Protocols in Pharmacology*. Enna, S., Williams, M., Barret, J.F., Ferkany, J.W., Kenakin, T., Porsolt, R.D., Eds.; John Wiley & Sons, Inc: Hoboken, NJ, USA, **2001**.
- [240] Maguire, J.J.; Kuc, R.E.; Davenport, A.P. Radioligand Binding Assays and Their Analysis. In: *Receptor Binding Techniques*. Davenport, A.P., Ed.; Humana Press: Totowa, NJ, **2012**; pp. 31–77.
- [241] Bylund, D.B.; Toews, M.L. Radioligand Binding Methods for Membrane Preparations and Intact Cells. In: *Receptor Signal Transduction Protocols*. Willars, G.B., Challiss, R.J., Eds.; Humana Press: Totowa, NJ, **2011**; pp. 135–164.
- [242] Morris, E.D.; Endres, C.J.; Schmidt, K.C.; Christian, B.T.; Muzic, R.F.; Fisher, R.E. Kinetic Modeling in Positron Emission Tomography. In: *Emission Tomography*; Elsevier, **2004**; pp. 499–540.
- [243] Gunn, R.N.; Gunn, S.R.; Cunningham, V.J. Positron Emission Tomography Compartmental Models. *Journal of Cerebral Blood Flow and Metabolism*, **2001**, *21*(6), 635–652.
- [244] Ichise, M.; Meyer, J.H.; Yonekura, Y. An Introduction to PET and SPECT Neuroreceptor Quantification Models. *The Journal of Nuclear Medicine*, **2001**, *42*(5), 755–763.
- [245] Laruelle, M.; Slifstein, M.; Huang, Y. Positron emission tomography: imaging and quantification of neurotransmitter availability. *Methods*, **2002**, *27*(3), 287–299.
- [246] Logan, J. Graphical Analysis of PET Data Applied to Reversible and Irreversible Tracers. *Nuclear Medicine and Biology*, **2000**, *27*(7), 661–670.
- [247] Logan, J. A review of graphical methods for tracer studies and strategies to reduce bias. *Nuclear Medicine and Biology*, **2003**, *30*(8), 833–844.
- [248] Zaidi, H.; Shidahara, M. Neuroreceptor Imaging. In: *Neural Metabolism In Vivo*. Choi, I.-Y., Gruetter, R., Eds.; Springer US: Boston, MA, **2012**; pp. 305–329.
- [249] Varga, J.; Szabo, Z. Modified Regression Model for the Logan Plot. *Journal of Cerebral Blood Flow & Metabolism*, **2002**, *22*(2), 240–244.
- [250] Kinahan, P.E.; Fletcher, J.W. Positron Emission Tomography-Computed Tomography Standardized Uptake Values in Clinical Practice and Assessing Response to Therapy. *Seminars in Ultrasound, CT and MRI*, **2010**, *31*(6), 496–505.
- [251] Katz, J.J.; Todd, M.M.; Warner, D.S. Quantitative Comparison of Cerebral Blood Volume in Rats Receiving Halothane or Isoflurane. *Anesthesiology*, **1988**, *69*(3A), A534.
- [252] Sheskin, D. *Handbook of parametric and nonparametric statistical procedures*, CRC Press: Boca Raton, Fla, **1997**.
- [253] Walpole, R.E. *Probability & statistics for engineers & scientists*, 8<sup>th</sup> ed.; Pearson Prentice Hall: Upper Saddle River, NJ, **2007**.
- [254] Snedecor, G.W.; Cochran, W.G. *Statistical methods*, 8<sup>th</sup> ed.; Iowa State University Press: Ames, **1989**.

- [255] Boslaugh, S.; Watters, P.A. *Statistics in a nutshell*, O'Reilly Media: Sebastopol, Calif, **2008**.
- [256] Tukey, J.W. Comparing Individual Means in the Analysis of Variance. *Biometrics*, **1949**, *5*(2), 99–114.
- [257] De Muth, J.E. *Basic statistics and pharmaceutical statistical applications*, 3<sup>rd</sup> ed.; CRC Press: Boca Raton, Fla, **2014**.
- [258] Domagk, G.; Chilla, R. Glucose-6-phosphate dehydrogenase from *Candida utilis*. In: *Methods in Enzymology*, Vol. 41, Carbohydrate Metabolism Part B, **1975**, pp. 205–208.
- [259] Peters, M.A.; Fouts, J.R. The Influence of Magnesium and Some Other Divalent Cations on Hepatic Microsomal Drug Metabolism *In Vitro*. *Biochemical Pharmacology*, **1970**, *19*(2), 533–544.
- [260] Good, N.E.; Izawa, S. Hydrogen ion buffers. *Methods in Enzymology*, **1972**, *24*, 53–68.
- [261] Scopes, R.K. Enzyme Activity and Assays. In: *Encyclopedia of Life Sciences*; John Wiley & Sons, Ltd: Chichester, **2002**.
- [262] Singh, S.; Anand, A.; Srivastava, P.K. Regulation and properties of glucose-6-phosphate dehydrogenase: A review. *International Journal of Plant Physiology and Biochemistry*, **2012**, *4*(1), 1-19.
- [263] Hickman, D.; Wang, J.-P.; Wang, Y.; Unadkat, J.D. Evaluation of the Selectivity of *In Vitro* Probes and Suitability of Organic Solvents for the Measurement of Human Cytochrome P450 Monooxygenase Activities. *Drug Metabolism and Disposition*, **1998**, *26*(3), 207–215.
- [264] Easterbrook, J.; Lu, C.; Sakai, Y.; Li, A.P. Effects of Organic Solvents on the Activities of Cytochrome P450 Isoforms, UDP-Dependent Glucuronyl Transferase, and Phenol Sulfotransferase in Human Hepatocytes. *Drug metabolism and disposition*, **2001**, *29*(2), 141–144.
- [265] Busby, W.F.; Ackermann, J.M.; Crespi, C.L. Effect of Methanol, Ethanol, Dimethyl Sulfoxide, and Acetonitrile on *In Vitro* Activities of cDNA-Expressed Human Cytochromes P-450. *Drug Metabolism and Disposition*, **1999**, *27*(2), 246–249.
- [266] Chauret, N.; Gauthier, A.; Nicoll-Griffith, D.A. Effect of Common Organic Solvents on *In Vitro* Cytochrome P450-Mediated Metabolic Activities in Human Liver Microsomes. *Drug metabolism and disposition*, **1998**, *26*(1), 1–4.
- [267] Nirogi, R.; Kandikere, V.; Bhyrapuneni, G.; Ponnamaneni, R.K.; Palacharla, R.c.; Manoharan, A. Effect of Dimethyl Sulfoxide on *In Vitro* Cytochrome P4501A2 Mediated Phenacetin O-Deethylation in Human Liver Microsomes. *Drug Metabolism and Disposition*, **2011**, *39*(11), 2162–2164.
- [268] Li, D.; Han, Y.; Meng, X.; Sun, X.; Yu, Q.; Li, Y.; Wan, L.; Huo, Y.; Guo, C. Effect of Regular Organic Solvents on Cytochrome P450-Mediated Metabolic Activities in Rat Liver Microsomes. *Drug Metabolism and Disposition*, **2010**, *38*(11), 1922–1925.

- [269] Kappus, H. Metabolic Reactions: Role of Cytochrome P-450 in the Formation of Reactive Oxygen Species. In: *Cytochrome P450*. Schenkman, J.B., Greim, H., Eds.; Springer Berlin Heidelberg: Berlin, Heidelberg, **1993**, pp. 145–154.
- [270] Bernhardt, R. Cytochrome P450: Structure, Function, and Generation of Reactive Oxygen Species. *Reviews of Physiology, Biochemistry and Pharmacology*, **1995**, *127*, 137–221.
- [271] Letelier, M.E.; López-Valladares, M.; Peredo-Silva, L.; Rojas-Sepúlveda, D.; Aracena, P. Microsomal oxidative damage promoted by acetaminophen metabolism. *Toxicology in Vitro*, **2011**, *25*(7), 1310–1313.
- [272] Dubin, M.; Fernandez Villamil, S.H.; Paulino de Blumenfeld, M; Stoppani, A.O.M. Inhibition of Microsomal Lipid Peroxidation and Cytochrome P-450-Catalyzed Reactions by Nitrofurans. *Free Radical Research Communications*, **1991**, *14*(5-6), 419–431.
- [273] Dubin, M.; Grinblat, L.; Fernandez Villamil, S.H.; Stoppani, A.O.M. Nitrofurans inhibition of microsomal lipid peroxidation. *FEBS Letters*, **1987**, *220*(1), 197–200.
- [274] Mishin, V.; Heck, D.E.; Laskin, D.L.; Laskin, J.D. Human Recombinant Cytochrome P450 Enzymes Display Distinct Hydrogen Peroxide Generating Activities During Substrate Independent NADPH Oxidase Reactions. *Toxicological Sciences*, **2014**, *141*(2), 344–352.
- [275] Karuzina, I.I.; Archakov, A.I. Hydrogen Peroxide-Mediated Inactivation of Microsomal Cytochrome P450 During Monooxygenase Reactions. *Free Radical Biology & Medicine*, **1994**, *17*(6), 557–567.
- [276] Schlezinger, J.J.; White, R.D.; Stegeman, J.J. Oxidative Inactivation of Cytochrome P-450 1A (CYP1A) Stimulated by 3,3',4,4'-Tetrachlorobiphenyl: Production of Reactive Oxygen by Vertebrate CYP1As. *Molecular Pharmacology*, **1999**, *56*(3), 588–597.
- [277] Lowry, O.H.; Passonneau, J.V.; Rock, M.K. The Stability of Pyridine Nucleotides. *The Journal of Biological Chemistry*, **1961**, *236*(10), 2756–2759.
- [278] Wu, J.T.; Wu, L.H.; Knight, J.A. Stability of NADPH: Effect of Various Factors on the Kinetics of Degradation. *Clinical chemistry*, **1986**, *32*(2), 314–319.
- [279] Wills, E.D. Lipid Peroxide Formation in Microsomes. The Role of Non-Haem Iron. *The Biochemical Journal*, **1969**, *113*(2), 325–332.
- [280] De Matteis, F.; Sparks, R.G. Iron-Dependent Loss of Liver Cytochrome P -450 Haem *In Vivo* and *In Vitro*. *FEBS Letters*, **1973**, *29*(2), 141–144.
- [281] Levin, W.; Lu, A.Y.H.; Jacobson, M.; Kuntzman, R.; Lee Poyer, J.; McCay, P.B. Lipid Peroxidation and the Degradation of Cytochrome P-450 Heme. *Archives of Biochemistry and Biophysics*, **1973**, *158*(2), 842–852.
- [282] Pederson, T.C.; Aust, S.D. The Mechanism of Liver Microsomal Lipid Peroxidation. *Biochimica et Biophysica Acta*, **1975**, *385*(2), 232–241.

- [283] Bondy, S.C.; Naderi, S. Contribution of Hepatic Cytochrome P450 Systems to the Generation of Reactive Oxygen Species. *Biochemical Pharmacology*, **1994**, *48*(1), 155–159.
- [284] Ding, Y.; Chen, Z.-J.; Liu, S.; Che, D.; Vetter, M.; Chang, C.-H. Inhibition of Nox-4 activity by plumbagin, a plant-derived bioactive naphthoquinone. *The Journal of Pharmacy and Pharmacology*, **2005**, *57*(1), 111–116.
- [285] Aldieri, E.; Riganti, C.; Polimeni, M.; Gazzano, E.; Lussiana, C.; Campia, I.; Ghigo, D. Classical Inhibitors of NOX NAD(P)H Oxidases Are Not Specific. *Current Drug Metabolism*, **2008**, *9*(8), 686–696.
- [286] Szilagy, J.T.; Mishin, V.; Heck, D.E.; Jan, Y.-H.; Aleksunes, L.M.; Richardson, J.R.; Heindel, N.D.; Laskin, D.L.; Laskin, J.D. Selective Targeting of Heme Protein in Cytochrome P450 and Nitric Oxide Synthase by Diphenyleneiodonium. *Toxicological Sciences*, **2016**, *151*(1), 150–159.
- [287] Riganti, C.; Gazzano, E.; Polimeni, M.; Costamagna, C.; Bosia, A.; Ghigo, D. Diphenyleneiodonium Inhibits the Cell Redox Metabolism and Induces Oxidative Stress. *Journal of Biological Chemistry*, **2004**, *279*(46), 47726–47731.
- [288] Bier, D.; Holschbach, M.H.; Wutz, W.; Olsson, R.A.; Coenen, H.H. Metabolism of the A<sub>1</sub> Adenosine Receptor Positron Emission Tomography Ligand [<sup>18</sup>F]8-Cyclopentyl-3-(3-Fluoropropyl)-1-Propylxanthine ([<sup>18</sup>F]CPFPX) in Rodents and Humans. *Drug Metabolism and Disposition*, **2006**, *34*(4), 570–576.
- [289] Matusch, A.; Meyer, P.T.; Bier, D.; Holschbach, M.H.; Woitalla, D.; Elmenhorst, D.; Winz, O.H.; Zilles, K.; Bauer, A. Metabolism of the A<sub>1</sub> adenosine receptor PET ligand [<sup>18</sup>F]CPFPX by CYP1A2: implications for bolus/infusion PET studies. *Nuclear Medicine and Biology*, **2006**, *33*(7), 891–898.
- [290] Holschbach, M.H.; Bier, D.; Wutz, W.; Willbold, S.; Olsson, R.A. Synthesis of the Main Metabolite in Human Blood of the A<sub>1</sub> Adenosine Receptor Ligand [<sup>18</sup>F]CPFPX. *Organic Letters*, **2009**, *11*(19), 4266–4269.
- [291] Shimada, T.; Mimura, M.; Inoue, K.; Nakamura, S.; Oda, H.; Ohmori, S.; Yamazaki, H. Cytochrome P450-dependent drug oxidation activities in liver microsomes of various animal species including rats, guinea pigs, dogs, monkeys, and humans. *Archives of Toxicology*, **1997**, *71*(6), 401–408.
- [292] Tanaka, E.; Ishikawa, A.; Horie, T. *In vivo* and *in vitro* trimethadione oxidation activity of the liver from various animal species including mouse, hamster, rat, rabbit, dog, monkey and human. *Human & Experimental Toxicology*, **1999**, *18*(1), 12–16.
- [293] Souhaili-El Amri, H.; Batt, A.M.; Siest, G. Comparison of cytochrome P-450 content and activities in liver microsomes of seven animal species, including man. *Xenobiotica*, **1986**, *16*(4), 351–358.
- [294] Skaanild, M.T.; Friis, C. Cytochrome P450 Sex Differences in Minipigs and Conventional Pigs. *Pharmacology & Toxicology*, **1999**, *85*(4), 174–180.
- [295] Stevens, J.C.; Shipley, L.A.; Cashman, J.R.; Vandenbranden, M.; Wrighton, S.A. Comparison of Human and Rhesus Monkey *In Vitro* Phase I and Phase II Hepatic Drug Metabolism Activities. *Drug Metabolism and Disposition*, **1993**, *21*(5), 753–760.

- [296] Shimada, T.; Yamazaki, H.; Mimura, M.; Inui, Y.; Guengerich, F.P. Interindividual variations in human liver cytochrome P-450 enzymes involved in the oxidation of drugs, carcinogens and toxic chemicals: studies with liver microsomes of 30 Japanese and 30 Caucasians. *The Journal of Pharmacology and Experimental Therapeutics*, **1994**, *270*(1), 414–423.
- [297] Nedelcheva, V.; Gut, I. P450 in the rat and man: methods of investigation, substrate specificities and relevance to cancer. *Xenobiotica*, **1994**, *24*(12), 1151–1175.
- [298] Eguchi, K.; Nishibe, Y.; Baba, T.; Ohno, K. Quantitation of cytochrome P450 enzymes (CYP1A1/2, 2B11, 2C21 and 3A12) in dog liver microsomes by enzyme-linked immunosorbent assay. *Xenobiotica*, **1996**, *26*(7), 755–763.
- [299] Edwards, R.J.; Murray, B.P.; Murray, S.; Schulz, T.; Neubert, D.; Gant, T.W.; Thorgeirsson, S.S.; Boobis, A.R.; Davies, D.S. Contribution of CYP1A1 and CYP1A2 to the activation of heterocyclic amines in monkeys and human. *Carcinogenesis*, **1994**, *15*(5), 829–836.
- [300] Sakuma, T.; Hieda, M.; Igarashi, T.; Ohgiya, S.; Nagata, R.; Nemoto, N.; Kamataki, T. Molecular Cloning and Functional Analysis of Cynomolgus Monkey CYP1A2. *Biochemical Pharmacology*, **1998**, *56*(1), 131–139.
- [301] Uehara, S.; Murayama, N.; Nakanishi, Y.; Zeldin, D.C.; Yamazaki, H.; Uno, Y. Immunochemical Detection of Cytochrome P450 Enzymes in Liver Microsomes of 27 Cynomolgus Monkeys. *Journal of Pharmacology and Experimental Therapeutics*, **2011**, *339*(2), 654–661.
- [302] Bullock, P.; Pearce, R.; Draper, A.; Podval, J.; Bracken, W.; Veltman, J.; Thomas, P.; Parkinson, A. Induction of Liver Microsomal Cytochrome P450 in Cynomolgus Monkeys. *Drug metabolism and Disposition*, **1995**, *23*(7), 736–748.
- [303] Sadrieh, N.; Snyderwine, E.G. Cytochromes P450 in cynomolgus monkeys mutagenically activate 2-amino-3-methylimidazo[4,5-f]quinoline (IQ) but not 2-amino-3,8-dimethylimidazo[4,5-f]quinoxaline (MeIQx). *Carcinogenesis*, **1995**, *16*(7), 1549–1555.
- [304] Berthou, F.; Guillois, B.; Riche, C.; Dreano, Y.; Jacqz-Aigrain, E.; Beaune, P.H. Interspecies variations in caffeine metabolism related to cytochrome P4501A enzymes. *Xenobiotica*, **1992**, *22*(6), 671–680.
- [305] Bogaards, J.J.P.; Bertrand, M.; Jackson, P.; Oudshoorn, M.J.; Weaver, R.J.; van Bladeren, P. J.; Walther, B. Determining the best animal model for human cytochrome P450 activities: a comparison of mouse, rat, rabbit, dog, micropig, monkey and man. *Xenobiotica*, **2000**, *30*(12), 1131–1152.
- [306] Chauret, N.; Gauthier, A.; Martin, J.; Nicoll-Griffith, D.A. *In Vitro* Comparison of Cytochrome P450-Mediated Metabolic Activities in Human, Dog, Cat, and Horse. *Drug Metabolism and Disposition*, **1997**, *25*(10), 1130–1136.
- [307] Nishimuta, H.; Nakagawa, T.; Nomura, N.; Yabuki, M. Species differences in hepatic and intestinal metabolic activities for 43 human cytochrome P450 substrates between humans and rats or dogs. *Xenobiotica*, **2013**, *43*(11), 948–955.

- [308] Nishimuta, H.; Sato, K.; Mizuki, Y.; Yabuki, M.; Komuro, S. Species Differences in Intestinal Metabolic Activities of Cytochrome P450 isoforms between Cynomolgus Monkeys and Humans. *Drug Metabolism and Pharmacokinetics*, **2011**, *26*(3), 300–306.
- [309] Sharer, J.E.; Shipley, L.A.; Vandenbranden, M.R.; Binkley, S.N.; Wrighton, S.A. Comparisons of Phase I and Phase II *In Vitro* Hepatic Enzyme Activities of Human, Dog, Rhesus Monkey, and Cynomolgus Monkey. *Drug Metabolism and Disposition*, **1995**, *23*(11), 1231–1241.
- [310] Weaver, R.J.; Thompson, S.; Smith, G.; Dickins, M.; Elcombe, C.R.; Mayer, R.T.; Burke, M.D. A Comparative Study of Constitutive and Induced Alkoxyresorufin O-Dealkylation and Individual Cytochrome P450 Forms in Cynomolgus Monkey (*Macaca Fascicularis*), Human, Mouse, Rat and Hamster Liver Microsomes. *Biochemical Pharmacology*, **1994**, *47*(5), 763–773.
- [311] Berthou, F.; Flinois, J.P.; Ratanasavanh, D.; Beaune, P.; Riche, C.; Guillouzo, A. Evidence for the Involvement of Several Cytochromes P-450 in the First Steps of Caffeine Metabolism by Human Liver Microsomes. *Drug Metabolism and Disposition*, **1991**, *19*(3), 561–567.
- [312] Yamazaki, M.; Wakasugi, C. Postmortem changes in drug-metabolizing enzymes of rat liver microsome. *Forensic Science International*, **1994**, *67*(3), 155–168.
- [313] MacLeod, S.M.; Renton, K.W.; Eade, N.R. Post Mortem Characteristics of the Hepatic Microsomal Drug Oxidising Enzyme System. *Chemico-Biological Interactions*, **1973**, *7*(1), 29–37.
- [314] Leadbeater, L.; Davies, D.R. The Stability of the Drug Metabolising Enzymes of Liver Microsomal Preparations. *Biochemical Pharmacology*, **1964**, *13*(12), 1607–1617.
- [315] Jakobsson, S.W.; Okita, R.T.; Mock, N.I.; Masters, B.S.S.; Buja, L.M.; Prough, R.A. Monooxygenase Activities of Human Liver, Lung, and Kidney Microsomes - A Study of 42 *post mortem* Cases. *Acta Pharmacologica et Toxicologica*, **1982**, *50*(5), 332–341.
- [316] Jondorf, W.R.; Donahue, J.D. Post-Mortem Changes in Liver Microsomal Protein-Synthesizing Activity. *The Biochemical Journal*, **1970**, *119*(5), 50P-51P.
- [317] Sapirstein, L.A.; Vidt, D.G.; Mandel, M.J.; Hanusek, G. Volumes of Distribution and Clearances of Intravenously Injected Creatinine in the Dog. *The American Journal of Physiology*, **1955**, *181*(2), 330–336.
- [318] Piepsz, A.; Gordon, I.; Hahn, K.; Kolinska, J.; Kotzerke, J.; Sixt, R. Determination of the technetium-99m mercaptoacetyltriglycine plasma clearance in children by means of a single blood sample: a multicentre study. *European Journal of Nuclear Medicine*, **1993**, *20*(3), 244-248.
- [319] Wanasundara, S.N.; Wesolowski, M.J.; Barnfield, M.C.; Waller, M.L.; Murray, A.W.; Burniston, M.T.; Babyn, P.S.; Wesolowski, C.A. Accurate and precise plasma clearance measurement using four <sup>99m</sup>Tc-DTPA plasma samples over 4 h. *Nuclear medicine communications*, **2016**, *37*(1), 79–86.

- [320] Lipinski, C.A.; Lombardo, F.; Dominy, B.W.; Feeney, P.J. Experimental and computational approaches to estimate solubility and permeability in drug discovery and development settings. *Advanced Drug Delivery Reviews*, **1997**, *23*(1-3), 3–25.
- [321] Di, L.; Kerns, E.H. Profiling drug-like properties in discovery research. *Current Opinion in Chemical Biology*, **2003**, *7*(3), 402–408.
- [322] Cornish, B.H.; Ward, L.C.; Thomas, B.J. Measurement of Extracellular and Total Body Water of Rats Using Multiple Frequency Bioelectrical Impedance Analysis. *Nutrition Research*, **1992**, *12*(4-5), 657–666.
- [323] Ward, L.C.; Battersby, K.J. Assessment of Body Composition of Rats by Bioimpedance Spectroscopy: Validation Against Dual-Energy X-ray Absorptiometry. *Scandinavian Journal of Laboratory Animal Sciences*, **2009**, *36*(3), 253–261.
- [324] Liu, X.; Chen, C. Free Drug Hypothesis for CNS Drug Candidates In: *Blood-Brain Barrier in Drug Discovery*. Di, L., Kerns, E.H., Eds.; John Wiley & Sons, Inc: Hoboken, NJ, **2015**; pp. 42–65.
- [325] Smith, D.A.; Di, L.; Kerns, E.H. The effect of plasma protein binding on *in vivo* efficacy: misconceptions in drug discovery. *Nature Reviews Drug Discovery*, **2010**, *9*(12), 929–939.
- [326] Poulin, P.; Burczynski, F.J.; Haddad, S. The Role of Extracellular Binding Proteins in the Cellular Uptake of Drugs: Impact on Quantitative *In Vitro*-to-*In Vivo* Extrapolations of Toxicity and Efficacy in Physiologically Based Pharmacokinetic-Pharmacodynamic Research. *Journal of Pharmaceutical Sciences*, **2016**, *105*(2), 497–508.
- [327] Poulin, P.; Haddad, S. Albumin and Uptake of Drugs in Cells: Additional Validation Exercises of a Recently Published Equation that Quantifies the Albumin-Facilitated Uptake Mechanism(s) in Physiologically Based Pharmacokinetic and Pharmacodynamic Modeling Research. *Journal of Pharmaceutical Sciences*, **2015**, *104*(12), 4448–4458.
- [328] Baker, M.; Parton, T. Kinetic determinants of hepatic clearance: Plasma protein binding and hepatic uptake. *Xenobiotica*, **2007**, *37*(10-11), 1110–1134.
- [329] Pardridge, W.M. Targeted Delivery of Hormones to Tissues by Plasma Proteins. In: *Comprehensive Physiology*. Terjung, R., Ed.; John Wiley & Sons, Inc: Hoboken, NJ, USA, **2010**; pp. 335–382.
- [330] Jones, D.R.; Hall, S.D.; Jackson, E.K.; Branch, R.A.; Wilkinson, G.R. Brain uptake of benzodiazepines: effects of lipophilicity and plasma protein binding. *The Journal of Pharmacology and Experimental Therapeutics*, **1988**, *245*(3), 816–822.
- [331] Levine, W.G. Biliary Excretion of Drugs and Other Xenobiotics. *Annual Review of Pharmacology and Toxicology*, **1978**, *18*, 81–96.
- [332] Hughes, R.D.; Millburn, P.; Williams, R.T. Molecular Weight as a Factor in the Excretion of Monoquaternary Ammonium Cations in the Bile of the Rat, Rabbit and Guinea Pig. *The Biochemical Journal*, **1973**, *136*(4), 967–978.

- [333] Atkinson, A.J.; Abernethy, D.R.; Daniels, C.E.; Dedrick, R.L.; Markey, S.P., Eds. *Principles of Clinical Pharmacology, 2<sup>nd</sup> ed.*; Elsevier: Amsterdam, Oxford, **2007**.
- [334] Toutain, P.L.; Bousquet-Mélou, A. Plasma terminal half-life. *Journal of Veterinary Pharmacology and Therapeutics*, **2004**, *27*(6), 427–439.
- [335] Iwatsubo, T.; Hirota, N.; Ooie, T.; Suzuki, H.; Shimada, N.; Chiba, K.; Ishizaki, T.; Green, C.E.; Tyson, C.A.; Sugiyama, Y. Prediction of *In Vivo* Drug Metabolism in the Human Liver from *In Vitro* Metabolism Data. *Pharmacology & Therapeutics*, **1997**, *73*(2), 147–171.
- [336] Poulin, P.; Kenny, J.R.; Hop, C.E.; Haddad, S. *In Vitro–In Vivo* Extrapolation of Clearance: Modeling Hepatic Metabolic Clearance of Highly Bound Drugs and Comparative Assessment with Existing Calculation Methods. *Journal of Pharmaceutical Sciences*, **2012**, *101*(2), 838–851.
- [337] Obach, R.S. Prediction of Human Clearance of Twenty-Nine Drugs from Hepatic Microsomal Intrinsic Clearance Data: An Examination of *In Vitro* Half-Life Approach and Nonspecific Binding to Microsomes. *Drug Metabolism and Disposition*, **1999**, *27*(11), 1350–1359.
- [338] Obach, R.S.; Baxter, J.G.; Liston, T.E.; Silber, B.M.; Jones, B.C.; MacIntyre, F.; Rance, D.J.; Wastall, P. The Prediction of Human Pharmacokinetic Parameters from Preclinical and *In Vitro* Metabolism Data. *The Journal of Pharmacology and Experimental Therapeutics*, **1997**, *283*(1), 46–58.
- [339] Ito, K.; Houston, J.B. Comparison of the Use of Liver Models for Predicting Drug Clearance Using *in Vitro* Kinetic Data from Hepatic Microsomes and Isolated Hepatocytes. *Pharmaceutical Research*, **2004**, *21*(5), 785–792.
- [340] Hallifax, D.; Foster, J.A.; Houston, J.B. Prediction of Human Metabolic Clearance from *In Vitro* Systems: Retrospective Analysis and Prospective View. *Pharmaceutical Research*, **2010**, *27*(10), 2150–2161.
- [341] Mohutsky, M.A.; Chien, J.Y.; Ring, B.J.; Wrighton, S.A. Predictions of the *In Vivo* Clearance of Drugs from Rate of Loss Using Human Liver Microsomes for Phase I and Phase II Biotransformations. *Pharmaceutical Research*, **2006**, *23*(4), 654–662.
- [342] Ito, K.; Houston, J.B. Prediction of Human Drug Clearance from *in Vitro* and Preclinical Data Using Physiologically Based and Empirical Approaches. *Pharmaceutical Research*, **2005**, *22*(1), 103–112.
- [343] Poulin, P.; Haddad, S. Toward a New Paradigm for the Efficient *In Vitro–In Vivo* Extrapolation of Metabolic Clearance in Humans from Hepatocyte Data. *Journal of Pharmaceutical Sciences*, **2013**, *102*(9), 3239–3251.
- [344] Poulin, P.; Hop, C.E.; Ho, Q.; Halladay, J.S.; Haddad, S.; Kenny, J.R. Comparative Assessment of *In Vitro–In Vivo* Extrapolation Methods used for Predicting Hepatic Metabolic Clearance of Drugs. *Journal of Pharmaceutical Sciences*, **2012**, *101*(11), 4308–4326.
- [345] Rawden, H.C.; Carlile, D.J.; Tindall, A.; Hallifax, D.; Galetin, A.; Ito, K.; Houston, J.B. Microsomal prediction of *in vivo* clearance and associated interindividual variability of six benzodiazepines in humans. *Xenobiotica*, **2005**, *35*(6), 603–625.

- [346] Riley, R.J.; McGinnity, D.F.; Austin, R.P. A Unified Model for Predicting Human Hepatic, Metabolic Clearance from In Vitro Intrinsic Clearance Data in Hepatocytes and Microsomes. *Drug Metabolism and Disposition*, **2005**, *33*(9), 1304–1311.
- [347] Shiran, M.R.; Proctor, N.J.; Howgate, E.M.; Rowland-Yeo, K.; Tucker, G.T.; Rostami-Hodjegan, A. Prediction of metabolic drug clearance in humans: *In vitro*–*in vivo* extrapolation vs allometric scaling. *Xenobiotica*, **2006**, *36*(7), 567–580.
- [348] Fischer, J.; Ganellin, C.R. *Analogue-based Drug Discovery*; Wiley-VCH Verlag GmbH & Co. KGaA: Weinheim, FRG, **2006**.
- [349] Wermuth, C.G. Similarity in drugs: reflections on analogue design. *Drug Discovery Today*, **2006**, *11*(7-8), 348–354.
- [350] Hammarlund-Udenaes, M.; Fridén, M.; Syvänen, S.; Gupta, A. On The Rate and Extent of Drug Delivery to the Brain. *Pharmaceutical Research*, **2008**, *25*(8), 1737–1750.
- [351] Sihver, W.; Holschbach, M.H.; Bier, D.; Wutz, W.; Schulze, A.; Olsson, R.A.; Coenen, H.H. Evaluation of radioiodinated 8-Cyclopentyl-3-[(*E*)-3-iodoprop-2-en-1-yl]-1-propylxanthine ([\*I]CPIPX) as a new potential A<sub>1</sub> adenosine receptor antagonist for SPECT. *Nuclear Medicine and Biology*, **2003**, *30*(6), 661–668.
- [352] Chu, X.; Bleasby, K.; Evers, R. Species differences in drug transporters and implications for translating preclinical findings to humans. *Expert Opinion on Drug Metabolism & Toxicology*, **2013**, *9*(3), 237–252.
- [353] Syvänen, S.; Lindhe, O.; Palner, M.; Kornum, B.R.; Rahman, O.; Långström, B.; Knudsen, G.M.; Hammarlund-Udenaes, M. Species Differences in Blood-Brain Barrier Transport of Three Positron Emission Tomography Radioligands with Emphasis on P-Glycoprotein Transport. *Drug Metabolism and Disposition*, **2009**, *37*(3), 635–643.
- [354] Deo, A.K.; Theil, F.-P.; Nicolas, J.-M. Confounding Parameters in Preclinical Assessment of Blood–Brain Barrier Permeation: An Overview With Emphasis on Species Differences and Effect of Disease States. *Molecular Pharmaceutics*, **2013**, *10*(5), 1581–1595.

## 7 Appendix

The calculations are performed exemplarily for one exponential term of each polyexponential function. For both functions,  $\lambda > 0$  is assumed.

### 7.1 Definite integral of $C(t)dt$ (Eq. 4)

$$\int_0^{\infty} A e^{-\lambda t} dt \quad \text{Eq. 7.1.1}$$

Since A is a constant parameter:

$$A \int_0^{\infty} e^{-\lambda t} dt \quad \text{Eq. 7.1.2}$$

Substitution:

$$u = \lambda t \quad \text{Eq. 7.1.3}$$

$$du = \lambda dt \quad \text{Eq. 7.1.4}$$

$$\frac{1}{\lambda} du = dt \quad \text{Eq. 7.1.5}$$

Substituting into Eq. 7.1.2:

$$A \int_0^{\infty} \frac{1}{\lambda} e^{-u} du \quad \text{Eq. 7.1.6}$$

$$\frac{A}{\lambda} \int_0^{\infty} e^{-u} du \quad \text{Eq. 7.1.7}$$

$$-\frac{A}{\lambda} e^{-u} \Big|_0^{\infty} \quad \text{Eq. 7.1.8}$$

Back transformation:

$$-\frac{A}{\lambda} e^{-\lambda t} \Big|_0^{\infty} \quad \text{Eq. 7.1.9}$$

Considering the characteristics of the exponential function

$$\lim_{t \rightarrow \infty} e^{-t} = 0 \quad \text{Eq. 7.1.10}$$

thus

$$-\frac{A}{\lambda} (0 - 1) = \frac{A}{\lambda} \quad \text{Eq. 7.1.11}$$

## 7.2 Definite integral of $tC(t)dt$ (Eq. 5)

$$\int_0^{\infty} t A e^{-\lambda t} dt \quad \text{Eq. 7.2.1}$$

Since A is a constant parameter:

$$A \int_0^{\infty} t e^{-\lambda t} dt \quad \text{Eq. 7.2.2}$$

Substitution:

$$u = \lambda t \quad \text{Eq. 7.2.3}$$

$$t = \frac{u}{\lambda} \quad \text{Eq. 7.2.4}$$

$$du = \lambda dt \quad \text{Eq. 7.2.5}$$

$$\frac{1}{\lambda} du = dt \quad \text{Eq. 7.2.6}$$

Substituting into Eq. 7.2.2:

$$A \int_0^{\infty} \frac{u}{\lambda} e^{-u} \frac{du}{\lambda} \quad \text{Eq. 7.2.7}$$

This integral represents a gamma function

$$\frac{A}{\lambda^2} \Gamma(2) = \frac{A}{\lambda^2} \quad \text{Eq. 7.2.8}$$

## Danksagung

Meinem Doktorvater, Herrn Prof. Dr. J. Ermert, danke ich für die Überlassung des Themas und die geduldige und umfassende Betreuung der Arbeit.

Mein besonderer Dank gilt Herrn Prof. Dr. A. Bauer, der mir die Möglichkeit eröffnet hat, an seinem Institut zu promovieren. Ich möchte ihm für das mir entgegengebrachte Vertrauen und die anregenden Gespräche danken.

Herrn Prof. Dr. U. Baumann danke ich für die Bereitschaft, meine Arbeit zu begutachten und mich im Rigorosum zu prüfen.

Herrn Prof. Dr. A. Klein möchte ich ebenfalls für seine Bereitschaft danken, mich im Rigorosum zu prüfen.

Ich danke Herrn Prof. Dr. B. Neumaier dafür, dass er mich und meine Arbeit vorbehaltlos unterstützt hat.

Bei Herrn Dr. D. Bier möchte ich mich herzlich für die intensive, persönliche Betreuung bedanken. Er war für mich Mentor, wissenschaftlicher Ansprechpartner und geduldiger Zuhörer bei Problemen aller Art.

Herrn Dr. M. Holschbach möchte ich für die wissenschaftliche Unterstützung danken, für die Bereitstellung der Referenzsubstanzen und dafür, dass er immer ein offenes Ohr für meine Sorgen und Nöte hatte.

Bei Frau F. Wedekind möchte ich mich für die anregenden wissenschaftlichen Diskussionen bedanken und dafür, dass sie mein Interesse an Statistik neu belebt hat.

Herrn Dr. C. Drerup danke ich für die wertvolle Unterstützung bei der Hochskalierung der Radiosynthesen.

Frau M. Vögeling danke ich für ihre unermüdliche Einsatzbereitschaft bei den PET-Messungen und dafür, dass ich mich bei Problemen stets an sie wenden konnte.

Herrn Dr. A. Matusch danke ich für viele unterhaltsame und lehrreiche Konversationen, die mir insbesondere am späten Abend, am Wochenende oder an Feiertagen die Zeit weniger lang erscheinen ließen.

Für die hervorragende technische Unterstützung bei den PET-Messungen möchte ich mich bei allen beteiligten Kollegen und Kolleginnen des INM-2 bedanken, insbesondere bei Frau A. Oskamp, Frau A. Radermacher, Frau A. Drechsel, Frau S. Köhler-Dibowski und Frau S. Krause.

Dem Produktionsteam des INM-5, besonders Frau B. Palm und Herrn T. Wicher, möchte ich für die Produktion der Tracer danken.

Meinen beiden Mitdotorandinnen, Frau Dr. D. Nabbi-Schröter und Frau S. Laskowski danke ich für die emotionale Unterstützung und die entspannte Atmosphäre im Büro.

Frau A. Khezami danke ich für die schnelle, unkomplizierte Hilfe bei allen Problemen hinsichtlich des Strahlenschutzes und für so manches aufbauende Gespräch.

Generell möchte ich mich bei allen Kollegen & Kolleginnen des INM-2, INM-5 und der INM Verwaltung für ihre Hilfsbereitschaft und die freundliche Arbeitsatmosphäre bedanken.

Zu guter Letzt möchte ich meinen Eltern dafür danken, dass sie mich all die Jahre vorbehaltlos unterstützt und an mich geglaubt haben.

Ich versichere, dass ich die von mir vorgelegte Dissertation selbständig angefertigt, die benutzten Quellen und Hilfsmittel vollständig angegeben und die Stellen der Arbeit – einschließlich Tabellen, Karten und Abbildungen –, die anderen Werken im Wortlaut oder dem Sinn nach entnommen sind, in jedem Einzelfall als Entlehnung kenntlich gemacht habe; dass diese Dissertation noch keiner anderen Fakultät oder Universität zur Prüfung vorgelegen hat; dass sie – abgesehen von unten angegebenen Teilpublikationen – noch nicht veröffentlicht worden ist, sowie, dass ich eine solche Veröffentlichung vor Abschluss des Promotionsverfahrens nicht vornehmen werde. Die Bestimmungen der Promotionsordnung sind mir bekannt. Die von mir vorgelegte Dissertation ist von Prof. Dr. J. Ermert betreut worden.

---

Jülich, Juli 2017